INEEL/EXT-04-02539

Finding Hidden Geothermal Resources in the Basin and Range Using Electrical Survey Techniques

A Computational Feasibility Study

J. W. Pritchett

December 2004

Idaho National Engineering and Environmental Laboratory
Bechtel BWXT Idaho, LLC

INEEL/EXT-04-02539

Finding Hidden Geothermal Resources in the Basin and Range Using Electrical Survey Techniques

J. W. Pritchett

December 2004

Idaho National Engineering and Environmental Laboratory
Idaho Falls, Idaho 83415

Prepared for the
U.S. Department of Energy
Assistant Secretary for Environmental Management
Under DOE Idaho Operations Office
Contract DE-AC07-99ID13727

TABLE OF CONTENTS

LIST OF FIGURES

LIST OF TABLES

ABSTRACT

For many years, there has been speculation about “hidden” or “blind” geothermal systems—reservoirs that lack an obvious overlying surface fluid outlet. At present, it is simply not known whether “hidden” geothermal reservoirs are rare or common. An approach to identifying promising drilling targets using methods that are cheaper than drilling is needed. These methods should be regarded as reconnaissance tools, whose primary purpose is to locate high-probability targets for subsequent deep confirmation drilling.

The purpose of this study was to appraise the feasibility of finding “hidden” geothermal reservoirs in the Basin and Range using electrical survey techniques, and of adequately locating promising targets for deep exploratory drilling based on the survey results. The approach was purely theoretical. A geothermal reservoir simulator was used to carry out a lengthy calculation of the evolution of a synthetic but generic Great Basin-type geothermal reservoir to a quasi-steady “natural state.” Postprocessors were used to try to estimate what a suite of geophysical surveys of the prospect would see. Based on these results, the different survey techniques were compared and evaluated in terms of their ability to identify suitable drilling targets. This process was completed for eight different “reservoir models.” Of the eight cases considered, four were “hidden” systems, so that the survey techniques could be appraised in terms of their ability to detect and characterize such resources and to distinguish them from more conventionally situated geothermal reservoirs. It is concluded that the best way to find “hidden” basin and range geothermal resources of this general type is to carry out simultaneous SP and low-frequency MT surveys, and then to combine the results of both surveys with other pertinent information using mathematical “inversion” techniques to characterize the subsurface quantitatively. Many such surveys and accompanying analyses can be carried out for the cost of a single unsuccessful deep “discovery well.”

1 INTRODUCTION

The Basin and Range geological province incorporates a large fraction of the territory of the southwestern United States, including all of the state of Nevada and much of Arizona and New Mexico, as well as parts of California, Oregon, Idaho, Utah and west Texas. The Basin and Range also extends into northwestern Mexico; much of the states of Sonora and Chihuahua lie within the province. Since the Eocene (~45 Ma), the entire Basin and Range has been subjected to east-west tectonic extension, which has caused the surface area of the region to double since that time. The horizontal east-west stretching has been accompanied by the development of a large number of steeply dipping normal faults with a dominant north-south orientation distributed throughout the region. Vertical motions along these faults have created a series of north-south oriented hills and mountains (the "ranges") separated by sediment-filled valleys (the "basins").

This characteristic topographic pattern prevails throughout the Basin and Range (see Figure 1.1), with north-south oriented mountains and valleys and "rangefront faults" located on either side of each valley. For much of the Pleistocene many of the basins were inundated with glacial meltwaters, but since about 10,000 years ago these lakes have dried up and today the basins are generally dry with salt pans occupying the valley floors. The largest remnant is Utah's Great Salt Lake, which is only one-tenth the size of the vanished Lake Bonneville that covered much of the western part of the state 20,000 years ago. Extensional motions continue to this day (the stretching rate generally exceeds one centimeter per year), and the area is subject to pervasive and occasionally intense seismic activity and intermittent volcanism.

The extensional stretching responsible for the formation of the Basin and Range also caused thinning of the earth's crust in the area, to an average thickness of only around 10 kilometers (compared to the 30 km crustal thickness that prevails elsewhere in North America). As a consequence, the underlying mantle is closer to the earth surface in the Basin and Range, so that upward heat flow is enhanced in the entire area (Figure 1.2). The "Great Basin" (the northwestern part of the Basin and Range, including most of Nevada as well as parts of eastern California, southern Idaho, southeastern Oregon and western Utah), is bordered by the Sierra Nevada and Cascade ranges to the west and the Colorado Plateau to the east. The Great Basin is characterized by enhanced heat flow, with evidence of recent volcanism and numerous surface manifestations of subsurface geothermal activity such as hot springs, fumaroles and geysers. These surface manifestations are usually found in association with the rangefront faults.

Several geothermal power stations located in the Great Basin supply electricity to the grid (see Table 1.1). At present, the total geothermal electrical generation capacity of the region is either 260 MWe or 530 MWe, depending on whether or not the 270 MWe Coso geothermal field, located 50 miles west of Death Valley in southeastern California, is

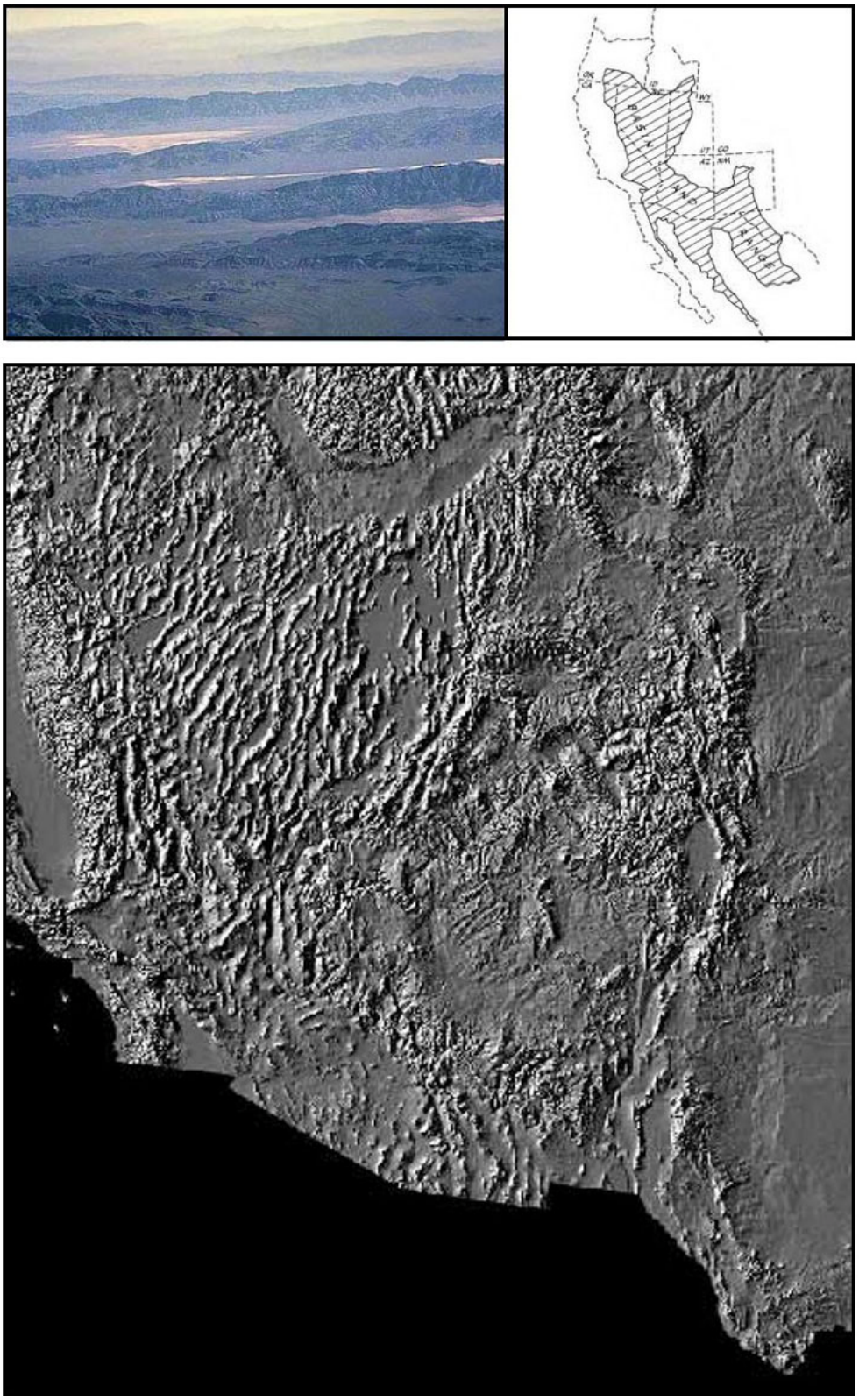

Figure 1.1. Basin and Range terrain. Images courtesy United States Geological Survey.

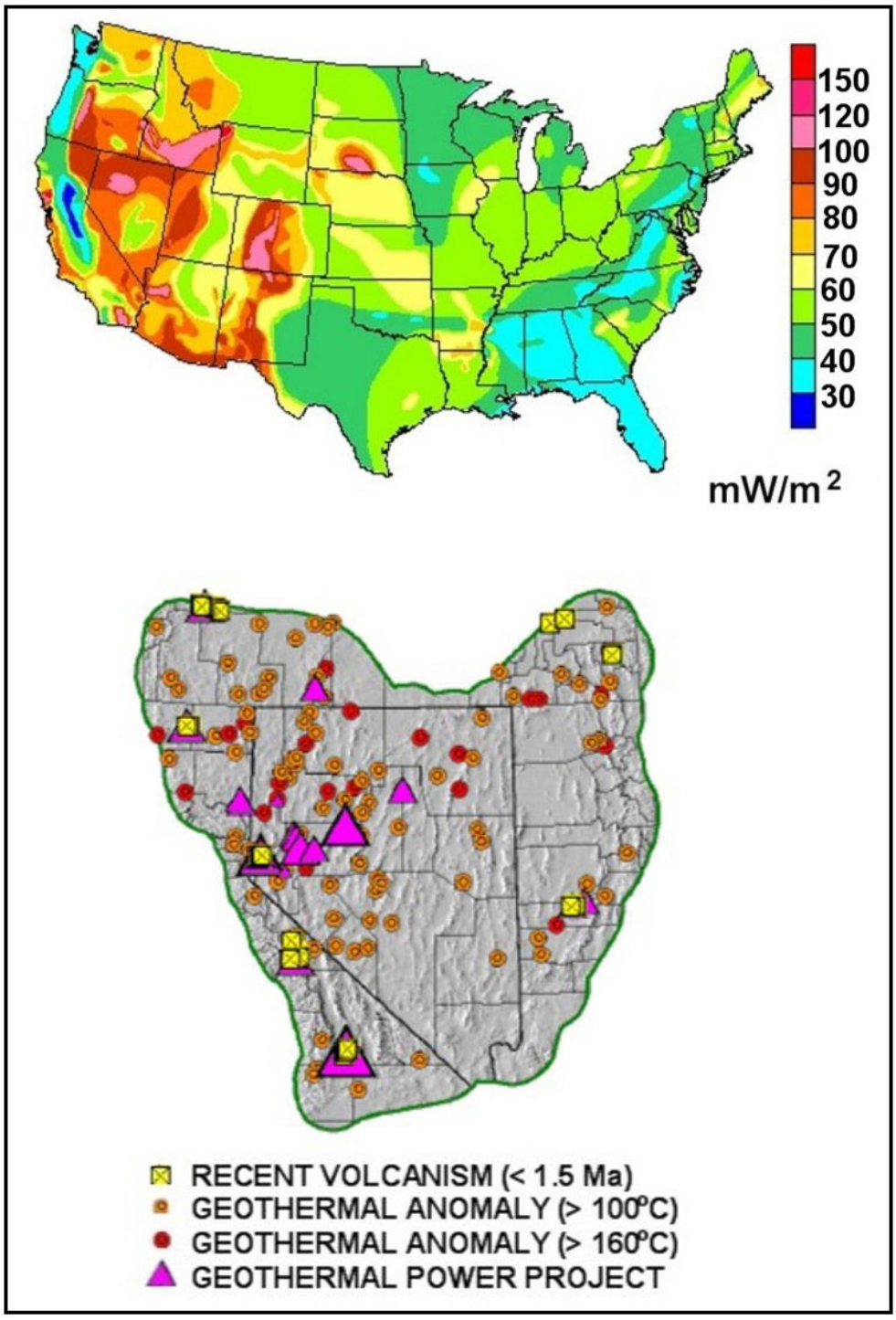

Figure 1.2. Geothermal potential of the Basin and Range. *Upper:* regional heat flow distribution in the 48 contiguous United States (image courtesy Geothermal Laboratory, Southern Methodist University). *Lower:* geothermal features of the Great Basin (image courtesy Great Basin Center for Geothermal Energy, University of Nevada at Reno).

Table 1.1. Geothermal power projects presently operating in the Basin and Range.

Field	Capacity	Type	Location
Coso	270 MWe	Flash	Inyo County, California
Steamboat	75 MWe	Flash/Binary	Washoe County, Nevada
Dixie Valley	62 MWe	Flash	Churchill County, Nevada
Brady Hot Springs	27 MWe	Flash/Binary	Churchill County, Nevada
Roosevelt Hot Springs	26 MWe	Flash	Beaver County, Utah
Soda Lake	23 MWe	Binary	Churchill County, Nevada
Beowawe	17 MWe	Flash	Eureka County, Nevada
Cove Fort	11 MWe	Flash/Binary	Beaver County, Utah
Desert Peak	10 MWe	Flash	Churchill County, Nevada
Empire	5 MWe	Binary	Washoe County, Nevada
Wabuska	2 MWe	Binary	Lyon County, Nevada
Amadee	2 MWe	Binary	Lassen County, California

considered part of the Great Basin (some authors include it, but not all). The total geothermal electrical capacity of the United States is presently about 2800 MWe, so despite the obvious promise of the heat flow found in the Basin and Range, the area represents only about 1/5 of this total (1/11 if Coso is excluded). The U. S. Department of Energy estimates that, using existing technology, the geothermal electrical generating capacity of the United States could be tripled in the near future by developing presently-untapped hydrothermal resources. Clearly, much of this growth will have to take place in the Basin and Range. Increasing Basin and Range geothermal electricity production by an order of magnitude or more in coming years constitutes a formidable challenge and will require the identification, location, characterization and development of many new subsurface geothermal reservoirs.

Existing geothermal electrical power projects (in the Basin and Range and elsewhere in the world) are fueled by geothermal reservoirs that were located by techniques analogous to the oil-exploration methods of the early 20th century – that is, "drilling on seeps". Subsurface geothermal systems are inherently dynamic, with vigorous convective flows that often result in outflows of hot fluids to the earth surface immediately above. Therefore, if deep wells are drilled in the neighborhood of surface geothermal manifestations such as areas of hydrothermal alteration, hot springs, geysers, sinter deposits, areas of steaming ground and/or fumaroles, a subsurface geothermal reservoir containing both sufficient hot fluid and sufficient permeability to support production operations will sometimes be found.

Usually, prior to major financial commitment to a power project, a series of shallow "heat flow holes" will be drilled in the immediate area of the surface features to try to establish the local vertical temperature gradient, which may then be extrapolated to estimate

temperatures at economically drillable depths. Chemical analyses of the fluids recovered from the natural surface discharges and from these shallow wells can be used to estimate the source temperature of the underlying geothermal system using various chemical "geothermometers". If these indications are favorable, one or more deep exploration wells may be drilled to directly ascertain the presence or absence of a permeable hot resource. Such deep drilling is very expensive (typically millions of dollars per well). In practice, most such deep exploration holes are unsuccessful – it has been estimated that the average success rate (deep exploration wells that prove capable of sustained steam discharge at economic rates for commercial generation of electricity) is less than 20%.

For many years, there has been speculation about "hidden" or "blind" geothermal systems – reservoirs that lack an obvious overlying surface fluid outlet. Many believe that such systems may be as common as the more "visible" systems, but of course there is no way to tell, since an actual field encounter with such a reservoir would be purely fortuitous. Deep exploration drilling is far too expensive to be undertaken in "random search" mode. At present, it is simply not known whether "hidden" geothermal reservoirs are rare or common. But whatever their frequency of occurrence, it is clear that what is needed is an approach to identifying promising drilling targets using methods that are far cheaper than drilling itself. These methods should be regarded as reconnaissance tools, whose primary purpose is to locate high-probability targets for subsequent deep confirmation drilling.

The present author has been engaged in the development and application of computer software for studying the behavior of geothermal reservoirs since the early 1970's, including the development and deployment of geothermal "reservoir simulators" – programs capable of simulating the transient multidimensional flow of fluid mass and heat deep within the earth using finite-difference computational techniques. During the past ten years or so, the capabilities of the "reservoir simulators" have been augmented by the development of "geophysical postprocessors" (*Pritchett*, 1995). Given a computed time-dependent history of subsurface conditions (representing the exploitation history of a particular geothermal field, for example), the "postprocessors" may be applied to calculate the temporal changes that would be observed at the earth surface using time-lapse geophysical surveys such as repeat microgravity, seismic or electrical surveys. If the "computed" histories are then compared with "measured" histories of the same quantities, constraints are provided for the reservoir modeling process, leading eventually to more robust computational models of the reservoir and more reliable predictions of future performance (*Pritchett et. al,* 2000). Postprocessors are presently available to represent microgravity surveys, electrical resistivity surveys (including conventional DC surveys, MT surveys and CSAMT surveys), and self-potential (SP) surveys (*Pritchett,* 2002; 2003). A postprocessor to represent active seismic survey results is also under development.

Although the postprocessors were originally developed for use in *time-lapse* mode in connection with computational "history-match" studies of reservoir behavior under production, some of them are also suitable for use in *static* mode in connection with "natural-state" calculations of the nearly steady pre-exploitation state of a geothermal reservoir, as it would be encountered during preliminary exploration. The microgravity postprocessor is of little use for this purpose, since no temporal changes will occur and the static pre-production

spatial distribution of gravity anomaly at the earth surface is dominated by (usually poorly constrained) subsurface geological structure and is relatively unaffected by the distributions of temperature and permeability crucial to resource assessment. The seismic postprocessor is likewise of little interest, since geothermal reservoirs (unlike oilfields) usually lack characteristic seismic reflection structures analogous to hydrocarbon-trapping sedimentary anticlines, and since seismic returns are only slightly affected by temperature or the presence or absence of permeability. Furthermore, seismic surveys are notoriously expensive to carry out compared to other more promising geophysical survey techniques suitable for geothermal exploration.

The remaining survey methods that the postprocessors can simulate (all electrical survey techniques) are much more promising. These include (1) conventional DC electrical resistivity surveys, (2) electromagnetic resistivity surveys such as natural magnetotelluric (MT) and controlled-source audio-frequency magnetotelluric (CSAMT) surveys, and (3) surveys of earth-surface electrical "self-potential" (SP). The resistivity surveys are useful because geothermal reservoirs are usually characterized by substantially reduced electrical resistivity relative to their surroundings. Solid rock itself is normally an excellent insulator, so electric current moving through the reservoir will pass mainly through the fluid-filled pore spaces and fractures. Therefore, the resistivity of the reservoir as a whole will depend upon the resistivity of the fluid itself (which decreases with increasing temperature and also decreases with increasing dissolved solids content, which is frequently a feature of deep magmatic fluids) and upon the continuity of the current paths through the rock (which will tend to increase with increasing rock permeability, further reducing overall electrical resistivity).

The self-potential (SP) technique is at least as promising, since the electrical potential distribution at the earth surface depends upon both the electrical resistivity of the earth and upon the distribution of natural subsurface electric current, according to Ohm's Law. The electric current, in turn, is caused by fluid flow dragging electrons along in the molecular-scale "electrical double layer" at the interfaces between the fluid and the rock surface (the surfaces of pores and fractures) – a process known as "electrokinetic coupling" (*Ishido and Mizutani,* 1981). As a result, the SP distribution measured at the surface is sensitive to the presence of subsurface convective flow, which is a feature characteristic of all liquid-dominated hydrothermal reservoirs, including all geothermal resources found to date within the Basin and Range.

The purpose of the present study was to appraise the feasibility of finding "hidden" geothermal reservoirs in the Basin and Range using these electrical survey techniques, and of adequately locating promising targets for deep exploratory drilling based on the survey results. The approach was purely theoretical. The STAR geothermal reservoir simulator (*Pritchett,* 2002) was used to carry out a lengthy calculation (representing 100,000 years of real time) of the evolution of a synthetic but generic Great Basin-type geothermal reservoir to a quasi-steady "natural state". Once this stable state was reached, the postprocessors were used to try to estimate what a suite of geophysical surveys of the prospect would see. Then, based on these results, the different survey techniques were compared and evaluated in terms of their ability to identify suitable drilling targets. This process was completed for eight

different “reservoir models”, which differed in the boundary conditions imposed at the bottom of the computational domain (and therefore in both the total resource potential for electricity production and the character of the final stable three-dimensional temperature distribution within the region). Of the eight cases considered, four were “hidden” systems so that the survey techniques could be appraised in terms of their ability to detect and characterize such resources and to distinguish them from more conventionally-situated geothermal reservoirs.

2 MODELING HYPOTHETICAL GEOTHERMAL SYSTEMS

The STAR numerical reservoir simulator was first used to calculate the "natural state" of each of the eight reservoir models. Figure 2.1 indicates the physical situation considered. The origin of coordinates is taken to lie at the earth surface, in the middle of a north-south oriented valley between two mountain ranges. The x-coordinate measures distance eastward of the origin, the y-coordinate measures distance northward, and the z-coordinate measures vertical elevation above the valley floor. For simplicity, the elevation of the ground surface (z_S) is taken to depend on x (east-west position) only. Between $x = 0$ and $x = +3$ km, the terrain is flat ($z_S = 0$). Then, the surface begins to rise at a 12.5% slope, reaching 250 meters elevation at $x = +5$ km. Between $x = +5$ km and $x = +9$ km, the slope decreases, and the surface again becomes horizontal (at $z_S = +500$ meters) beyond x = +9 km. The topography is symmetrical in the westward direction, so that $z_S(-x) = z_S(+x)$.

The "flow grid" occupies 500 cubic kilometers (10 km north-south × 10 km east-west centered on the origin, and extending from the valley floor to 5 km depth). This is the region within which the STAR reservoir simulator was applied to calculate fluid mass and heat flow. An even larger region was used to calculate electrical effects arising from hydrothermal phenomena taking place within the "flow grid" – the "electrical grid" overlaps the "flow grid" and extends over -10 km $\le x \le +10$ km, -10 km $\le y \le +10$ km, and from the earth surface down to –10 km elevation (a total volume of 4097 km^3).

To accurately delineate the sharp gradients that frequently appear in geothermal systems, the STAR "flow grid" uses a high degree of spatial resolution, as indicated in Figure 2.2. The same computational grid geometry was used for all eight cases. In the vertical direction, 25 layers (each 200 meters thick) were assigned. In the north-south (y) direction, the space interval size was likewise uniform, at 400 meters per block. In the east-west (x) direction, 200 meter resolution was used within the valley floor region, with 400-meter resolution beyond. The total number of STAR grid blocks was 25,000 (40 × 25 × 25 in the x-, y-, and z-directions respectively).

In the interests of simplicity, all rock formations within the 500 km^3 STAR "flow grid" computational volume were taken to have the following uniform properties:

Porosity	10 %
Grain density	2700 kg/m^3
Dry density	2430 kg/m^3
Grain heat capacity	1000 J/kg-°C
Thermal conductivity	3 W/m-°C

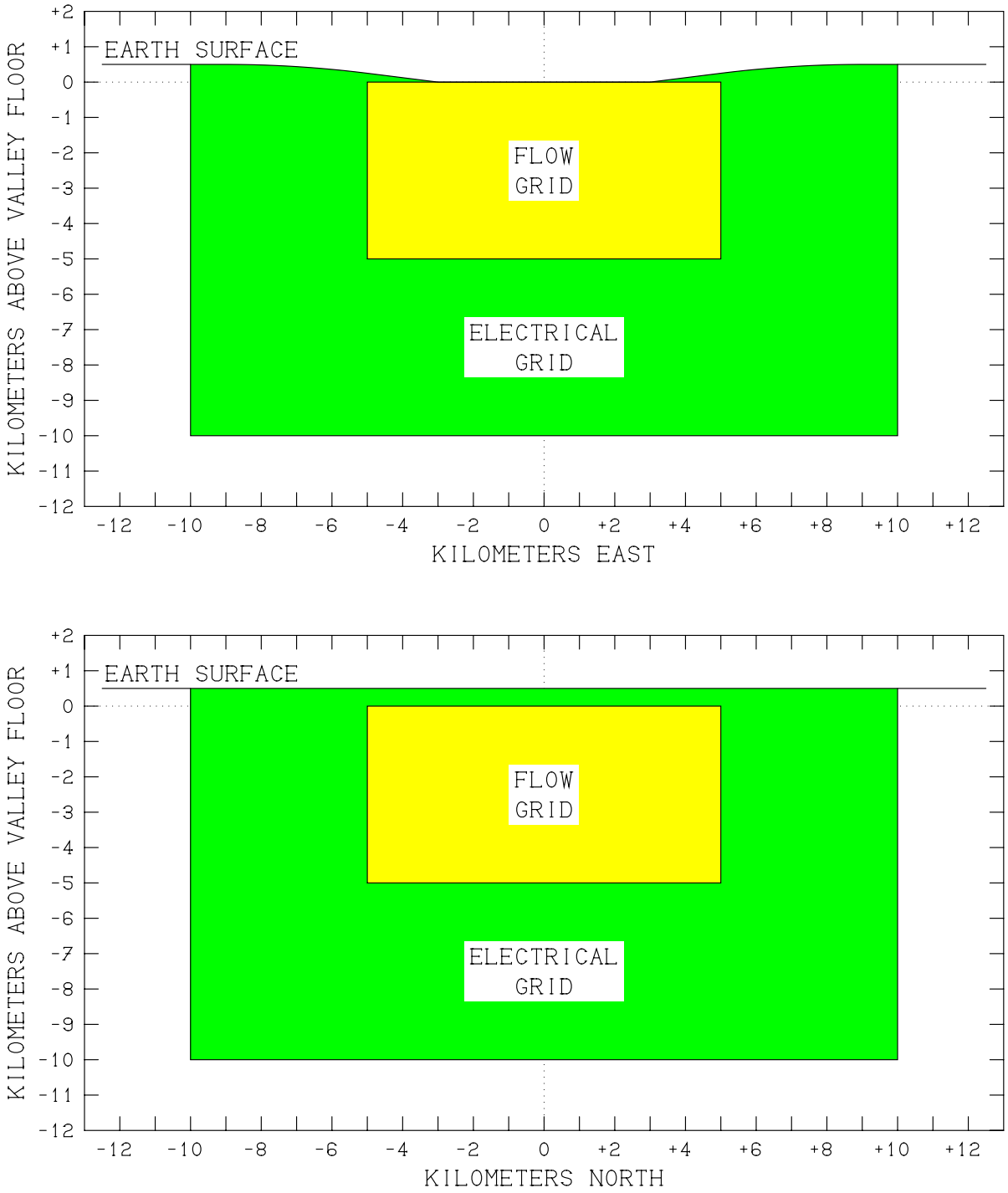

Figure 2.1. Spatial extent of computational grids employed for calculation of fluid mass and heat flow using the STAR reservoir simulator (*yellow*) and of electrical potentials using the DC, MT and SP geophysical postprocessors (*green*).

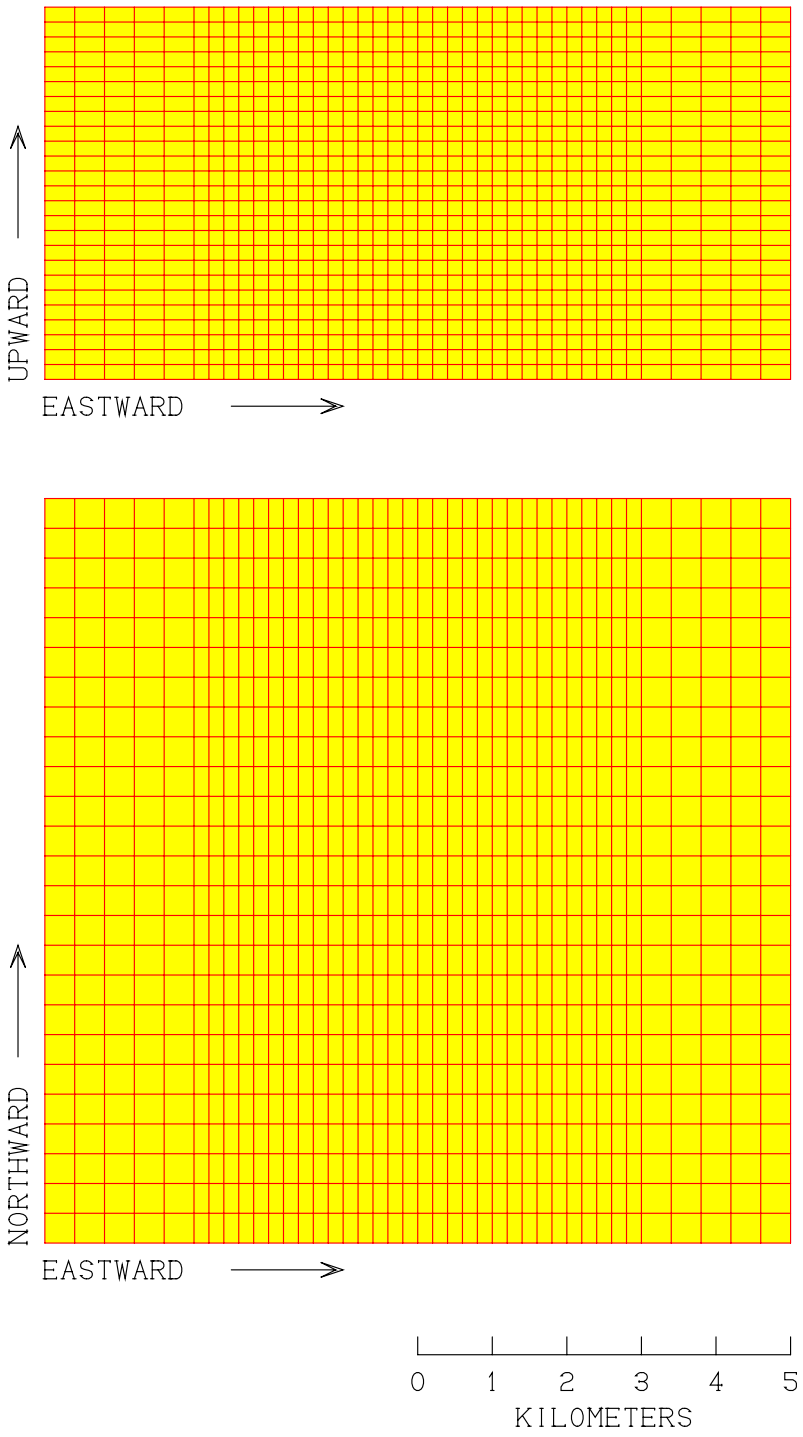

Figure 2.2. Spatial discretization of STAR computational grid used to calculate fluid mass and heat flow. Grid spacing is either 200 or 400 meters. Total grid volume is 500 cubic kilometers. Total number of grid blocks is 25,000.

but the distribution of absolute permeability was markedly non-uniform, as will be seen below. Models were also assigned for relative permeability and capillary pressure effects, but none of the eight "synthetic reservoirs" ever developed a two-phase (water/steam) region in the subsurface, so these models were never used.

To assign the permeability distribution throughout the STAR grid volume, it was assumed that the subsurface structure could be subdivided into seven different "formations", as follows (also see Figures 2.3 – 2.10):

(1) ***Peripheral Rock.*** This formation occupies all the volume with $x < -3$ km, $x > +3$ km, $y < -3$ km or $y > +3$ km, and is of very low permeability (horizontal permeability $k_H = 1/4$ millidarcy and vertical permeability $k_V = 1/16$ millidarcy). Note that one millidarcy is taken to be equal to 10^{-15} m^2 exactly for purposes of this study. This formation occupies 64% of the total grid volume.

(2) ***Deep Aquitard.*** This formation occupies all the volume within -2.8 km $\le x \le +2.8$ km, -3.0 km $\le y \le +3.0$ km, and from the grid base at $z = -5.0$ km up to a plane with average elevation -3.2 km and a down-dip to the west of 9.46° (1:6 gradient), and occupies 12.096% of the total grid volume. The permeability ($k_H = 1$ md, $k_V = 1/4$ md) is greater than that of the "peripheral rock", but is still low.

(3) ***Lower Aquifer.*** This formation overlies the "deep aquitard' and is of constant thickness (1000 meters), occupying 6.72% of the total grid volume. The permeability is moderate ($k_H = 4$ md, $k_V = 1$ md).

(4) ***Upper Aquifer.*** This formation would presumably be the main productive horizon if the hypothetical geothermal reservoir were developed for electric power production, and has high permeability ($k_H = 16$ md, $k_V = 4$ md). It directly overlies the "lower aquifer" and is similarly 1000 meters thick. The depth to reach this productive horizon increases with increasing westward distance. Like the "lower aquifer", this formation occupies 6.72% of the grid volume.

(5) ***Western Fault Zone.*** Also of high permeability, this formation is vertically oriented and moreover has vertical permeability exceeding horizontal permeability ($k_H = 4$ md, $k_V = 16$ md). It represents the "rangefront fault" which forms the western boundary of the valley. Such faults are usually steeply dipping (> 60°) – for simplicity, the fault zone was taken as entirely vertical in the present model. This region is only 200 meters thick in the east-west direction (-3.0 km $\le x \le -2.8$ km), extends over -3.0 km $\le y \le +3.0$ km in the north-south direction, and reaches from the bottom of the study volume up to the local base of the impermeable "caprock" at $z = -1.6$ km. Note that this fault is "buried" and does not reach all the way to the ground surface. The fault zone's volume is only 0.816% of the total grid volume.

Continued on page 2-13

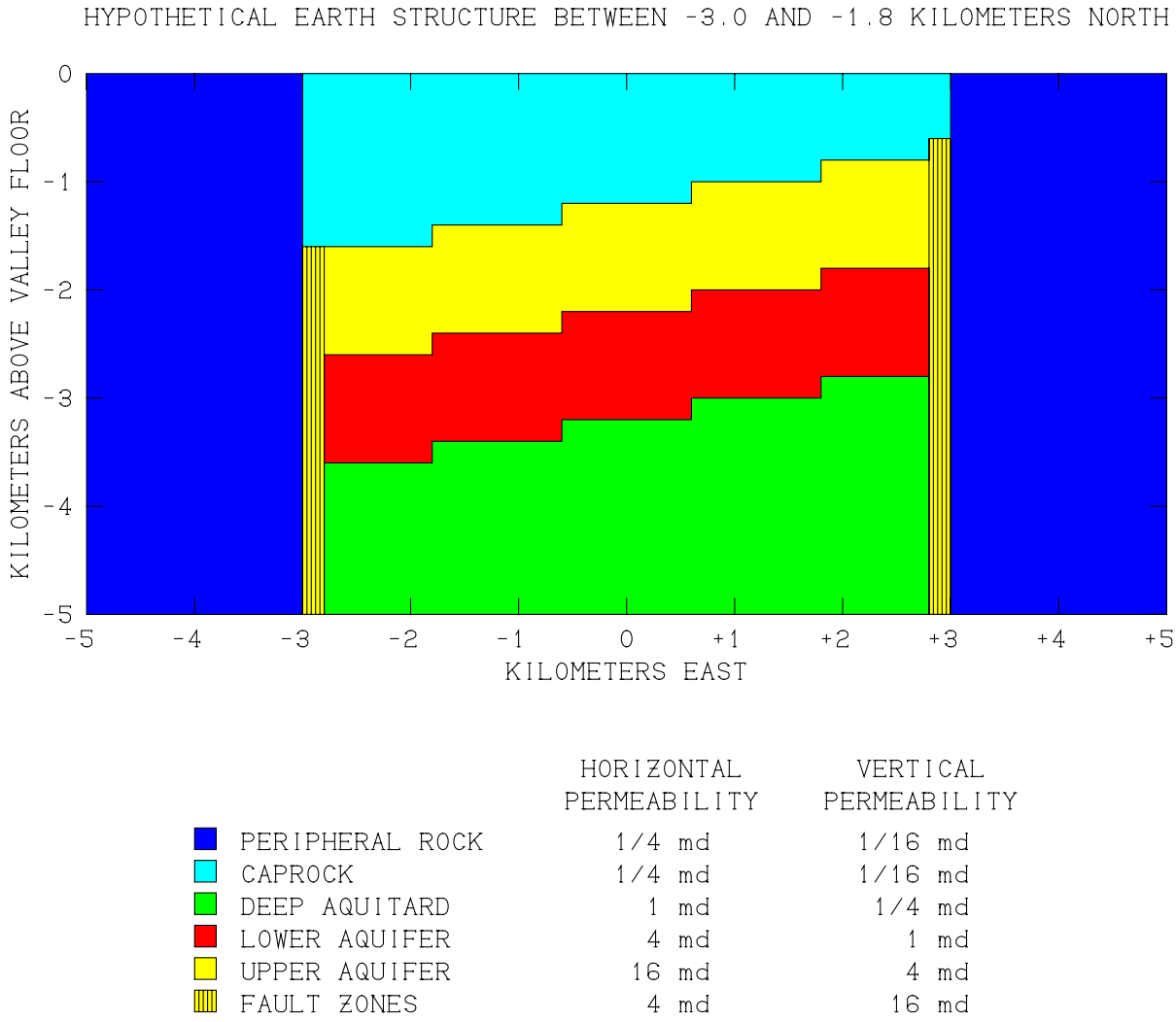

Figure 2.3. East-west vertical cross-section showing distribution of formation permeability between $y = -3.0$ and $y = -1.8$ kilometers North ($j = 6 - 8$).

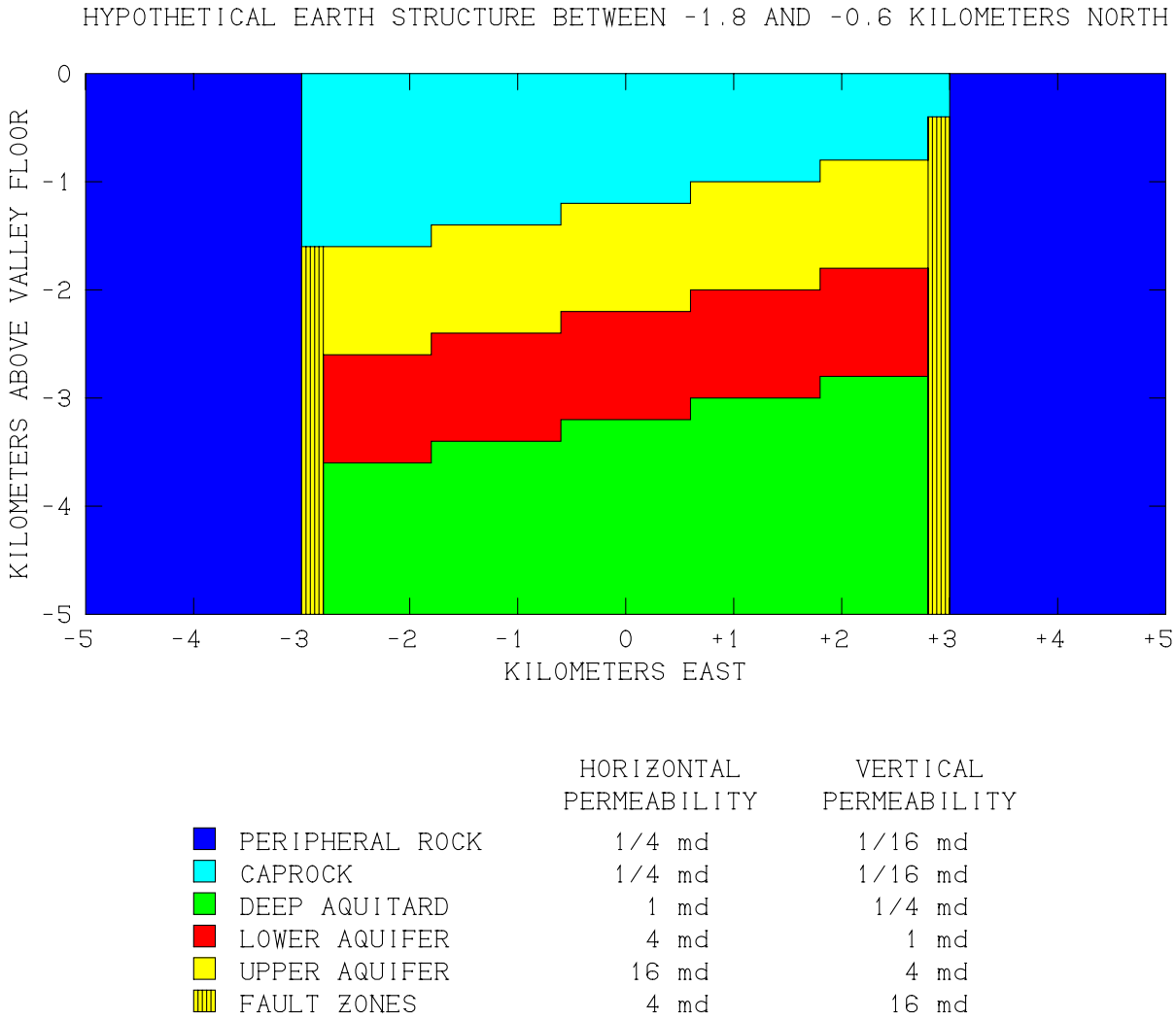

Figure 2.4. East-west vertical cross-section showing distribution of formation permeability between $y = -1.8$ and $y = -0.6$ kilometers North ($j = 9 - 11$).

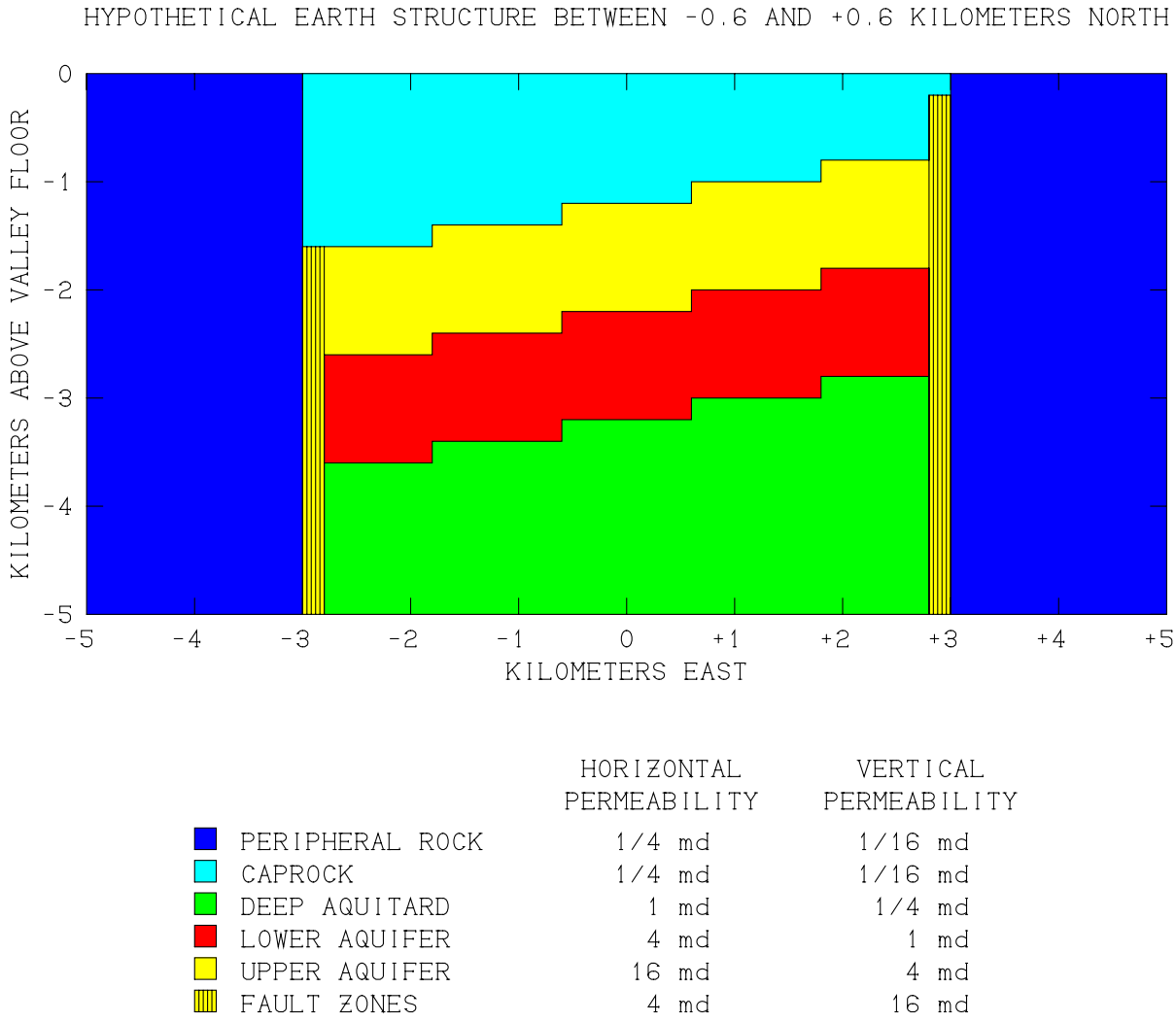

Figure 2.5. East-west vertical cross-section showing distribution of formation permeability between $y = -0.6$ and $y = +0.6$ kilometers North ($j = 12 - 14$).

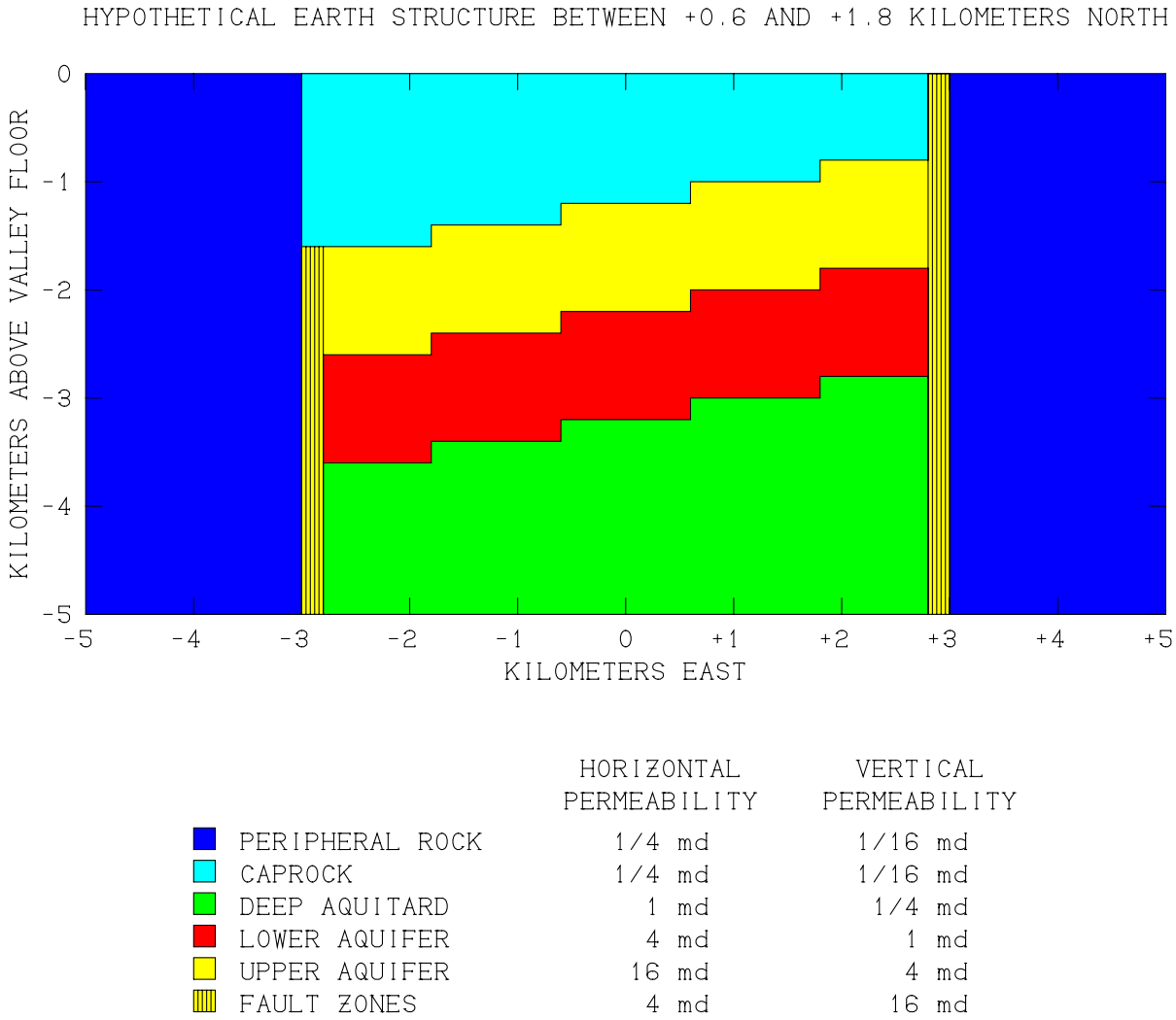

Figure 2.6. East-west vertical cross-section showing distribution of formation permeability between y = +0.6 and y = +1.8 kilometers North (j = 15 – 17). Note that eastern fault zone intersects the earth surface in this region.

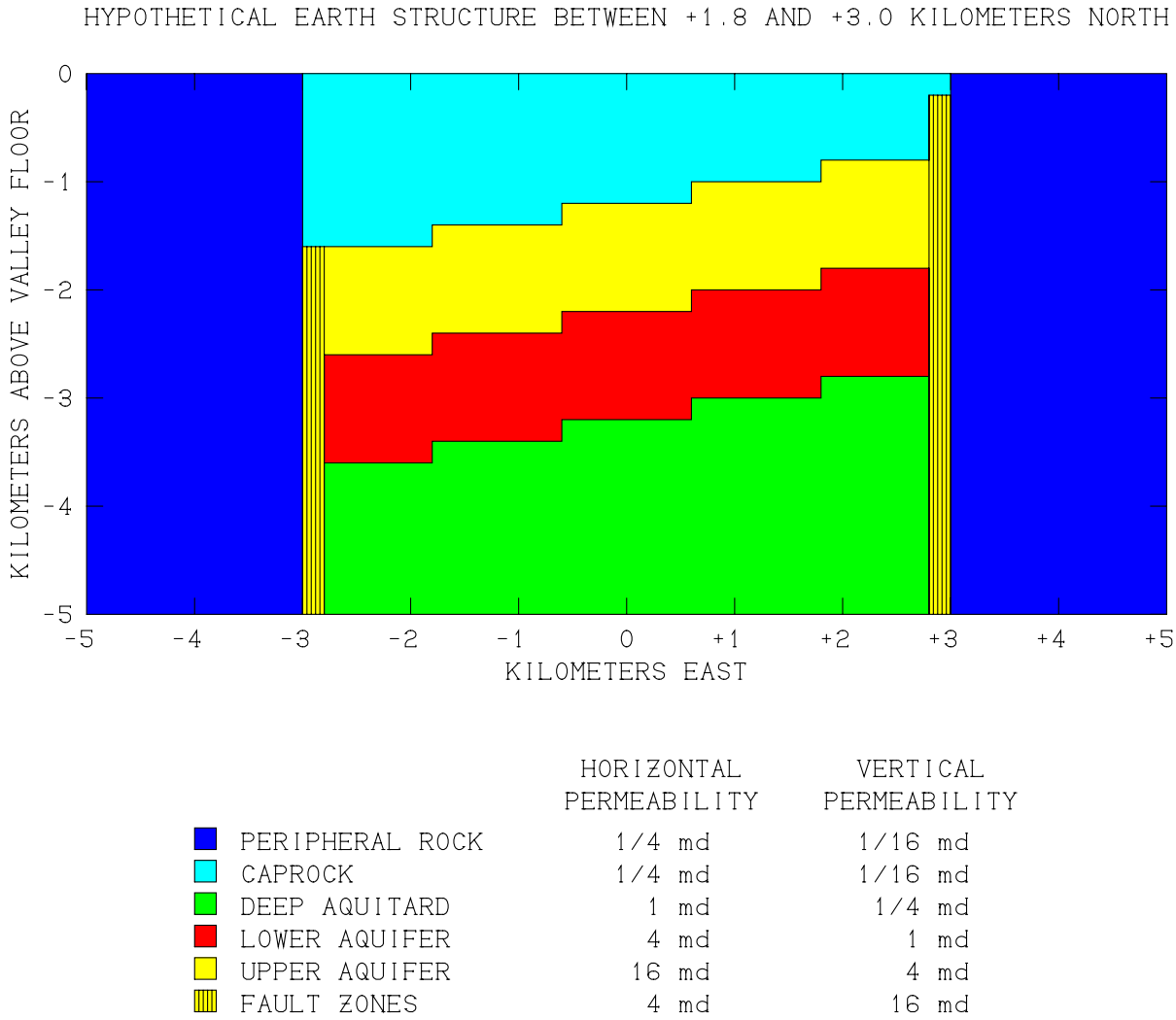

Figure 2.7. East-west vertical cross-section showing distribution of formation permeability between y = +1.8 and y = +3.0 kilometers North (j = 18 – 20).

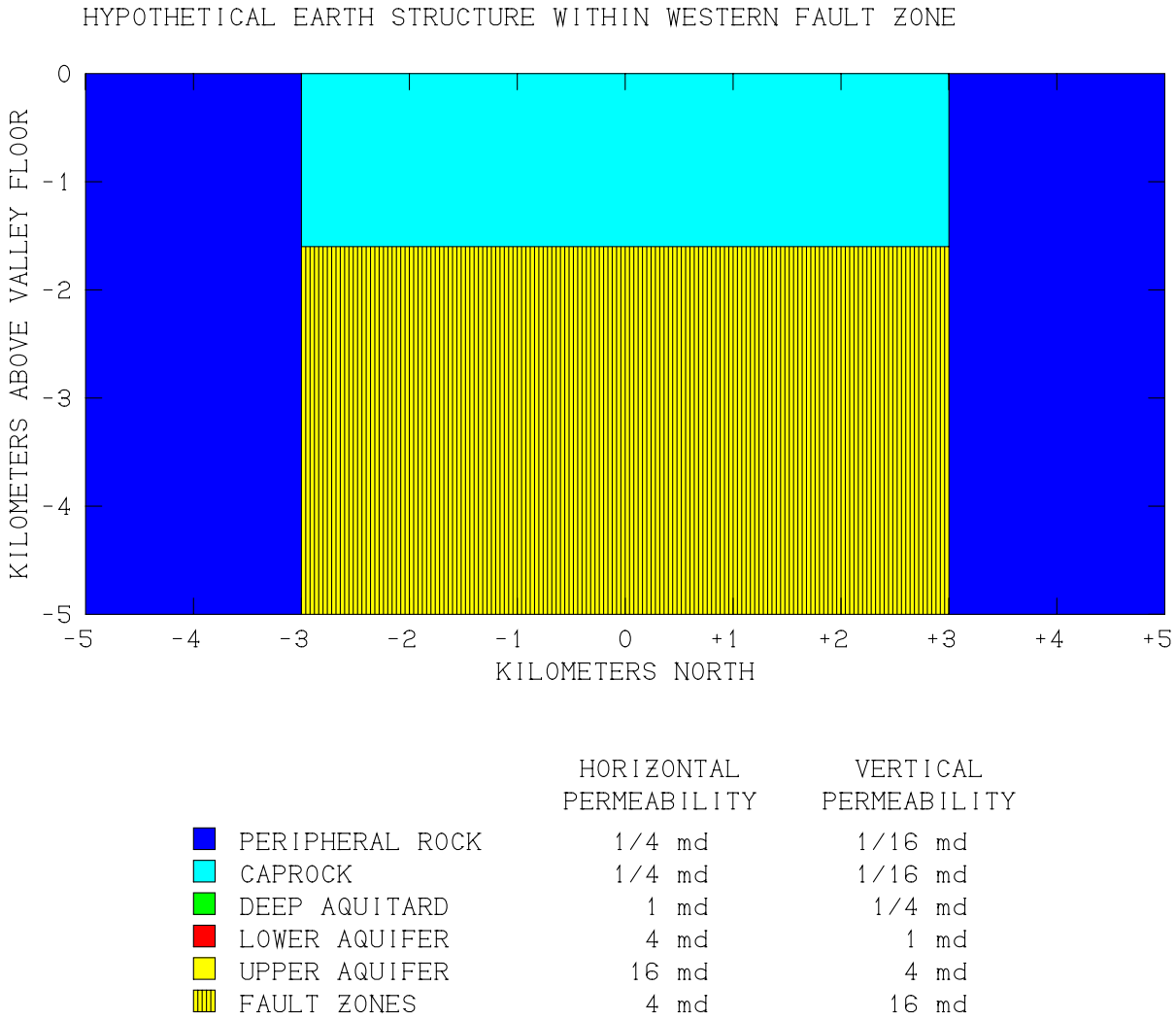

Figure 2.8. North-south vertical cross-section showing distribution of formation permeability in the plane of the western fault zone ($i = 6$).

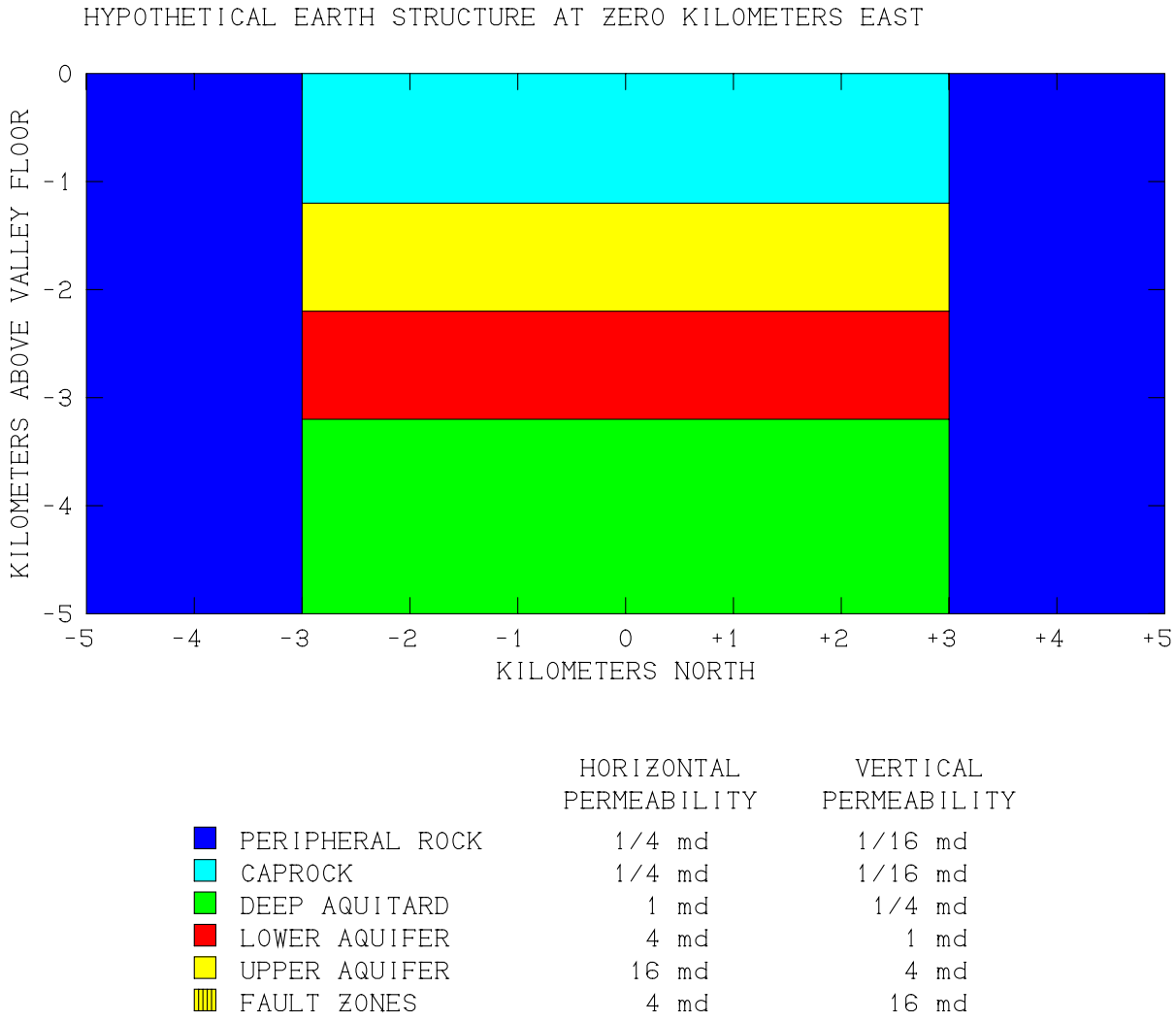

Figure 2.9. North-south vertical cross-section showing distribution of formation permeability between $x = -0.6$ and $x = +0.6$ kilometers East ($i = 18 - 23$).

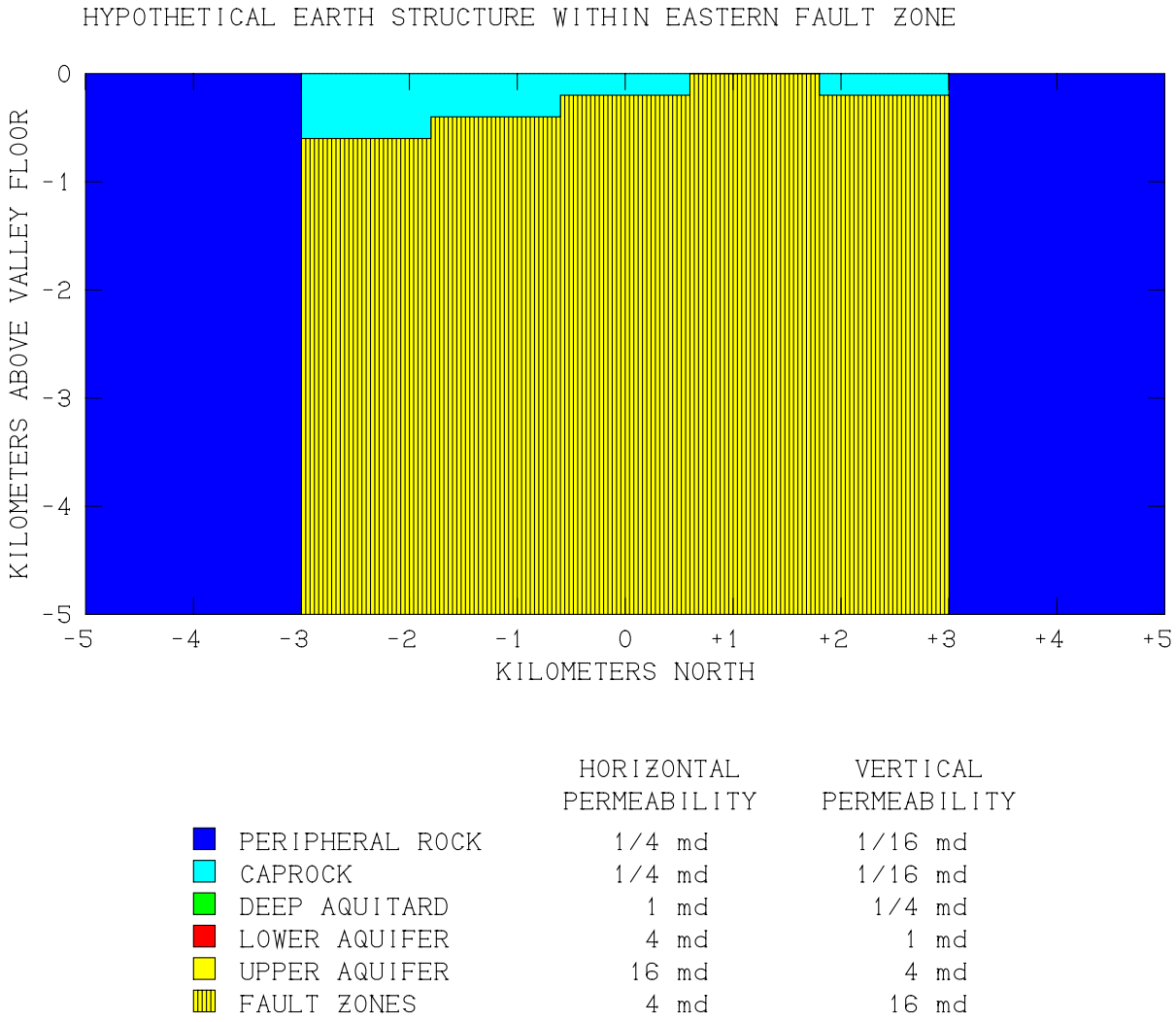

Figure 2.10. North-south vertical cross-section showing distribution of formation permeability in the plane of the eastern fault zone ($i = 35$).

(6) ***Eastern Fault Zone.*** Similarly, this formation is vertically oriented with a high vertical permeability (k_H = 4 md, k_V = 16 md – same as the "western fault zone"), and represents the rangefront fault on the east side of the valley. In the horizontal plane, it is also 200 meters thick (+2.8 km ≤ x ≤ +3.0 km), and extends over –3.0 km ≤ y ≤ +3.0 km in the north-south direction. The fault zone extends from the bottom of the study volume at z = –5 km up to a level that varies with north-south position as indicated in Figure 2.10. Note that this fault is exposed between y = +0.6 km and y = +1.8 km, and is only buried shallowly elsewhere. The formation occupies 1.1328% of the total grid volume.

(7) ***Caprock.*** The "caprock" occupies the remainder of the study volume (8.5152%) in the region –3 km ≤ x ≤ +3 km, –3 km ≤ y ≤ +3 km and extends downward from the earth surface to either the top of the "upper aquifer" or the top of the "fault zones". The permeability is very low, and is the same as that of the "peripheral rocks" (k_H = 1/4 md, k_V = 1/16 md).

The above properties (porosity, grain density, heat capacity, thermal conductivity and absolute permeability) suffice to describe the rock formations for purposes of calculating single-phase unsteady fluid and heat flow within the system. The subsurface fluid is treated as pure H_2O with a "tracer" used to track dissolved solids. The *"total dissolved solids"* content – "TDS" – does not exceed 3000 ppm (*"parts per million"*) by mass, and will therefore have negligible effects on fluid thermomechanical properties, justifying the "tracer" treatment.

Additional properties are needed, however, for application of the DC resistivity, MT resistivity, and SP ("self-potential") postprocessors. The SP postprocessor requires values for the parameters "δpH" and "tortuosity", as described by *Ishido and Mizutani* (1981). The following "default" values were adopted for the present study:

$$\delta\mathrm{pH} = 5$$

$$\mathrm{tortuosity} = 1.4$$

and were used for all formations for all computed cases. The main additional requirement imposed by the electrical postprocessors is the specification of a model for the electrical resistivity of the subsurface, and how it is likely to vary with changing subsurface conditions. Several models are available in the literature for estimating electrical resistivity, but probably the most widely accepted is "Archie's Law", which specifies the electrical resistivity of the formation as a whole (Ω) in terms of the resistivity of the fluid occupying the pore spaces (Ω_F) by:

$$\Omega = \frac{\Omega_F}{\left(C_A \varphi^2\right)}$$

where φ represents porosity (equal to 0.1 for all formations here) and C_A is a dimensionless constant of order unity. Archie's Law was adopted for all calculations reported herein. To obtain the fluid resistivity (Ω_F), it was assumed that the dissolved solids consist exclusively of sodium chloride – the electrical resistivity of dilute NaCl brines as functions of temperature, pressure and salt concentration is well-known and subroutines are available in the various postprocessors for its automatic evaluation. This representation treats the resistivity as independent of temperature if $T < 25°C$, but resistivity decreases rapidly with increasing temperature above that value. Resistivity is also a strongly decreasing function of TDS (NaCl) content. In the range of present interest, the dependence upon pressure is very weak. Finally, it has long been recognized that, all else being equal, the electrical resistivities of saturated rock formations of high permeability tend to be smaller than those of relatively impermeable rocks, owing to the better continuity of fluid (and electric current) flow paths. Somewhat arbitrarily, the dimensionless constant "C_A" (above) was assigned the following values for purposes of these calculations to take this into account:

Eastern fault zone, western fault zone and upper aquifer: $C_A = 2$
All other formations: $C_A = 1$

The resulting dependence of formation electrical resistivity upon temperature and TDS content for both the "high-permeability" ($C_A = 2$) and "low-permeability" ($C_A = 1$) formations is depicted in Figure 2.11. As noted above, the effect of pressure is essentially negligible but was retained anyway in these calculations – the values depicted in Figure 2.11 are therefore, strictly speaking, only valid for 200 bars pressure.

Resistivities are required for the entire volume of the "electrical grid" (Figure 2.1), not just the STAR "flow grid" volume. This includes not just the region beyond ±5 km lateral distance, but the volume of the "mountains" above $z = 0$ and the entire region below $z = –5$ km. For this purpose, it was assumed that, for elevations above –5 km, the same "Archie's Law" treatment could be applied, using a porosity of 0.1, a temperature distribution that is linear between T = 10°C at $z = 0$ and T = 210°C at $z = –5$ km, a uniform TDS of 1000 ppm, and a constant "C_A" value of unity ("low permeability"). Below $z = –5$ km, the resistivity was taken to be constant (84.1 ohm meters) and above $z = –0.375$ km (the location of the 25°C isotherm), resistivity is again constant (491.5 ohm-meters). This outer resistivity distribution is illustrated in Figure 2.12. Note that resistivity in the outer zone depends on vertical elevation only.

Next, it was necessary to assign initial conditions – the values for temperature, TDS and fluid pressure that prevailed in each of the 25,000 computational grid blocks at the beginning of the stabilization period (100,000 years ago). The same prescription was applied for all eight cases considered (see Figure 2.13). The TDS content was assumed to be uniform (1000 ppm) and temperature was taken as varying linearly with depth, starting at 10°C at $z = 0$ and increasing at a rate of 40°C per kilometer of depth. This means that the initial temperature at the bottom of the grid volume ($z = –5$ km) was 210°C. These are the same distributions of temperature and TDS that were used to assign the "exterior" distribution of

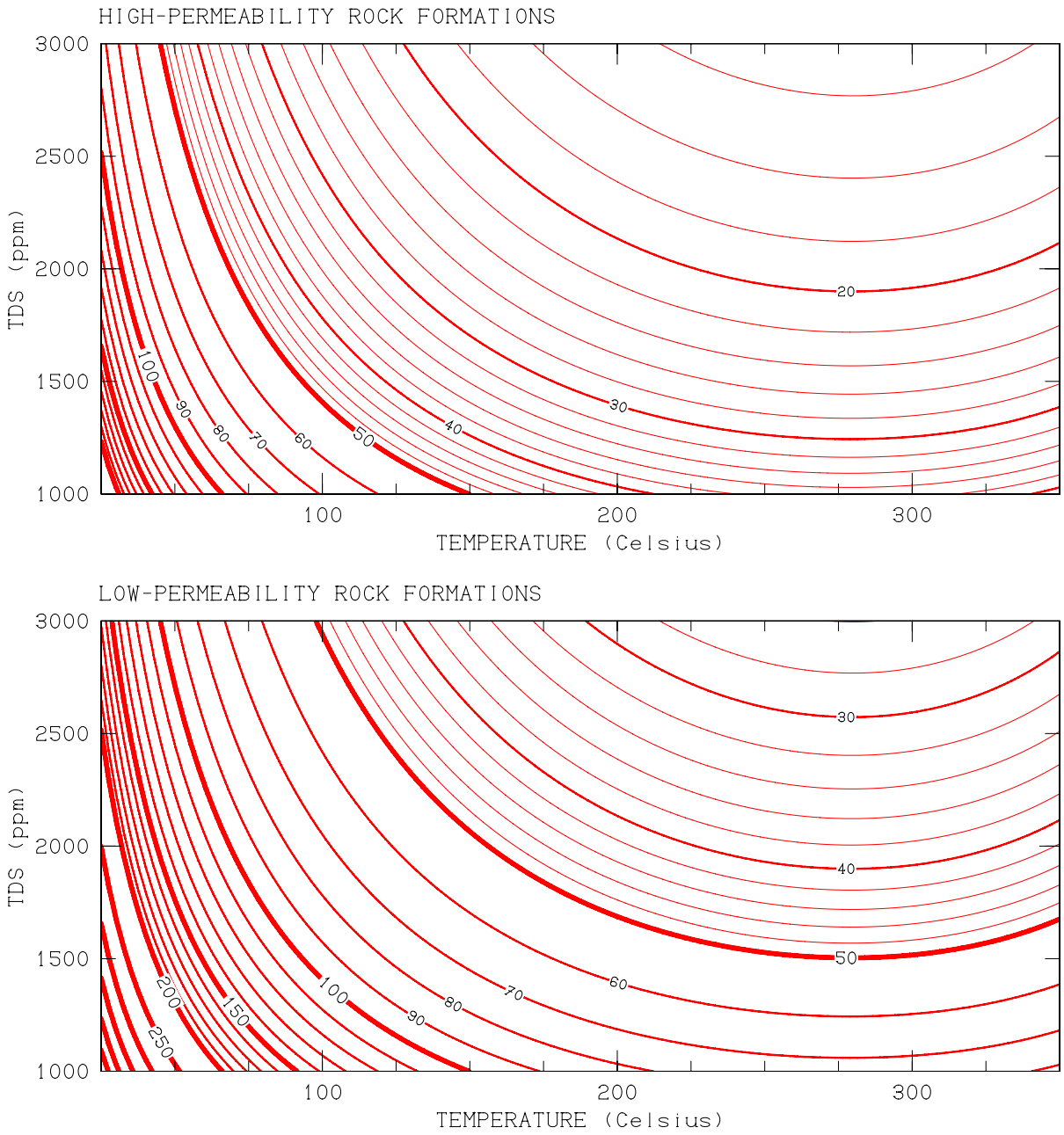

Figure 2.11. Effect of fluid temperature and dissolved solids content upon formation electrical resistivity for (upper) "high-permeability formations" (*Upper Aquifer* and *Fault Zones*) and (lower) "low-permeability formations" (the remainder). Resistivities expressed in ohm-meters.

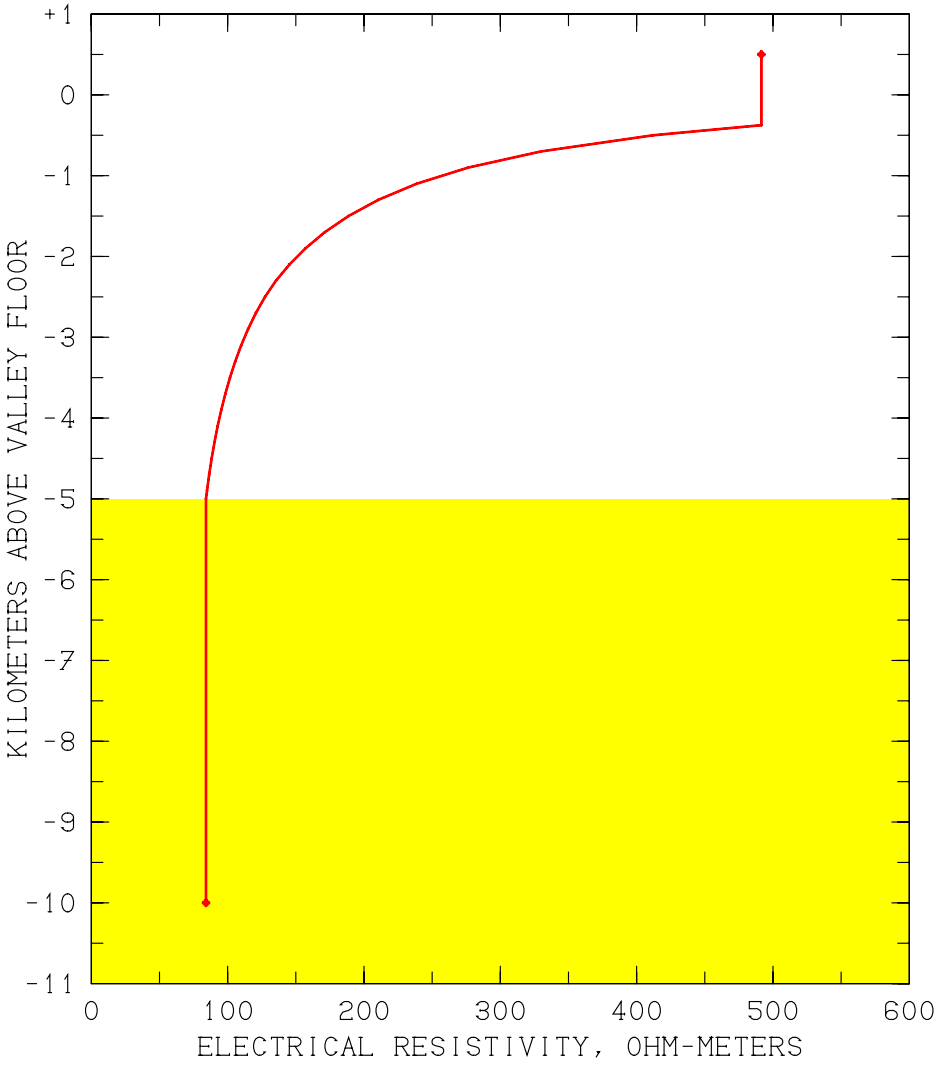

Figure 2.12. Electrical resistivity distribution applied outside STAR grid volume ($x < -5$ km East, $x > +5$ km East, $y < -5$ km North, $y > +5$ km North, $z < -5$ km, or $z > 0$). Resistivity depends on elevation only in this outer region, and is constant (84.1 ohm-m) below $z = -5$ km.

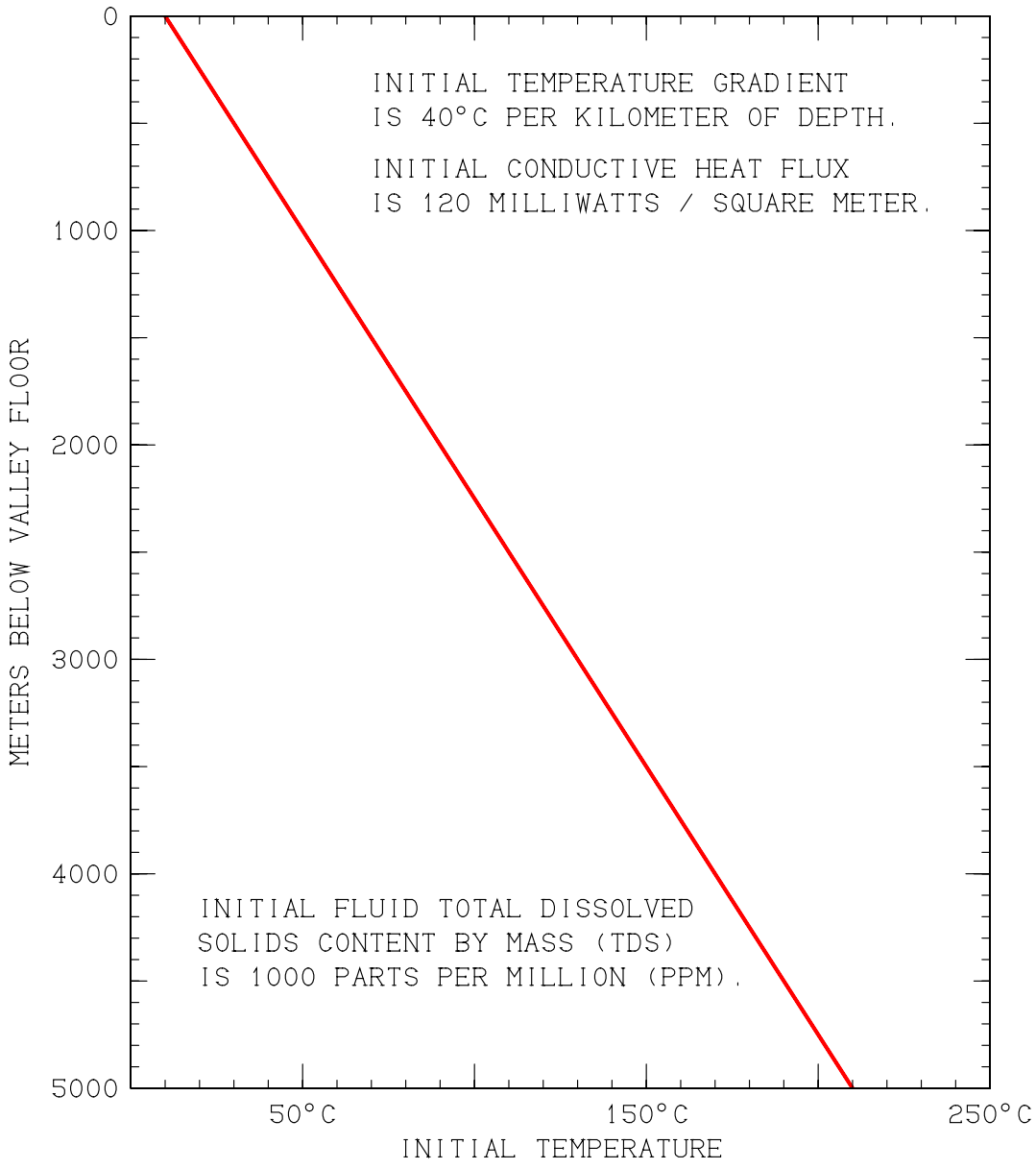

Figure 2.13. Initial conditions imposed at t = 0 for all computed cases. Temperature is distributed linearly between 10°C at the earth surface and 210°C at five kilometers depth. Fluid dissolved solids content initially uniform and equal to 1000 ppm ("parts per million") by mass.

electrical resistivity (see above). Initial pressures were assumed to be hydrostatic. Note that this 40°C/km temperature gradient, taken together with the uniform 3 W/m-°C thermal conductivity value assigned to each of the grid blocks, yields a uniform initial upward conductive heat flux of 120 milliwatts per square meter – a representative value for the Basin and Range (Figure 1.2).

Boundary conditions are required on all six external faces of the grid volume (see Figure 2.14). Along the four vertical boundaries (at $x = \pm 5$ km and $y = \pm 5$ km), no horizontal fluid flow was permitted through the boundary, and the temperature was maintained at the initial elevation-dependent value. Along the top surface, temperature was maintained at 10°C. It was assumed that the "water table" lies at 100 meters depth below the local ground surface everywhere, so the pressure was maintained at one bar (0.1 MPa) at elevation $z = -0.1$ km (the center of the uppermost layer of grid blocks) throughout the region for –3 km East $\leq x \leq$ +3 km East. Outside these bounds, the pressure imposed at $z = -0.1$ km elevation increased linearly with east-west distance, reaching 26 bars at $x = \pm 5$ km to reflect the increase in ground surface elevation beyond the rangefront faults. This "fixed pressure" prescription along the upper boundary allows both upflow and downflow of fluid to develop naturally across the boundary. Anywhere that fluid flows downward into the grid from the top surface, it was assumed that the inflowing fluid enters at 10°C with a TDS content of 1000 ppm.

It is the boundary conditions applied to the bottom surface at $z = -5$ km that distinguish the eight cases considered in this study. Over most of the 100 km^2 bottom surface, no vertical fluid flow was permitted, and a fixed upward conductive heat flux (120 mW/m^2, the same as the initial conductive flux throughout the grid volume) was imposed at the boundary. But at the locations where the "Eastern Fault Zone" and the "Western Fault Zone" intersect the lower boundary (between –3 km $\leq y \leq$ +3 km, and between –3.0 km $\leq x \leq$ –2.8 km or +2.8 km $\leq x \leq$ +3.0 km for the "Western" and "Eastern" faults respectively – total surface area 1.2 km^2 for each fault), various prescriptions were imposed, as discussed below (also see Table 2.1).

Table 2.1. Prescribed deep basal recharge of 3000 ppm waters for the various computed cases.

	WESTERN FAULT ZONE		***EASTERN FAULT ZONE***	
	Flow rate	**Temperature**	**Flow rate**	**Temperature**
Case 0.0	0	---	0	---
Case 0.1	0	---	100 t/h	210°C
Case 0.2	0	---	100 t/h	255°C
Case 0.3	0	---	100 t/h	300°C
Case 1.0	100 t/h	210°C	0	---
Case 2.0	100 t/h	255°C	0	---
Case 3.0	100 t/h	300°C	0	---
Case 4.0	100 t/h	345°C	0	---

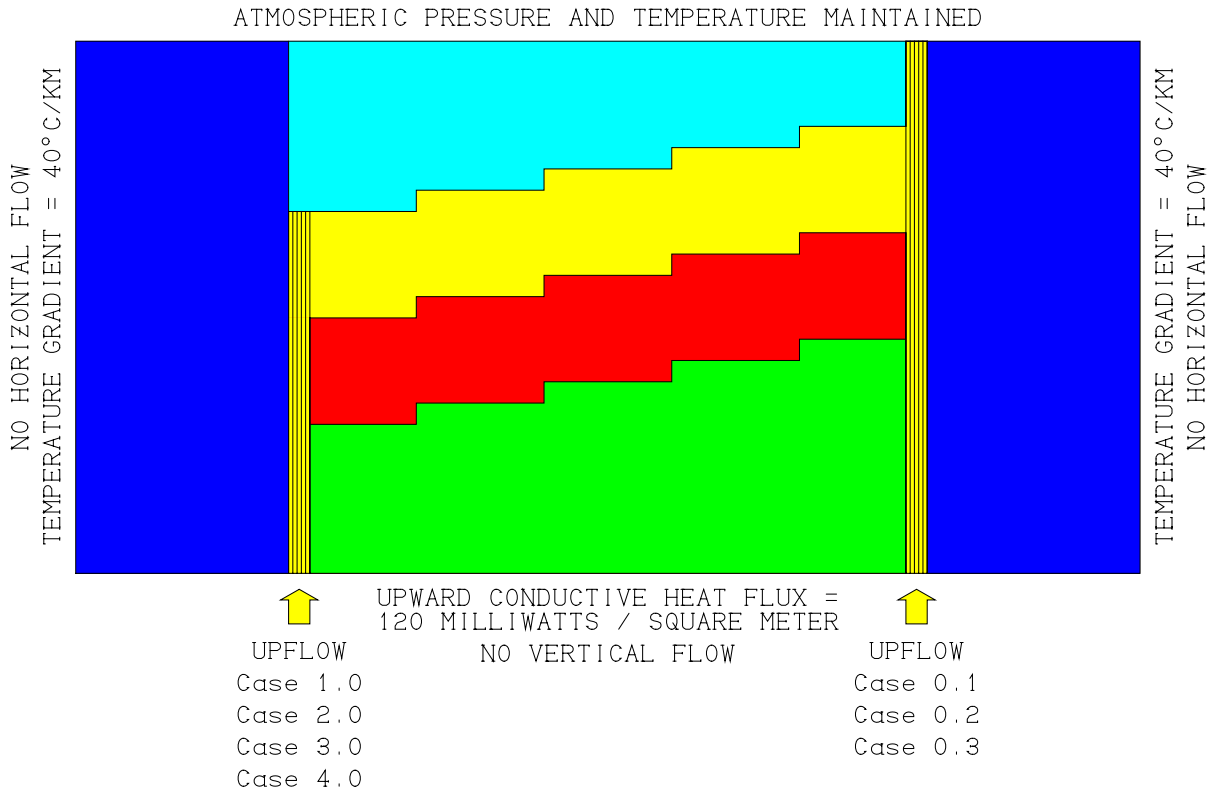

Figure 2.14. Boundary conditions. *Upper surface* (z = 0): initial pressure and temperature maintained, permitting upflow and downflow of heat and fluid mass. Any downflowing recharge water from earth surface has 1000 ppm TDS and temperature = 10°C. *Lateral boundaries* (x,y = ± 5 km): initial temperature maintained, no horizontal flow. *Lower surface* (z = –5 km): no vertical flow, uniform upward conductive heat flux (120 mW/m^2), except possibly where fault zones intersect lower boundary. *Case 0.0:* no upflow through either fault zone. *Cases 0.1, 0.2 and 0.3:* no upflow to western fault zone, 100 t/h upflow imposed at base of eastern fault zone. *Cases 1.0, 2.0, 3.0 and 4.0:* no upflow to eastern fault zone, 100 t/h upflow imposed at base of western fault zone.

For ***Case 0.0,*** no special treatment was applied to the bases of the fault zones. Like the rest of the bottom surface, these areas are characterized by constant upward conductive heat flux (120 mW/m^2) and no vertical fluid flow.

For ***Cases 0.1, 0.2 and 0.3,*** the base of the "Western Fault Zone" was similarly impermeable, with a fixed conductive heat flux. But along the intersection of the "Eastern Fault Zone" with the $z = -5$ km plane, convective upward fluid flow was prescribed, at a fixed rate of 100 metric tons per hour (100 t/h; 27.8 kg/s). Furthermore, this upflow was not uniformly distributed along the fault length, but attained a maximum flow rate at $y = +1$ km North and declined to zero at $y = \pm 3$ km (see Figure 2.15, upper frame). The inflowing fluid is characterized by TDS = 3000 ppm; three times greater than the fluid initially present in the system but still quite dilute (for comparison, ordinary seawater has a TDS content of about 35,000 ppm). The distinction between Cases 0.1, 0.2 and 0.3 is the temperature assigned to the fluid entering the fault zone from below. For Case 0.1, the inflowing fluid temperature is the same as the initial temperature at that depth (210°C). Case 0.2 involves recharge water that is 45°C hotter (255°C) and Case 0.3 is hotter yet (300°C; 90°C higher than Case 0.1).

The situation is reversed for ***Cases 1.0, 2.0, 3.0 and 4.0***. In these cases, the "Eastern Fault Zone" had no basal upflow and a fixed conductive heat flux, but 100 t/h of upward convective flow were prescribed into the bottom of the "Western Fault Zone". Again, the upflow distribution along the fault length was non-uniform, with the maximum value at $y = -1$ km North (Figure 2.15, lower frame). Inflowing deep fluid was characterized by TDS = 3000 ppm, as before. Recharge fluid temperature was 210°C, 255°C, 300°C or 345°C for Cases 1.0, 2.0, 3.0 and 4.0 respectively.

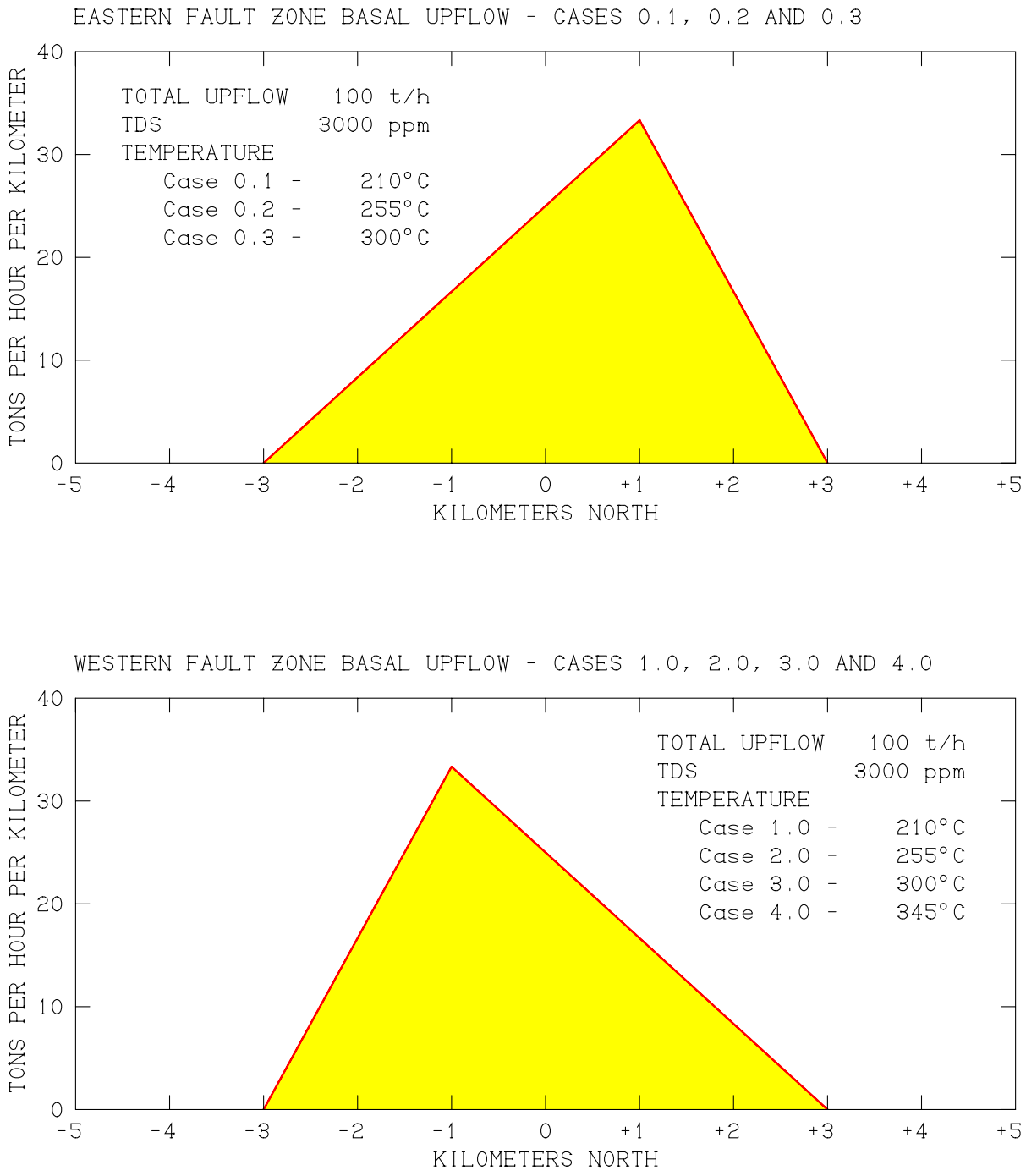

Figure 2.15. Spatial distribution of z = –5 km upflow into fault zones for Cases 0.1 – 4.0. Upflowing fluid contains 3000 ppm dissolved solids, and fluid temperature is 210°C *(Cases 0.1 and 1.0)*, 255°C *(Cases 0.2 and 2.0)*, 300°C *(Cases 0.3 and 3.0)* or 345°C *(Case 4.0).*

3 COMPUTED SUBSURFACE CONDITIONS

The STAR numerical simulator was used to calculate temporal changes in each of the eight cases outlined above over a 100,000-year stabilization period using time-steps of ten years duration. Except for Case 0.0, the deep hot water recharge from depth results in rapid increases with time of total system energy (early system heating rates range from 11 MWt for Case 1.0 to 55 MWt for Case 4.0; "MWt" means "thermal megawatts"), but gradually the system stabilizes as indicated in Figure 3.1. After 100,000 years, Case 4.0 is still heating up but only at about 1.5 MWt (< 3% of the initial heating rate), and the other cases are even closer to steady conditions. Accordingly, the 100,000-year stabilization period appears to be sufficient; for practical purposes, all eight cases may be regarded as in a steady condition.

It is particularly noteworthy that, as Figure 3.1 shows, the cases involving deep inflow along the "Western Fault Zone" result in far more heating of the system volume as a whole than the others. The increase in total system energy from the starting conditions (characterized by a linear temperature gradient of 40°C per kilometer of depth) for each case is as follows:

Case 0.0	-0.61×10^{18} Joules	(no deep recharge)
Case 0.1	$+5.21 \times 10^{18}$ Joules	(100 t/h eastern recharge at 210°C)
Case 0.2	$+5.45 \times 10^{18}$ Joules	(100 t/h eastern recharge at 255°C)
Case 0.3	$+7.73 \times 10^{18}$ Joules	(100 t/h eastern recharge at 300°C)
Case 1.0	$+20.43 \times 10^{18}$ Joules	(100 t/h western recharge at 210°C)
Case 2.0	$+26.78 \times 10^{18}$ Joules	(100 t/h western recharge at 255°C)
Case 3.0	$+34.78 \times 10^{18}$ Joules	(100 t/h western recharge at 300°C)
Case 4.0	$+46.11 \times 10^{18}$ Joules	(100 t/h western recharge at 345°C)

The reason for the difference is that, in Cases 0.1 – 0.3, the deep recharge takes place into the Eastern Fault Zone, which has a direct outlet to the surface. As a result, hot fluid has a tendency to rise directly upward and exit at the surface without causing a great deal of heating of the western part of the system. Cases 1.0 – 4.0, by contrast, represent "hidden" geothermal systems. The Western Fault Zone is buried below impermeable caprock and has no direct surface outlet, so deep source waters first flow up the fault zone, then encounter the caprock and move horizontally eastward (mainly through the permeable Upper Aquifer layer) until they finally reach the Eastern Fault Zone and can discharge to the surface. As a result, a great deal more volume is swept and the system stores four to five times as much excess heat at equilibrium.

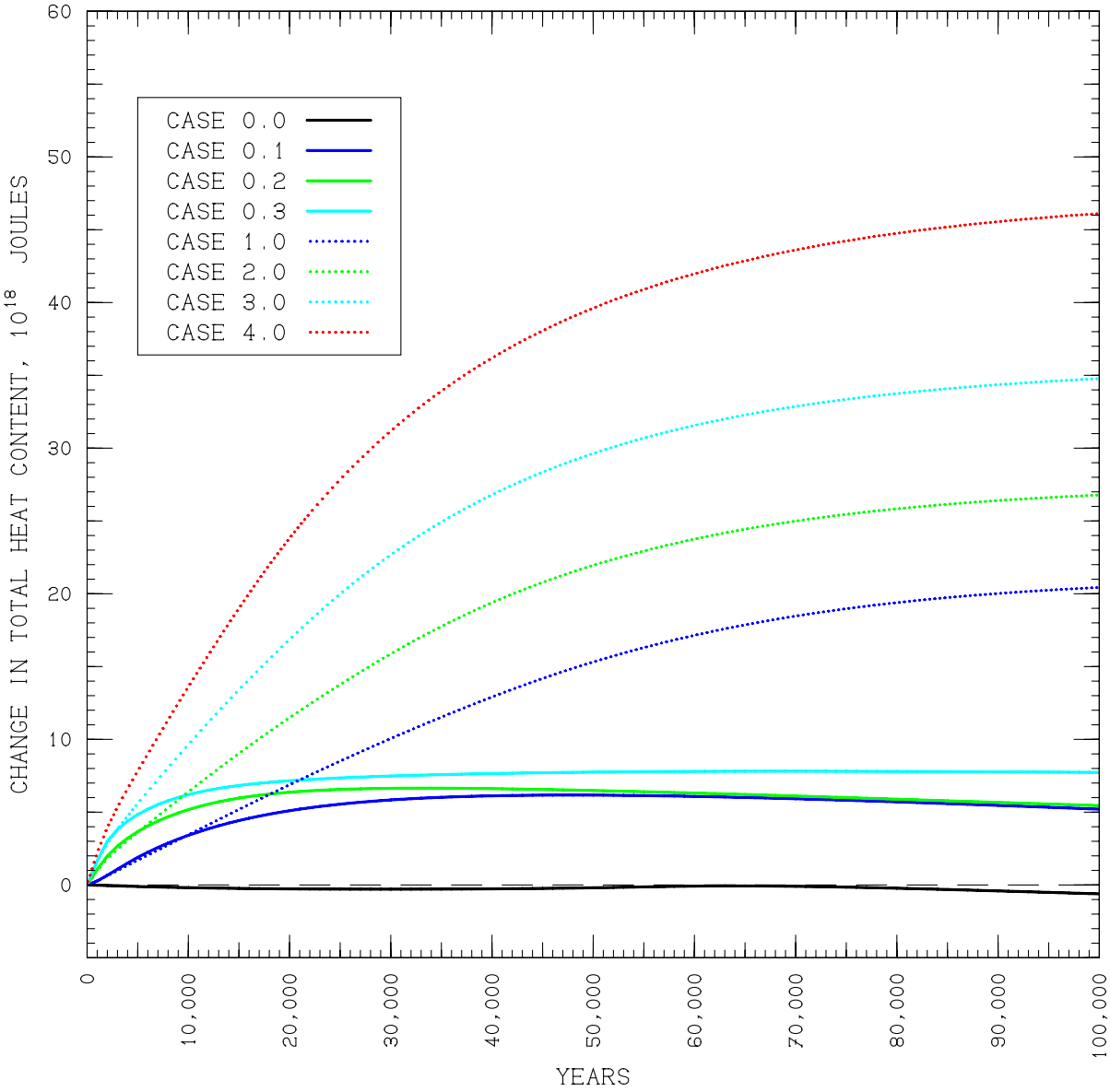

Figure 3.1. The approach to equilibrium – difference from initial total system heat content as a function of time.

It should be pointed out that some of these "synthetic" geothermal reservoirs would be of substantial commercial interest if they actually existed in nature. The excess energy in the most energetic case (Case 4.0) is 46×10^{18} Joules of heat energy (relative to the "conductive" case with a linear temperature gradient). If only 10% of this excess heat energy could be recovered by a properly-designed wellfield, and if the heat energy were then converted into electricity at only 10% efficiency, 46×10^{16} Joules of electrical energy would become available. To produce the same amount of electricity, the existing 62 MWe Dixie Valley geothermal power station would have to operate continuously at full capacity for 235 years. These issues of probable generating capacity and field lifetime are taken up at greater length in Section 9.

It is also noteworthy that the "no deep recharge" case (Case 0.0) actually contains slightly less heat energy after 100,000 years than it did at the beginning of the calculation. The reason is simply that, even though no "forced" convection is imposed at the bottom boundary, the system is partially permeable and therefore natural thermal convection cells develop within it. These thermal convection cells transfer heat upward toward the earth surface, augmenting the conductive heat transfer. Since at equilibrium the total heat output at the surface must match the prescribed conductive input at the bottom (120 $mW/m^2 \times 100$ km^2 = 12 MWt), it follows that conductive heat transfer must be lower at equilibrium than the initial value, since some of the conductive heat transfer has been replaced by convection. System temperature is fixed at the top of the system (at $z = 0$), at 10°C. If conductive heat transfer at equilibrium is less than the initial value, it follows that the average temperature at the bottom surface ($z = –5$ km) must be lower at equilibrium than the initial value of 210°C (the average vertical temperature gradient has declined). Since deep subsurface temperatures are lower, the system as a whole stores less thermal energy at equilibrium than it did initially.

This equilibrium state of the "no deep recharge" calculation (Case 0.0) is depicted in Figures 3.2 – 3.6, which show vertical east-west cross-sections through the study volume at $y = –2.4$, –1.2, 0, +1.2 and +2.4 km North, respectively. Since no deep recharge is involved, the TDS remains uniform and constant throughout at 1000 ppm. The yellow background color denotes the locations of "high permeability" formations (the fault zones and the Upper Aquifer). The effects of a complex convection pattern can be discerned. Downflow is taking place in both fault zones to the extreme north and south (Figures 3.2 and 3.6), but upflow is taking place within the Western fault and in the upper portion of the Eastern fault near $y = 0$ (Figure 3.4). In the neighborhood of the Eastern fault near +1.2 km North (Figure 3.5), the temperature distribution is dominated by substantial upflow of hot water to the surface through the fault zone, which is exposed in this area. Compensating downflow takes place in a diffuse fashion through the low-permeability caprock throughout the area, particularly in the high-elevation locations beyond the fault zones to the extreme east and west.

Figures 3.7 – 3.11, 3.12 – 3.16 and 3.17 – 3.21 are similar, but show results for Cases 0.1, 0.2 and 0.3, respectively. Although subsurface temperatures generally increase as one progresses through these cases, the overall pattern is similar for all of them. The buried permeable Western Fault Zone serves as a "return leg" for a deep convection system, with

Continued on page 3-24

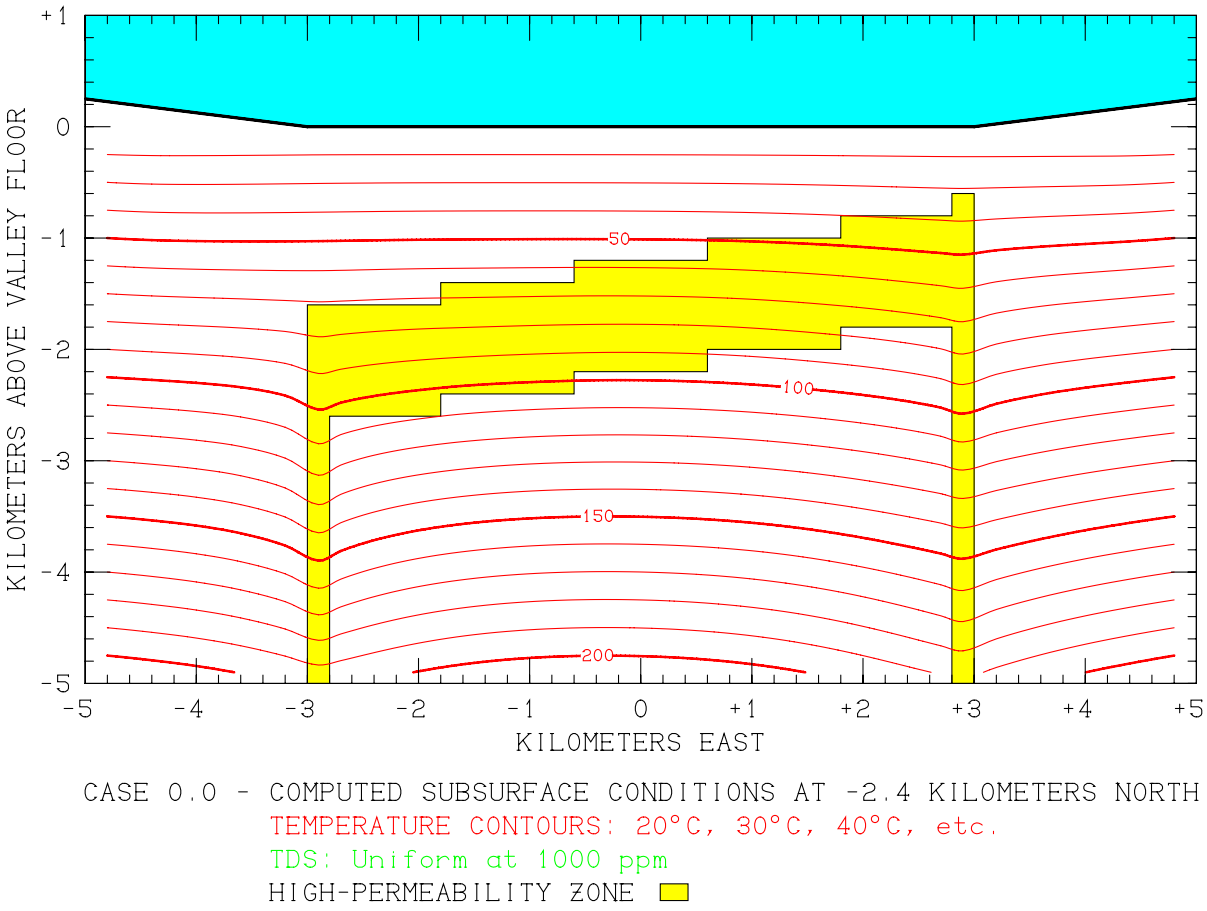

Figure 3.2. Computed stable subsurface conditions for Case 0.0 (no deep recharge) in east-west vertical cross-section at y = –2.4 km North.

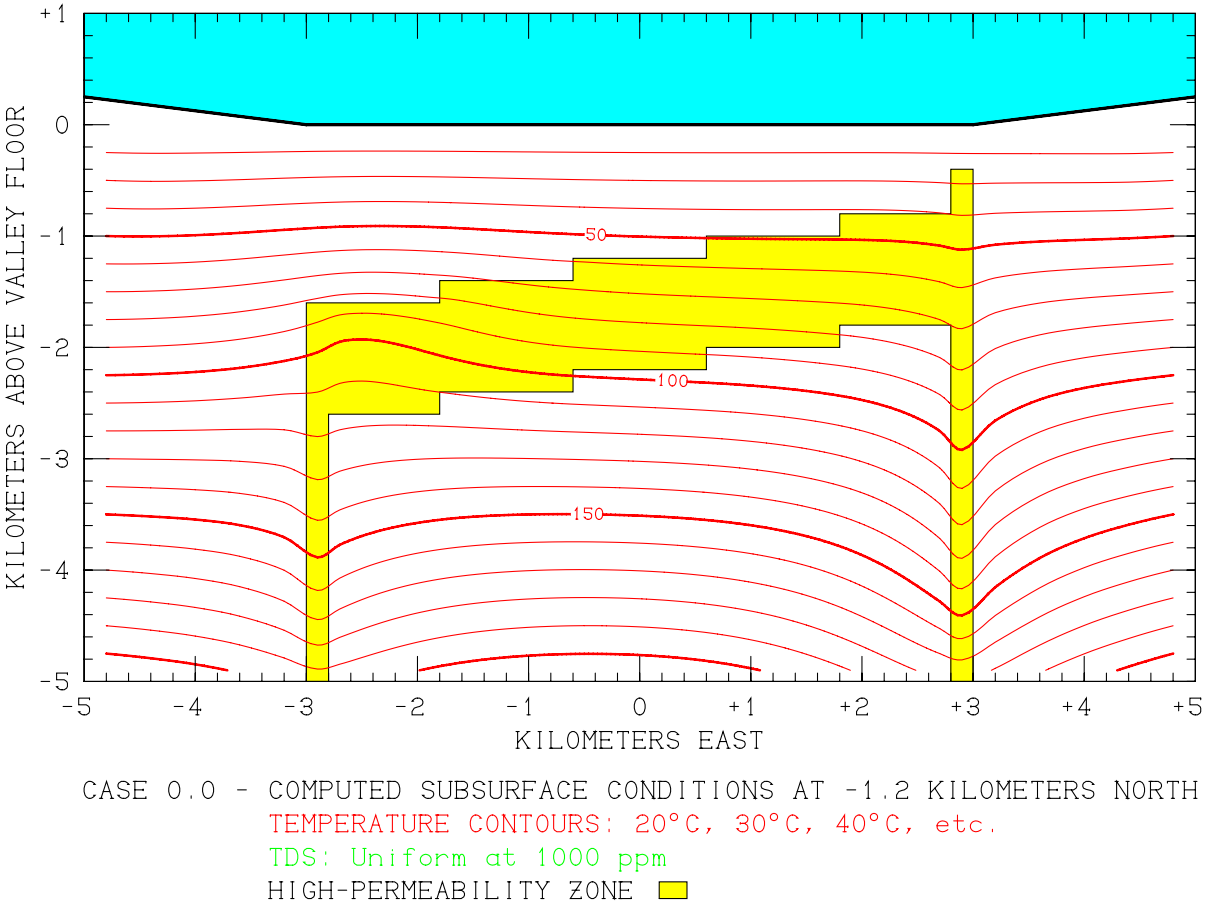

Figure 3.3. Computed stable subsurface conditions for Case 0.0 (no deep recharge) in east-west vertical cross-section at y = –1.2 km North.

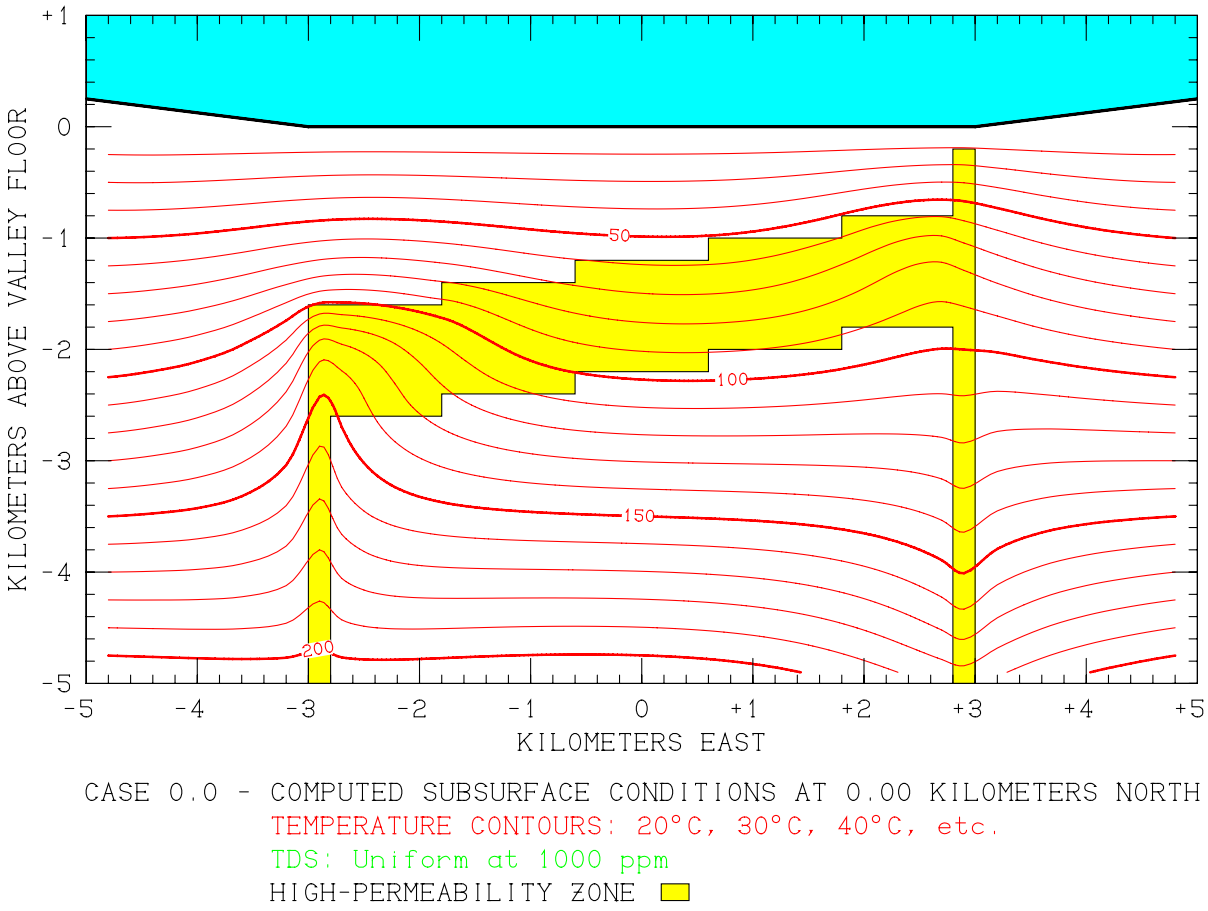

Figure 3.4. Computed stable subsurface conditions for Case 0.0 (no deep recharge) in east-west vertical cross-section at $y = 0$.

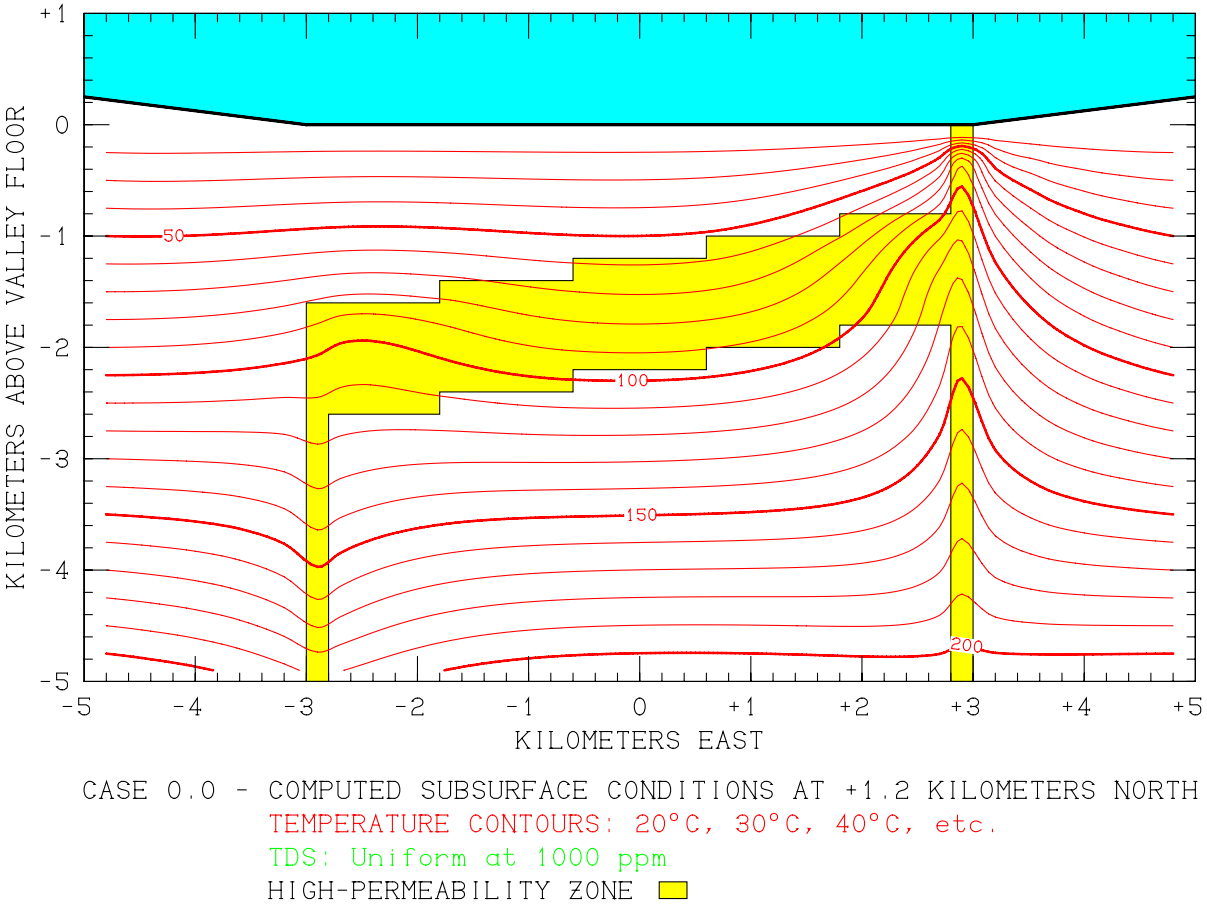

Figure 3.5. Computed stable subsurface conditions for Case 0.0 (no deep recharge) in east-west vertical cross-section at y = +1.2 km North.

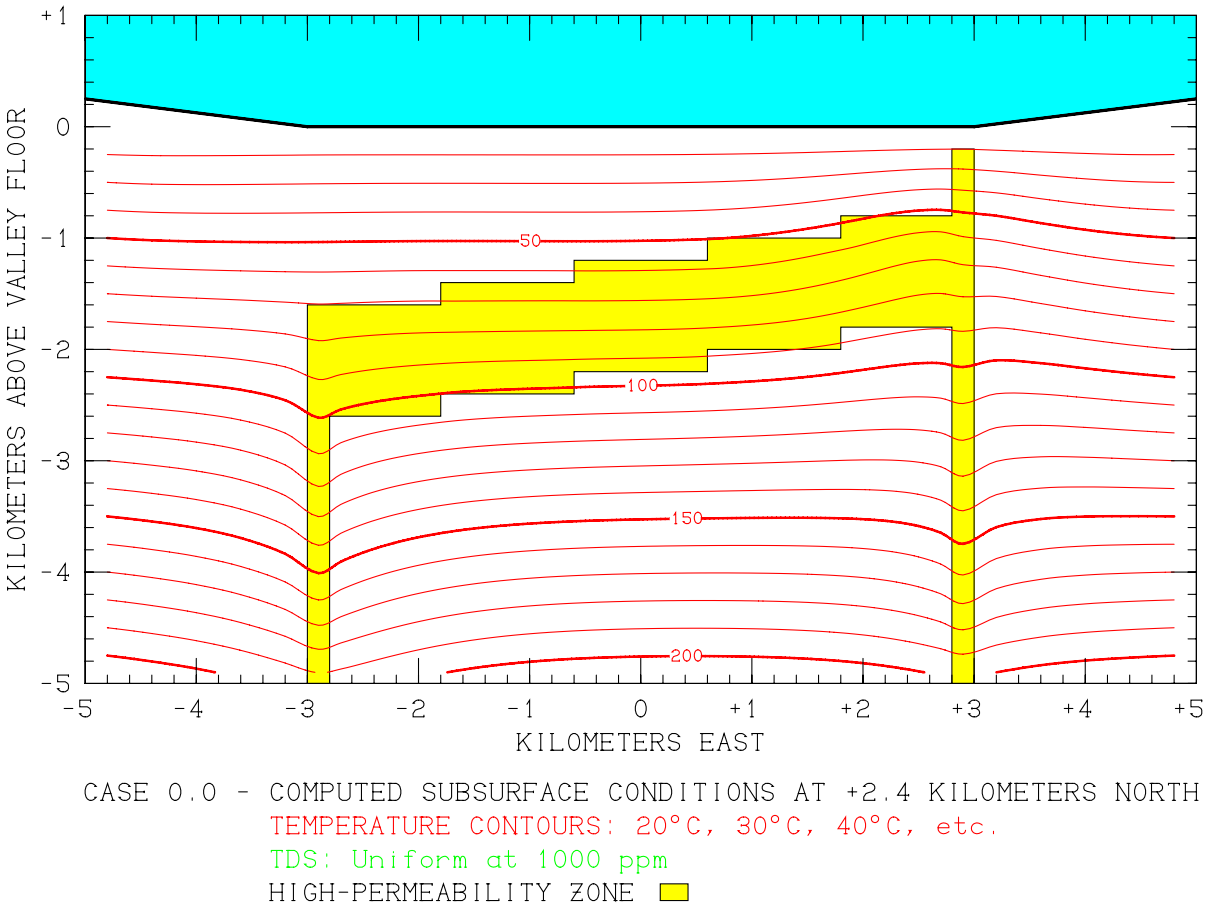

Figure 3.6. Computed stable subsurface conditions for Case 0.0 (no deep recharge) in east-west vertical cross-section at y = +2.4 km North.

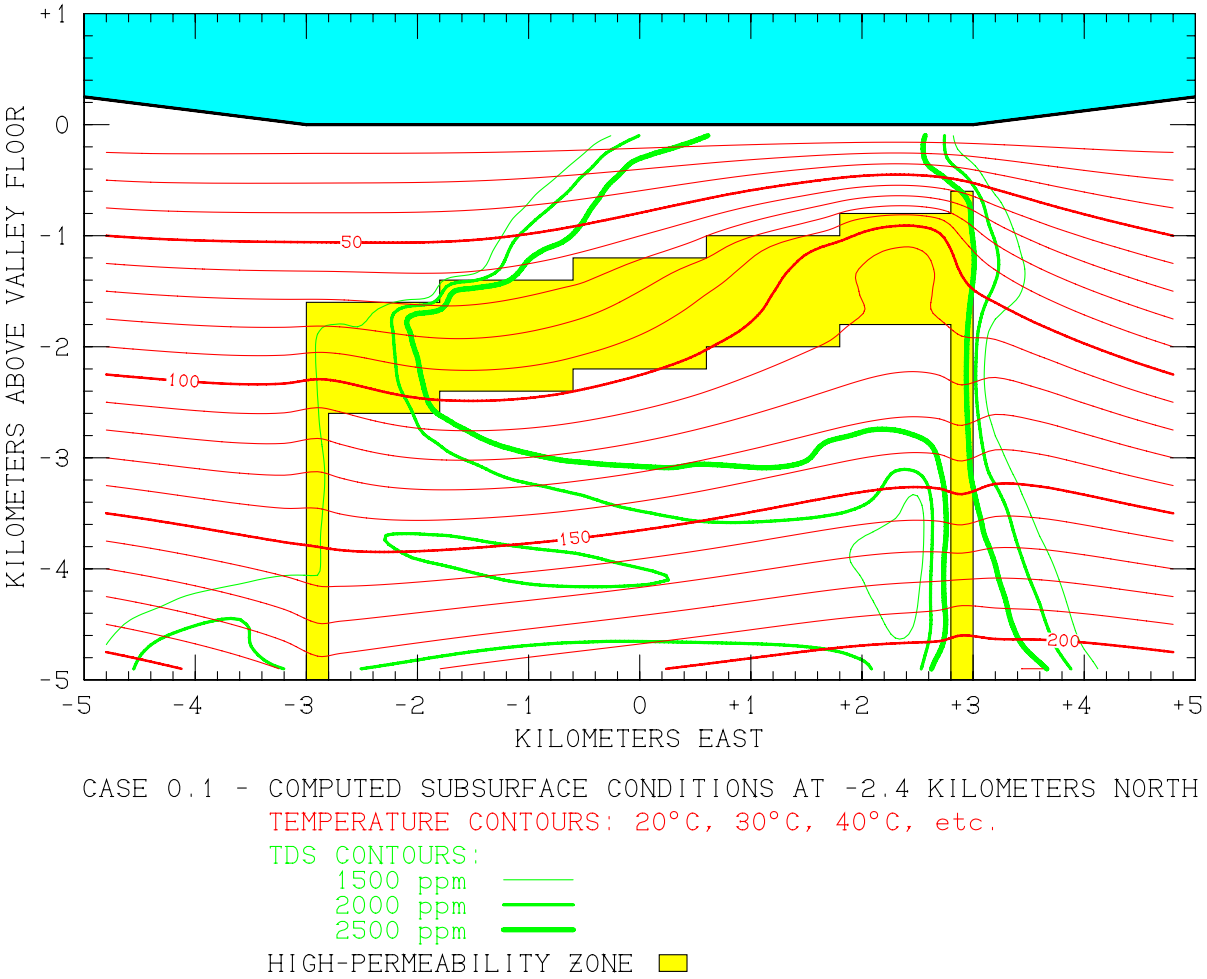

Figure 3.7. Computed stable subsurface conditions for Case 0.1 (100 t/h 3000 ppm 210°C deep recharge into eastern fault zone) in east-west vertical cross-section at y = –2.4 km North.

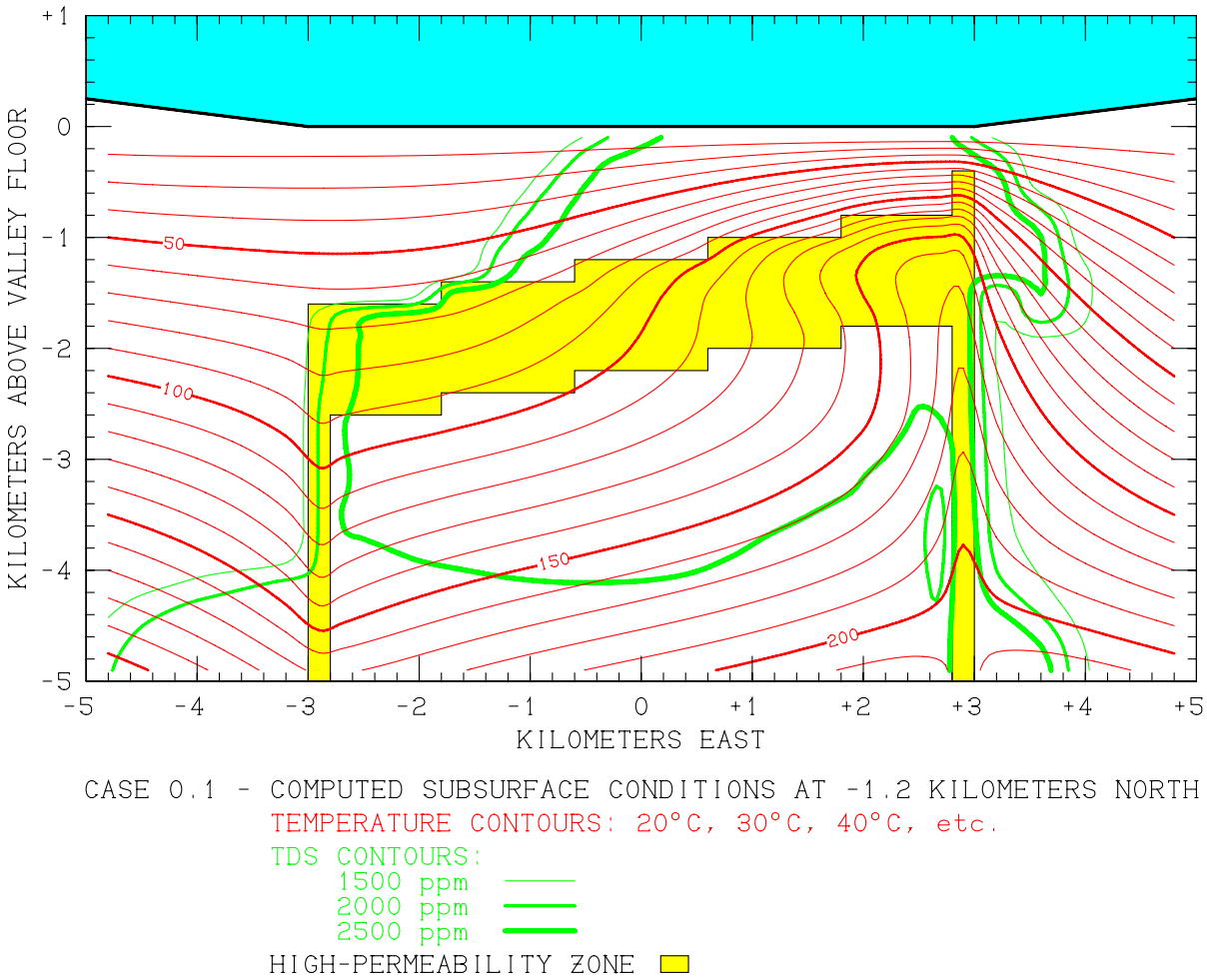

Figure 3.8. Computed stable subsurface conditions for Case 0.1 (100 t/h 3000 ppm 210°C deep recharge into eastern fault zone) in east-west vertical cross-section at $y = -1.2$ km North.

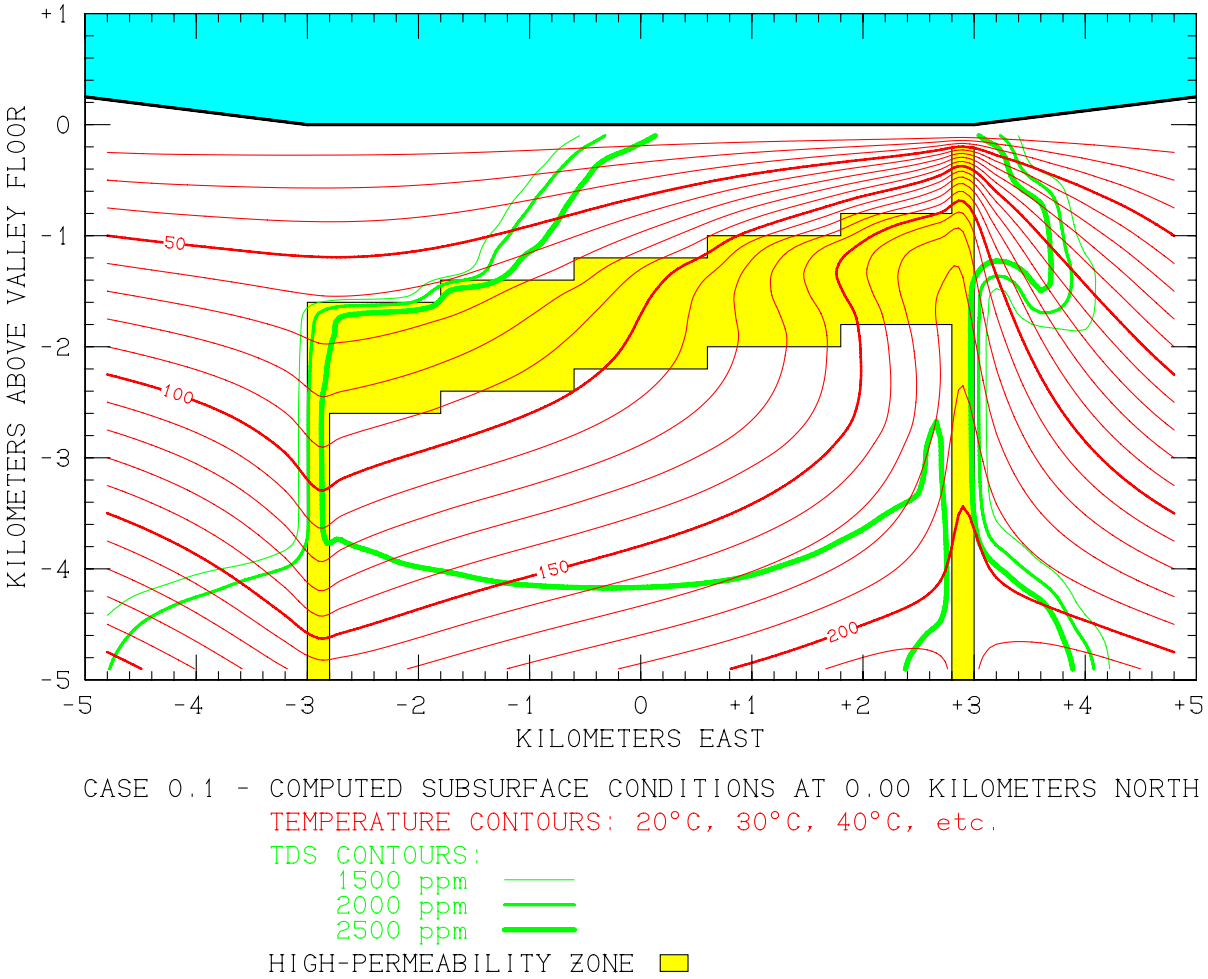

Figure 3.9. Computed stable subsurface conditions for Case 0.1 (100 t/h 3000 ppm 210°C deep recharge into eastern fault zone) in east-west vertical cross-section at $y = 0$.

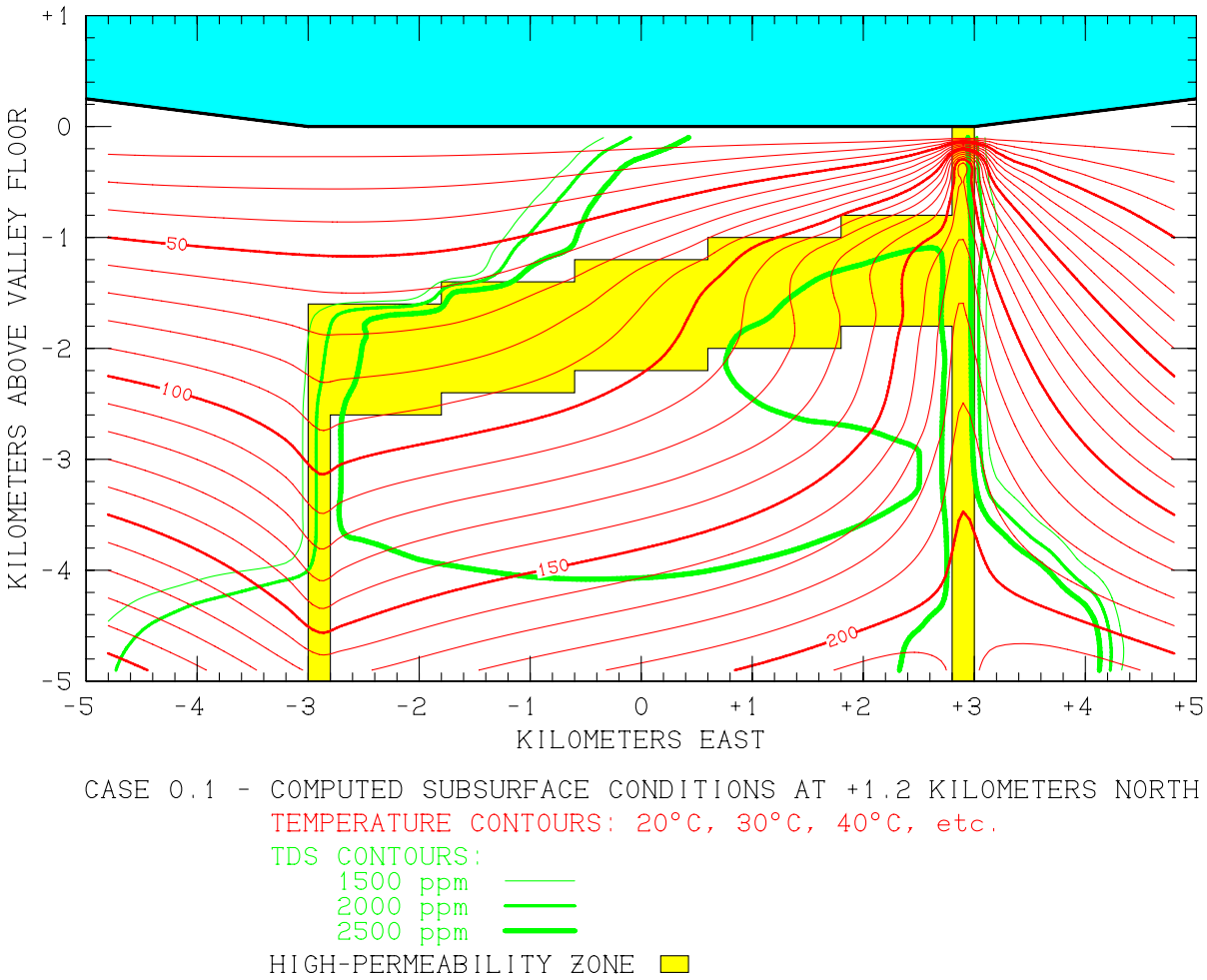

Figure 3.10. Computed stable subsurface conditions for Case 0.1 (100 t/h 3000 ppm 210°C deep recharge into eastern fault zone) in east-west vertical cross-section at y = +1.2 km North.

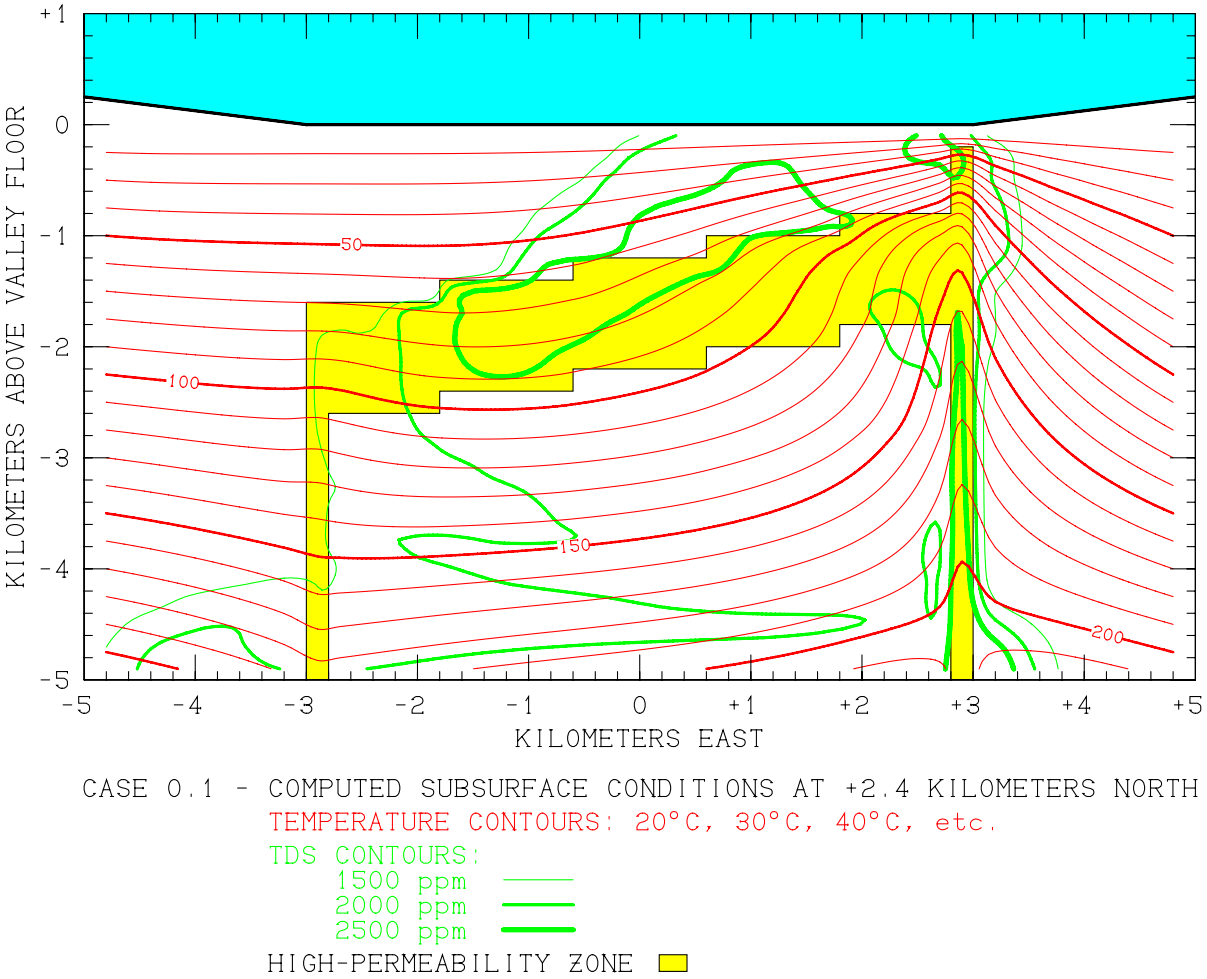

Figure 3.11. Computed stable subsurface conditions for Case 0.1 (100 t/h 3000 ppm 210°C deep recharge into eastern fault zone) in east-west vertical cross-section at *y* = +2.4 km North.

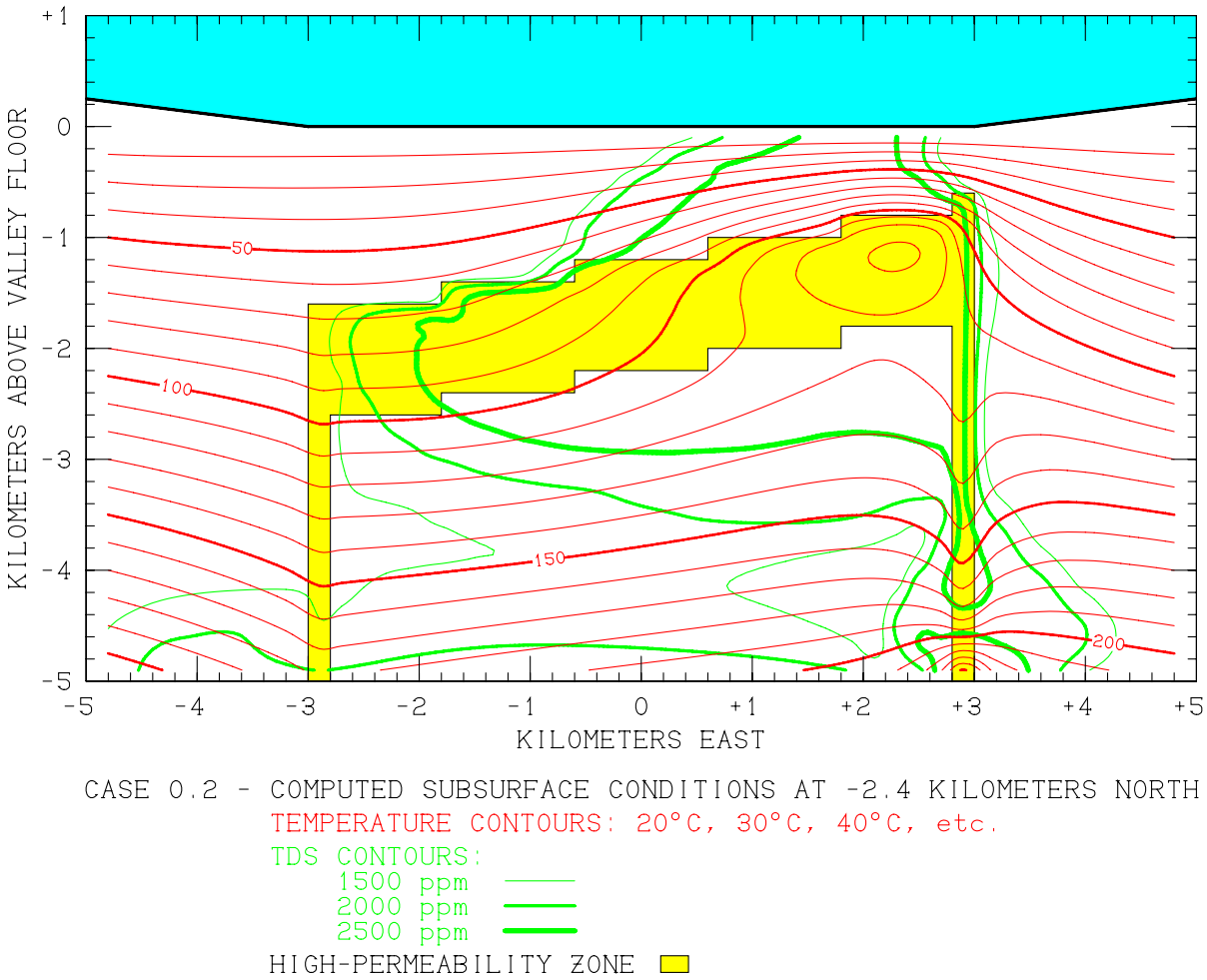

Figure 3.12. Computed stable subsurface conditions for Case 0.2 (100 t/h 3000 ppm 255°C deep recharge into eastern fault zone) in east-west vertical cross-section at $y = -2.4$ km North.

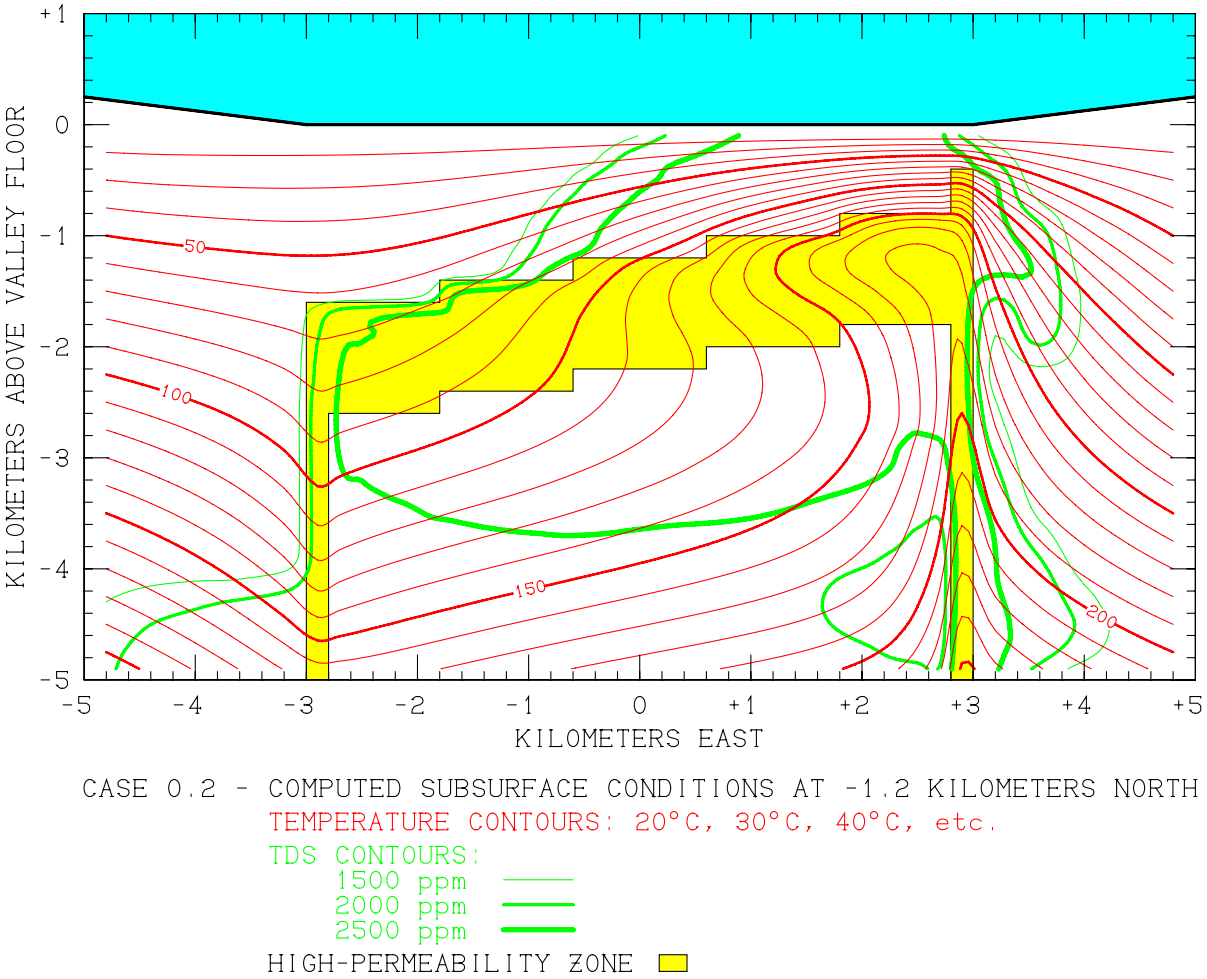

Figure 3.13. Computed stable subsurface conditions for Case 0.2 (100 t/h 3000 ppm 255°C deep recharge into eastern fault zone) in east-west vertical cross-section at $y = -1.2$ km North.

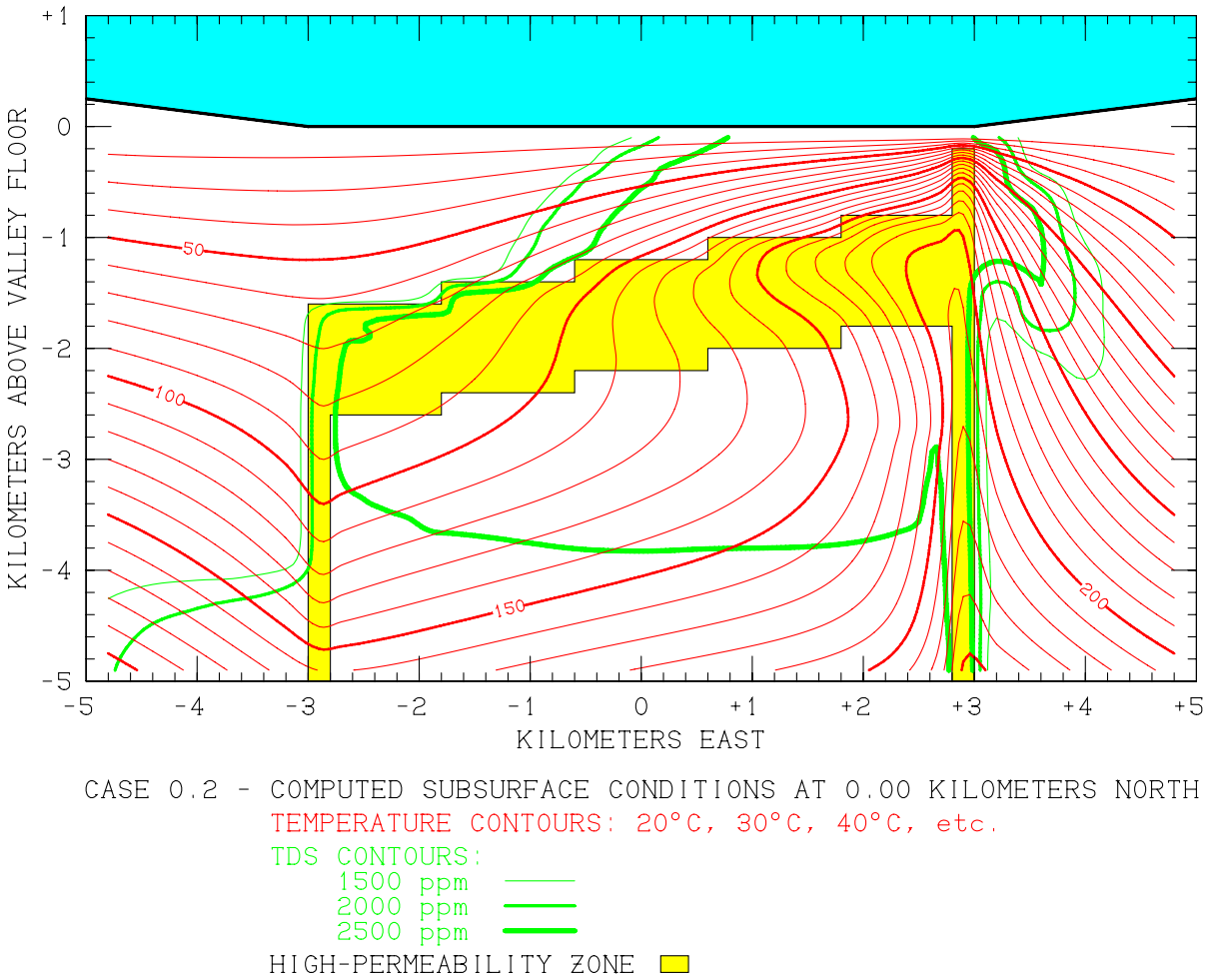

Figure 3.14. Computed stable subsurface conditions for Case 0.2 (100 t/h 3000 ppm 255°C deep recharge into eastern fault zone) in east-west vertical cross-section at $y = 0$.

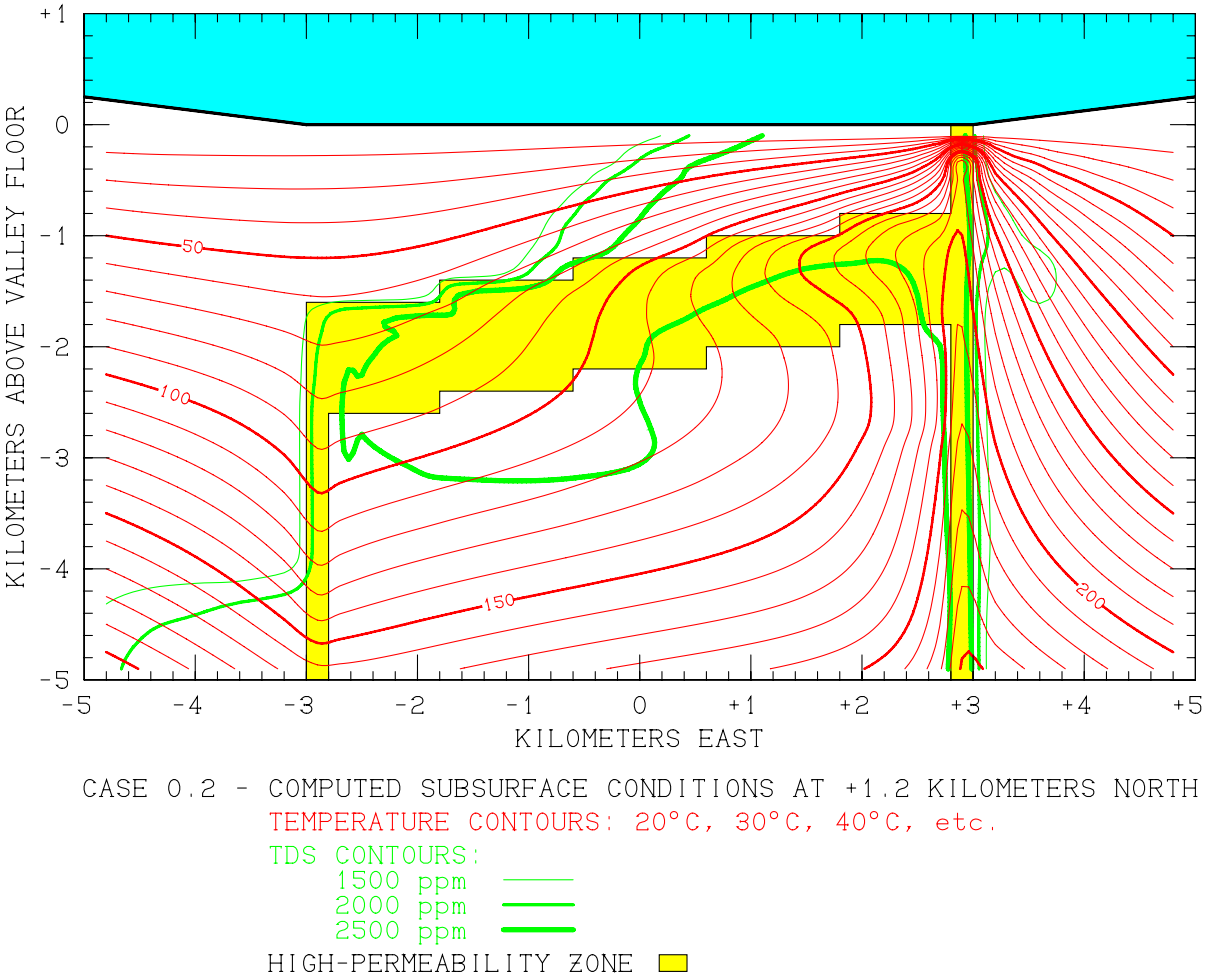

Figure 3.15. Computed stable subsurface conditions for Case 0.2 (100 t/h 3000 ppm 255°C deep recharge into eastern fault zone) in east-west vertical cross-section at y = +1.2 km North.

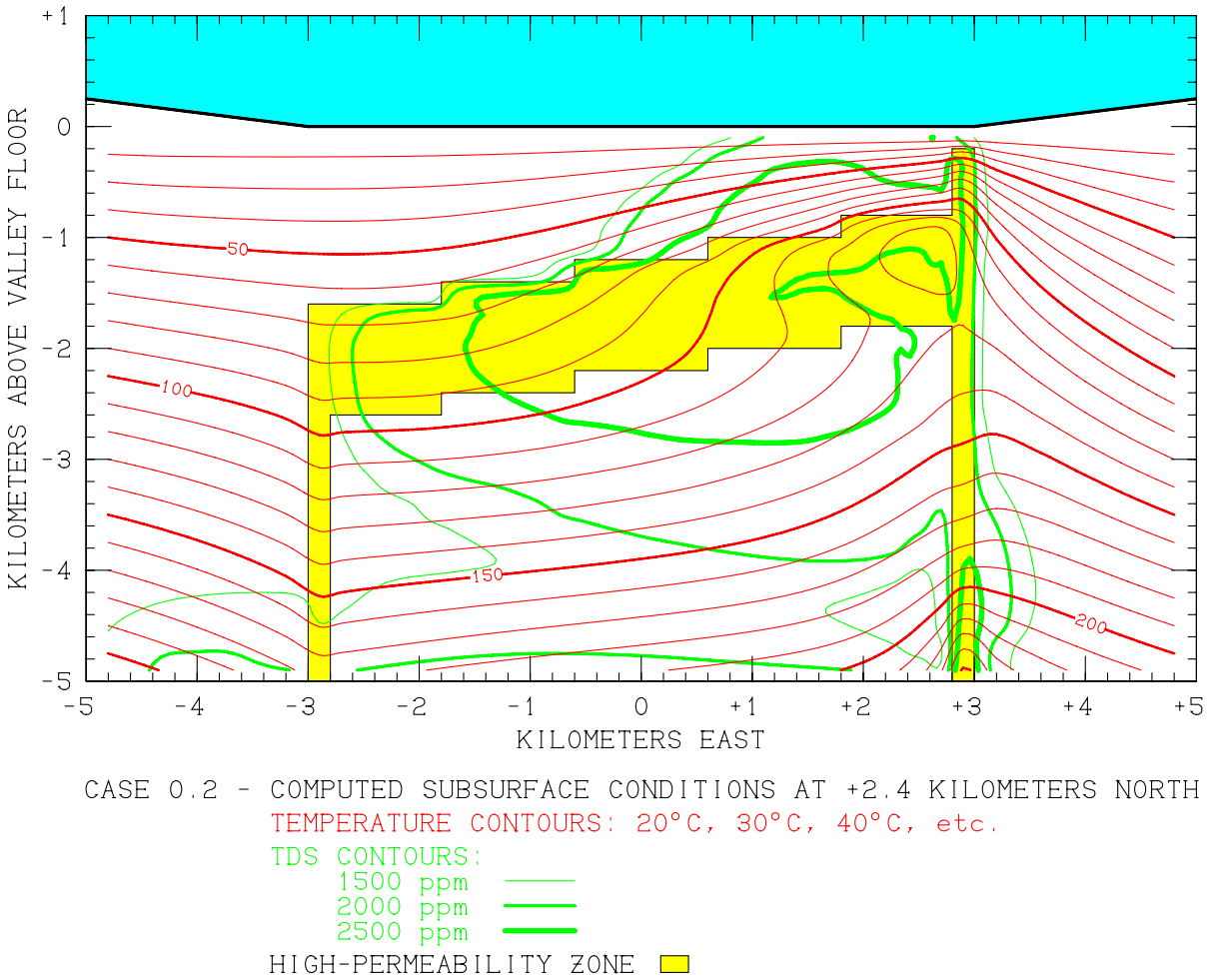

Figure 3.16. Computed stable subsurface conditions for Case 0.2 (100 t/h 3000 ppm 255°C deep recharge into eastern fault zone) in east-west vertical cross-section at y = +2.4 km North.

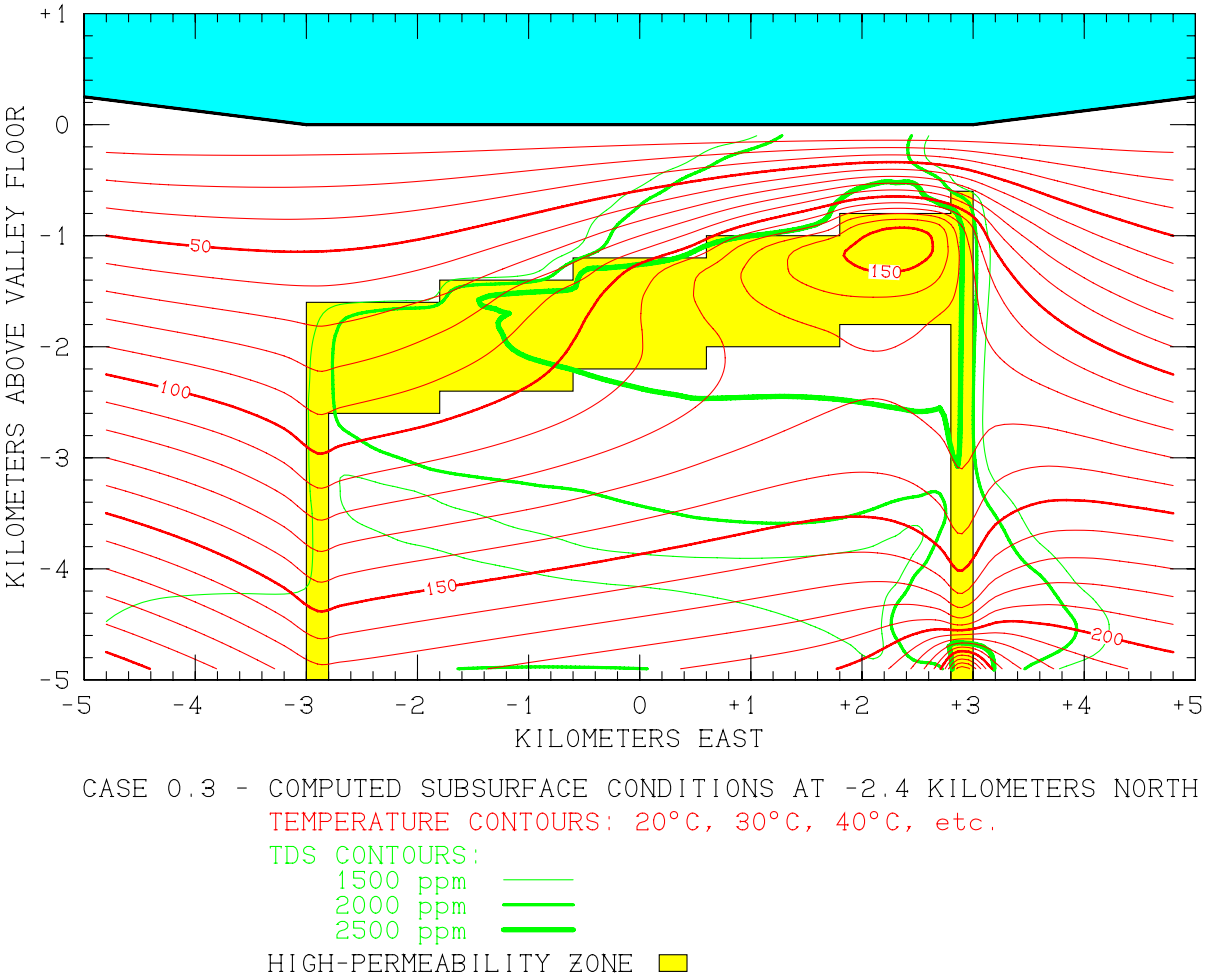

Figure 3.17. Computed stable subsurface conditions for Case 0.3 (100 t/h 3000 ppm 300°C deep recharge into eastern fault zone) in east-west vertical cross-section at y = –2.4 km North.

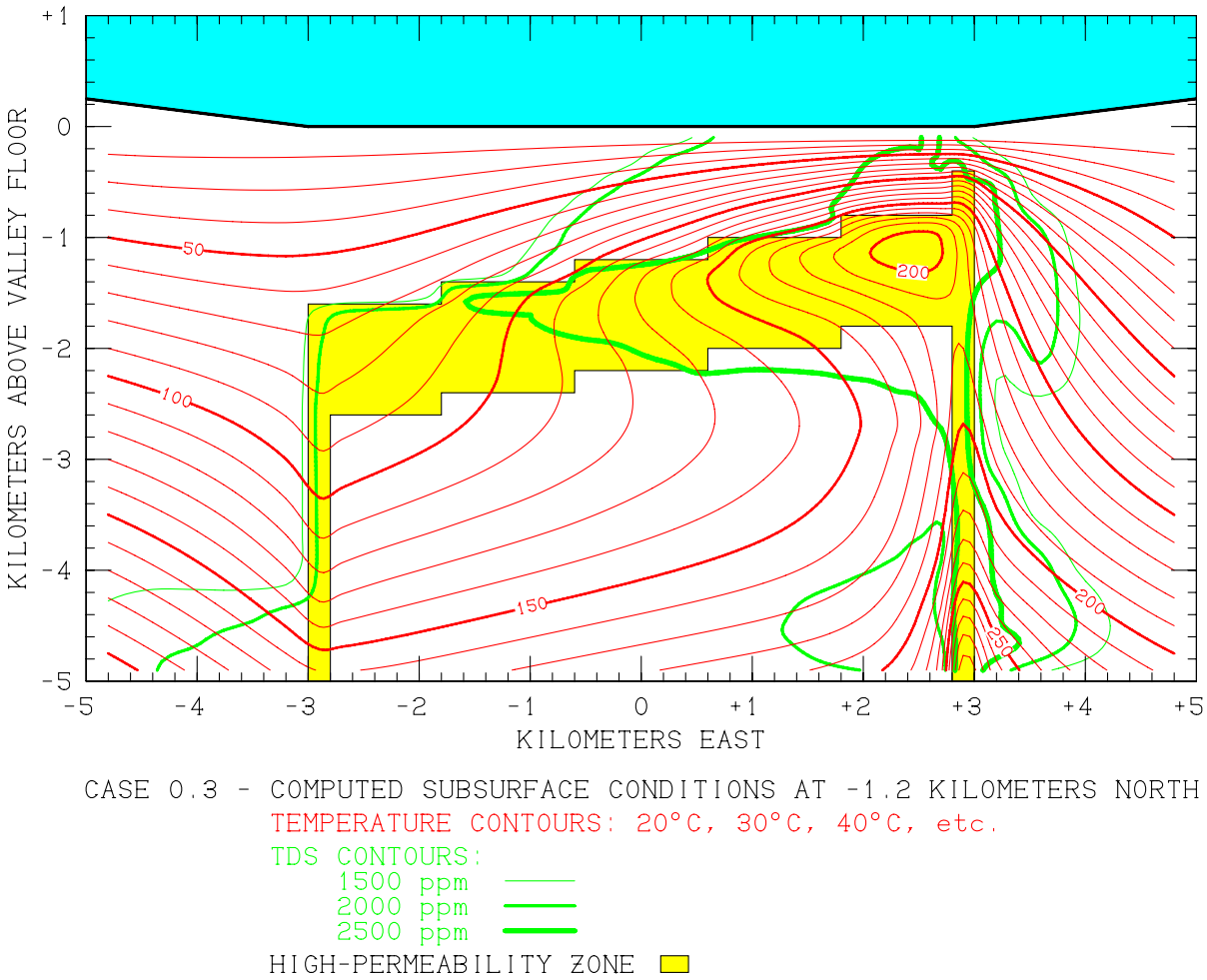

Figure 3.18. Computed stable subsurface conditions for Case 0.3 (100 t/h 3000 ppm 300°C deep recharge into eastern fault zone) in east-west vertical cross-section at $y = -1.2$ km North.

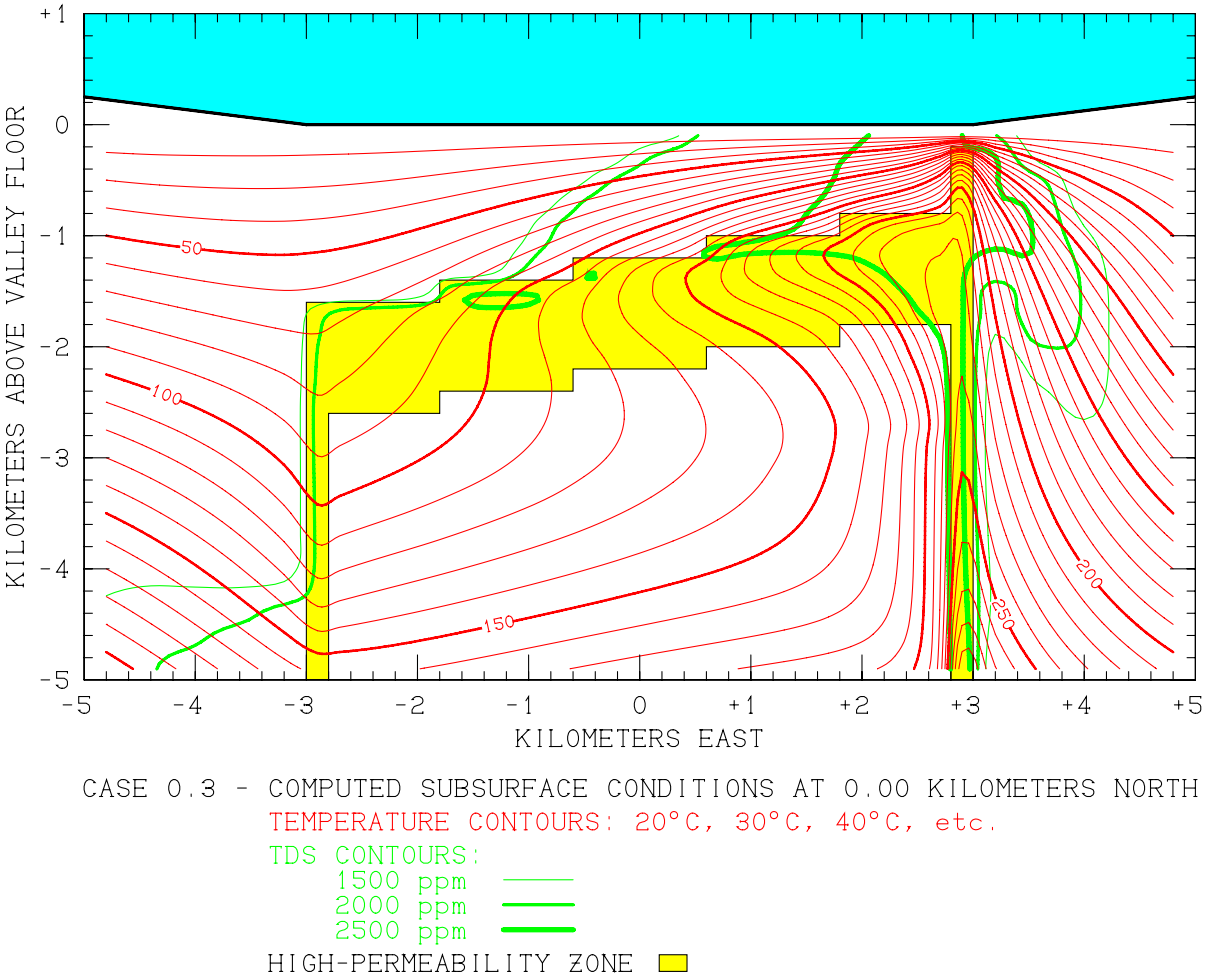

Figure 3.19. Computed stable subsurface conditions for Case 0.3 (100 t/h 3000 ppm 300°C deep recharge into eastern fault zone) in east-west vertical cross-section at $y = 0$.

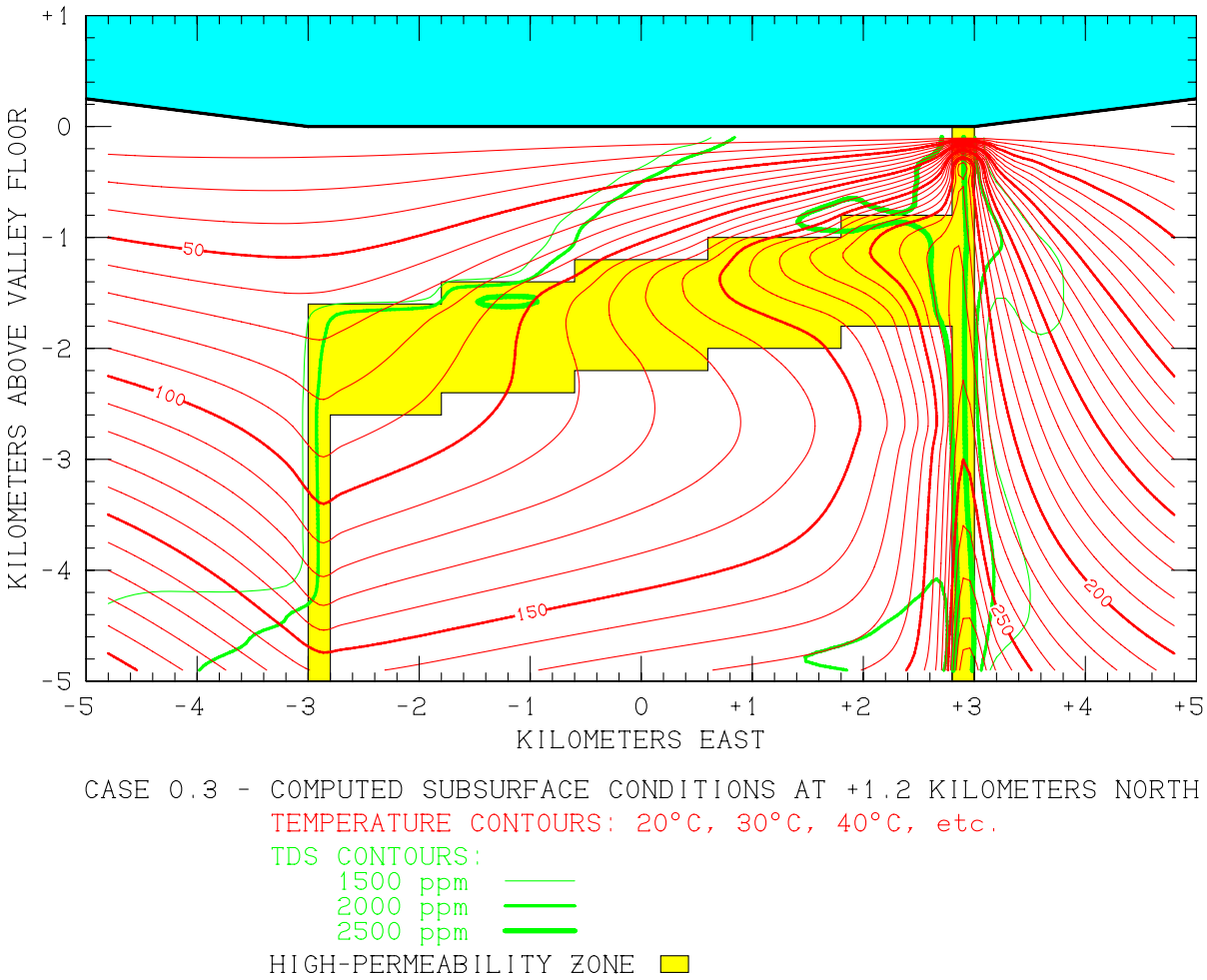

Figure 3.20. Computed stable subsurface conditions for Case 0.3 (100 t/h 3000 ppm 300°C deep recharge into eastern fault zone) in east-west vertical cross-section at y = +1.2 km North.

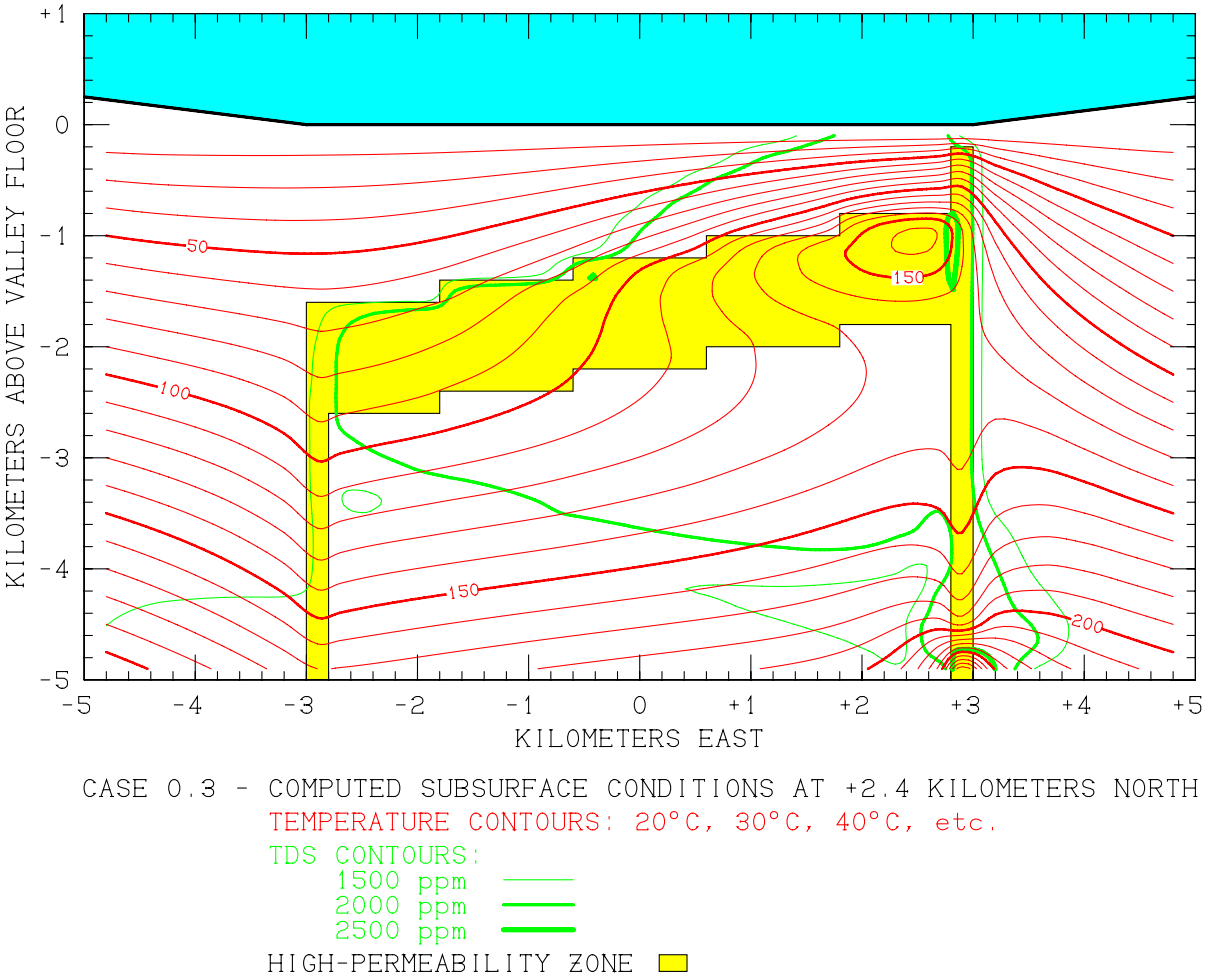

Figure 3.21. Computed stable subsurface conditions for Case 0.3 (100 t/h 3000 ppm 300°C deep recharge into eastern fault zone) in east-west vertical cross-section at *y* = +2.4 km North.

relatively low temperature waters flowing downward in the area. High rates of upflow prevail through most of the region surrounding the Eastern Fault Zone, with substantially elevated temperatures on both sides of the fault plane, particularly to the west where formations are more permeable. Highest temperatures are found adjacent to the northern part of the Eastern Fault Zone where fluids discharge directly to the surface. Deep recharge fluids with elevated TDS content fill much of the region between the fault zones at intermediate elevations owing to circulation westward through the Upper Aquifer accompanied by downflow in the Western Fault Zone.

Analogous results for the "hidden" systems that arise from deep recharge into the Western Fault Zone (Cases 1.0, 2.0, 3.0 and 4.0) are illustrated in Figures 3.22 – 3.26, 3.27 – 3.31, 3.32 – 3.36 and 3.37 – 3.41 respectively. A completely different subsurface hydrothermal convection system prevails in these cases. As noted above, hot fluids first rise upward through the Western Fault Zone, but are confined below 1600 meters depth by the impermeable "caprock" layer and are diverted eastward, where they flow up-dip towards the Eastern Fault Zone through the permeable Upper Aquifer, raising the temperature of that entire layer. By the time these hot fluids encounter the Eastern Fault Zone a significant amount of cooling and mixing has taken place, but they are still characterized by high TDS values and substantially elevated temperatures. Once within the Eastern Fault Zone, the fluids flow upward in the shallow part of the fault system and discharge at the earth surface where the fault is exposed.

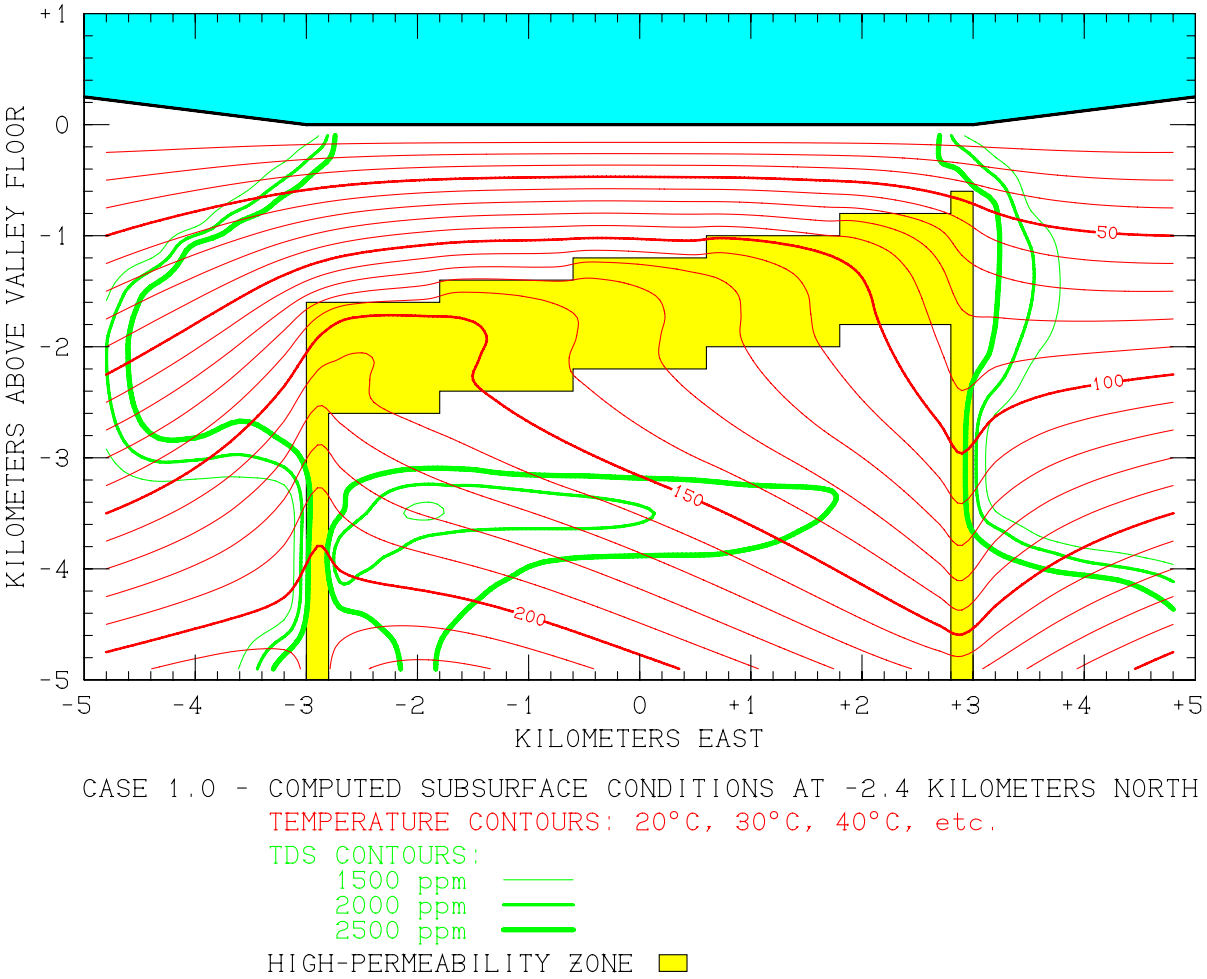

Figure 3.22. Computed stable subsurface conditions for Case 1.0 (100 t/h 3000 ppm 210°C deep recharge into western fault zone) in east-west vertical cross-section at y = –2.4 km North.

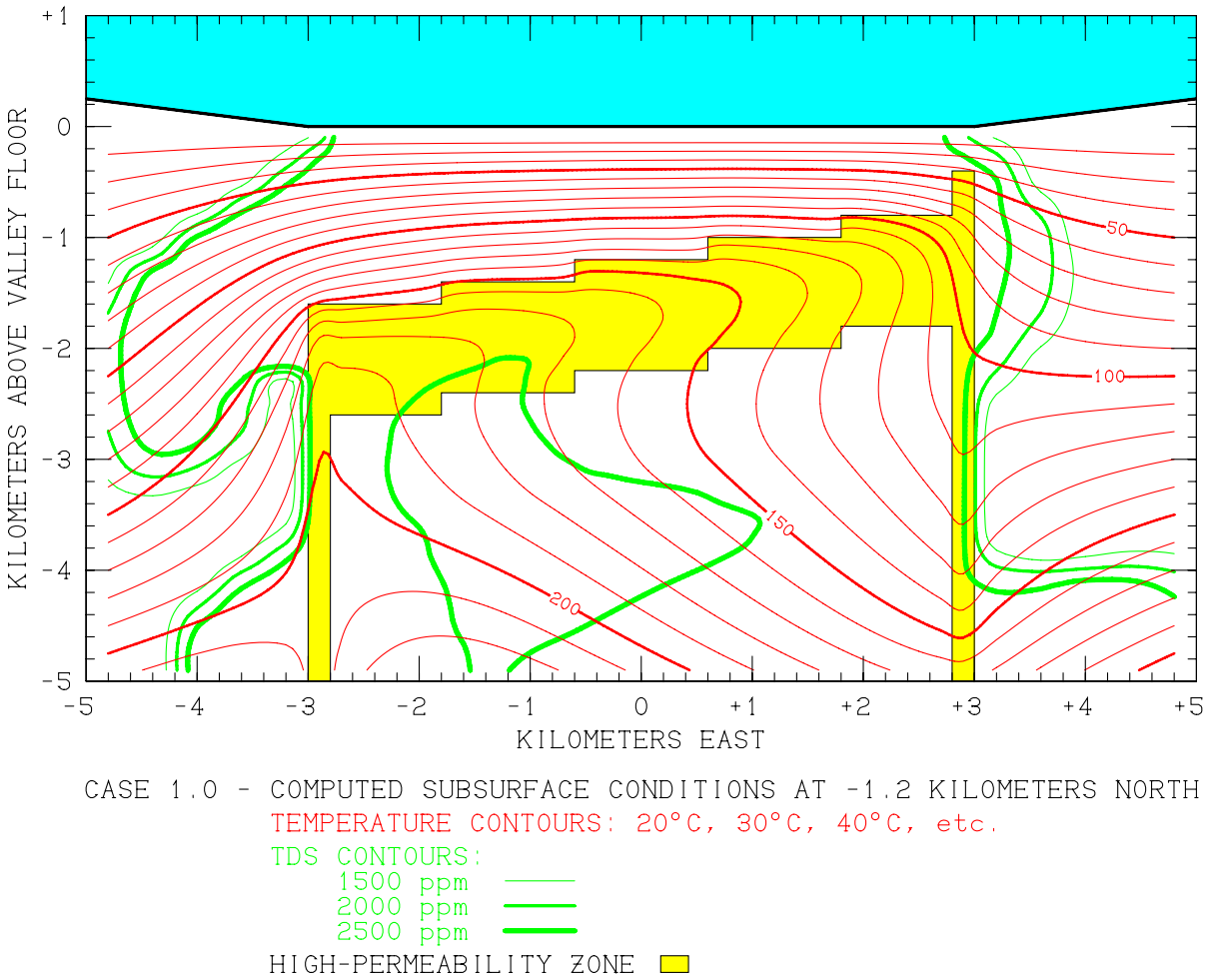

Figure 3.23. Computed stable subsurface conditions for Case 1.0 (100 t/h 3000 ppm 210°C deep recharge into western fault zone) in east-west vertical cross-section at $y = -1.2$ km North.

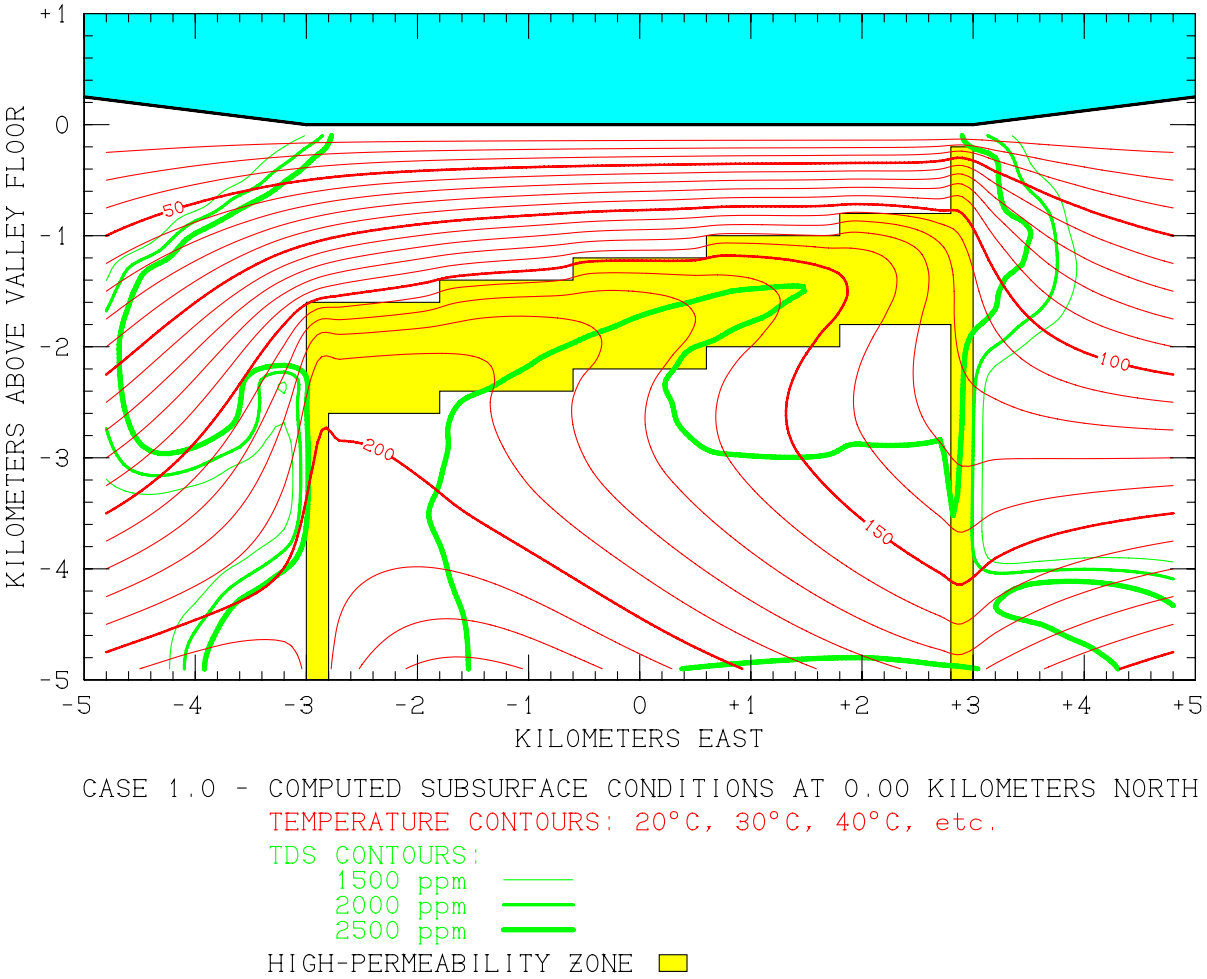

Figure 3.24. Computed stable subsurface conditions for Case 1.0 (100 t/h 3000 ppm 210°C deep recharge into western fault zone) in east-west vertical cross-section at $y = 0$.

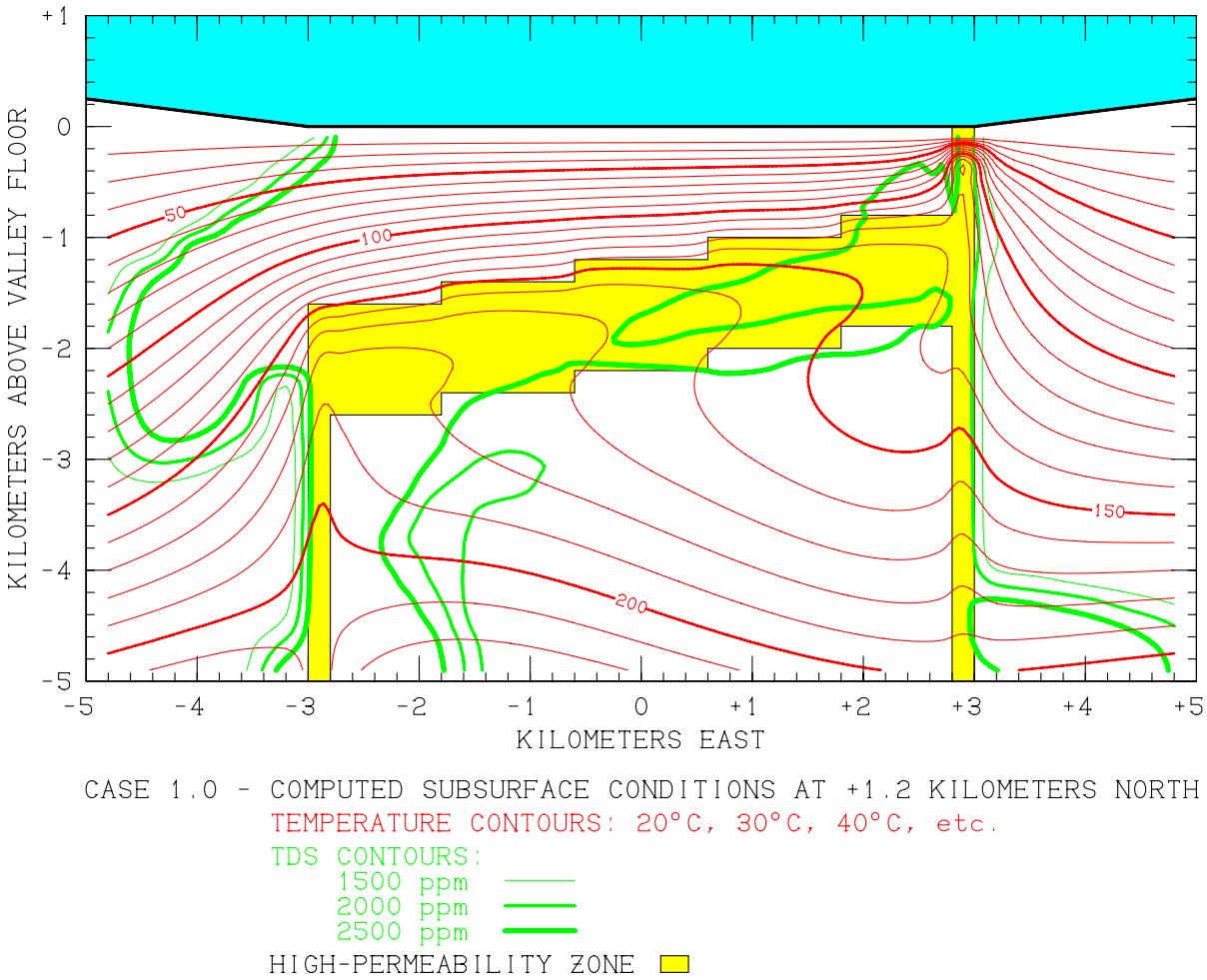

Figure 3.25. Computed stable subsurface conditions for Case 1.0 (100 t/h 3000 ppm 210°C deep recharge into western fault zone) in east-west vertical cross-section at y = +1.2 km North.

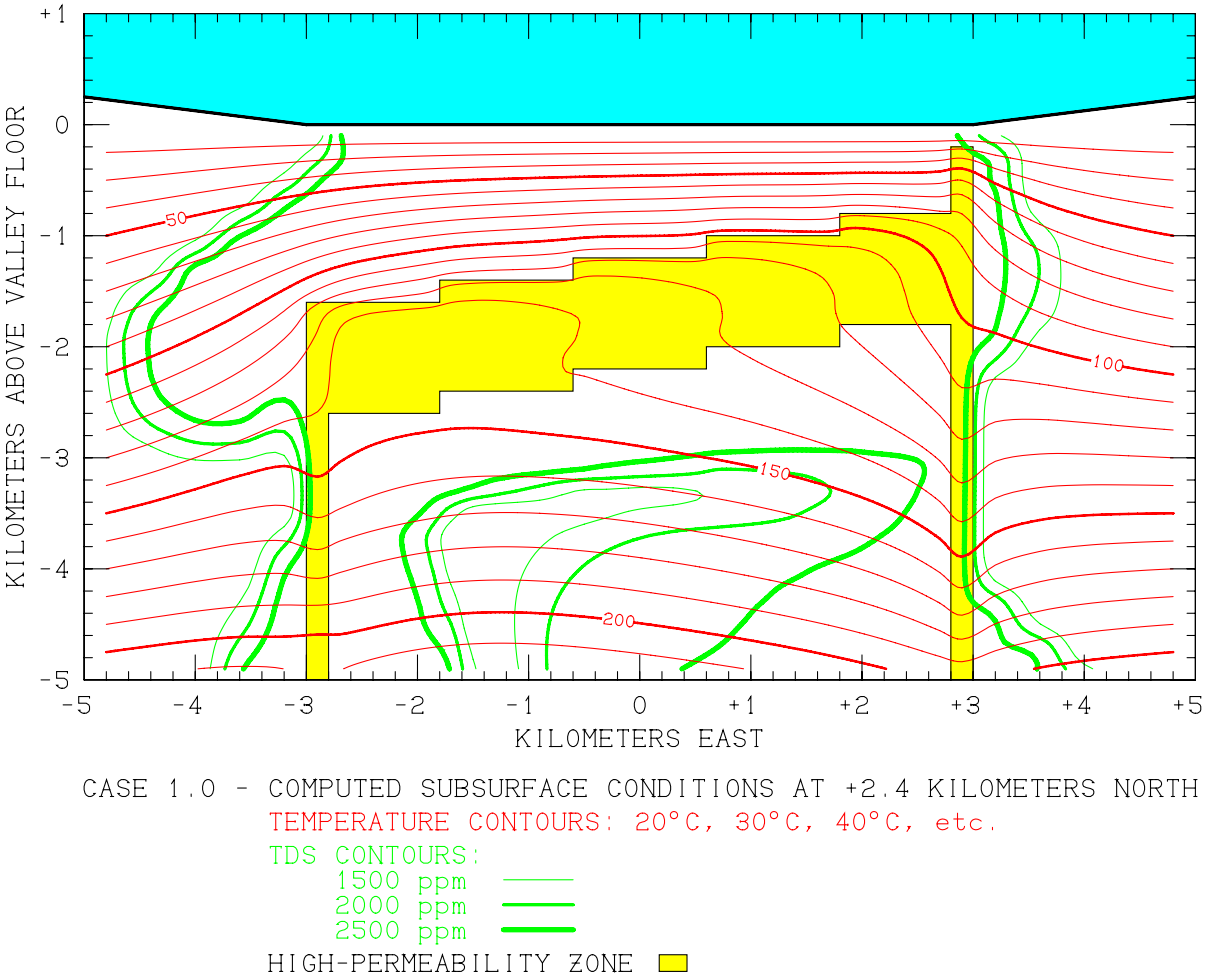

Figure 3.26. Computed stable subsurface conditions for Case 1.0 (100 t/h 3000 ppm 210°C deep recharge into western fault zone) in east-west vertical cross-section at *y* = +2.4 km North.

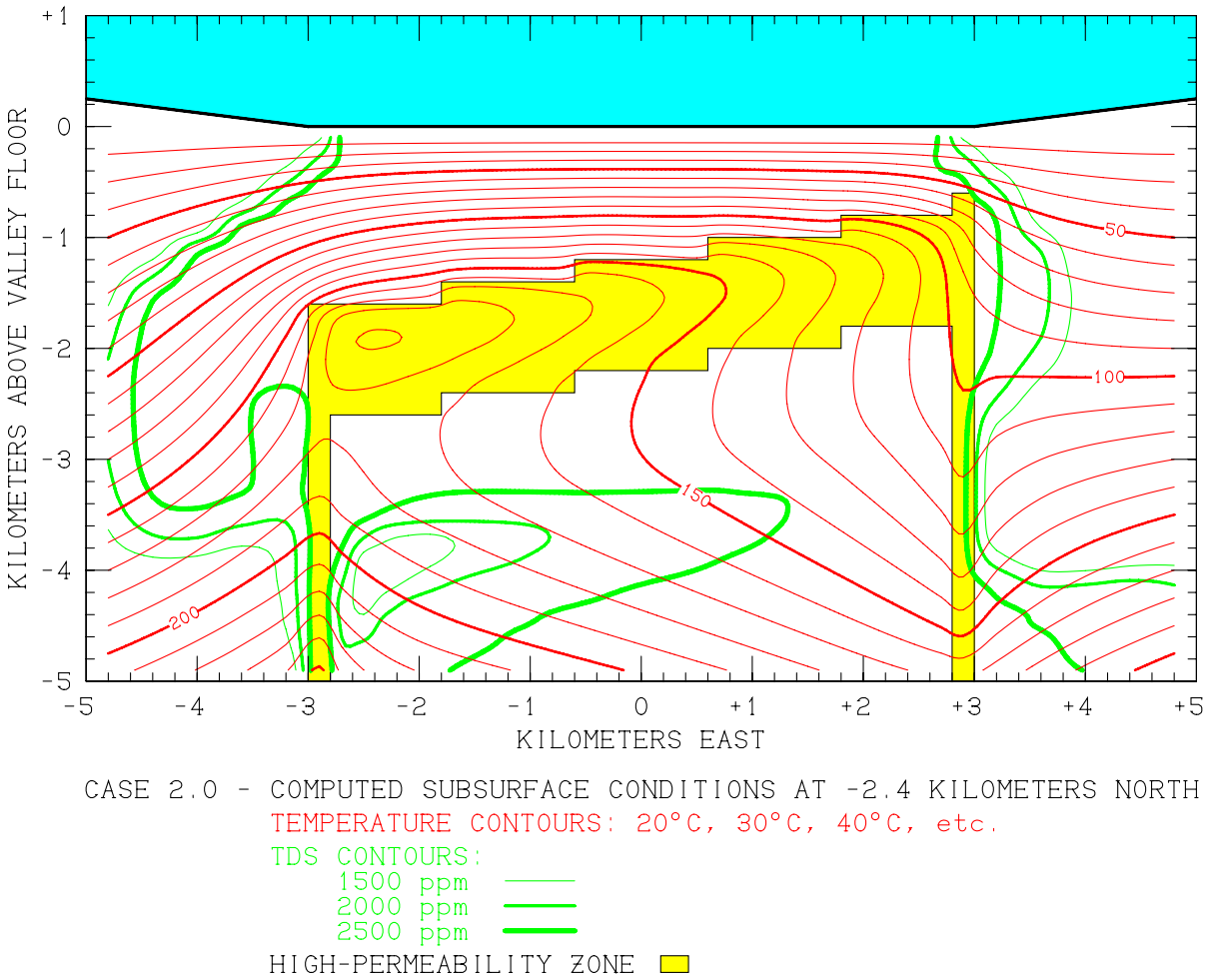

Figure 3.27. Computed stable subsurface conditions for Case 2.0 (100 t/h 3000 ppm 255°C deep recharge into western fault zone) in east-west vertical cross-section at y = –2.4 km North.

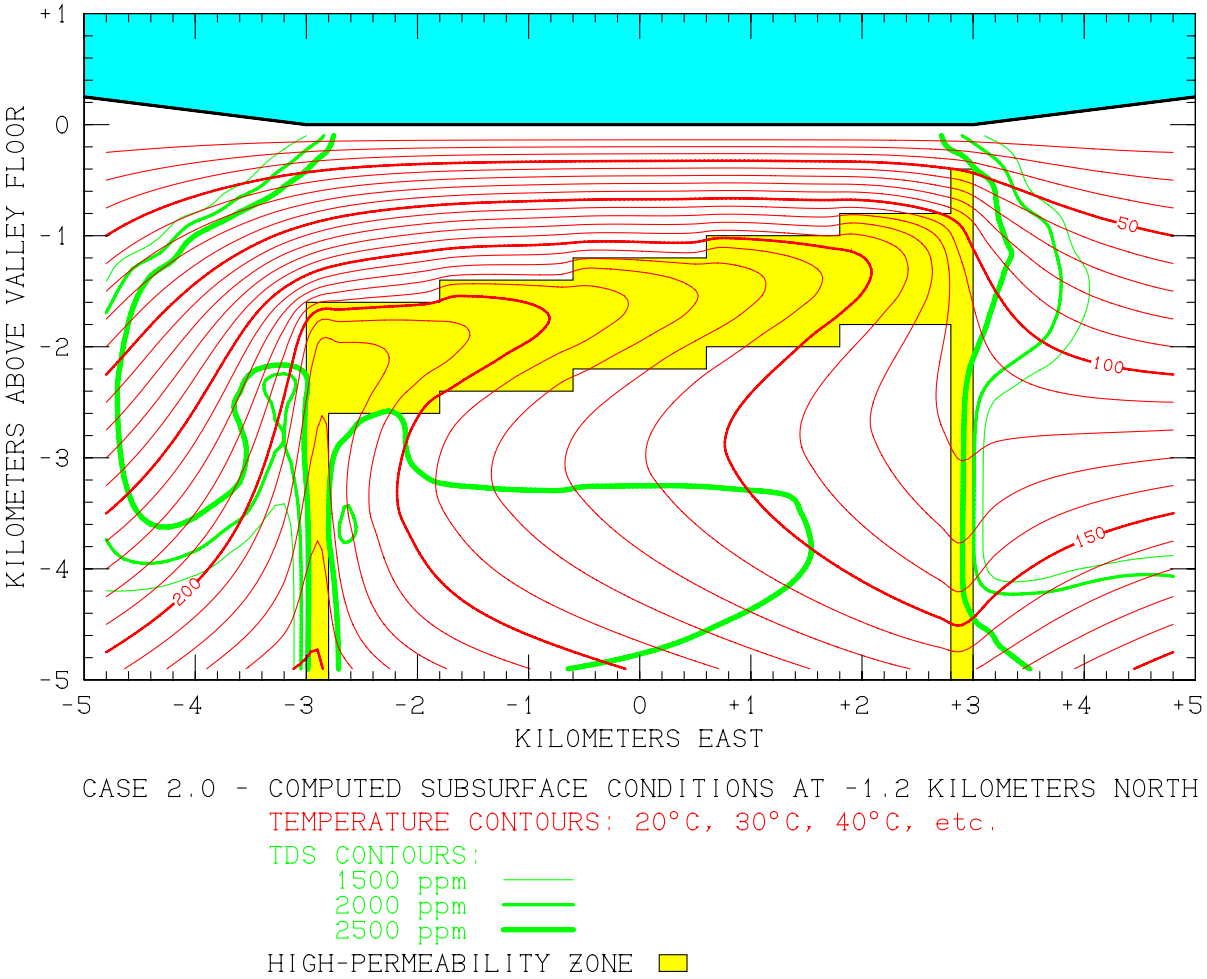

Figure 3.28. Computed stable subsurface conditions for Case 2.0 (100 t/h 3000 ppm 255°C deep recharge into western fault zone) in east-west vertical cross-section at $y = -1.2$ km North.

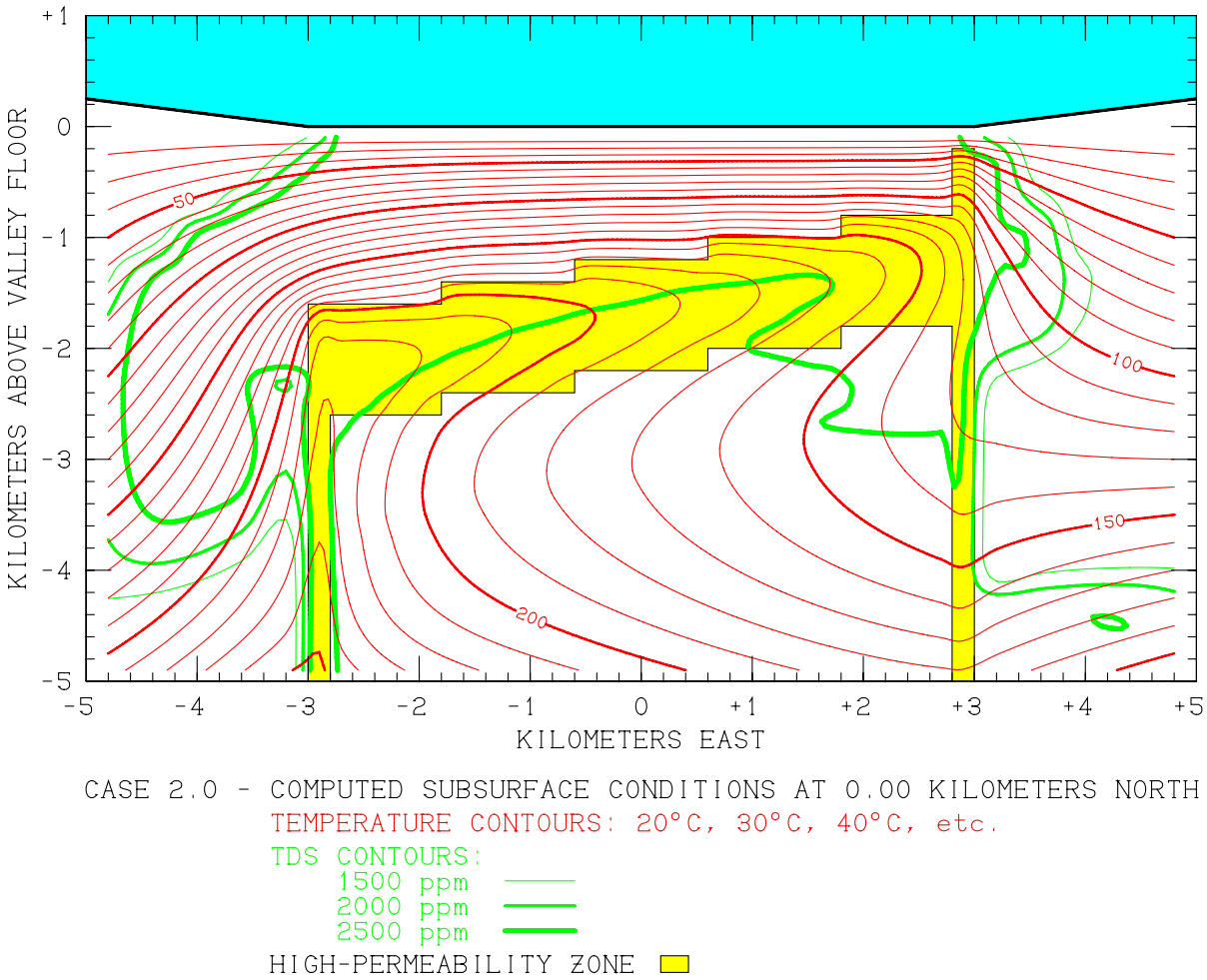

Figure 3.29. Computed stable subsurface conditions for Case 2.0 (100 t/h 3000 ppm 255°C deep recharge into western fault zone) in east-west vertical cross-section at $y = 0$.

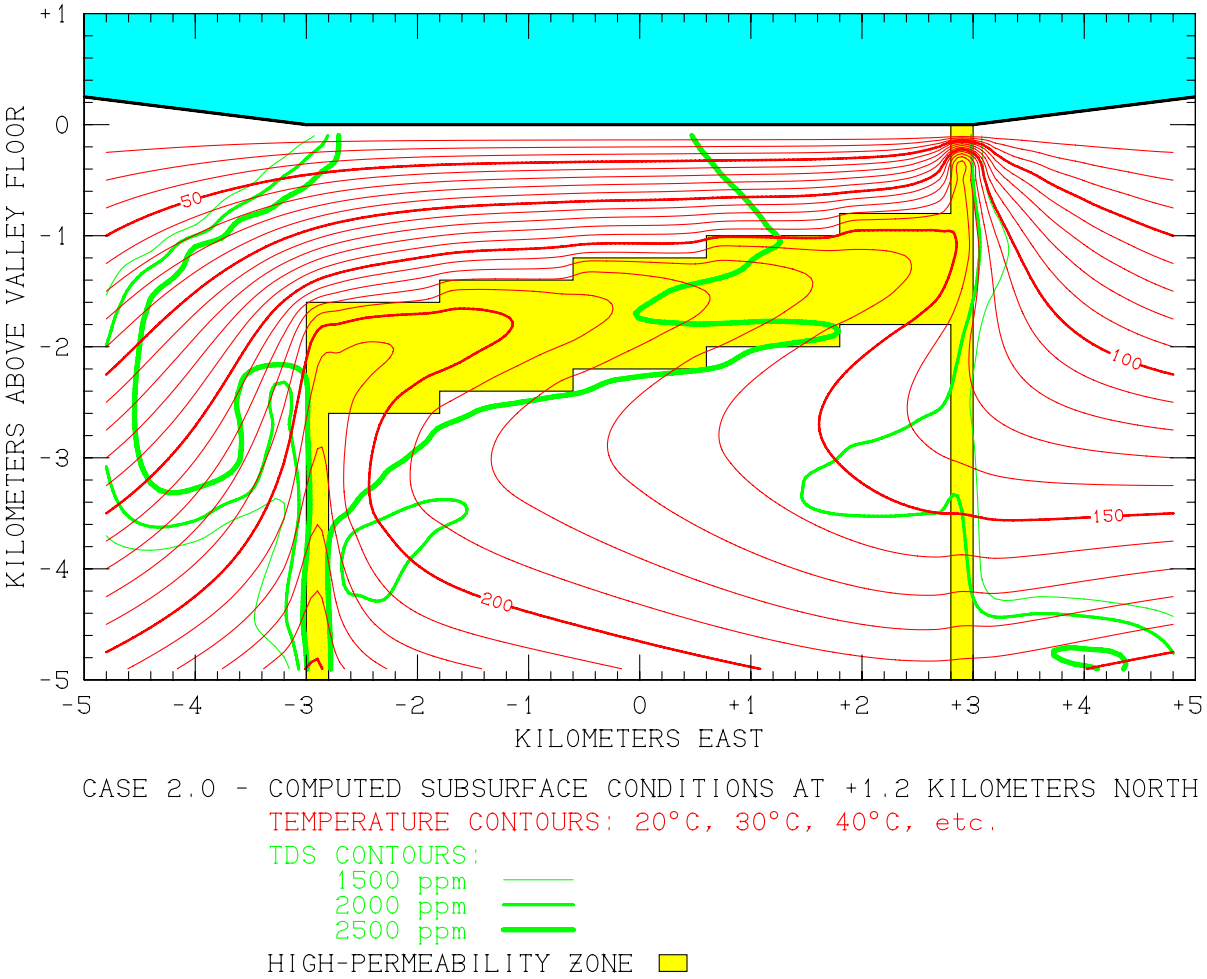

Figure 3.30. Computed stable subsurface conditions for Case 2.0 (100 t/h 3000 ppm 255°C deep recharge into western fault zone) in east-west vertical cross-section at *y* = +1.2 km North.

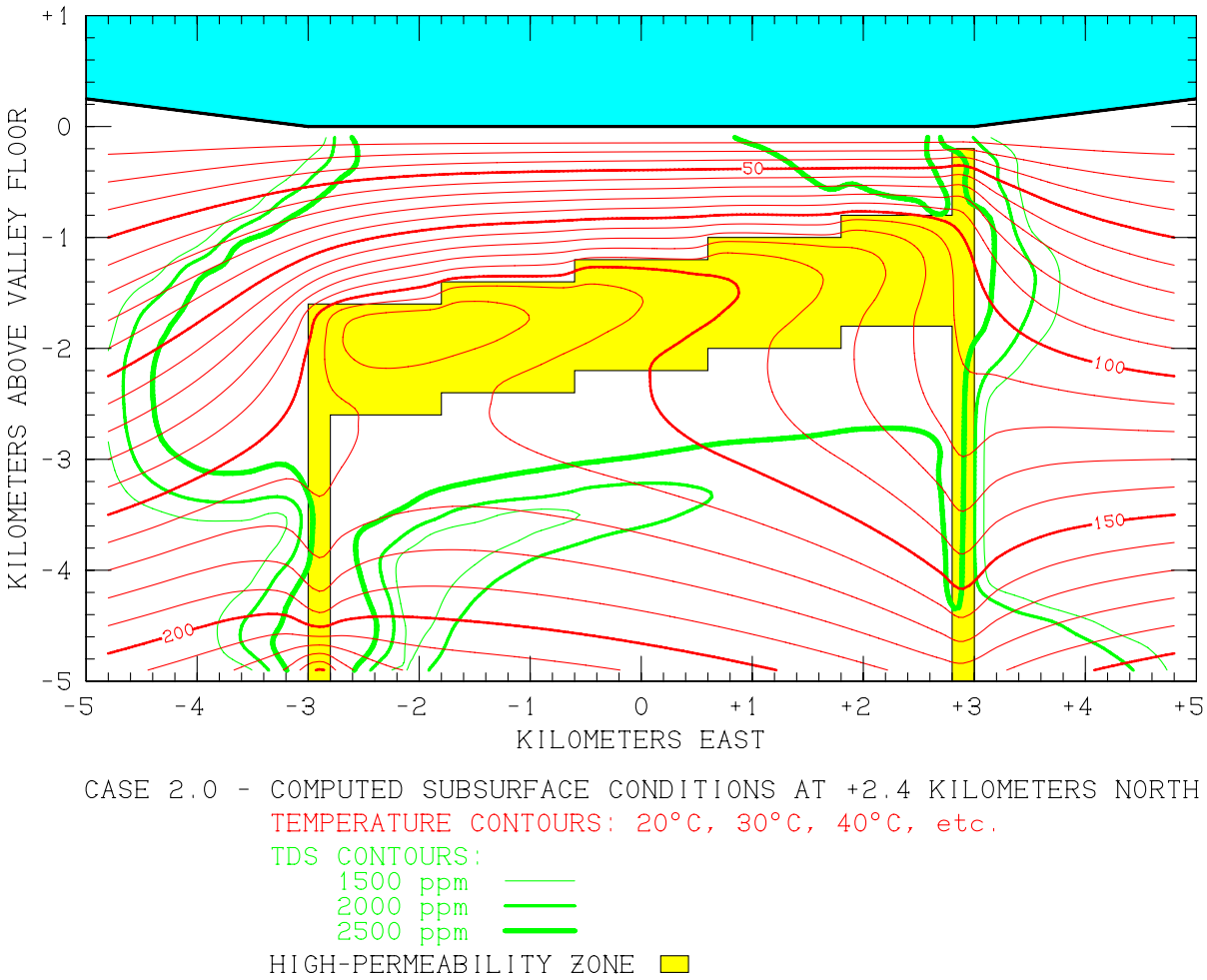

Figure 3.31. Computed stable subsurface conditions for Case 2.0 (100 t/h 3000 ppm 255°C deep recharge into western fault zone) in east-west vertical cross-section at *y* = +2.4 km North.

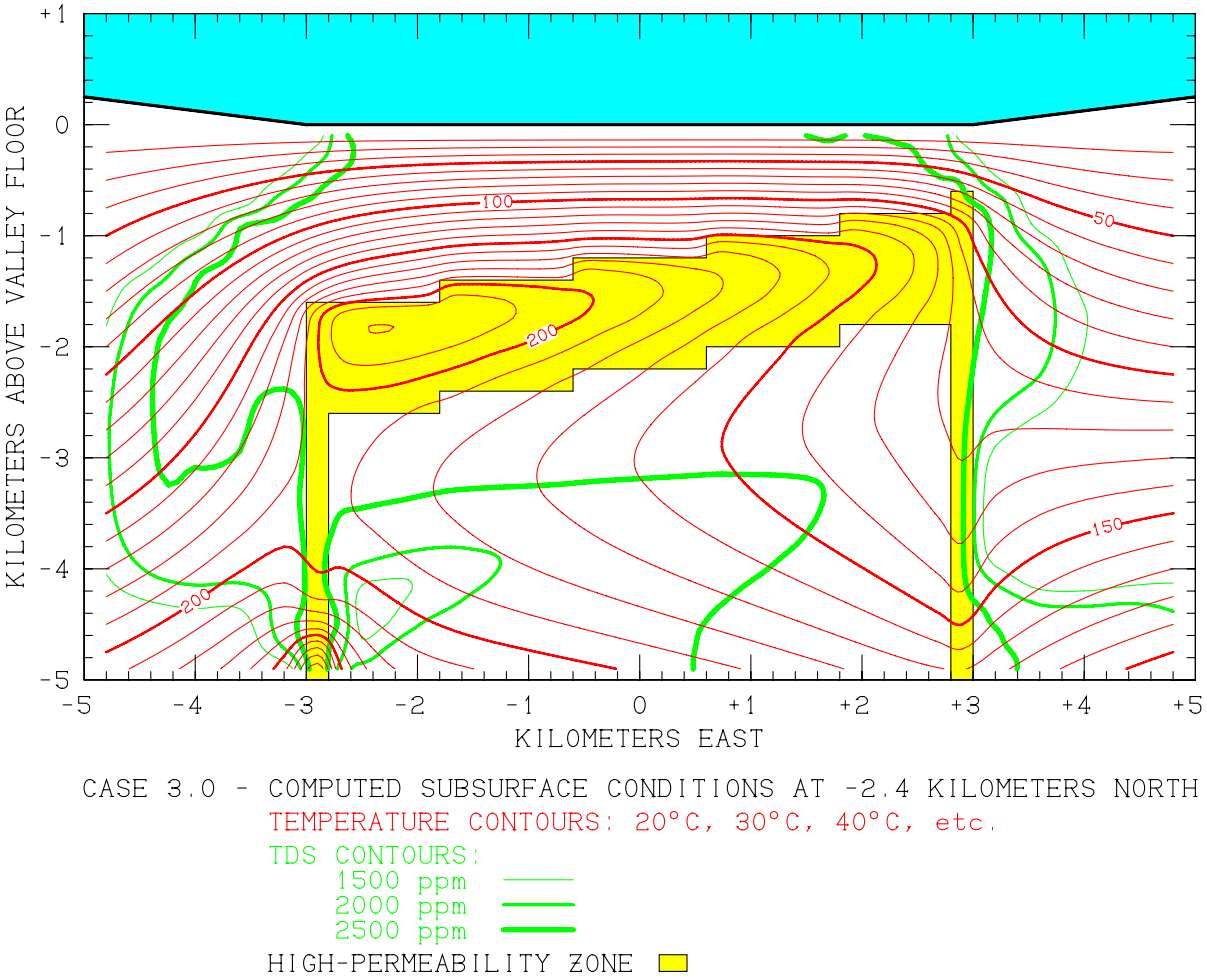

Figure 3.32. Computed stable subsurface conditions for Case 3.0 (100 t/h 3000 ppm 300°C deep recharge into western fault zone) in east-west vertical cross-section at y = –2.4 km North.

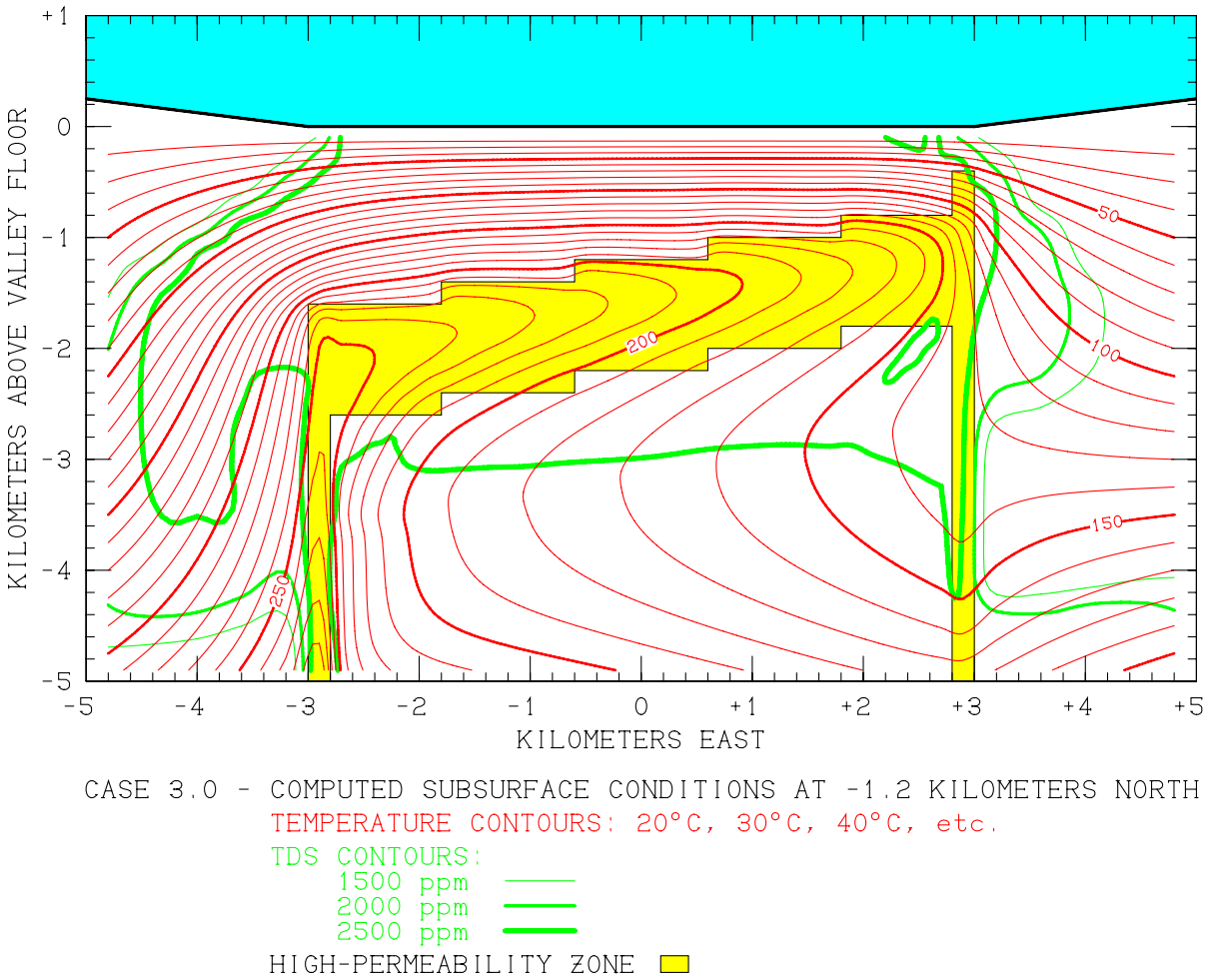

Figure 3.33. Computed stable subsurface conditions for Case 3.0 (100 t/h 3000 ppm 300°C deep recharge into western fault zone) in east-west vertical cross-section at $y = -1.2$ km North.

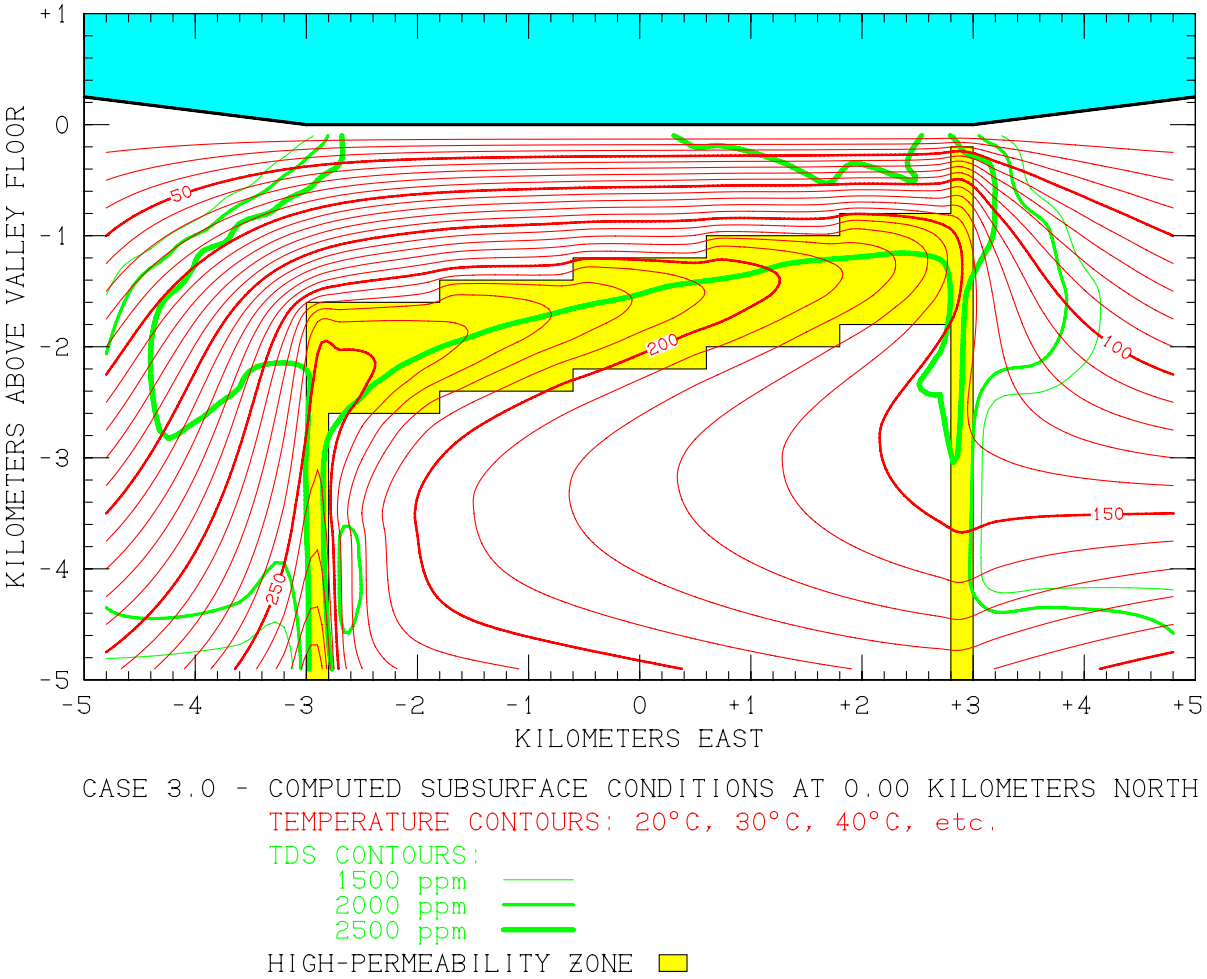

Figure 3.34. Computed stable subsurface conditions for Case 3.0 (100 t/h 3000 ppm 300°C deep recharge into western fault zone) in east-west vertical cross-section at $y = 0$.

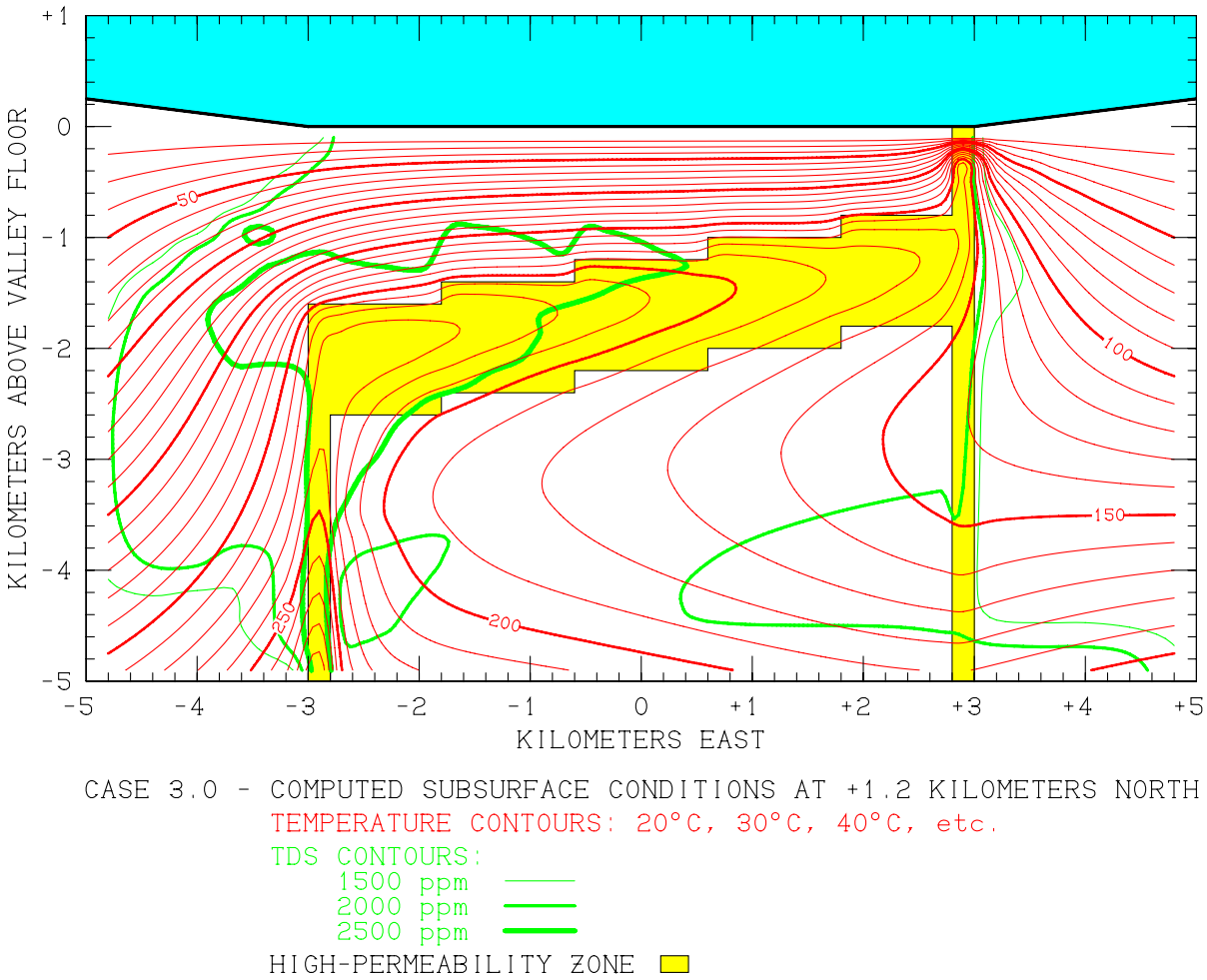

Figure 3.35. Computed stable subsurface conditions for Case 3.0 (100 t/h 3000 ppm 300°C deep recharge into western fault zone) in east-west vertical cross-section at y = +1.2 km North.

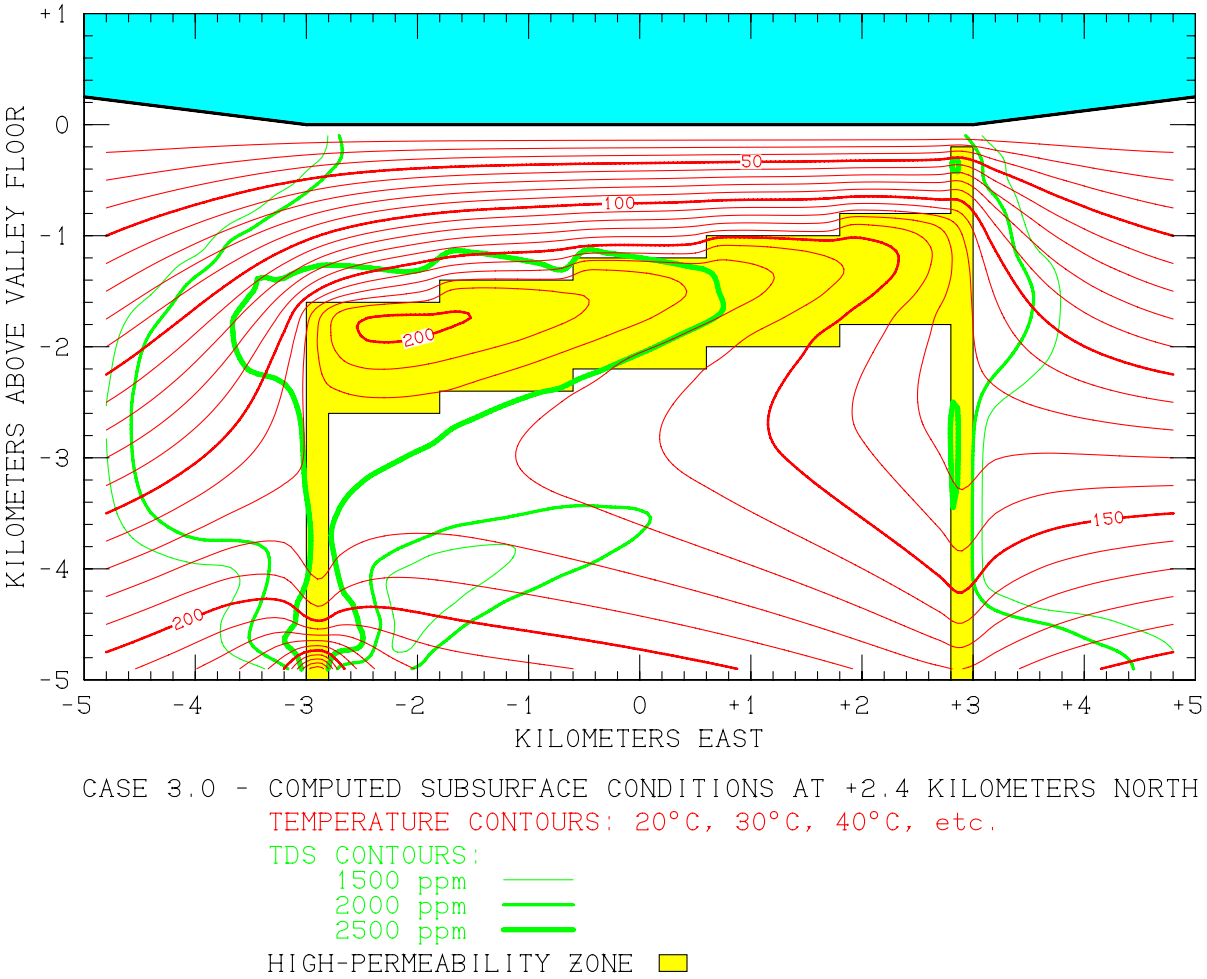

Figure 3.36. Computed stable subsurface conditions for Case 3.0 (100 t/h 3000 ppm 300°C deep recharge into western fault zone) in east-west vertical cross-section at *y* = +2.4 km North.

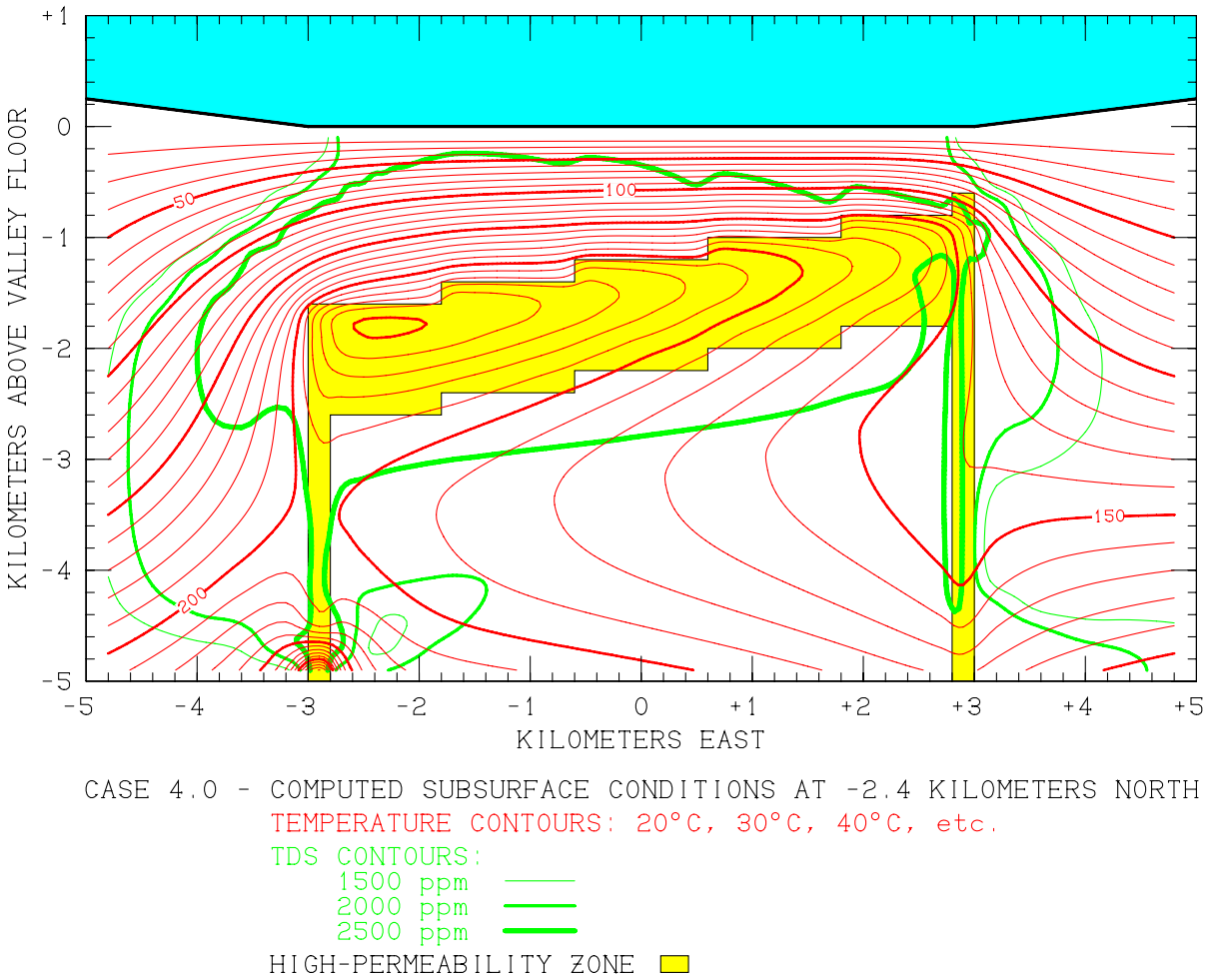

Figure 3.37. Computed stable subsurface conditions for Case 4.0 (100 t/h 3000 ppm 345°C deep recharge into western fault zone) in east-west vertical cross-section at y = –2.4 km North.

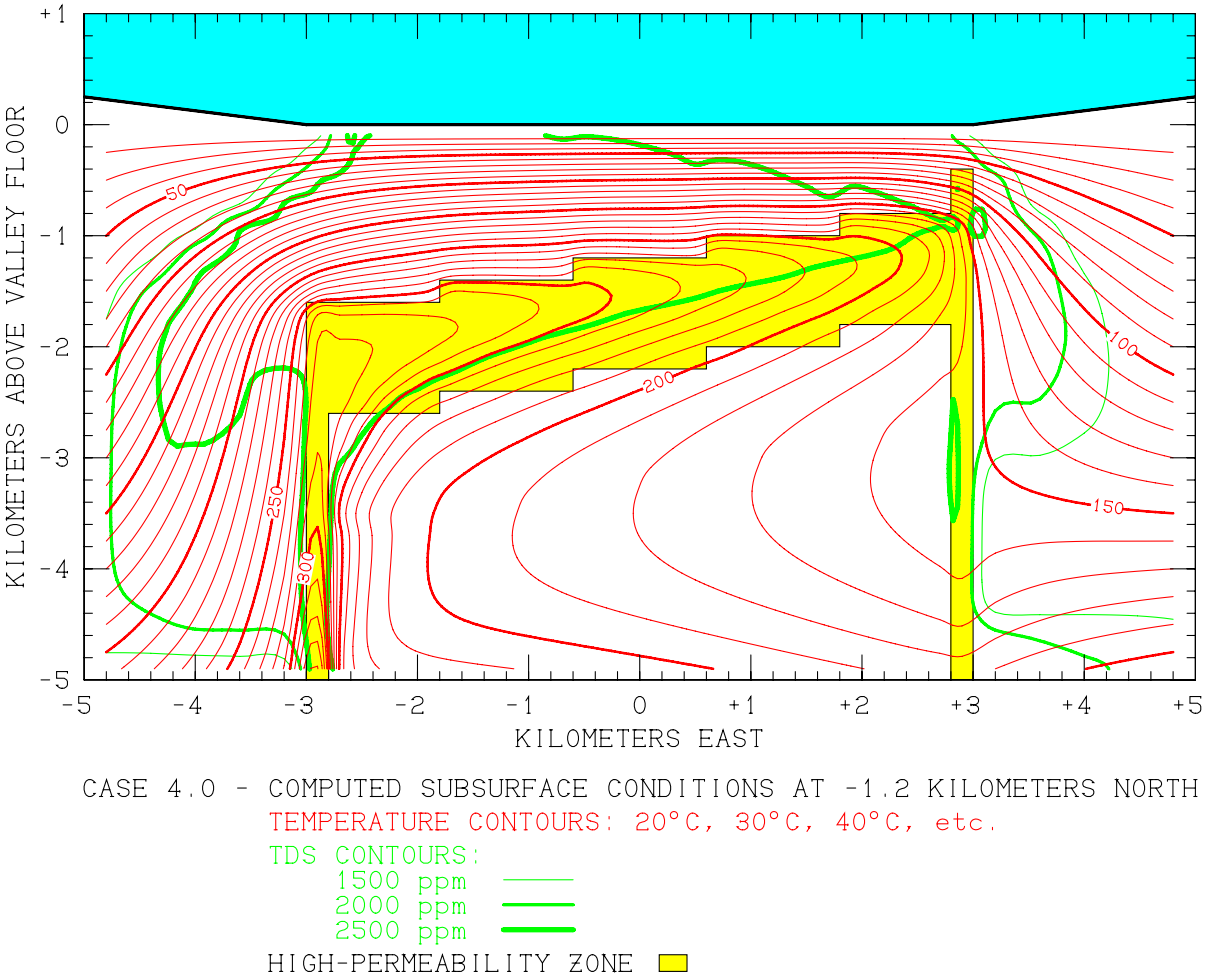

Figure 3.38. Computed stable subsurface conditions for Case 4.0 (100 t/h 3000 ppm 345°C deep recharge into western fault zone) in east-west vertical cross-section at $y = -1.2$ km North.

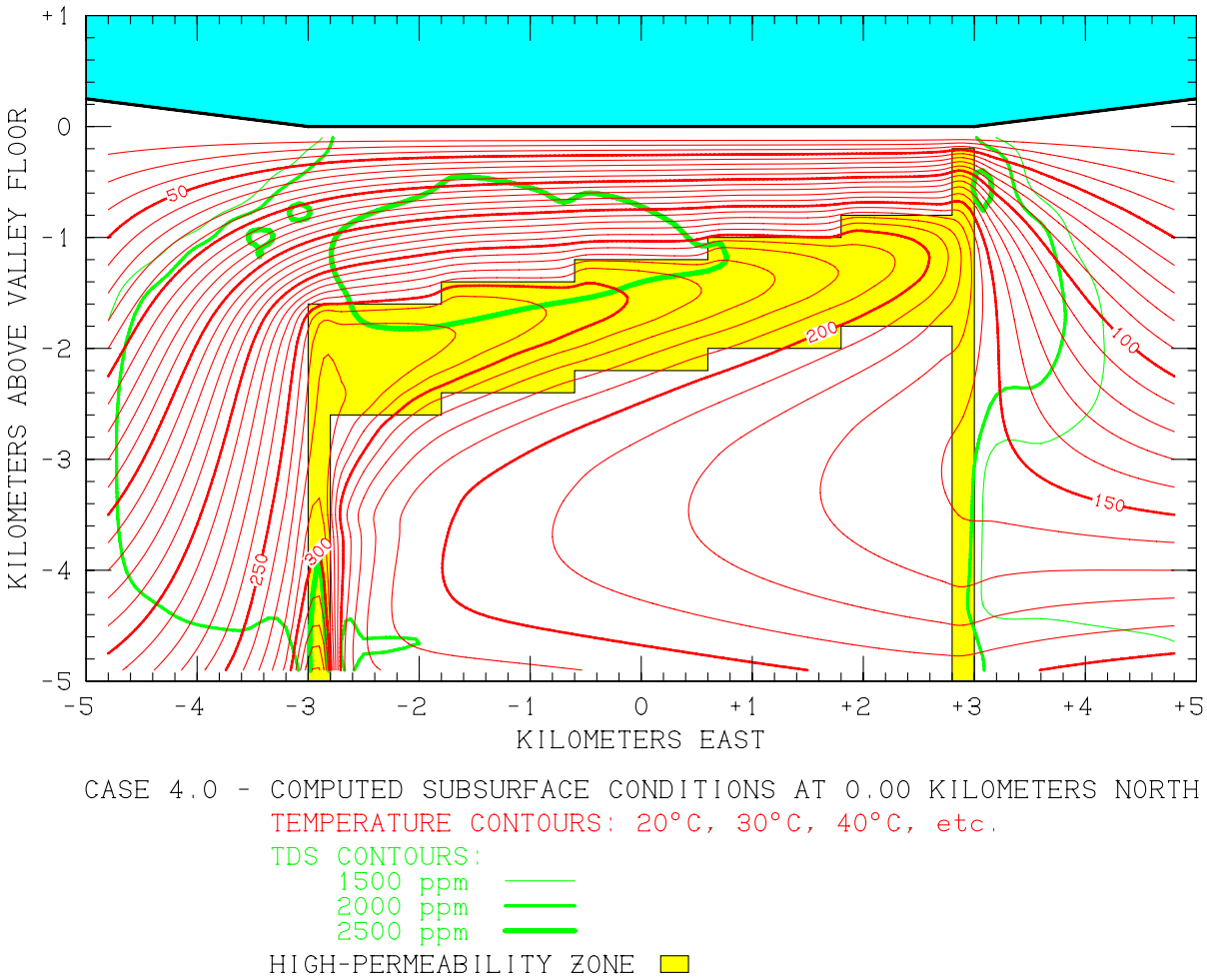

Figure 3.39. Computed stable subsurface conditions for Case 4.0 (100 t/h 3000 ppm 345°C deep recharge into western fault zone) in east-west vertical cross-section at $y = 0$.

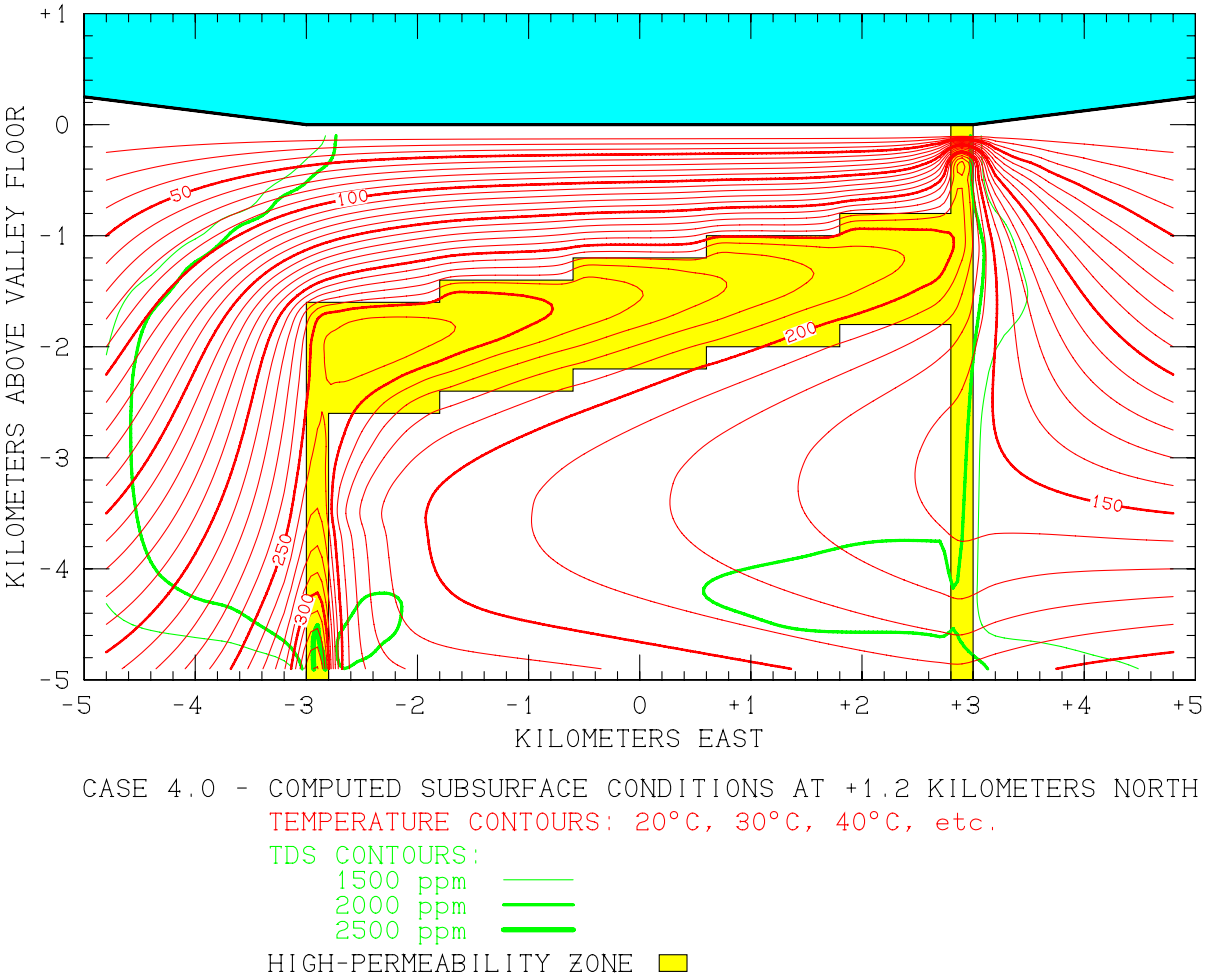

Figure 3.40. Computed stable subsurface conditions for Case 4.0 (100 t/h 3000 ppm 345°C deep recharge into western fault zone) in east-west vertical cross-section at *y* = +1.2 km North.

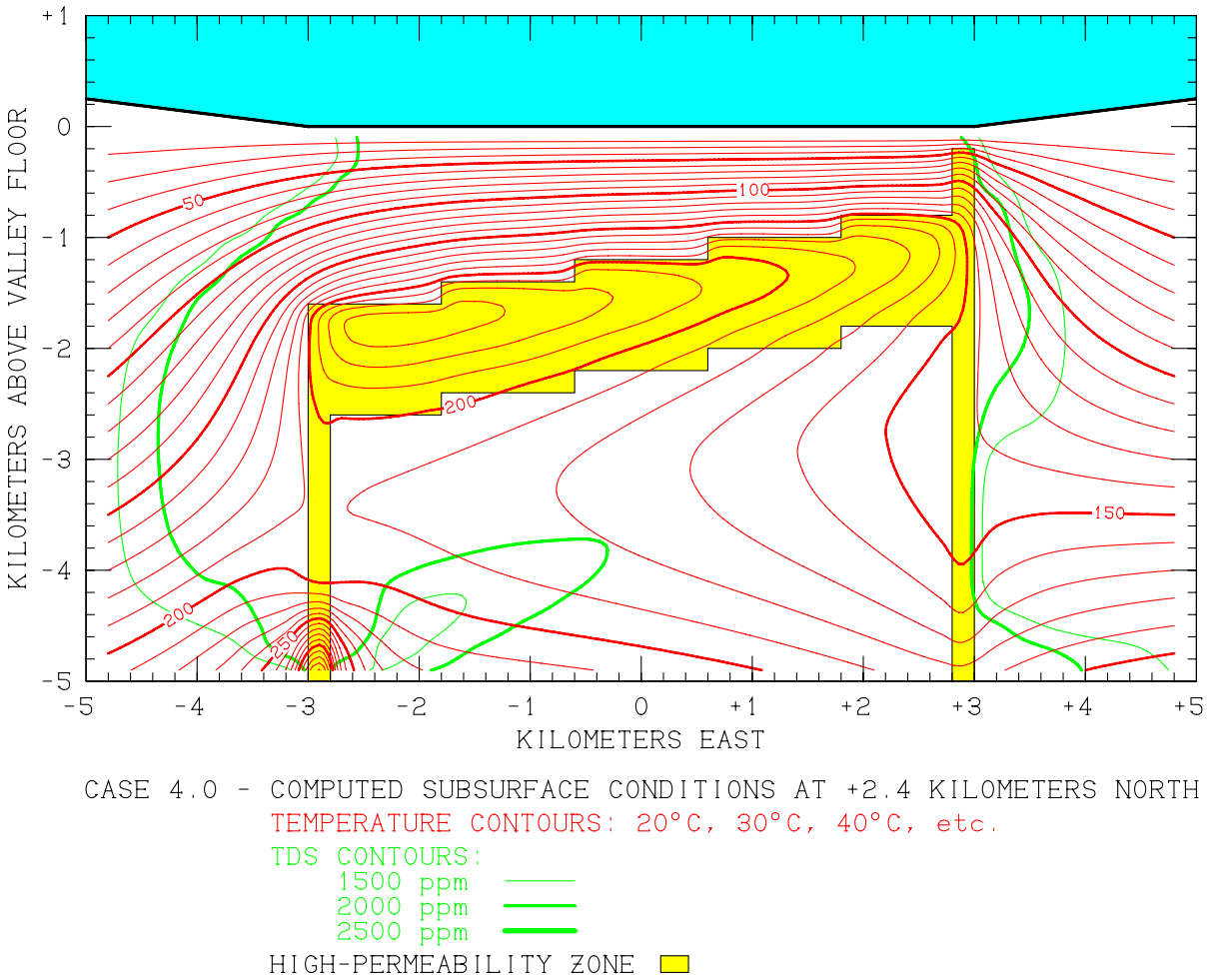

Figure 3.41. Computed stable subsurface conditions for Case 4.0 (100 t/h 3000 ppm 345°C deep recharge into western fault zone) in east-west vertical cross-section at y = +2.4 km North.

4 SURFACE MANIFESTATIONS OF GEOTHERMAL ACTIVITY

The first evidence of the presence of subsurface geothermal activity that will be encountered by the prospector will usually be visible surface manifestations arising from the upward leakage of geothermal fluids (water and/or steam). These may take a variety of forms, some quite spectacular (see Figure 4.1), others more subtle.

The present computed cases all involve the equilibrium flow of fluids both upward and downward across the earth surface. Most of the downflow is associated with the relatively high terrain to the extreme east and west of the study area. Total stabilized downflow for the various cases is equivalent to between one and three millimeters of rainfall annually over the 100 km^2 study area. Even in the arid Basin and Range, actual rainfall is vastly greater than this recharge requirement. Most of the Great Basin receives from 100 to 250 millimeters of precipitation per year. Even at Furnace Creek in Death Valley, rainfall averages 42 mm/year. Of the regions characterized by upflow, a relatively small area (the "Thermal Area" indicated in Figure 4.2, where the Eastern Fault Zone intersects the ground surface – total area 0.24 km^2) accounts for between 67% (Case 1.0) and 91% (Case 0.3) of all the fluid upflow over the entire 100 km^2 study area. This is presumably where any visible surface manifestations would appear.

Table 4.1 summarizes the computed properties of the discharges of geothermal fluids in the "Thermal Area" for each case. The upper part of the table provides the origin of the fluid discharge (that is, the portion of the discharge that represents the "deep sources" of 3000 ppm waters from the bases of the fault zones, as compared to shallow-origin 1000 ppm waters that flow downward in the surrounding mountains and then re-emerge in the Thermal Area) and compares the Thermal Area outflow to the total outflow from the entire 100 km^2 study area. The lower part of the table provides "observable" data concerning the surface discharges. In Case 0.0, no steam will form – the discharge is equivalent to 14.8 tons per hour of 1000 ppm (shallow origin) water at 59°C. In the other cases, the discharge is sufficiently energetic to boil at the surface, resulting in discharges of both liquid water and steam. Note that the TDS levels in the liquid-phase discharges exceed 3000 ppm in some of the cases – this is because of concentration of the brine by steam evaporation.

The Case 0.0 "Thermal Area" surface effects are much less pronounced than the others, of course. But the similarity between the "eastern reservoir" cases (Cases 0.1 – 0.3) and the "western reservoir" cases (1.0 – 4.0) is remarkable. Cases 0.1 – 0.3 are characterized by slightly higher total discharge rates, slightly higher steam/water ratios, and slightly higher TDS in the liquid phase, on the average. But, from a practical standpoint, there does not appear to be any definitive characteristic of these surface discharges that would alert a prospector to the fact that, in Cases 1.0 – 4.0, the main geothermal reservoir is much larger and does *not* underlie the Thermal Area but is instead located several kilometers to the west.

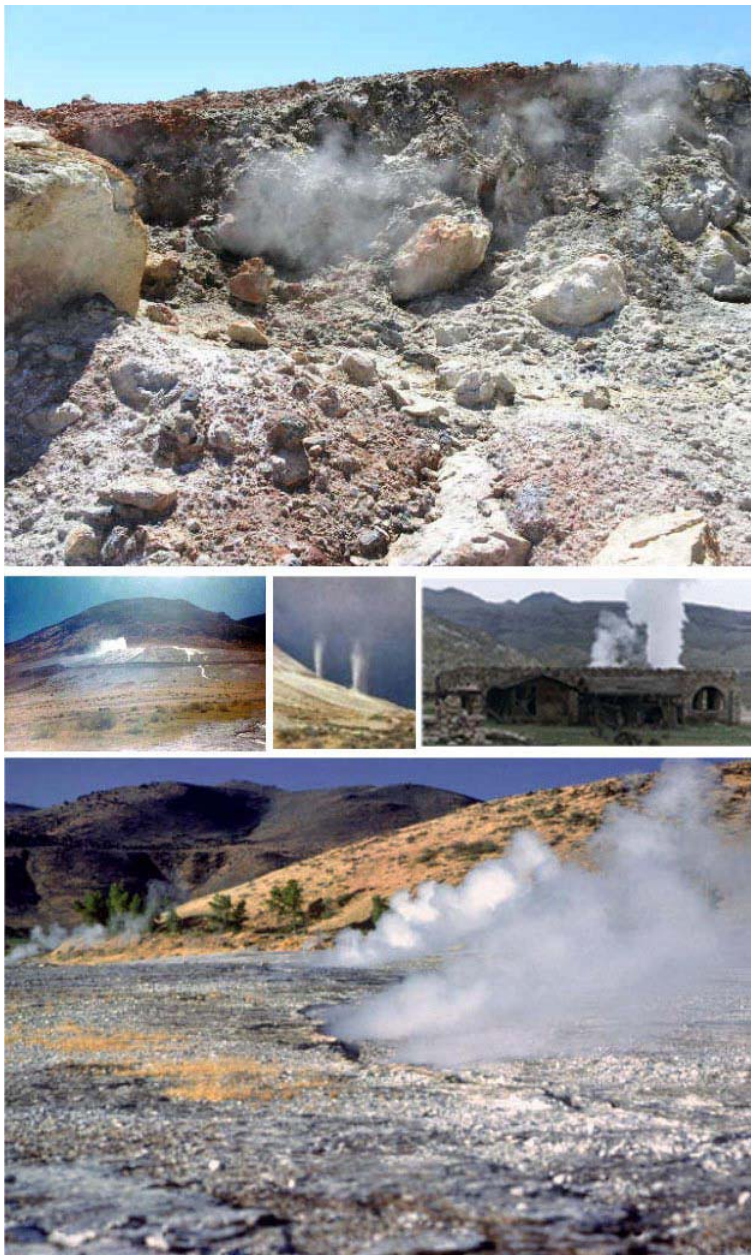

Figure 4.1. Representative natural surface manifestations of Great Basin geothermal reservoirs. *Upper:* mineralization at the Senator Fumarole on the Stillwater rangefront fault in Dixie Valley, Nevada. *Middle left:* geysers discharging above fault scarp at Beowawe, Nevada in 1971. *Middle center:* another view of the Beowawe geysers. *Middle right*: the former hot spring resort at Coso, California. *Lower:* geothermal discharge near base of Steamboat Hills, Nevada. *Photo credits:* Great Basin Geothermal LLC; Northeastern Nevada Museum, Elko; University of California at Santa Barbara; Naval Air Warfare Center, China Lake; and the National Renewable Energy Laboratory in Golden, Colorado, respectively.

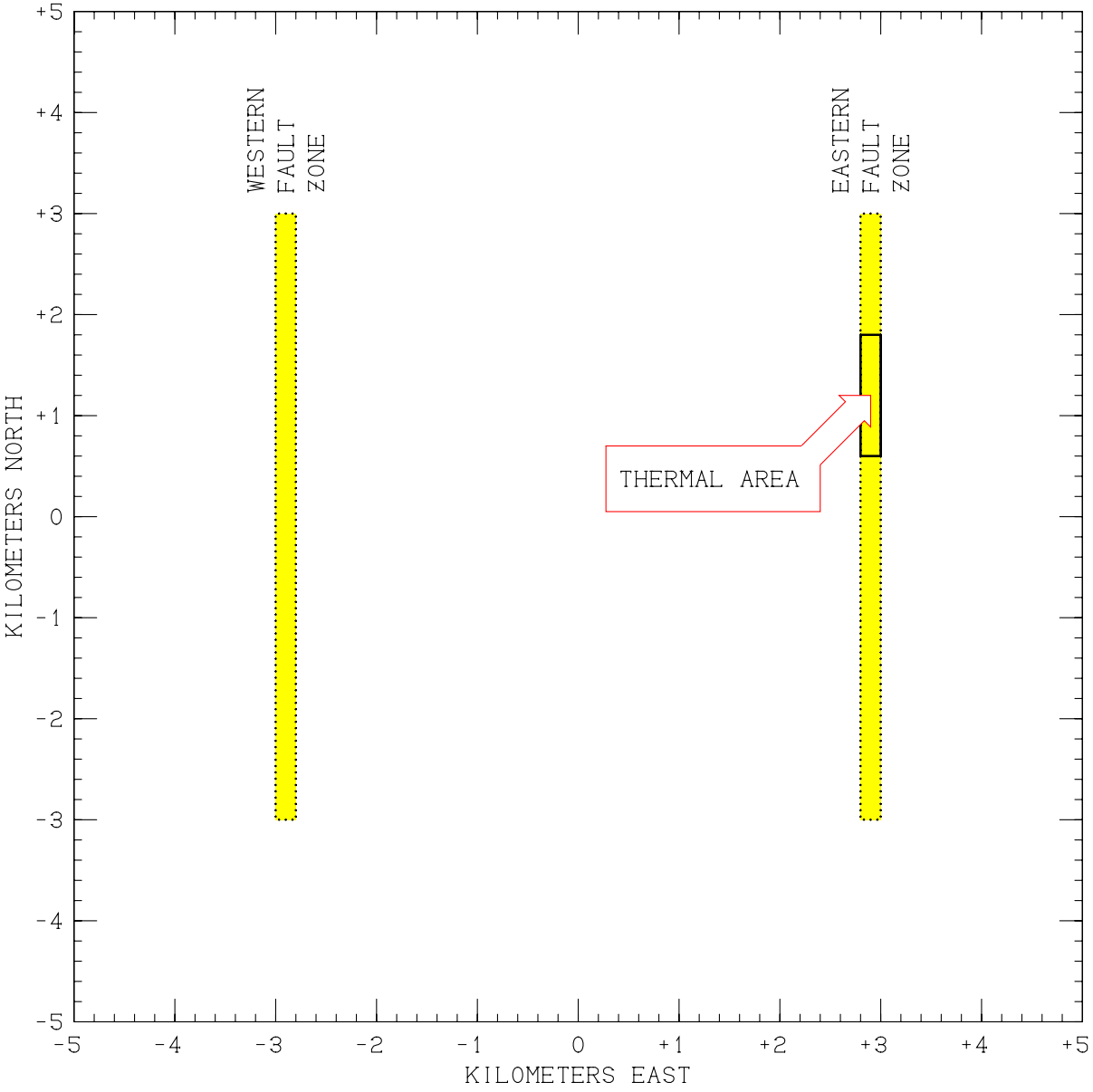

Figure 4.2. Location of the 0.24 km^2 *"Thermal Area"* along the eastern fault zone between +0.6 and +1.8 km North.

Table 4.1. Rates, origins and character of fluids discharged from the "Thermal Area".

	Thermal Area Deep Origin Outflow	Thermal Area Shallow Origin Outflow	Total Thermal Area Outflow	Total 100 km^2 Study Area Surface Outflow
Case 0.0	none	14.8 t/h	14.8 t/h	21.5 t/h
Case 0.1	84.7 t/h	13.0 t/h	97.7 t/h	117.5 t/h
Case 0.2	87.5 t/h	20.0 t/h	107.5 t/h	121.3 t/h
Case 0.3	88.7 t/h	28.2 t/h	116.9 t/h	128.8 t/h
Case 1.0	61.9 t/h	22.4 t/h	84.3 t/h	126.3 t/h
Case 2.0	60.6 t/h	23.9 t/h	84.5 t/h	126.0 t/h
Case 3.0	63.0 t/h	26.3 t/h	89.3 t/h	128.5 t/h
Case 4.0	65.7 t/h	33.1 t/h	98.8 t/h	134.5 t/h
	Thermal Area Water TDS	**Thermal Area Water Outflow**	**Thermal Area Steam Outflow**	**Total Thermal Area Outflow**
Case 0.0	1000 ppm	14.8 t/h	none	14.8 t/h
Case 0.1	2950 ppm	90.6 t/h	7.1 t/h	97.7 t/h
Case 0.2	3031 ppm	93.2 t/h	14.3 t/h	107.5 t/h
Case 0.3	3106 ppm	94.8 t/h	22.1 t/h	116.9 t/h
Case 1.0	2485 ppm	83.8 t/h	0.5 t/h	84.3 t/h
Case 2.0	2503 ppm	82.2 t/h	2.3 t/h	84.5 t/h
Case 3.0	2582 ppm	83.4 t/h	5.9 t/h	89.3 t/h
Case 4.0	2657 ppm	86.7 t/h	12.1 t/h	98.8 t/h

5 RESULTS FROM SHALLOW HEAT FLOW SURVEYS

It is common practice in geothermal prospecting to drill one or more relatively shallow "heat flow holes" (usually of small diameter) in the neighborhood of visible surface geothermal manifestations, to try to estimate the vertical temperature gradient and the lateral extent of the underlying geothermal reservoir. *Sass et al.* (1999) have collated downhole data from some 787 such exploratory wells drilled in the Great Basin by the geothermal industry prior to 1995 (mainly in Nevada and Utah). Locations of these wells are indicated in Figure 5.1. Of these 787 wells, less than half exceed 100 meters in total depth, and fewer than 6% are deeper than 300 meters.

Accordingly, next consider that the field developer chooses to drill a series of 300-meter heat flow holes in the region, centered on the Thermal Area, to try to locate and verify the presence of a geothermal resource. Figures 5.2 – 5.9 illustrate the distribution of temperature at 300 meters depth that would presumably be found by an extensive investigation of this type for each of the eight computed cases. For Cases 0.0 – 0.3, these isotherms clearly delineate the Thermal Area and the Eastern Fault Zone as the primary targets. Despite the fact that somewhat elevated temperatures are found at this depth farther to the west in Cases 1.0 – 4.0, it is still reasonably clear that the center of the shallow heat flow anomaly coincides with the Thermal Area in those cases as well.

If at this stage the developer chose to take the risk of drilling a multi-million dollar deep "discovery well", he would therefore have little choice but to site it in the Thermal Area. Figure 5.10 depicts the stable temperature profiles that would be observed in a 2500-meter vertical well located at x = +2.9 km East, y = +1.5 km North (the center of the Thermal Area), according to the STAR results. Unsurprisingly, Case 0.0 is not very interesting from the standpoint of electricity production. Cases 0.1 – 0.3 (particularly the latter two), by contrast, encounter temperatures at permeable levels (generally between 1000 and 2000 meters depth) that would be entirely suitable for development of an electric power project.

But results from the 2500-meter deep well would be very disappointing for Cases 1.0 – 4.0. A knowledgeable geothermal reservoir engineer examining these temperature profiles would correctly conclude that the profiles exhibit the temperature inversions that are usually characteristic of an "outflow zone" and that consequently the main part of the subsurface geothermal system must lie elsewhere. But the problem of delineating its actual location remains.

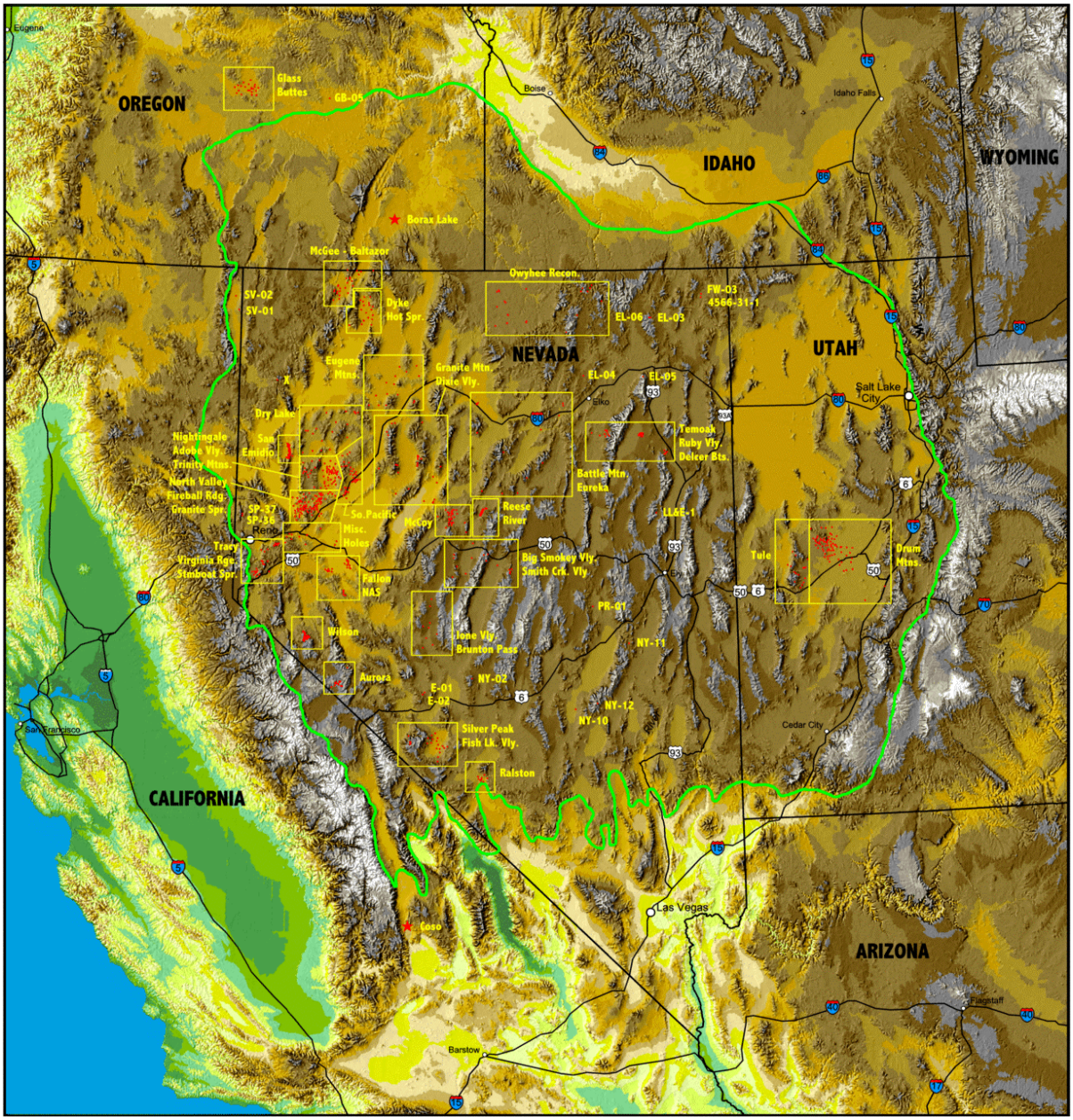

Figure 5.1. Locations of 787 Great Basin geothermal exploration wells with data compiled by *Sass et al.* (1999), drilled by geothermal development companies prior to 1995. Image courtesy United States Geological Survey.

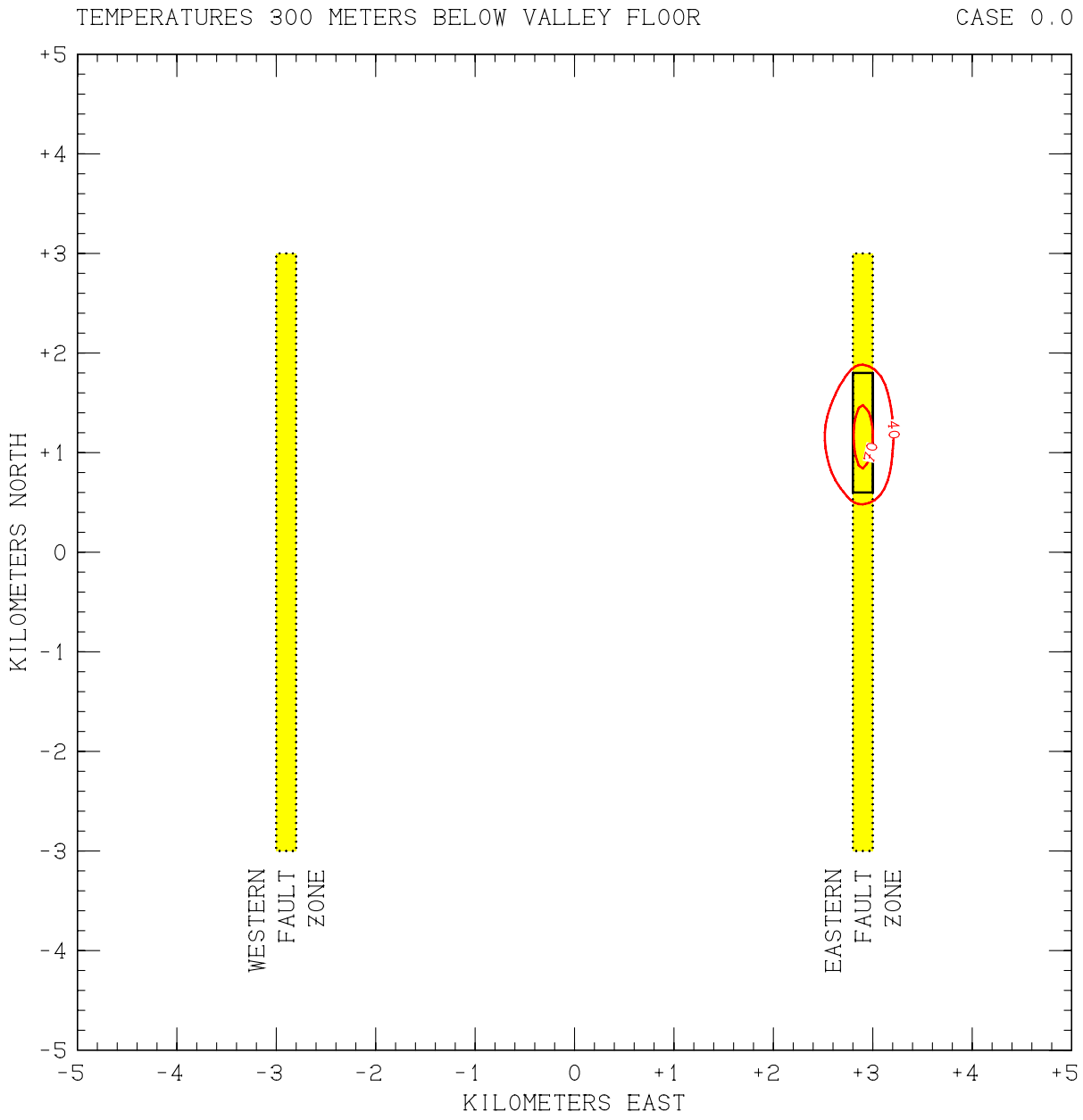

Figure 5.2. Maximum bottomhole temperatures obtained from a *"heat flow survey"* using 300-meter slim exploration holes for Case 0.0. Bottomhole temperature contours are 40°C and 70°C, corresponding to local conductive heat flow values of 300 mW/m^{2}and 600 mW/m^2.

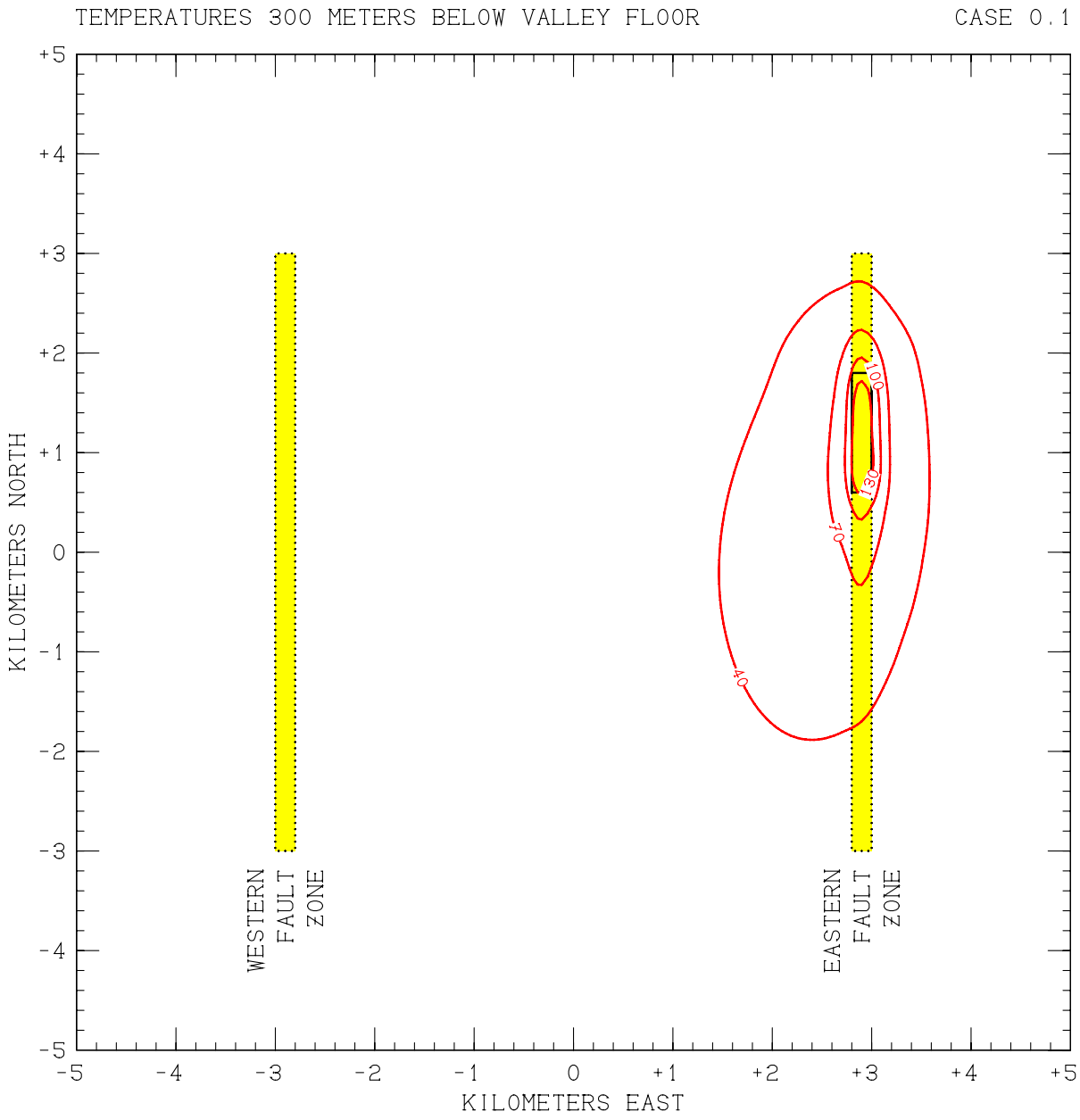

Figure 5.3. Maximum bottomhole temperatures obtained from a *"heat flow survey"* using 300-meter slim exploration holes for Case 0.1. Bottomhole temperature contours are 40°C, 70°C, 100°C *etc.* corresponding to local conductive heat flow values of 300 mW/m^2, 600 mW/m^2, 900 mW/m^2, *etc.*

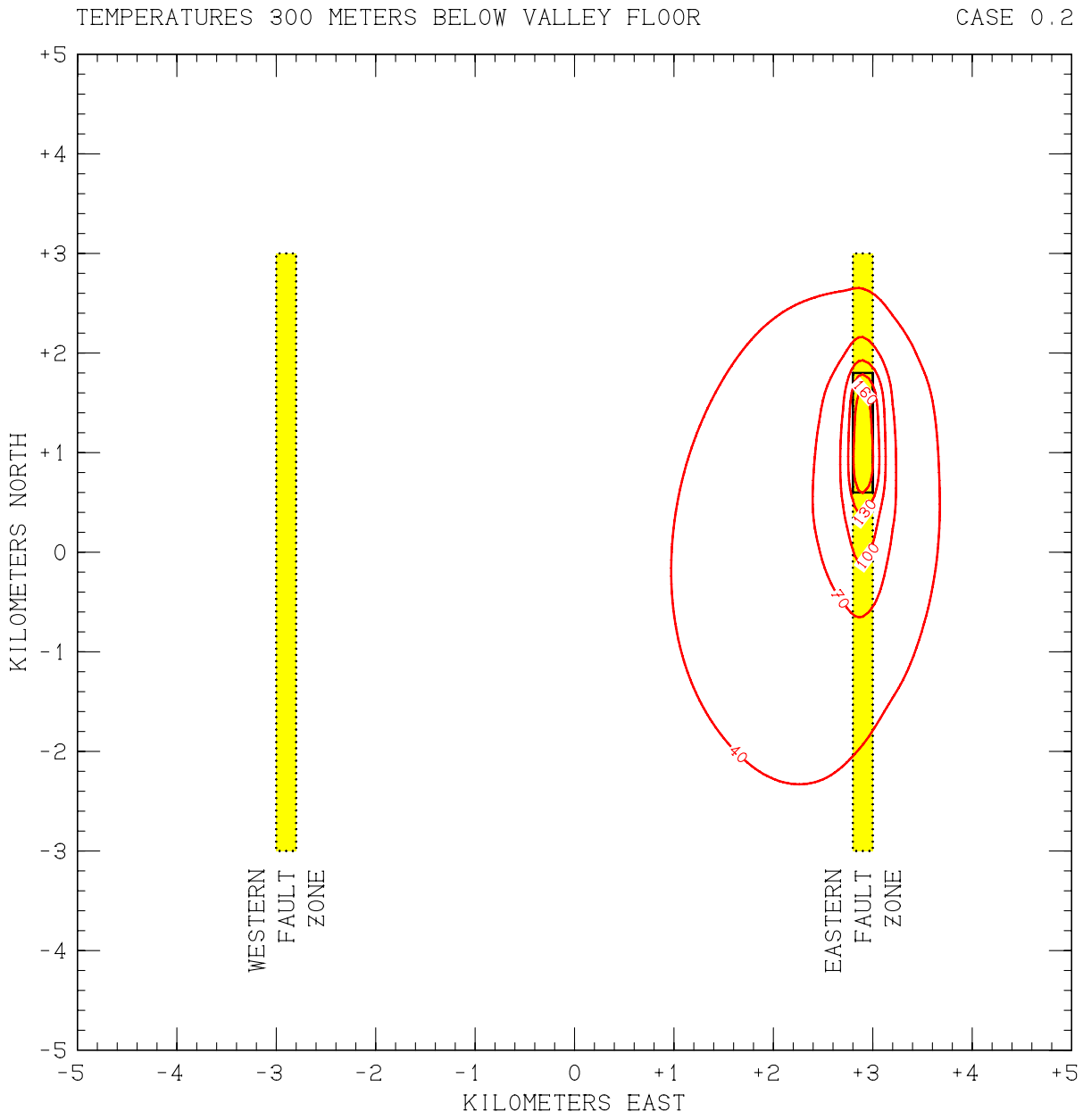

Figure 5.4. Maximum bottomhole temperatures obtained from a *"heat flow survey"* using 300-meter slim exploration holes for Case 0.2. Bottomhole temperature contours are 40°C, 70°C, 100°C *etc.* corresponding to local conductive heat flow values of 300 mW/m^2, 600 mW/m^2, 900 mW/m^2, *etc.*

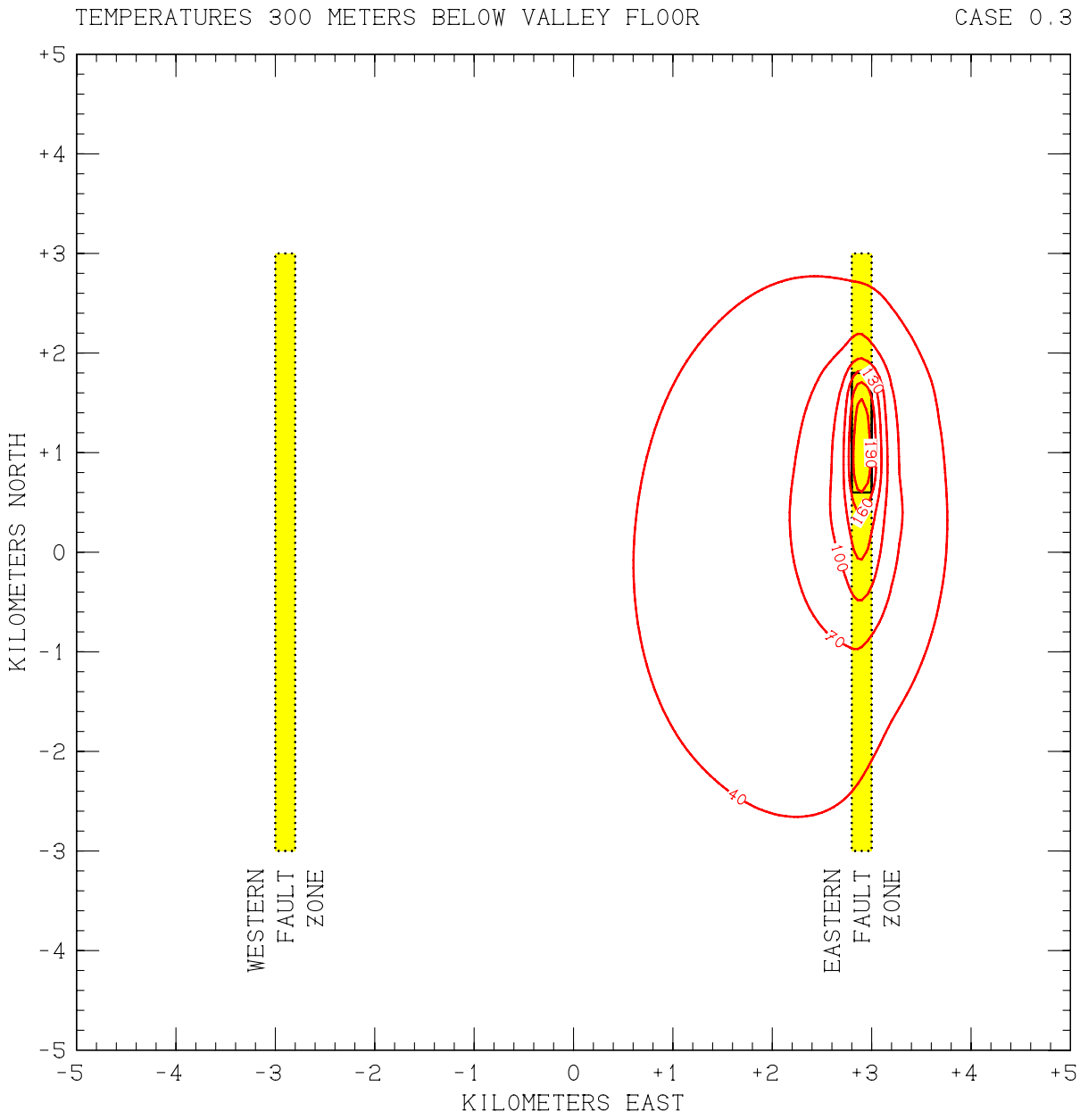

Figure 5.5. Maximum bottomhole temperatures obtained from a *"heat flow survey"* using 300-meter slim exploration holes for Case 0.3. Bottomhole temperature contours are 40°C, 70°C, 100°C *etc.* corresponding to local conductive heat flow values of 300 mW/m^2, 600 mW/m^2, 900 mW/m^2, *etc.*

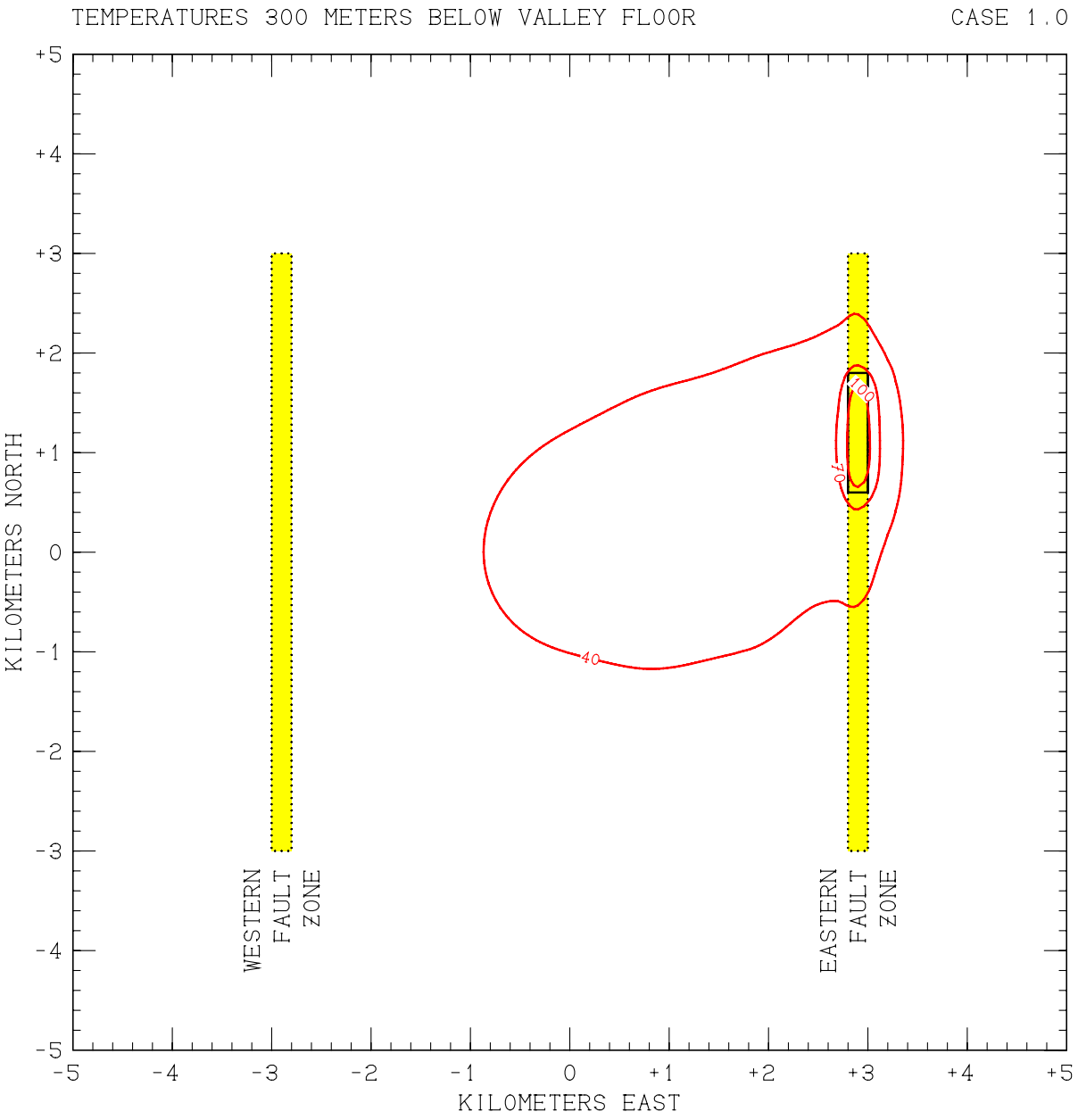

Figure 5.6. Maximum bottomhole temperatures obtained from a *"heat flow survey"* using 300-meter slim exploration holes for Case 1.0. Bottomhole temperature contours are 40°C, 70°C, 100°C *etc.* corresponding to local conductive heat flow values of 300 mW/m^2, 600 mW/m^2, 900 mW/m^2, *etc.*

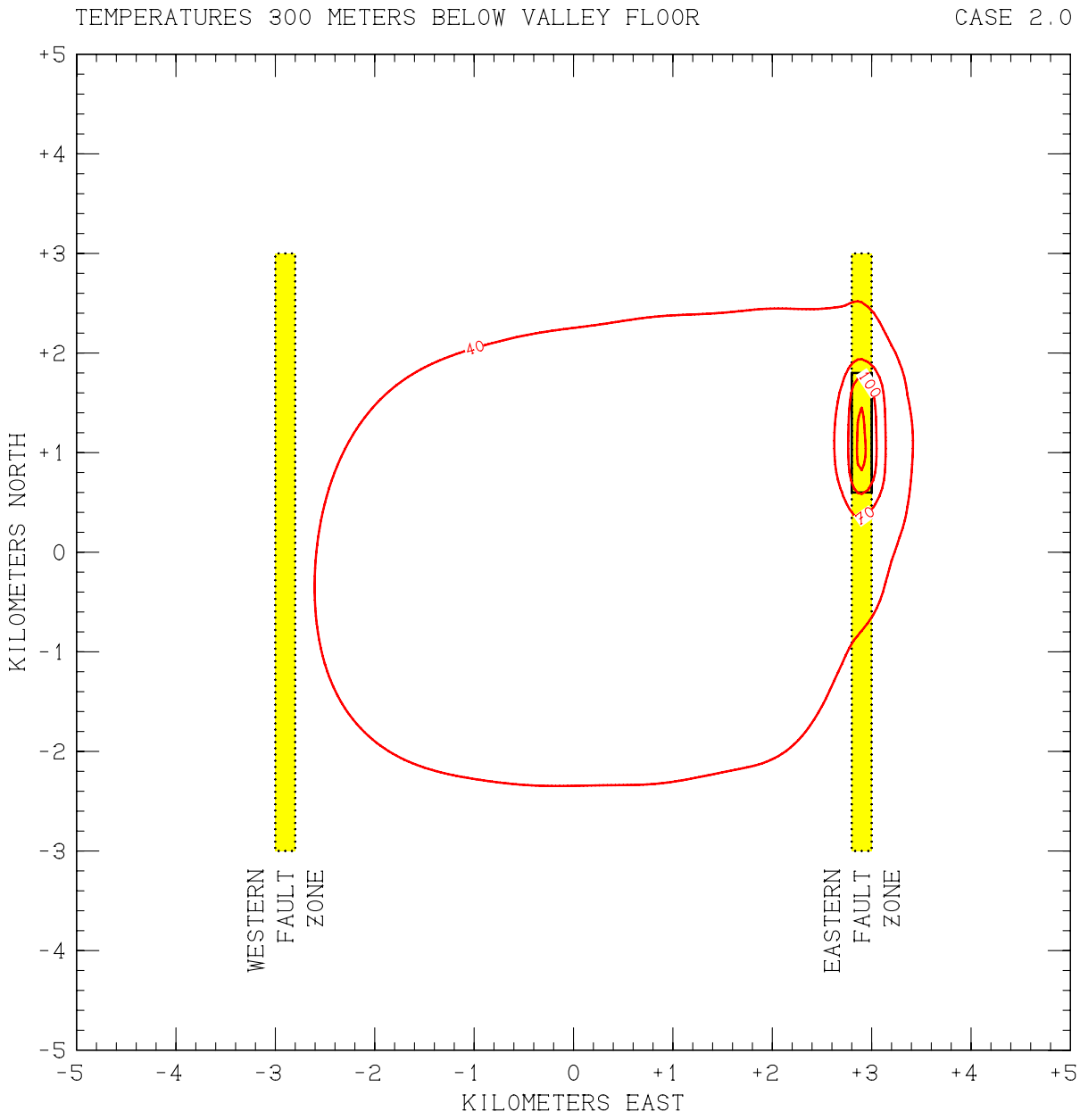

Figure 5.7. Maximum bottomhole temperatures obtained from a *"heat flow survey"* using 300-meter slim exploration holes for Case 2.0. Bottomhole temperature contours are 40°C, 70°C, 100°C *etc.* corresponding to local conductive heat flow values of 300 mW/m^2, 600 mW/m^2, 900 mW/m^2, *etc.*

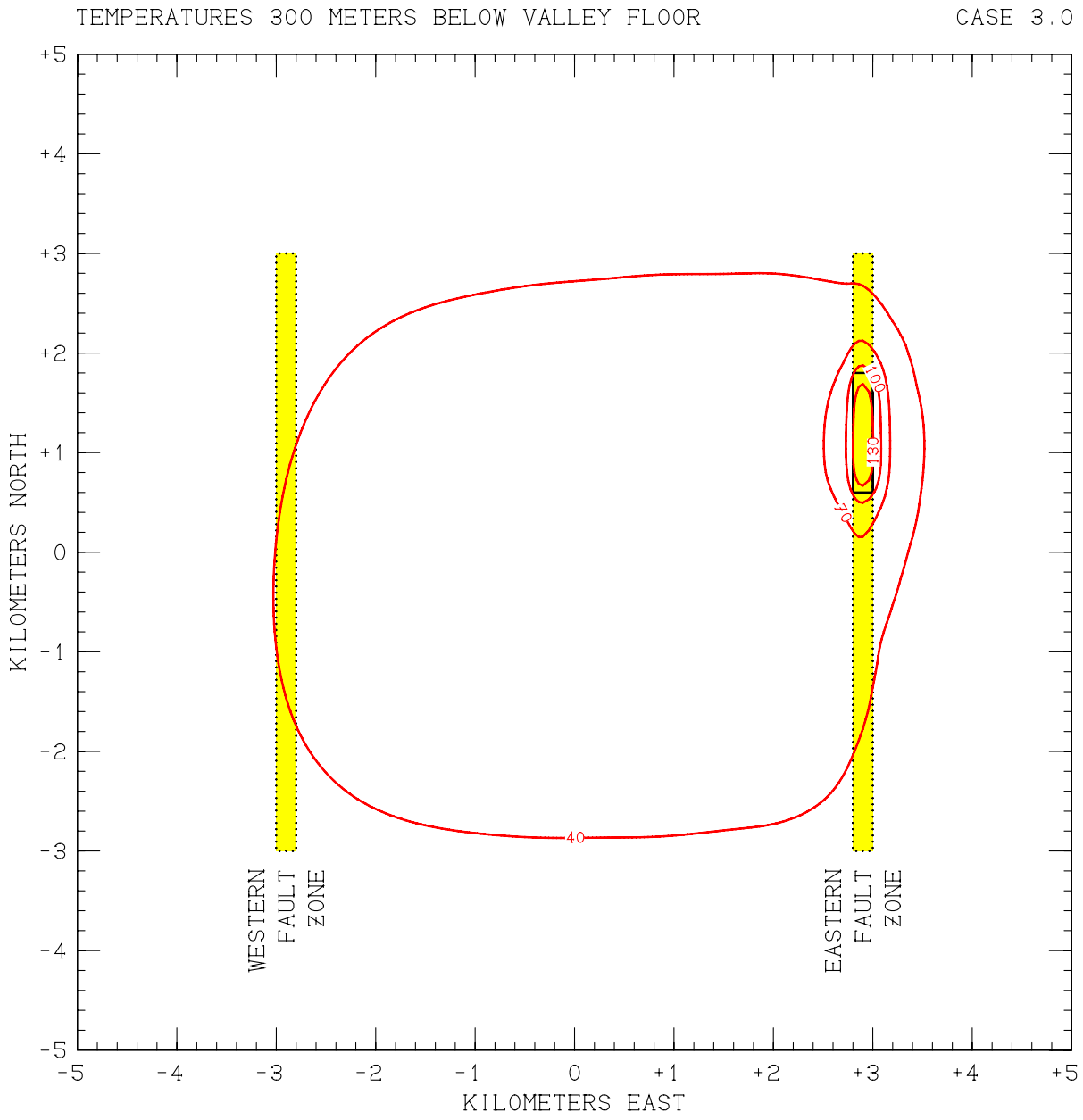

Figure 5.8. Maximum bottomhole temperatures obtained from a *"heat flow survey"* using 300-meter slim exploration holes for Case 3.0. Bottomhole temperature contours are 40°C, 70°C, 100°C *etc.* corresponding to local conductive heat flow values of 300 mW/m^2, 600 mW/m^2, 900 mW/m^2, *etc.*

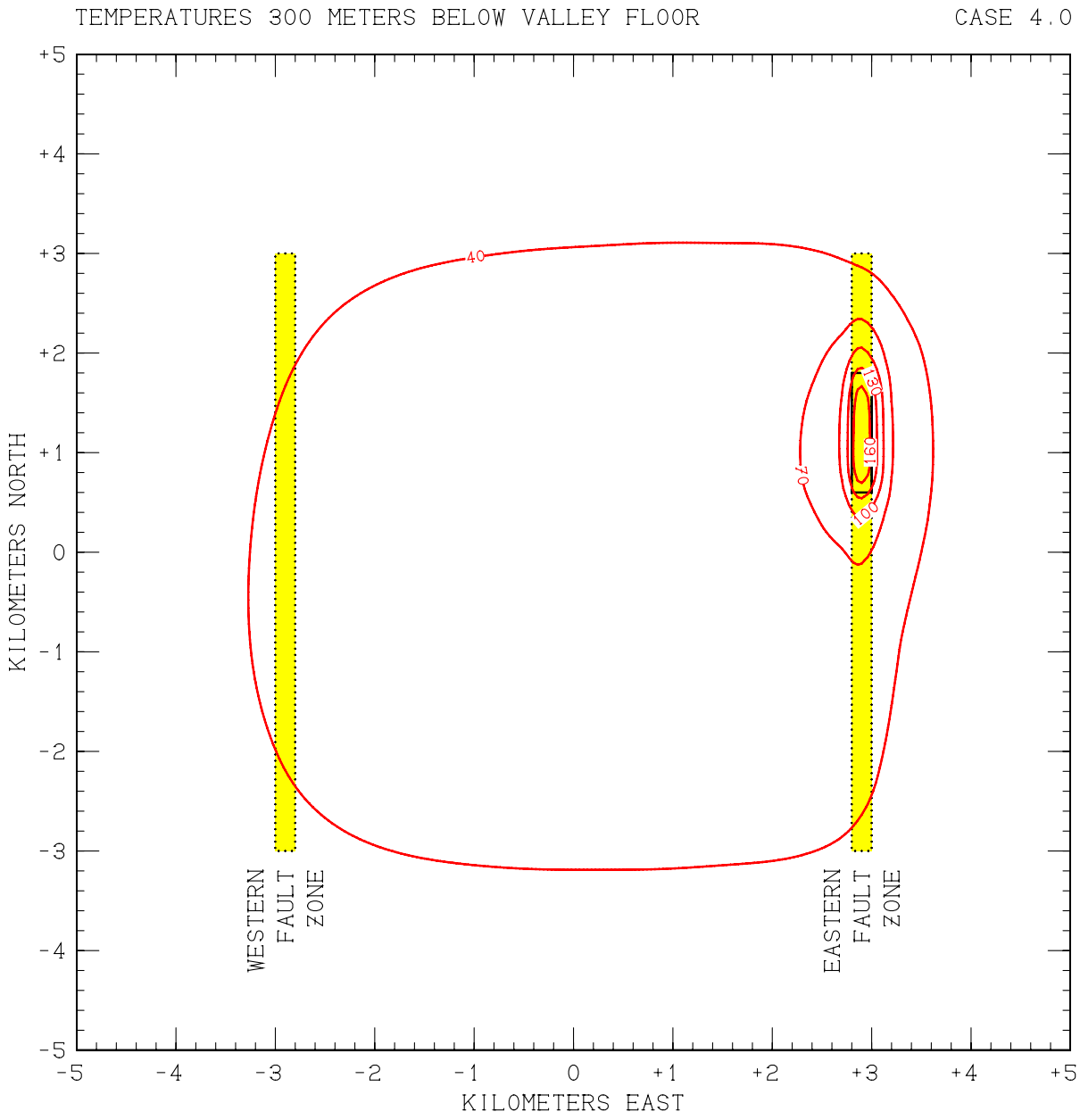

Figure 5.9. Maximum bottomhole temperatures obtained from a *"heat flow survey"* using 300-meter slim exploration holes for Case 4.0. Bottomhole temperature contours are 40°C, 70°C, 100°C *etc.* corresponding to local conductive heat flow values of 300 mW/m^2, 600 mW/m^2, 900 mW/m^2, *etc.*

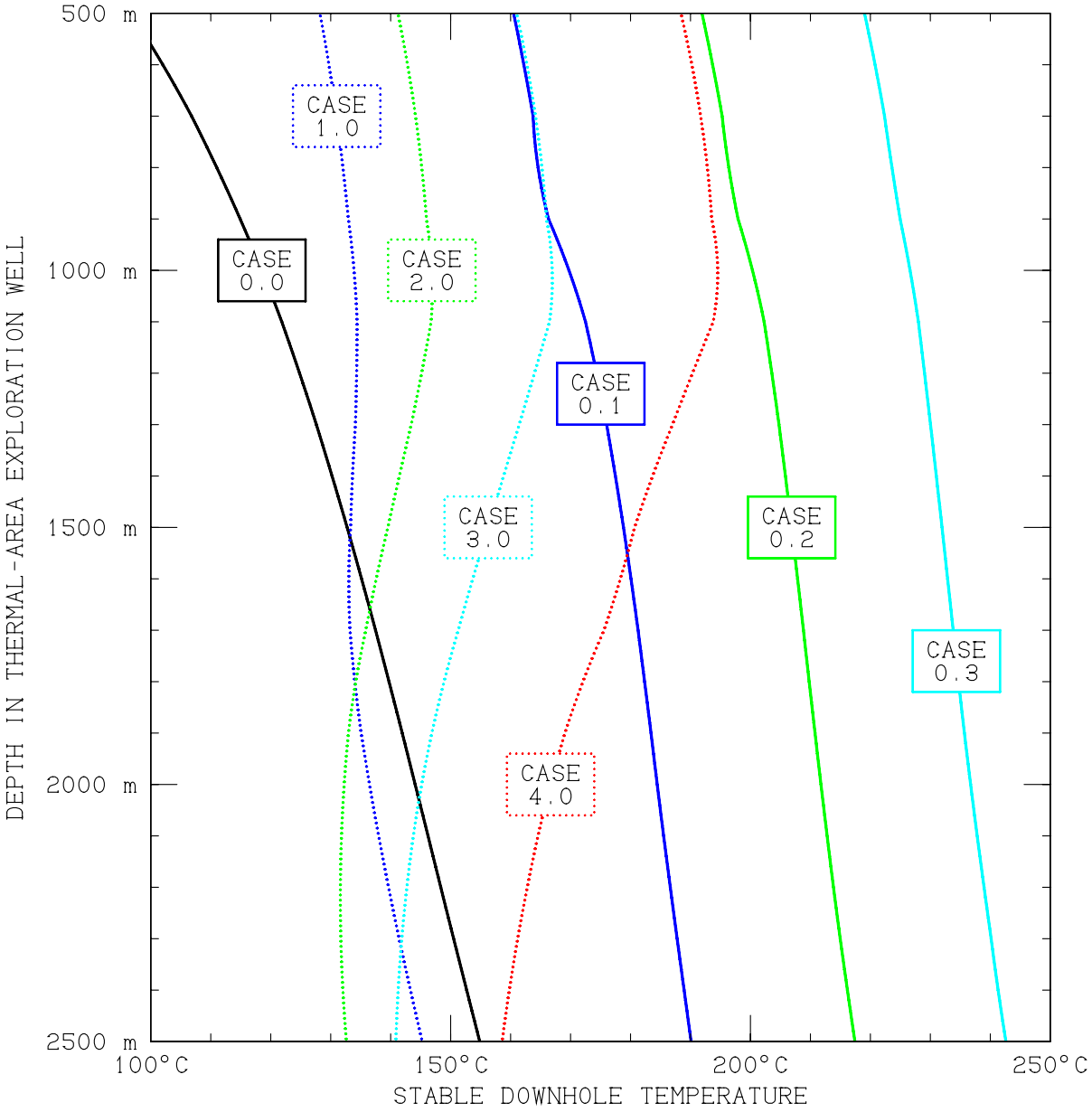

Figure 5.10. Stable temperature profile in hypothetical deep (2500 m) exploration well located in the center of the *"Thermal Area"* (*x* = +2900 m East, *y* = +1500 m North) for all eight cases considered.

6 RESULTS FROM DC RESISTIVITY SURVEYS

DC resistivity surveys have been widely employed for many years in geothermal exploration and field characterization. The Wairakei geothermal field in New Zealand was the first liquid-dominated geothermal field in the world to be developed for electricity production, and has been generating power for the grid since 1958. DC resistivity methods were employed from the beginning at Wairakei to help delineate the lateral boundaries of this shallow geothermal reservoir. Although DC techniques have begun to be supplanted by electromagnetic methods in recent years, DC resistivity surveying remains a powerful and familiar tool. Accordingly, the STAR "DC resistivity postprocessor" (see Chapter 14 of *Pritchett,* 2002) was applied to the final stabilized computed results from Cases 0.0 – 4.0 using an "electrical grid" representing 400 km^2 of surface area and 4097 km^3 of earth volume (see Figure 2.1). Outside the STAR "flow grid" volume, the actual *in-situ* electrical resistivity was taken to be a function of elevation only (Figure 2.12). Within the STAR grid volume, the *in-situ* resistivity for each grid block depends upon the stable temperature and TDS content of the fluids within the block, and upon whether the rock formation occupying the block is "high-permeability" or "low-permeability" (Figure 2.11). Then, given specifications for electrode array geometry and orientation, the DC postprocessor computes the "apparent resistivity" that would be observed by the measurement.

Generally speaking, a DC resistivity survey is carried out using an array of electrodes installed at the earth surface that is moved around from place to place within the study area to map out the "apparent resistivity", maintaining the electrode array geometry. Several such electrode array geometries have been used for geothermal exploration in the past, including dipole-dipole arrays, Schlumberger arrays, and many others. For the present investigation, the "Wenner" array configuration was chosen for its geometric simplicity, and was oriented north-south along the structure (Figure 6.1). The Wenner configuration is laid out along a straight line on the earth surface (oriented north-south in this case), with widely separated "current electrodes" and more closely spaced "voltage electrodes", and a fixed distance *("A")* between each electrode in the array. Note that the total linear extent of the array is $3 \times A$. Using this geometry, it may easily be shown that, if the earth is considered to be a uniform topography-free half-space of constant and uniform electrical resistivity "Ω" (ohm-meters), and if a particular value of electric current (*"I"* amperes) is passed through this uniform earth using the outer "current" electrode pair, the electrical potential difference that would be measured between the "voltage electrodes" (*"V",* in volts) will be given by:

$$V = \frac{I\Omega}{2\pi A}$$

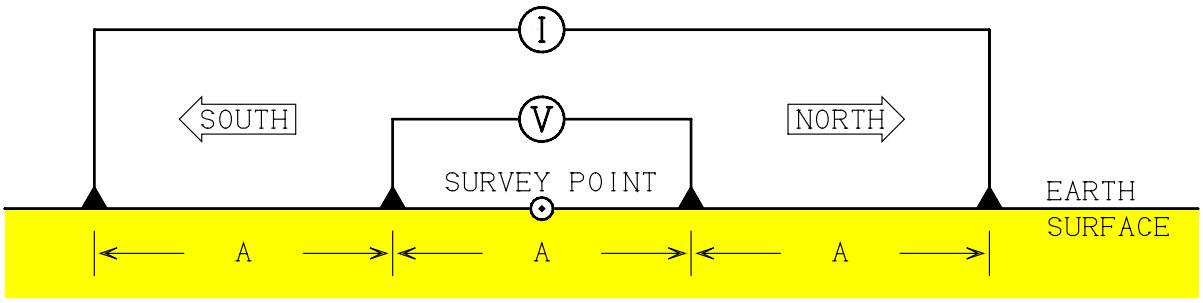

Figure 6.1. Geometry of a "Wenner" DC electrode array to measure subsurface electrical resistivity. Electric current *("I")* introduced using "current electrodes", and resulting electrical potential difference *("V")* measured between "voltage electrodes". Electrodes are laid out along a straight line on the earth surface as shown, with equal spacing *("A")* between them. The "apparent resistivity" is given by $\Omega_A = 2\pi AV/I$.

where *"A"* is electrode separation. If this same relationship is used (even if the earth surface is not flat and the subsurface resistivity distribution is non-uniform) and solved for electrical resistivity in terms of measured voltage and current, the result is termed the "apparent DC resistivity":

$$\Omega_A = \frac{2\pi AV}{I}$$

which will depend upon the actual distribution of electrical resistivity underground and the surface topography, as well as the electrode spacing and orientation.

Figure 6.2 shows the geometry considered for an east-west traverse of the study area (using a north-south Wenner electrode array with A = 2000 meters) at y = 0 (the "location" associated with each determination of apparent resistivity is usually taken to be the center of the array). After each determination, the entire electrode array is moved a fixed distance to the east, and the measurement is repeated. In this way, an east-west distribution of "apparent resistivity" may be constructed. Figure 6.3 illustrates the results that would be obtained from such a traverse for Case 0.0 (no deep upflow), for four different values of the electrode spacing A (800, 1200, 2000 and 3000 meters).

First, note that apparent resistivity Ω_A has a tendency to decrease with increasing electrode spacing A. This is because the actual *in-situ* electrical resistivity in the area decreases with increasing depth, and the "depth of penetration" for a particular DC electrode array increases with increasing electrode separation. In effect, larger arrays sample a thicker section of the earth's crust. Figure 6.4 shows the correlation between apparent resistivity and actual resistivity for a one-dimensional flat earth with the "undisturbed" resistivity distribution depicted earlier in Figure 2.12. The values obtained for apparent resistivity appear to correspond to the actual *in-situ* resistivity at a depth given approximately by $0.55 \times A$ for this particular case. Therefore, we can expect a Wenner survey using A = 2000

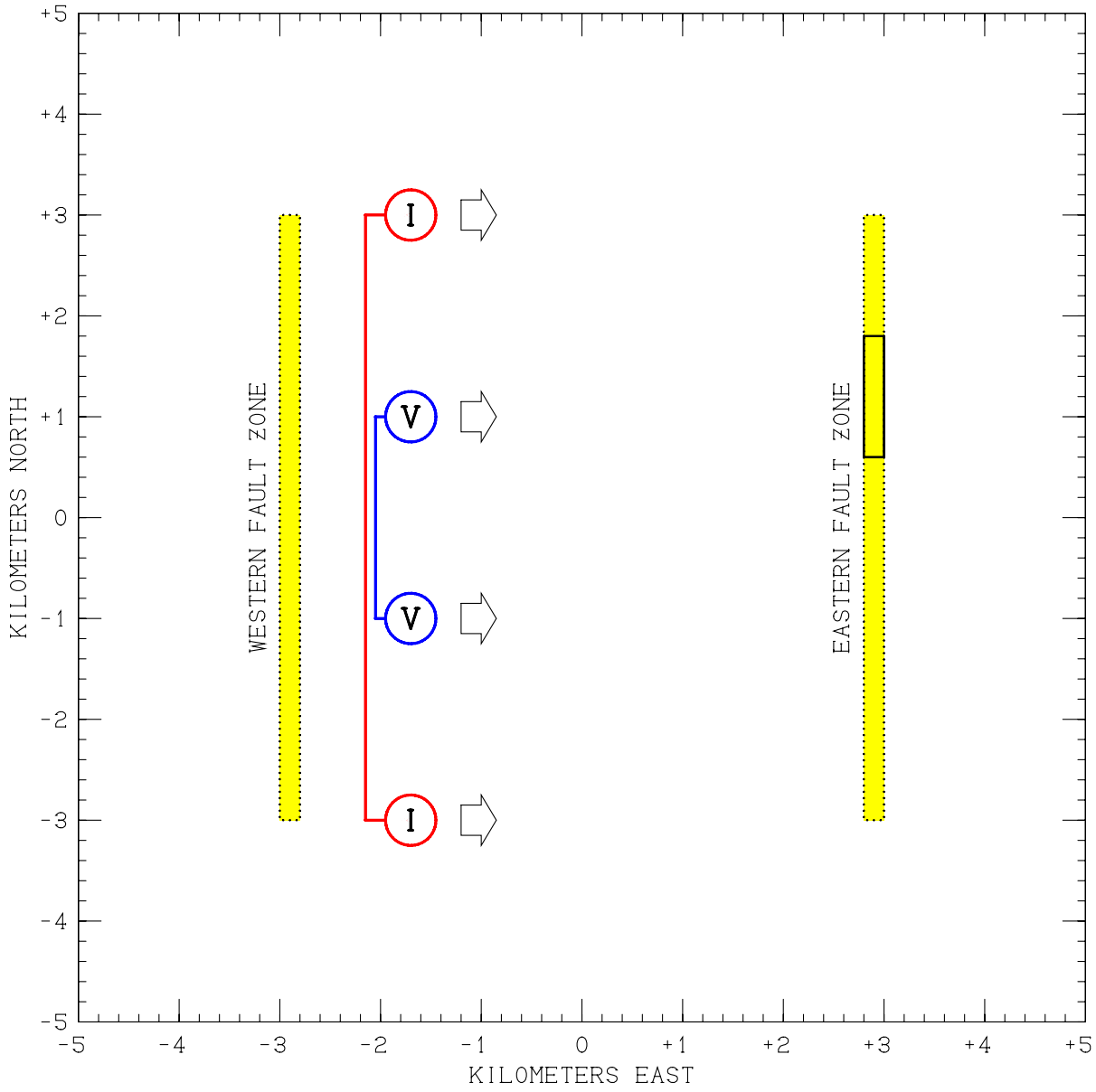

Figure 6.2. Geometry of a Wenner traverse of the study area. Electrodes oriented north-south, with array midpoint at $y = 0$. Geometry for $A = 2000$ meters illustrated.

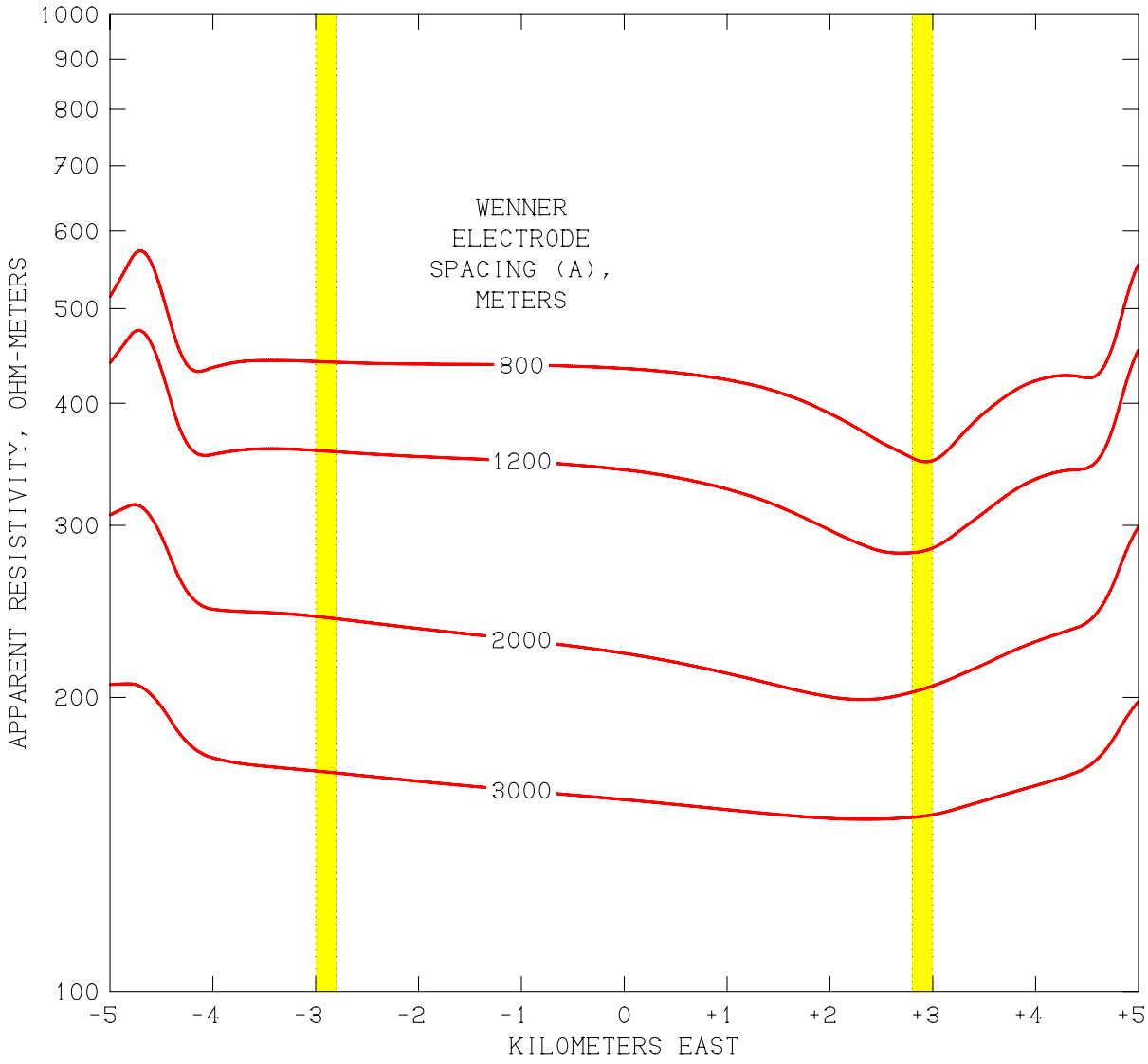

Figure 6.3. Computed results of east-west Wenner DC resistivity survey traverse at $y = 0$ using electrode array oriented north-south for Case 0.0, using various values of electrode spacing ("*A*").

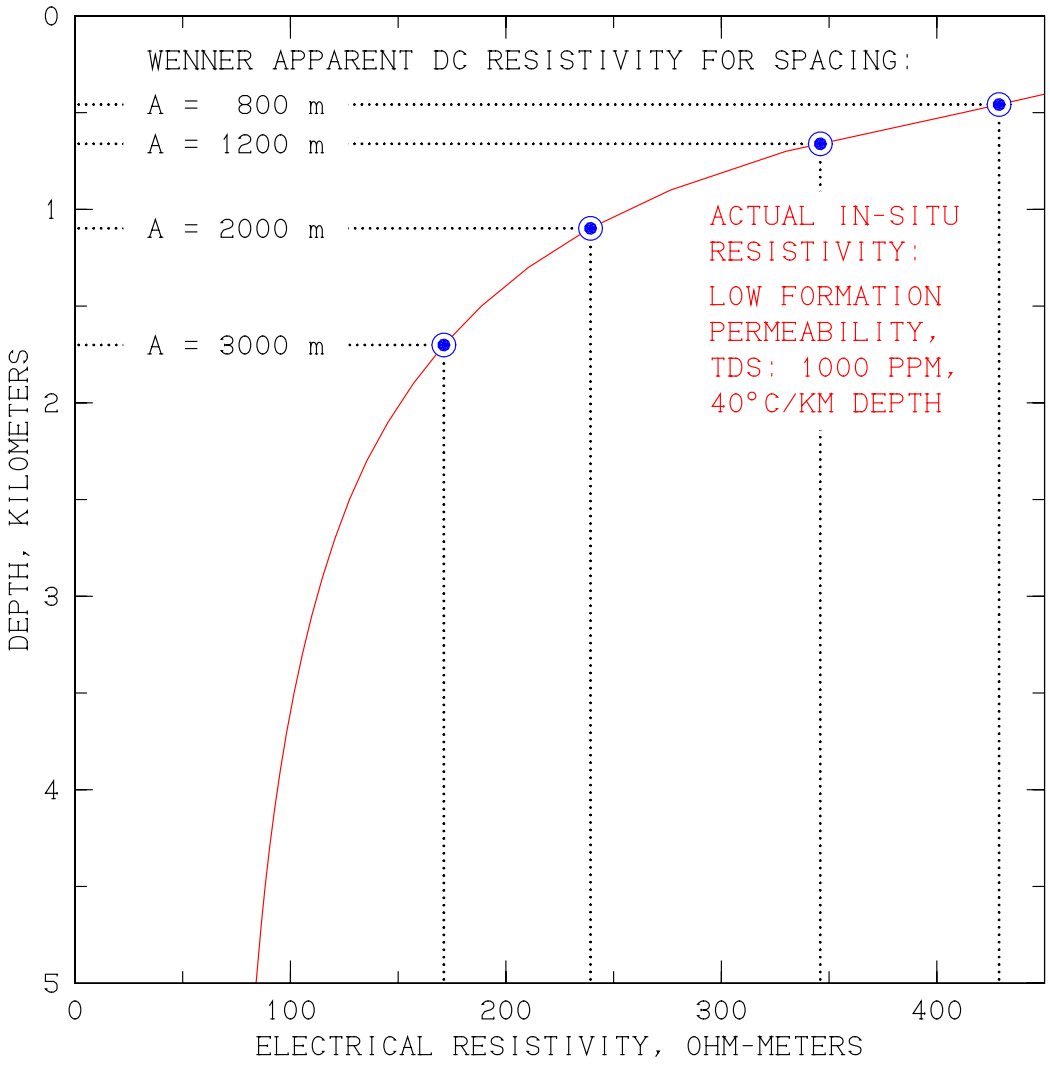

Figure 6.4. ***Red:*** **actual subsurface electrical resistivity distribution with depth for a region distant from geothermal anomaly, with uniform low-permeability rock formations, uniform TDS (1000 ppm) and temperature varying linearly with depth between 10°C at the surface and 210°C at 5 km. Actual resistivity taken as uniform (84 ohm-m) below 5 km.** ***Blue:*** **"apparent resistivity" obtained using Wenner DC resistivity survey of one-dimensional earth with various values of the electrode spacing, and the depths to which these values correspond on the actual resistivity profile.**

meters to "see" approximately 1100 meters down into the system, which is deep enough to reach through the caprock to the top part of the "upper aquifer". This is fortunate, since larger electrode spacings are likely to be impractical to use in a real field situation. This "depth of penetration" effect can be seen in the traverse results for Case 0.0 (Figure 6.3). The perturbations in apparent resistivity beyond $x = \pm 4$ km arise from topographic effects. Note that, between the fault zones, the A=800 m traverse yields essentially uniform apparent resistivity across most of the width of the valley, with a local minimum immediately adjacent to the Eastern Fault Zone which is relatively high-permeability (low resistivity) and encounters the earth surface in the area. At the other extreme, the traverse using $A = 3000$ meters indicates a smooth linear trend in apparent resistivity across the entire valley floor (with somewhat higher resistivities to the west where the high-permeability, low-resistivity Upper Aquifer is more deeply buried).

Figure 6.5 illustrates the results of similar east-west Wenner traverses (centered at $y = 0$ and using $A = 2000$ m) for all eight cases considered. Case 0.0 has already been discussed. Here, for the first time, is a definite, observable distinction between the "eastern reservoir" cases (0.1 – 0.3) and the "hidden western reservoir" cases (1.0 – 4.0). In the former cases, a substantial resistivity anomaly is observed (much more pronounced that for Case 0.0), but the anomaly is confined to the east side of the valley. In the latter cases, the anomaly covers the entire width of the valley.

Finally, consider that numerous such traverses are performed, moving the array north-south as well as east-west to construct a two-dimensional "apparent resistivity map" of the study area. Figures 6.6 – 6.13 depict the results for Cases 0.0 – 4.0 respectively. The short-wavelength fluctuations to the extreme north and south are synthetic and are of numerical origin: using $A = 2000$ meters, when the array is centered at the northern study area boundary, for example ($y = +5$ km), the northernmost current electrode is 3 km farther north, at $y = +8$ km and only 2 km from the outer boundary of the "electrical grid", resulting in poor resolution of the electrical potential field.

These 2-D resistivity maps clearly exhibit a major electrical resistivity low in the middle of the valley for all four "western recharge" cases (Cases 1.0 – 4.0), with a resistivity contrast exceeding 4 as compared to more distant values. The presence of such a large anomaly, offset so far from the visible discharges in the "Thermal Area", should be suggestive that deeply-buried geothermal resources may be present to the west of the natural surface discharge area.

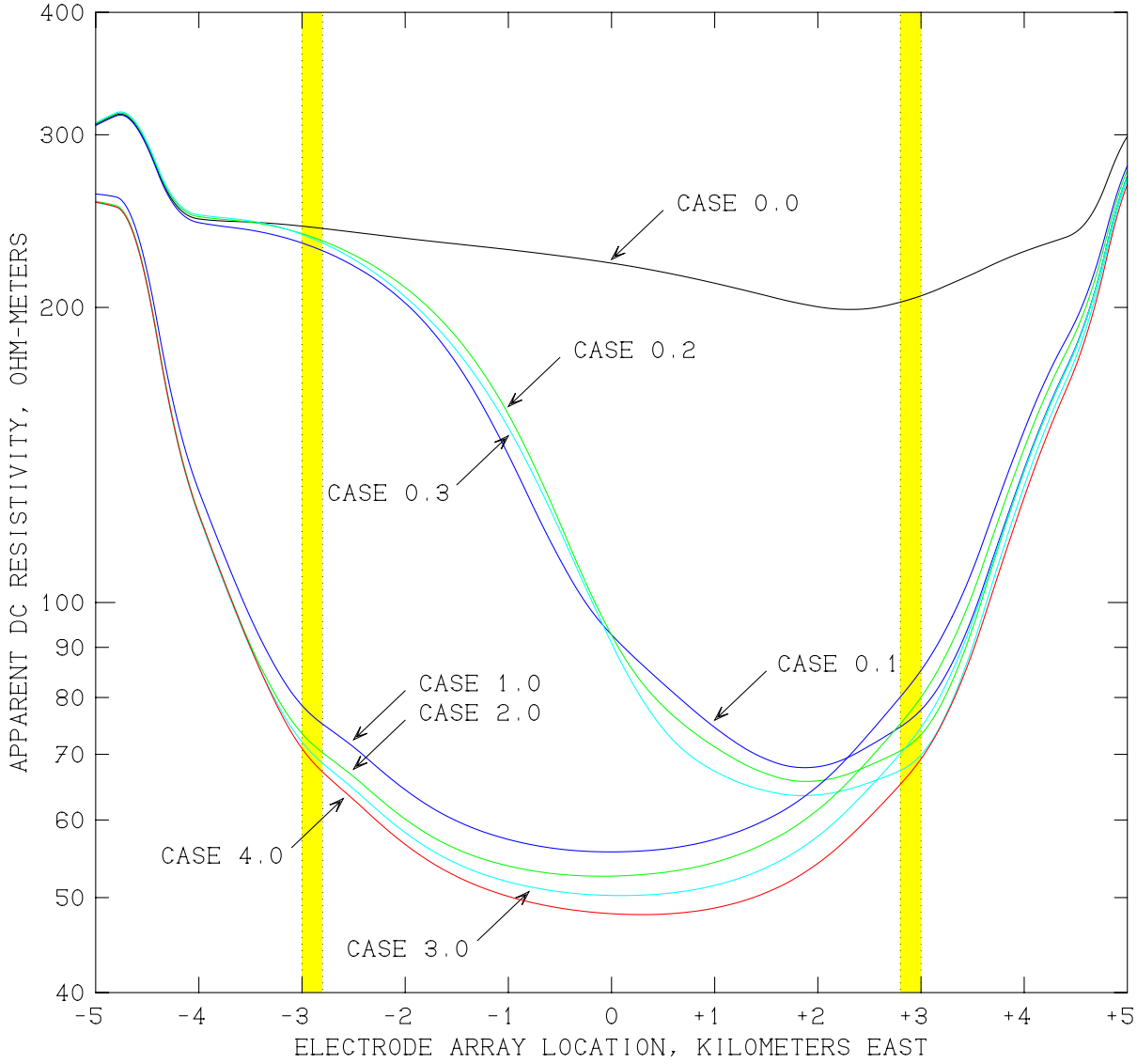

Figure 6.5. Computed results of east-west Wenner DC resistivity survey traverse at $y = 0$ using electrode spacing ("*A*") of 2000 meters and north-south electrode array orientation, for all eight cases considered.

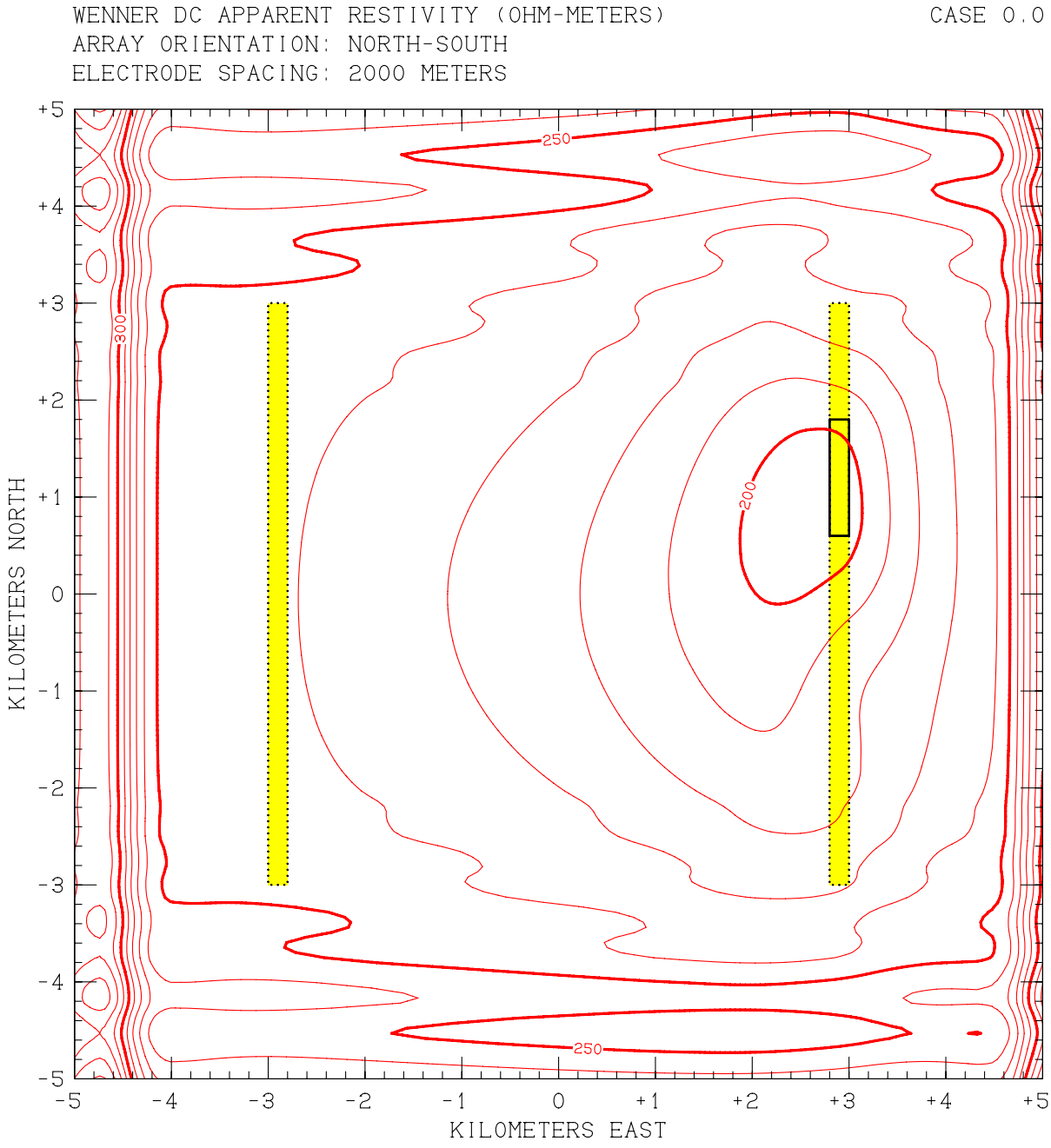

Figure 6.6. Computed results of Wenner DC resistivity survey of entire 100 km^2 study area for Case 0.0, using electrode spacing A = 2000 meters and north-south electrode array orientation.

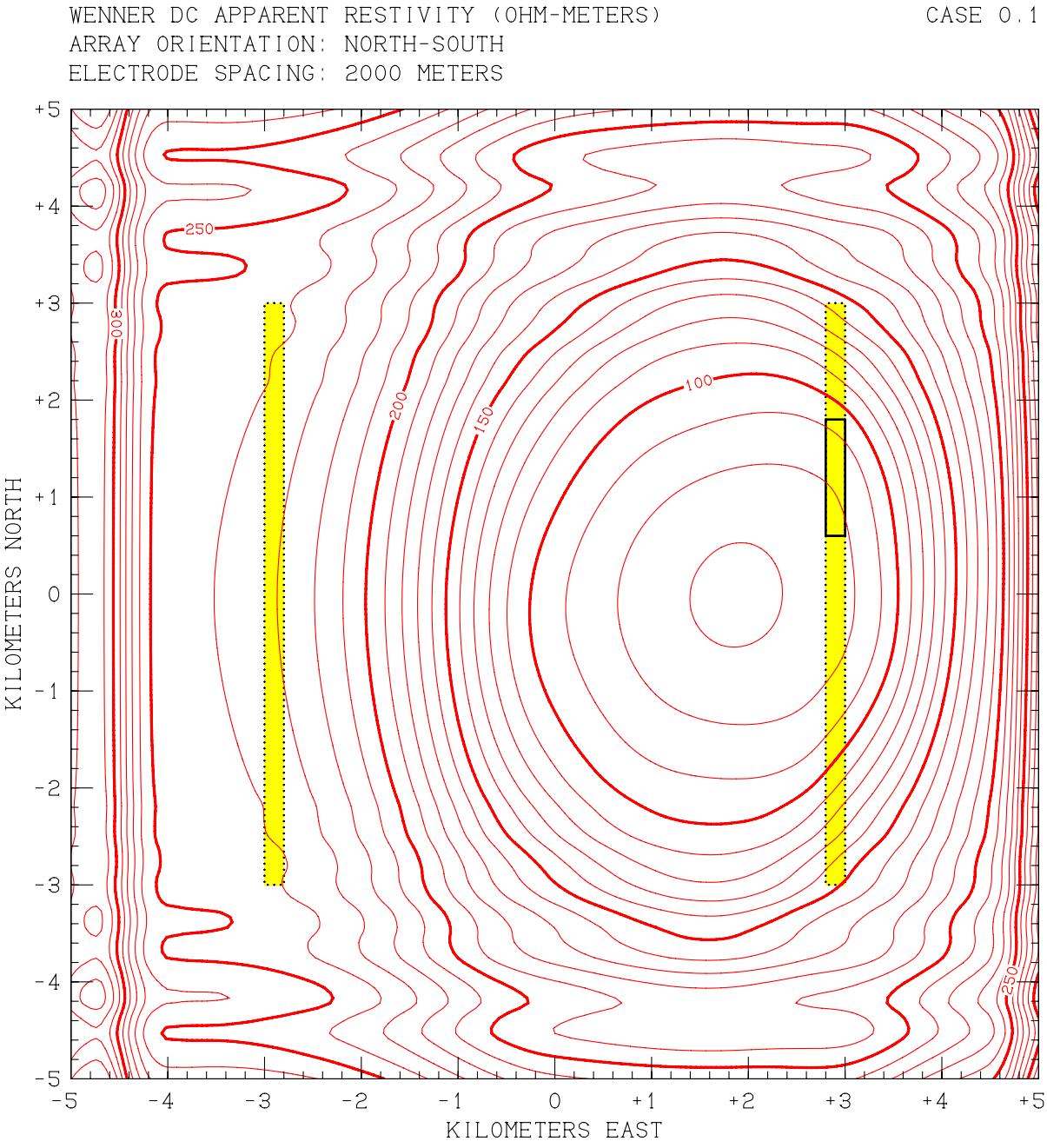

Figure 6.7. Computed results of Wenner DC resistivity survey of entire 100 km^2 study area for Case 0.1, using electrode spacing A = 2000 meters and north-south electrode array orientation.

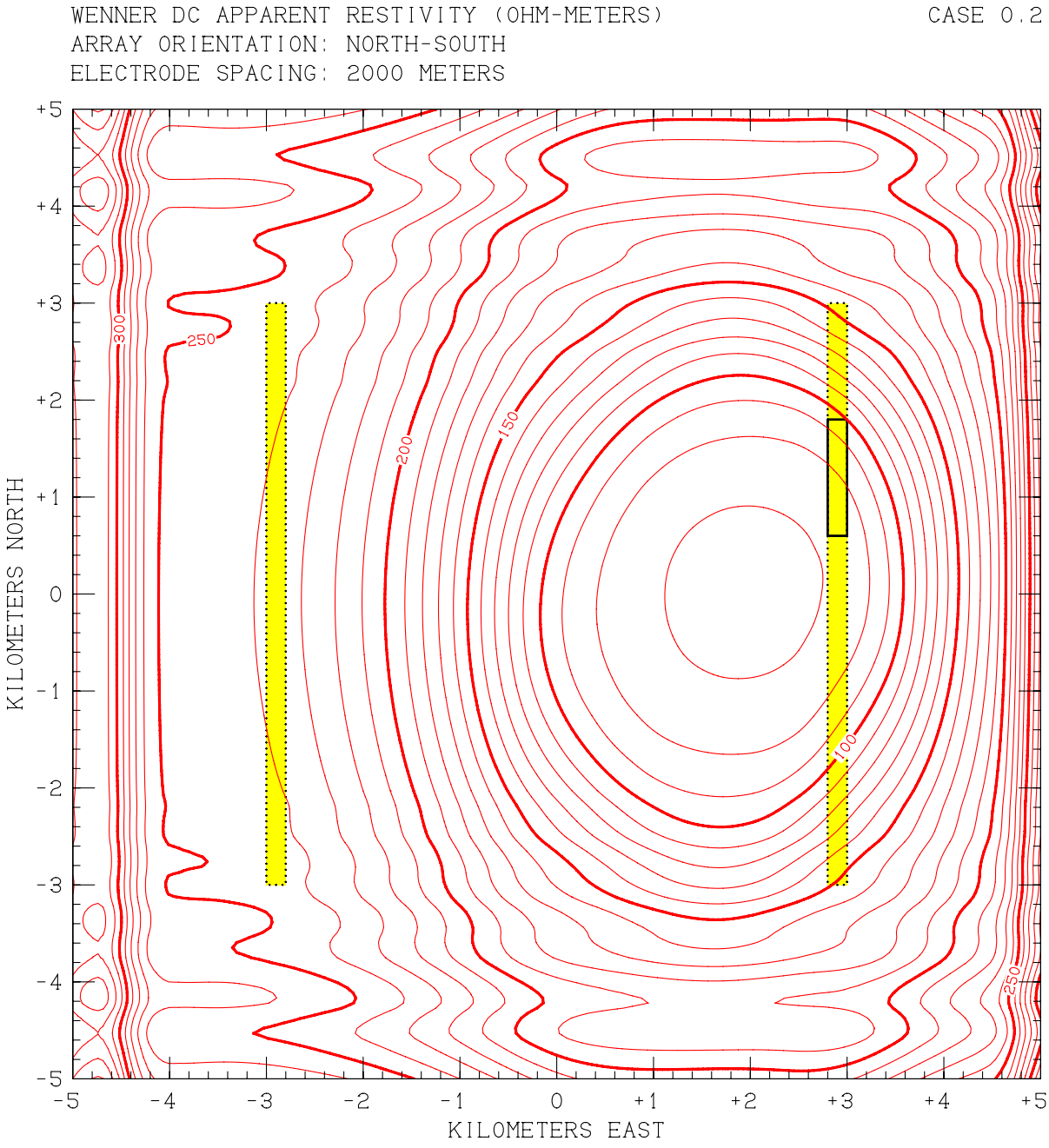

Figure 6.8. Computed results of Wenner DC resistivity survey of entire 100 km^2 study area for Case 0.2, using electrode spacing A = 2000 meters and north-south electrode array orientation.

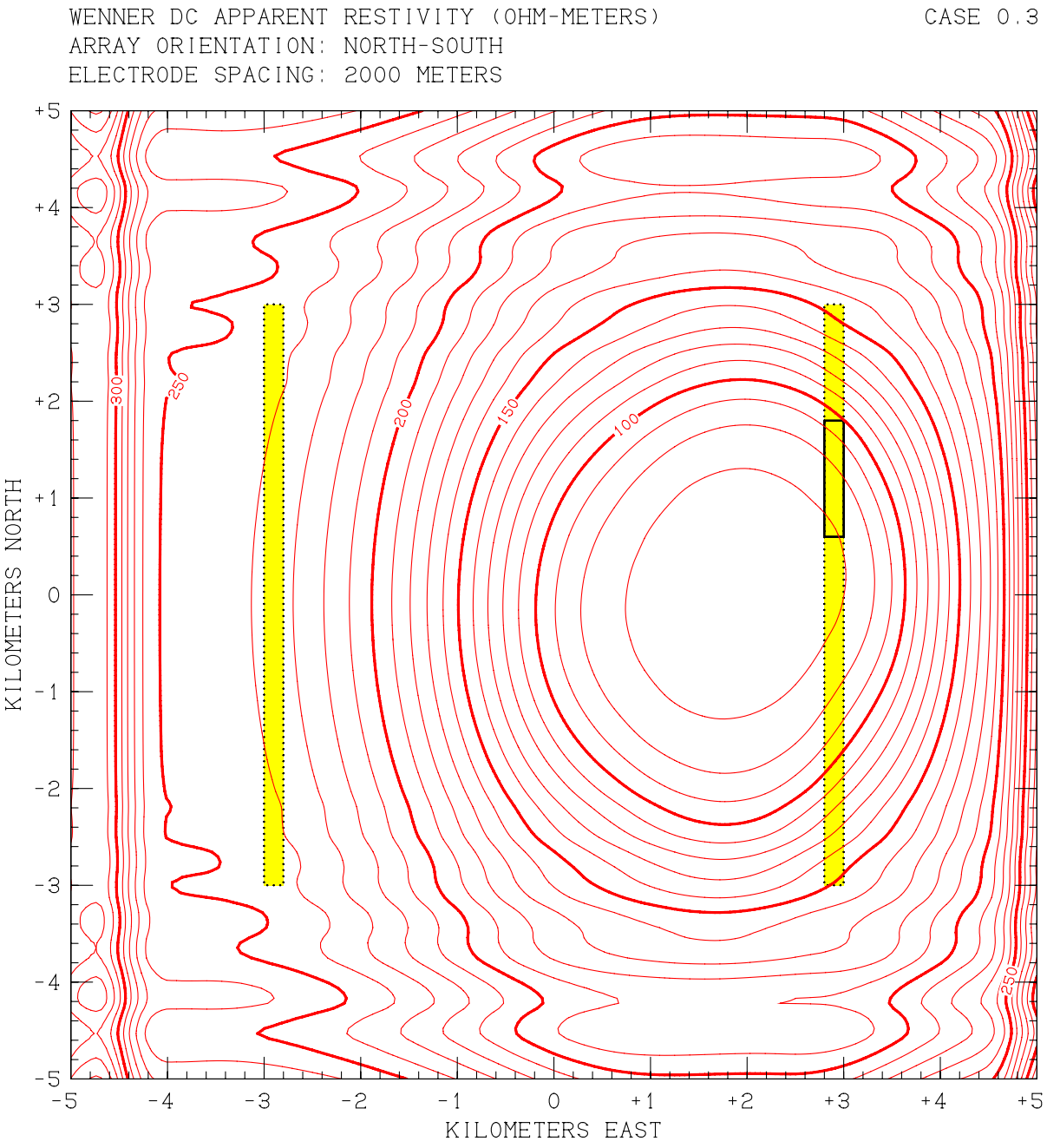

Figure 6.9. Computed results of Wenner DC resistivity survey of entire 100 km^2 study area for Case 0.3, using electrode spacing A = 2000 meters and north-south electrode array orientation.

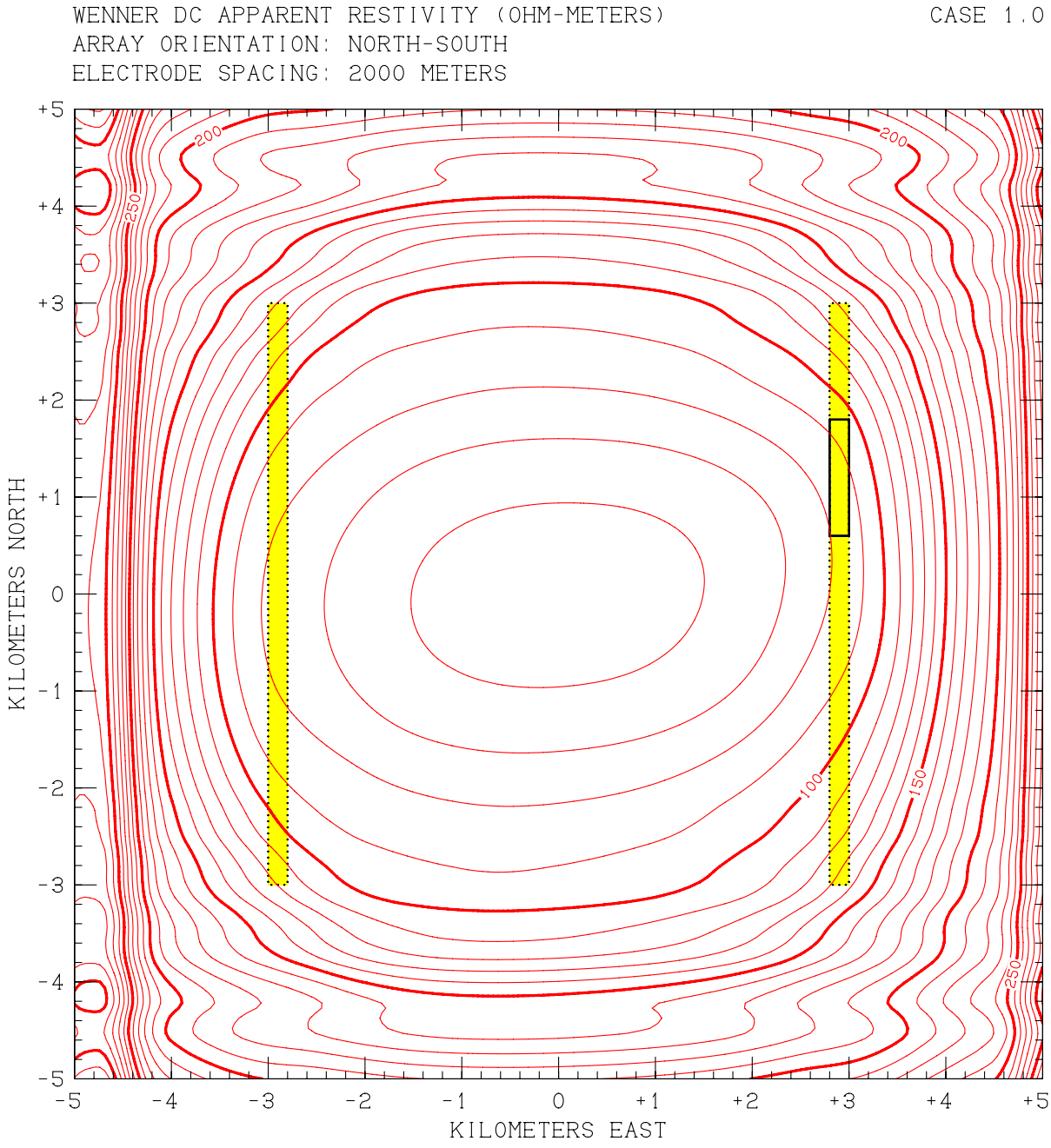

Figure 6.10. Computed results of Wenner DC resistivity survey of entire 100 km^2 study area for Case 1.0, using electrode spacing A = 2000 meters and north-south electrode array orientation.

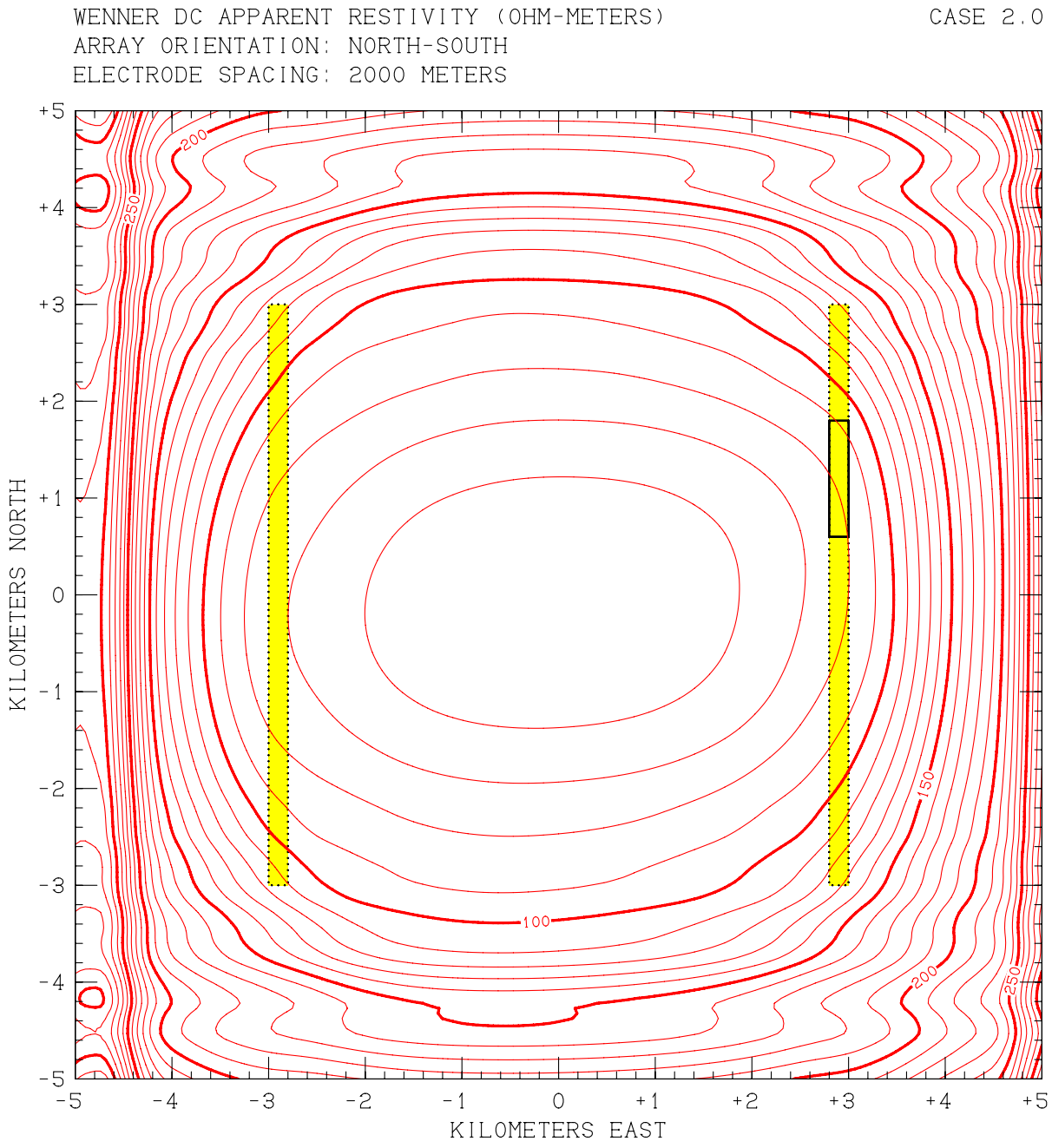

Figure 6.11. Computed results of Wenner DC resistivity survey of entire 100 km^2 study area for Case 2.0, using electrode spacing A = 2000 meters and north-south electrode array orientation.

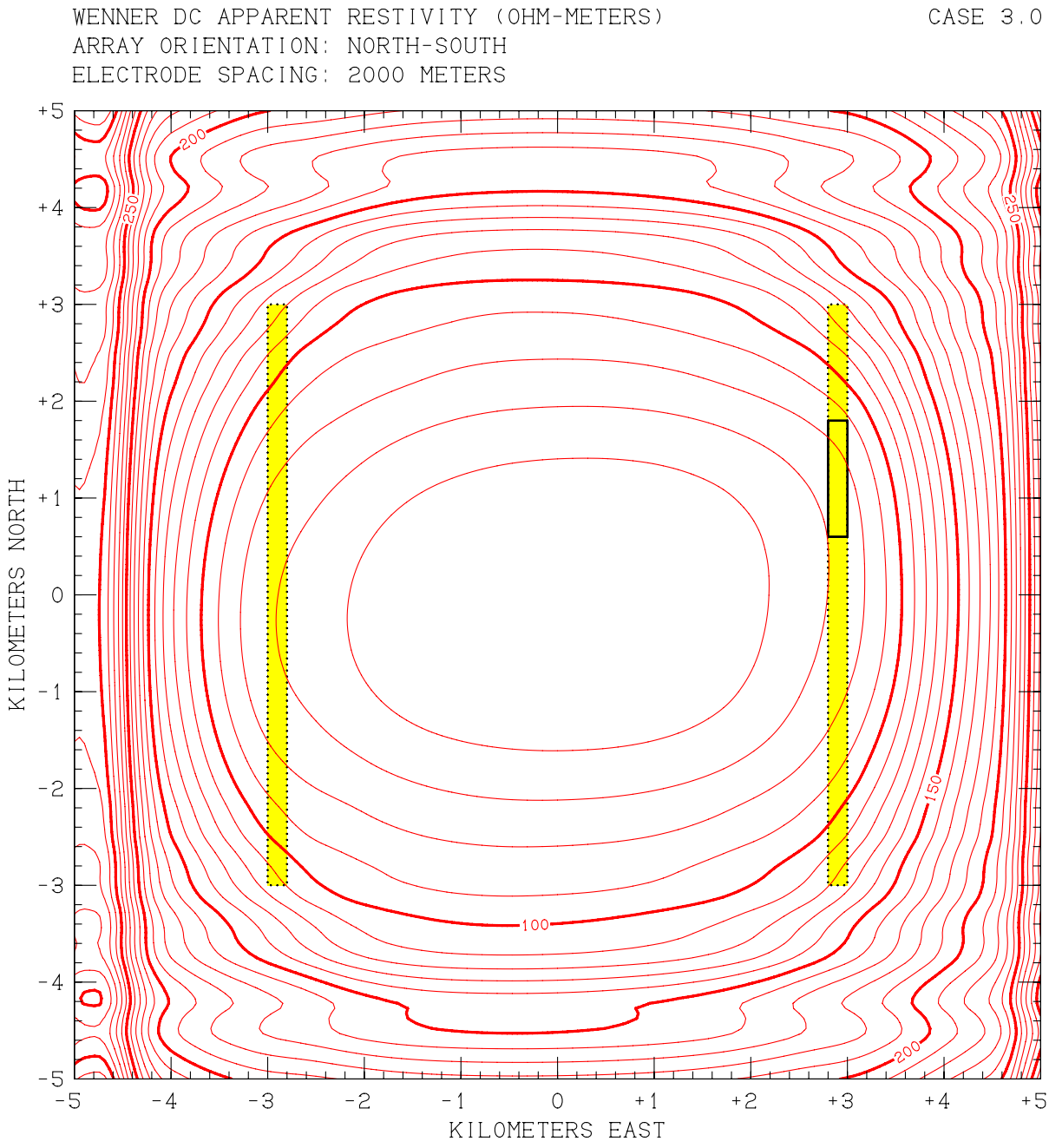

Figure 6.12. Computed results of Wenner DC resistivity survey of entire 100 km^2 study area for Case 3.0, using electrode spacing A = 2000 meters and north-south electrode array orientation.

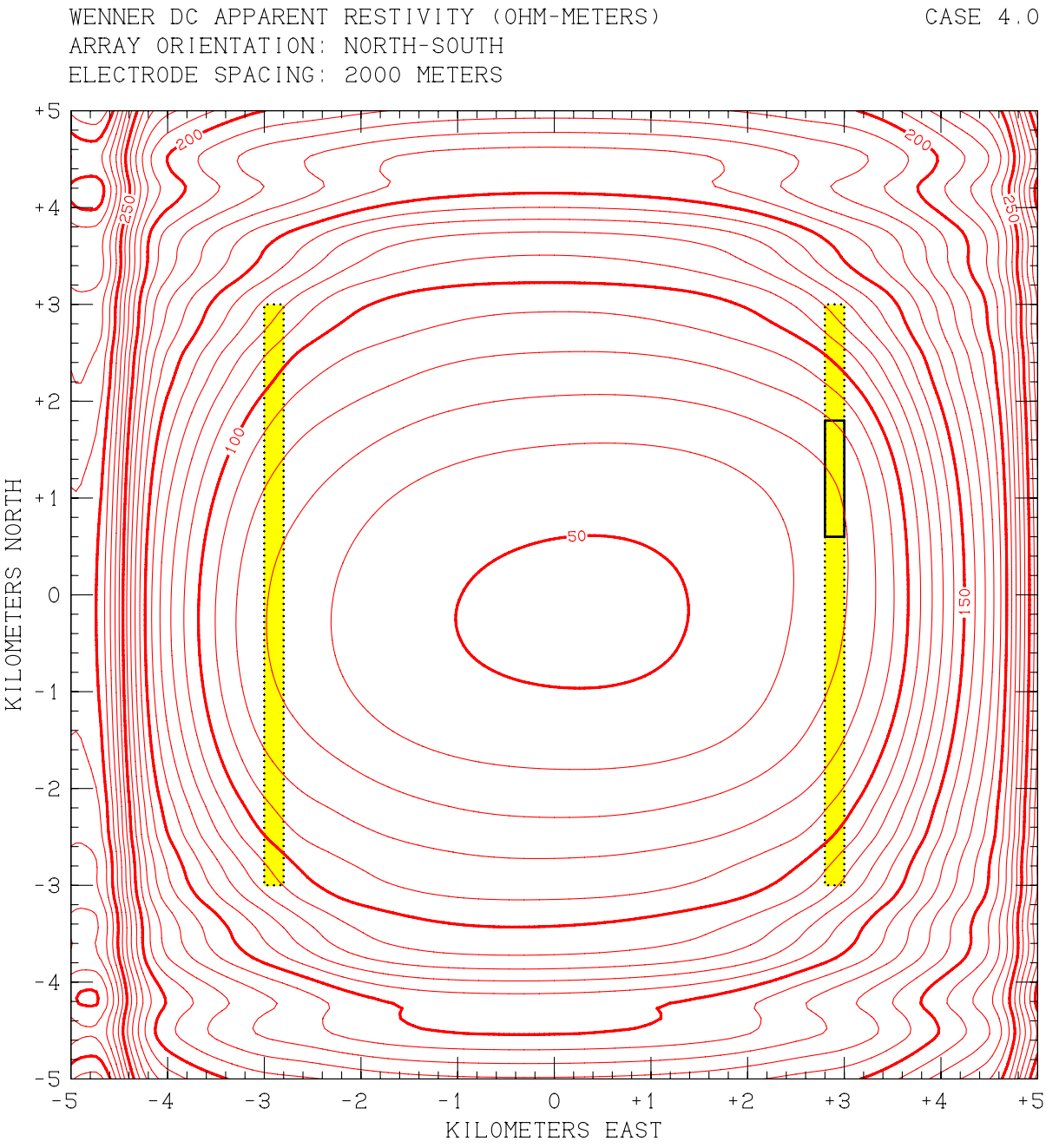

Figure 6.13. Computed results of Wenner DC resistivity survey of entire 100 km^2 study area for Case 4.0, using electrode spacing A = 2000 meters and north-south electrode array orientation.

7 RESULTS FROM MAGNETOTELLURIC SURVEYS

In recent years, magnetotelluric (MT) methods have begun to supplement (and even to replace) traditional DC resistivity surveys in geothermal prospecting. The MT method makes use of naturally occurring electromagnetic waves as sources to probe underground resistivity structure. At high frequencies (> 1 Hz or so) the signals are due to regional and global thunderstorm activity. At lower frequencies they result from regional electric current systems in the ionosphere and magnetosphere originating from fluctuations in solar wind intensity. Electromagnetic time-series data are collected and then decomposed into spectra, providing results as functions of frequency. Examining different frequencies in MT surveys is analogous to varying the electrode spacing A in a DC resistivity survey – the lower the frequency examined, the deeper the "depth of penetration". This is one of the major advantages of the MT method over traditional DC surveys; occupying a single field station and collecting measurements provides results for a whole range of penetration depths without the need to adjust electrode positions.

The "apparent resistivity" obtained (as a function of frequency) from an MT survey is defined in an analogous fashion to DC apparent resistivity – it is the value that would be obtained from the same measurement system for a uniform-resistivity flat earth. In addition to apparent resistivity, MT survey results may be manipulated to yield the impedance "phase angle" (between the E and H waves) as a function of frequency. For a uniform flat earth, the phase angle is independent of frequency and equal to 45° – substantial departures from this value are diagnostic of large gradients in underground electrical resistivity. The STAR "MT resistivity" postprocessor (described in Chapter 15 of *Pritchett,* 2002) uses a computational kernel developed by *Wannamaker* (2001) based on algorithms devised by *Sasaki* (1999; 2001).

Figure 7.1 shows results from the STAR "MT postprocessor" when applied to a one-dimensional flat earth (with the resistivity-depth structure illustrated previously for "undisturbed" regions in Figure 2.12) for frequencies between 0.01 and 100 Hz. Apparent resistivity decreases with decreasing frequency (increasing penetration depth), and asymptotically approaches the deep-resistivity limit (84 ohm-m) as frequency continues to decrease. The phase angle is generally above 45° and attains a maximum value of 55.9° at 2.6 Hz, but then declines asymptotically toward 45° as frequency decreases further. Figure 7.2 shows the correlation between "apparent MT resistivity" and the actual *in-situ* resistivity distribution (analogous to Figure 6.4 for the DC survey). This indicates another advantage of the MT approach –greater depths of penetration are practical, permitting exploration of the resistivity structure down to several kilometers.

First, consider a series of observation stations located along an east-west "MT Survey Line" at $y = 0$ (Figure 7.3). At each station along the line, both apparent resistivity and phase angle are obtained as functions of frequency. Then these results may be combined to obtain

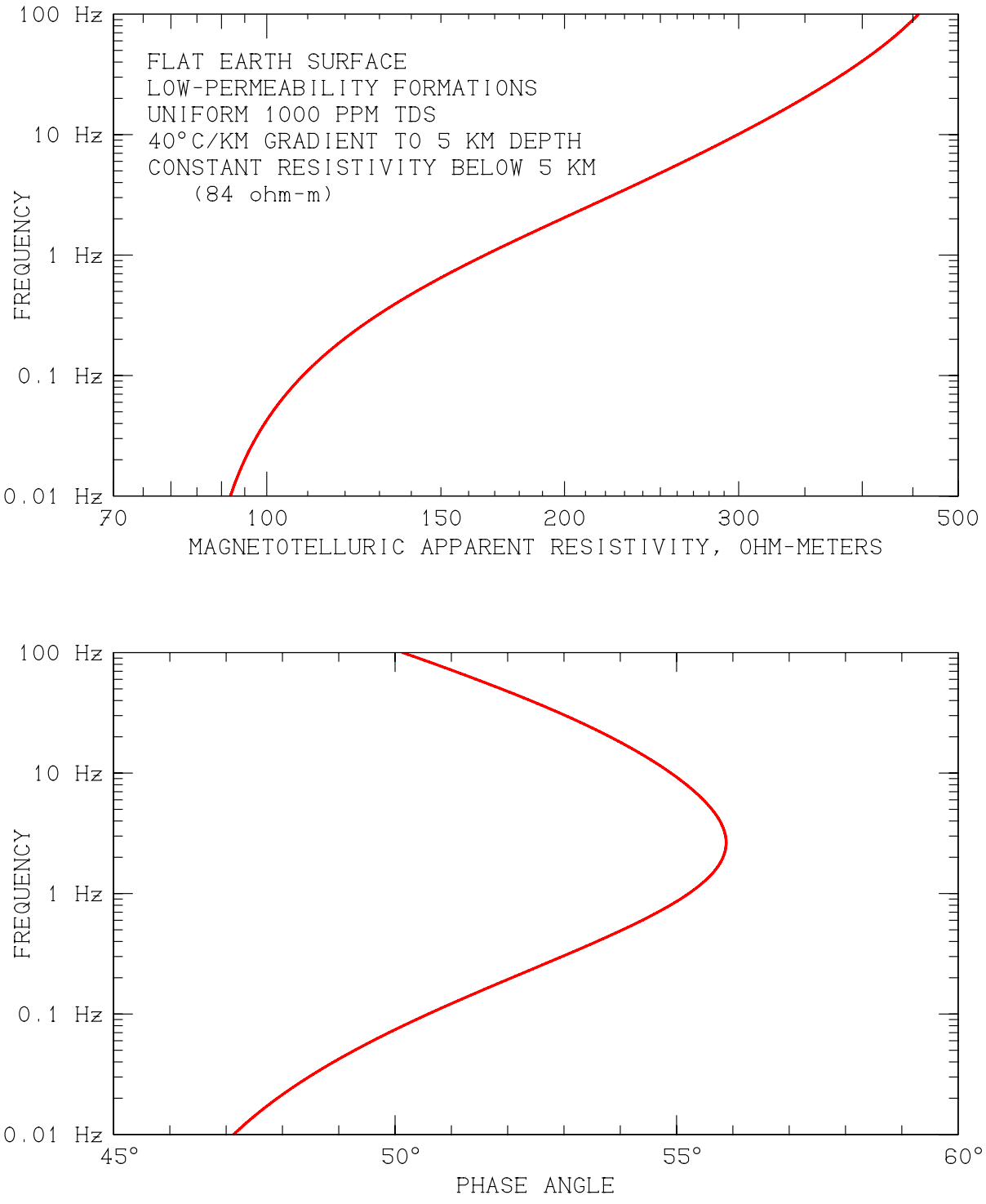

Figure 7.1. Computed results of magnetotelluric (MT) resistivity survey of a one-dimensional flat earth that has "undisturbed" actual resistivity distribution with depth. *Upper:* apparent resistivity. *Lower:* phase angle. Asymptotic values at infinite depth (zero frequency) are 84 ohm-meters and 45°, respectively.

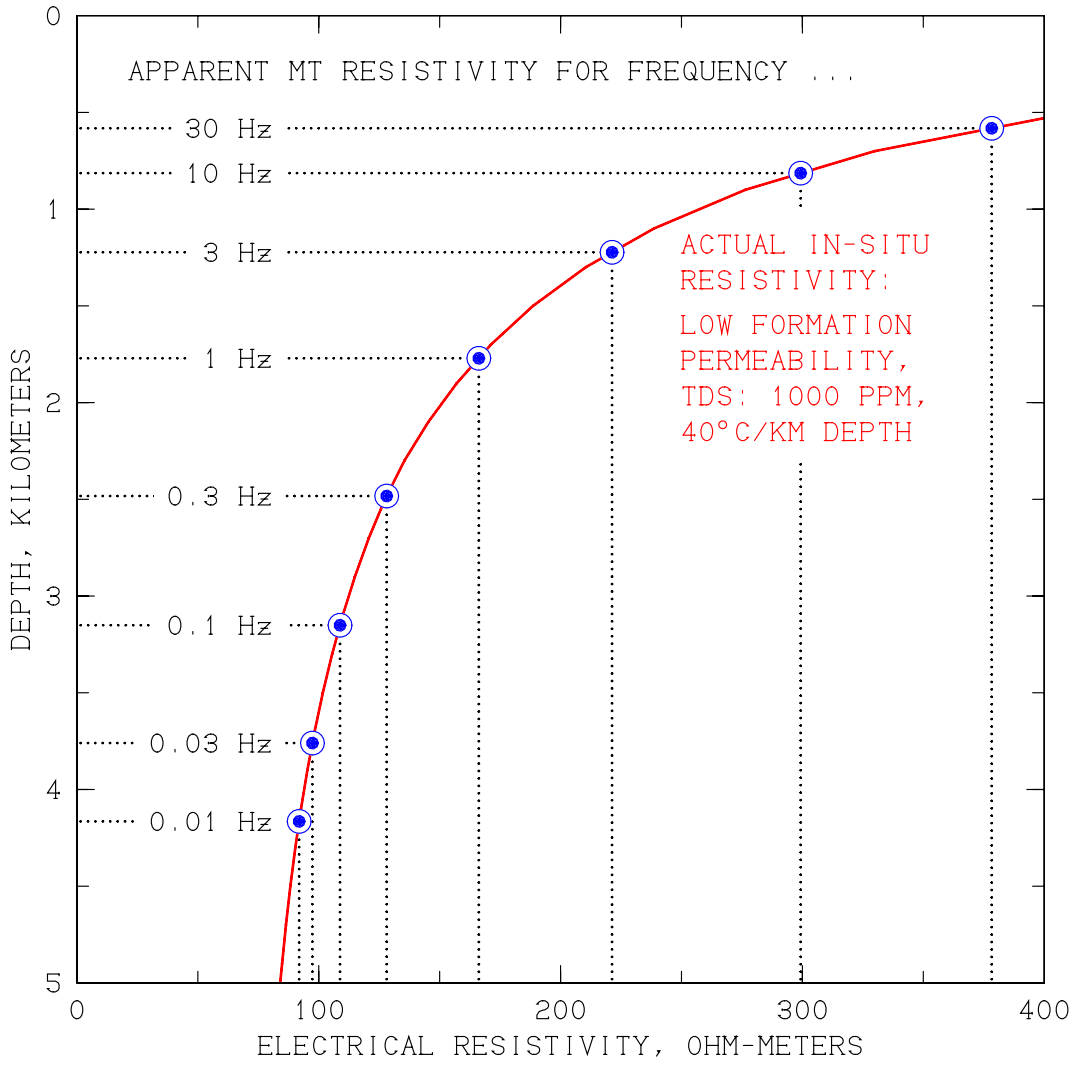

Figure 7.2. Correlation between "apparent resistivity" obtained from MT survey of one-dimensional earth (Fig. 7.1) and actual distribution of electrical resistivity.

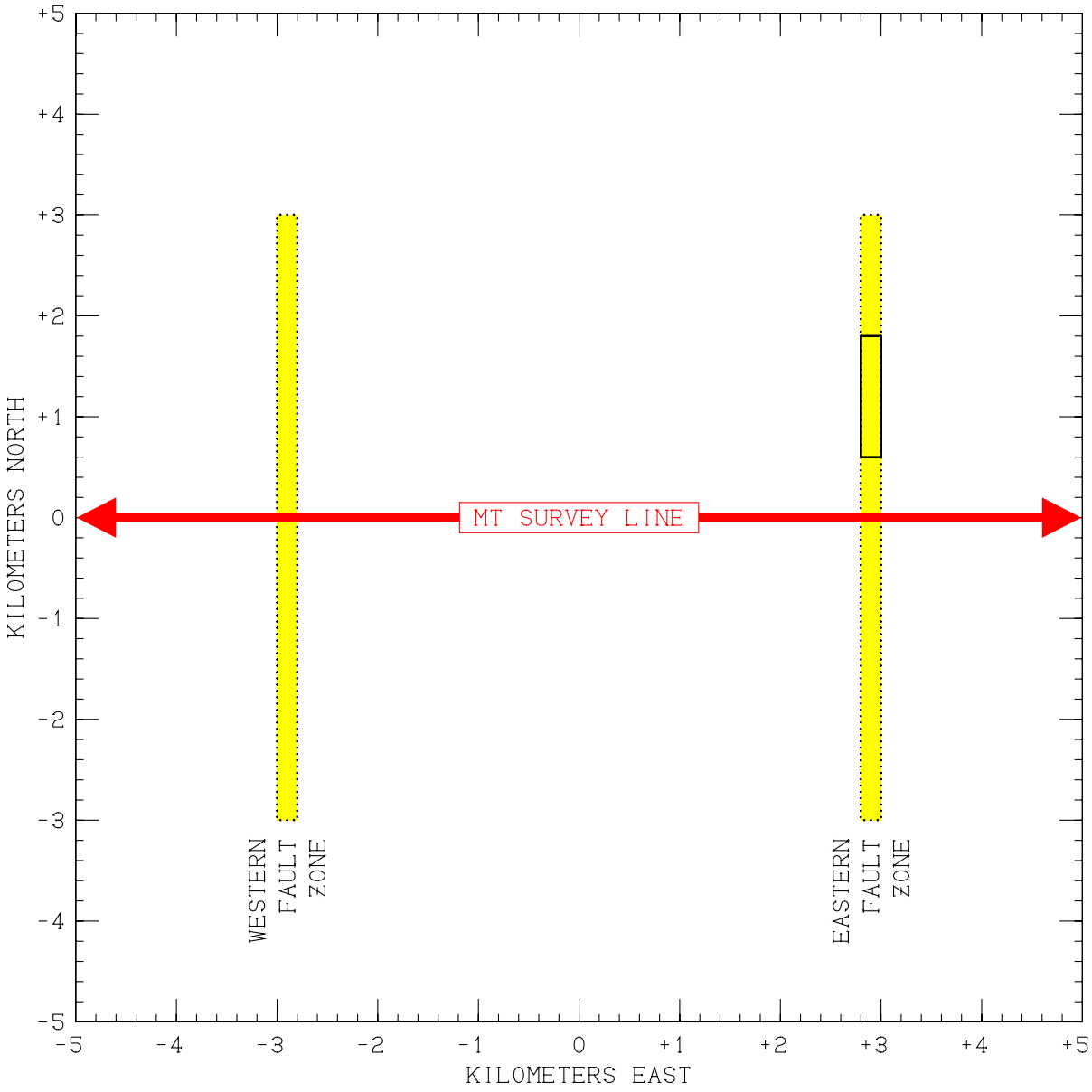

Figure 7.3. Location of "survey line" of stations occupied during east-west MT survey traverse of study area at $y = 0$.

"MT sounding profiles" of these quantities as functions of horizontal location and of frequency (which is inversely correlated with depth). Results obtained for all eight cases using the STAR "MT postprocessor" are depicted in Figures 7.4 – 7.11 for Cases 0.0 – 4.0 respectively.

These magnetotelluric sounding results appear to suggest great promise for the technique for purposes of finding "hidden geothermal reservoirs" of this type. Figure 7.4 (for the "no deep recharge" Case 0.0) is nearly featureless horizontally and appears to represent just a minor perturbation of the "one-dimensional earth" model examined above (Figure 7.1). But Figures 7.5 – 7.7 (for Cases 0.1 – 0.3) on the one hand, and Figures 7.8 – 7.11 (for Cases 1.0 – 4.0) on the other, constitute two very distinct families of MT sounding profiles that should be easy to distinguish in practice. The "eastern reservoir" cases (Figures 7.5 – 7.7) are very similar, with major low-resistivity anomalies centered at the Eastern Fault Zone at all frequencies; the region of reduced resistivity extends about halfway out into the valley. The western half of the valley, by contrast, remains resistive. The "hidden western reservoir" cases (Figures 7.8 – 7.11) all exhibit substantial and broad resistivity reductions which extend clear across the valley at all frequencies. At the lower frequencies, there even appear to be two distinct local resistivity minima corresponding to the (high-permeability, relatively low-resistivity) lower portions of the two fault zones. At frequencies less than 0.5 Hz or so, these surveys appear to "see" *below* the permeable Upper Aquifer to these deep recharge/circulation paths.

Figures 7.12 – 7.19 show that these same trends persist if the MT stations are displaced north-south as well as east-west, creating two-dimensional "MT apparent resistivity maps" of the study area. The apparent resistivity at 0.1 Hz is shown in these plots, but similar results would be obtained for other frequencies below 1 Hz or so. Case 0.0 exhibits a moderate resistivity anomaly (contrast ~2.5) confined to the immediate neighborhood of the "Thermal Area", but little else of note. All three of the "eastern reservoir" cases (Figures 7.13 – 7.15; Cases 0.1, 0.2 and 0.3) are characterized by intense elongated north-south oriented resistivity anomalies (contrast > 5) overlying the Eastern Fault Zone. The "hidden" reservoirs (Cases 1.0 – 4.0; Figures 7.16 – 7.19) exhibit broad low-resistivity anomalies (contrast > 2) that fill the entire valley floor and two local resistivity extrema (contrast > 4) that coincide with the Western and the Eastern fault zones. This latter pattern should certainly suggest the likelihood of the presence of significant geothermal activity underlying the west side of the valley, despite the lack of any evidence for such a system from natural surface discharges or from shallow drilling.

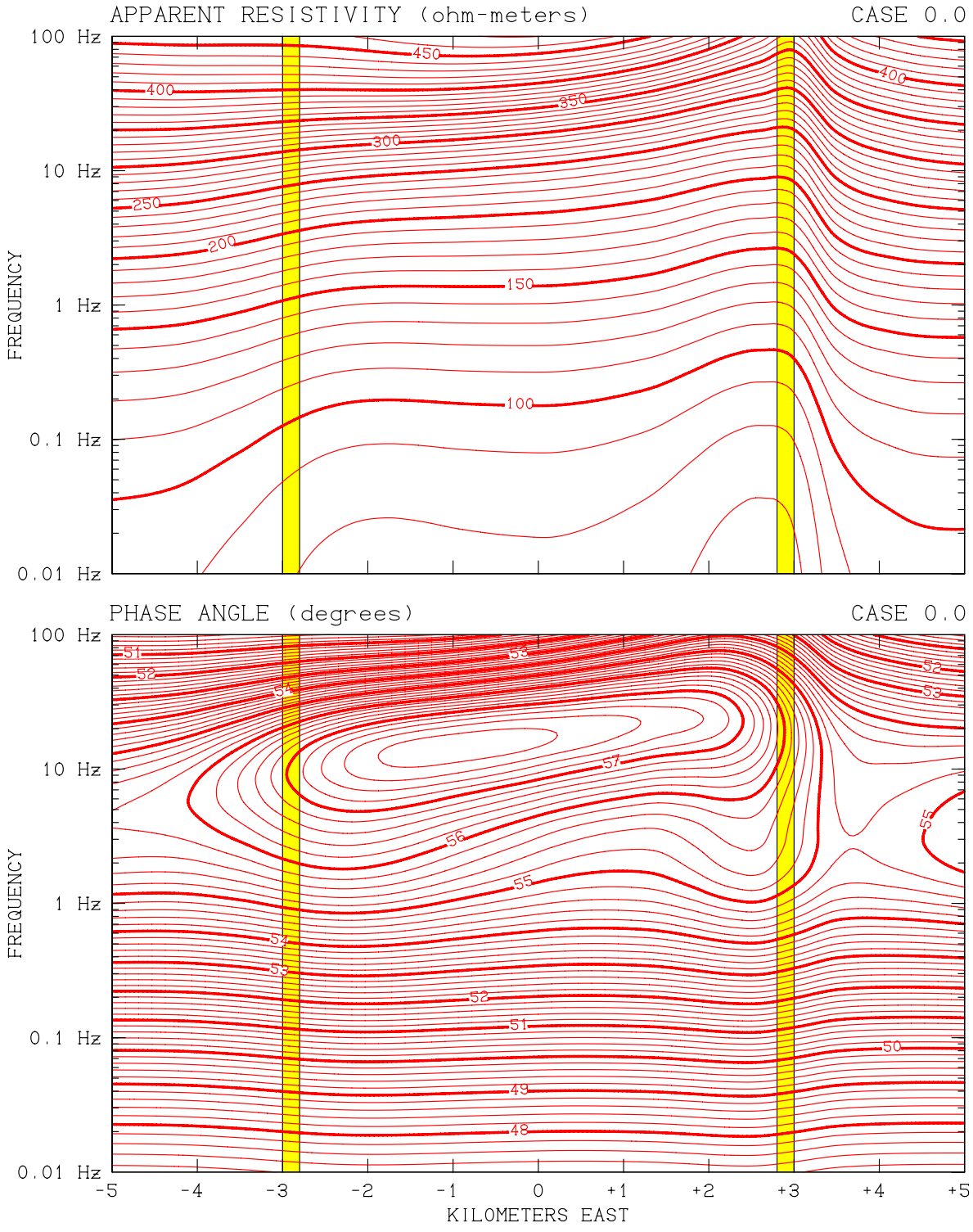

Figure 7.4. Computed results of east-west MT survey traverse of study area at $y = 0$ for Case 0.0. *Upper:* apparent resistivity. *Lower:* phase angle.

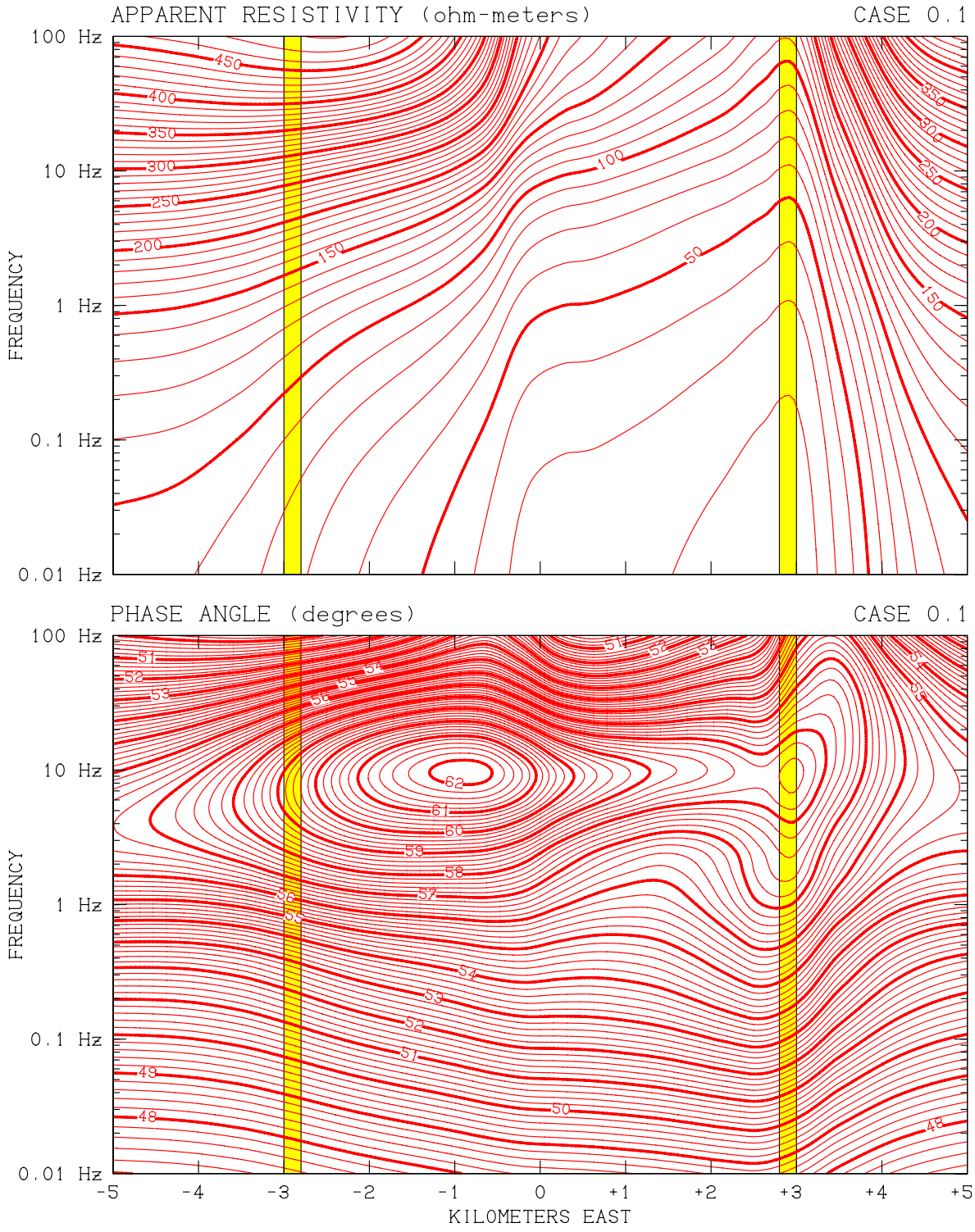

Figure 7.5. Computed results of east-west MT survey traverse of study area at $y = 0$ for Case 0.1. *Upper:* apparent resistivity. *Lower:* phase angle.

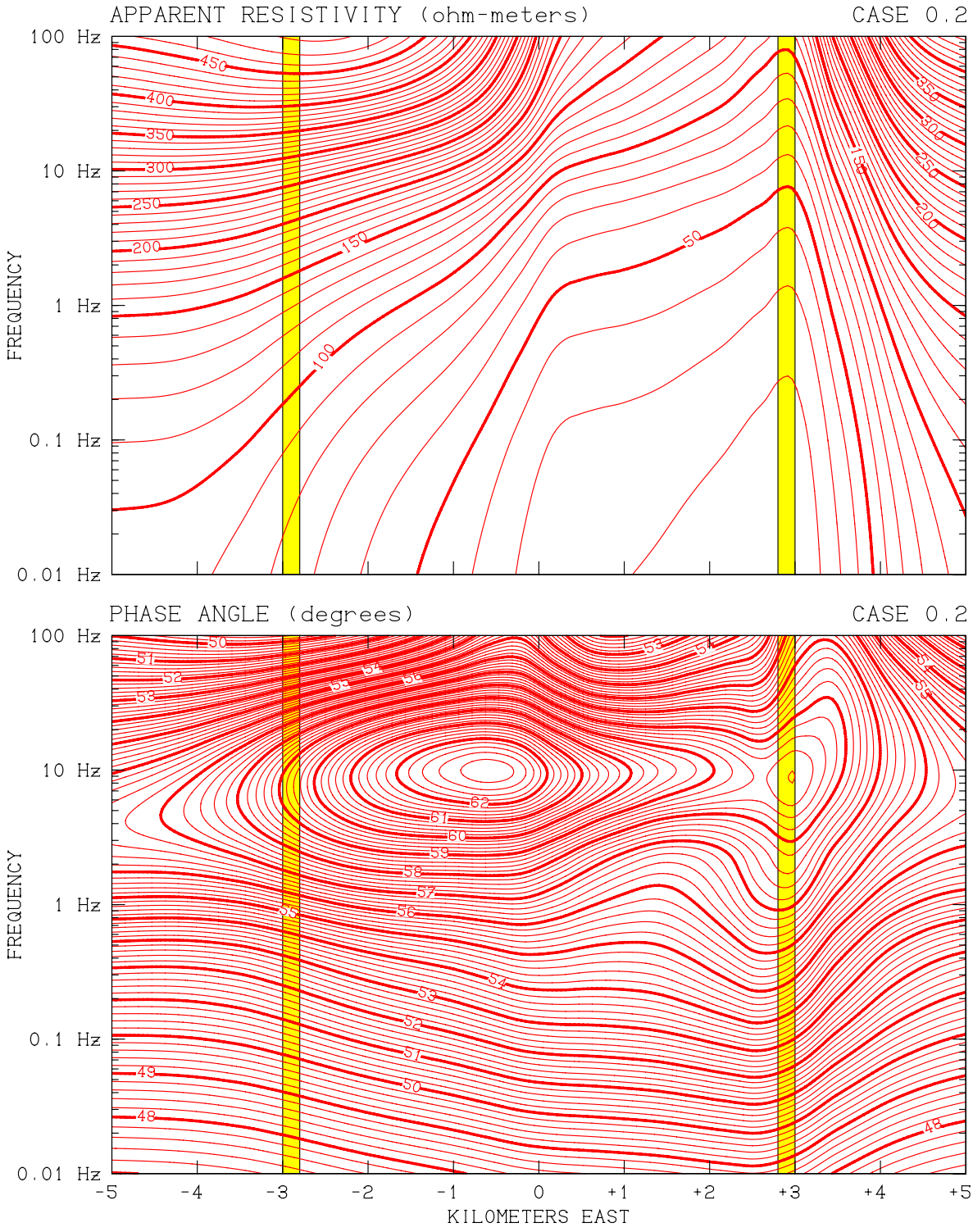

Figure 7.6. Computed results of east-west MT survey traverse of study area at $y = 0$ for Case 0.2. *Upper:* apparent resistivity. *Lower:* phase angle.

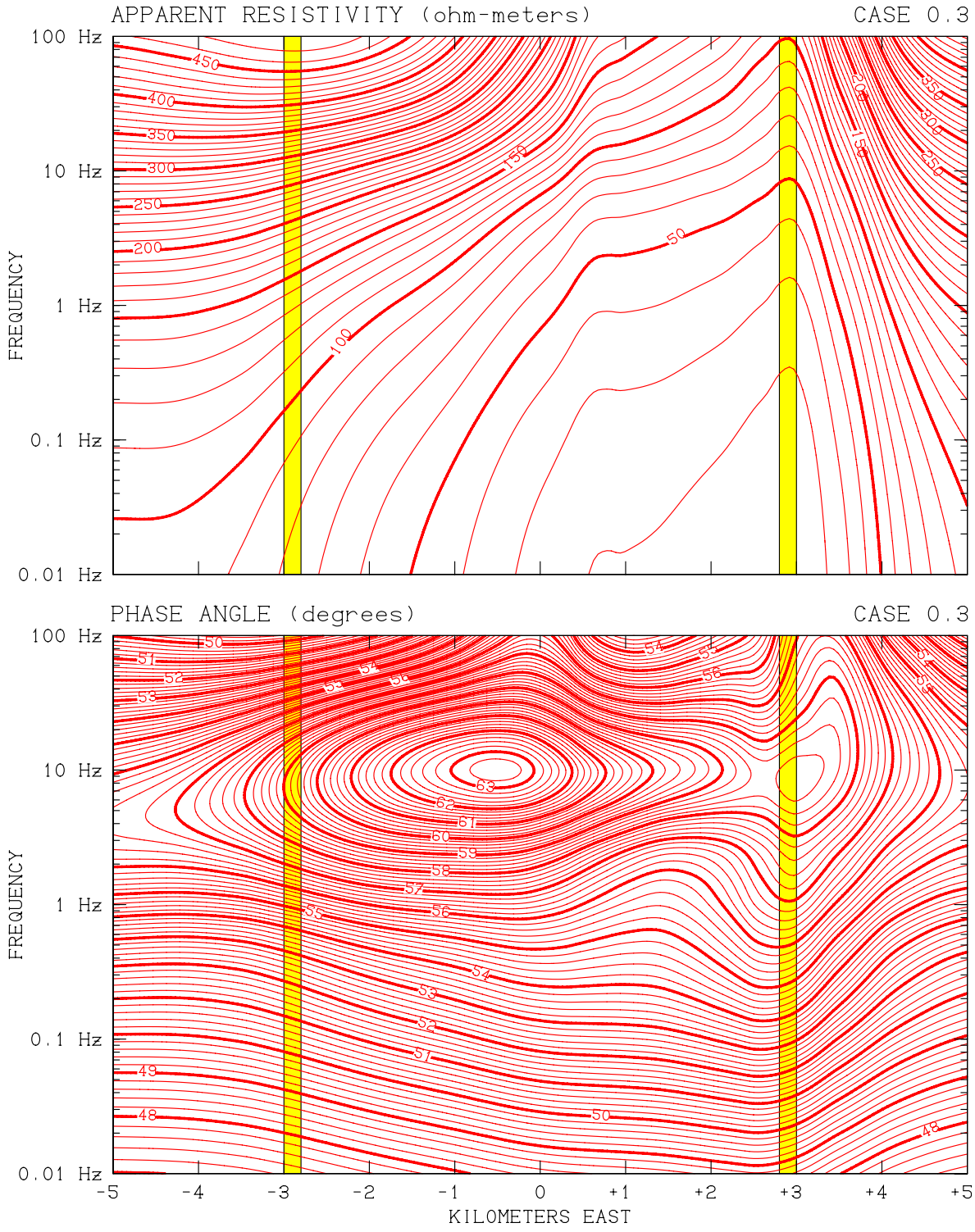

Figure 7.7. Computed results of east-west MT survey traverse of study area at $y = 0$ for Case 0.3. *Upper:* apparent resistivity. *Lower:* phase angle.

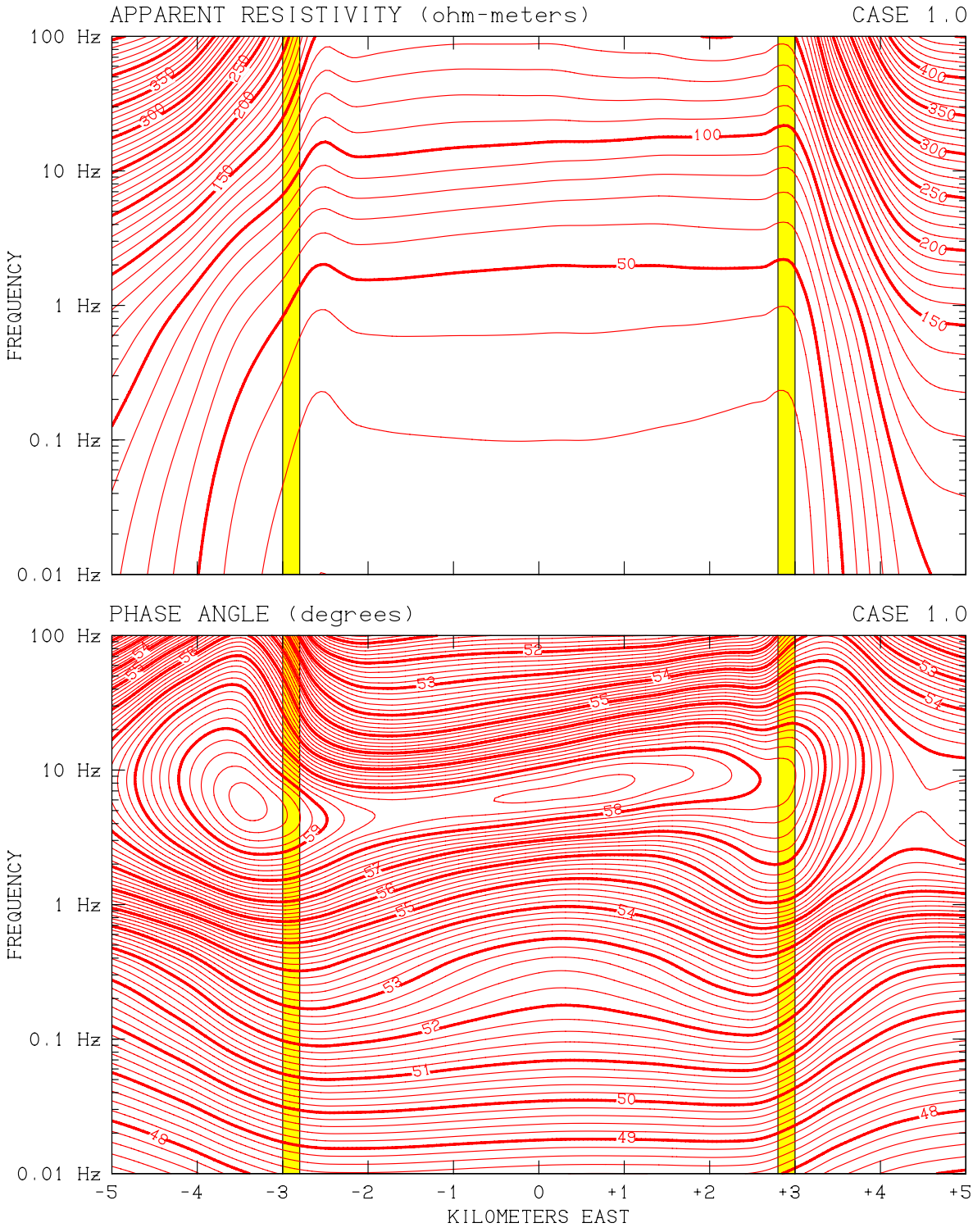

Figure 7.8. Computed results of east-west MT survey traverse of study area at $y = 0$ for Case 1.0. *Upper:* apparent resistivity. *Lower:* phase angle.

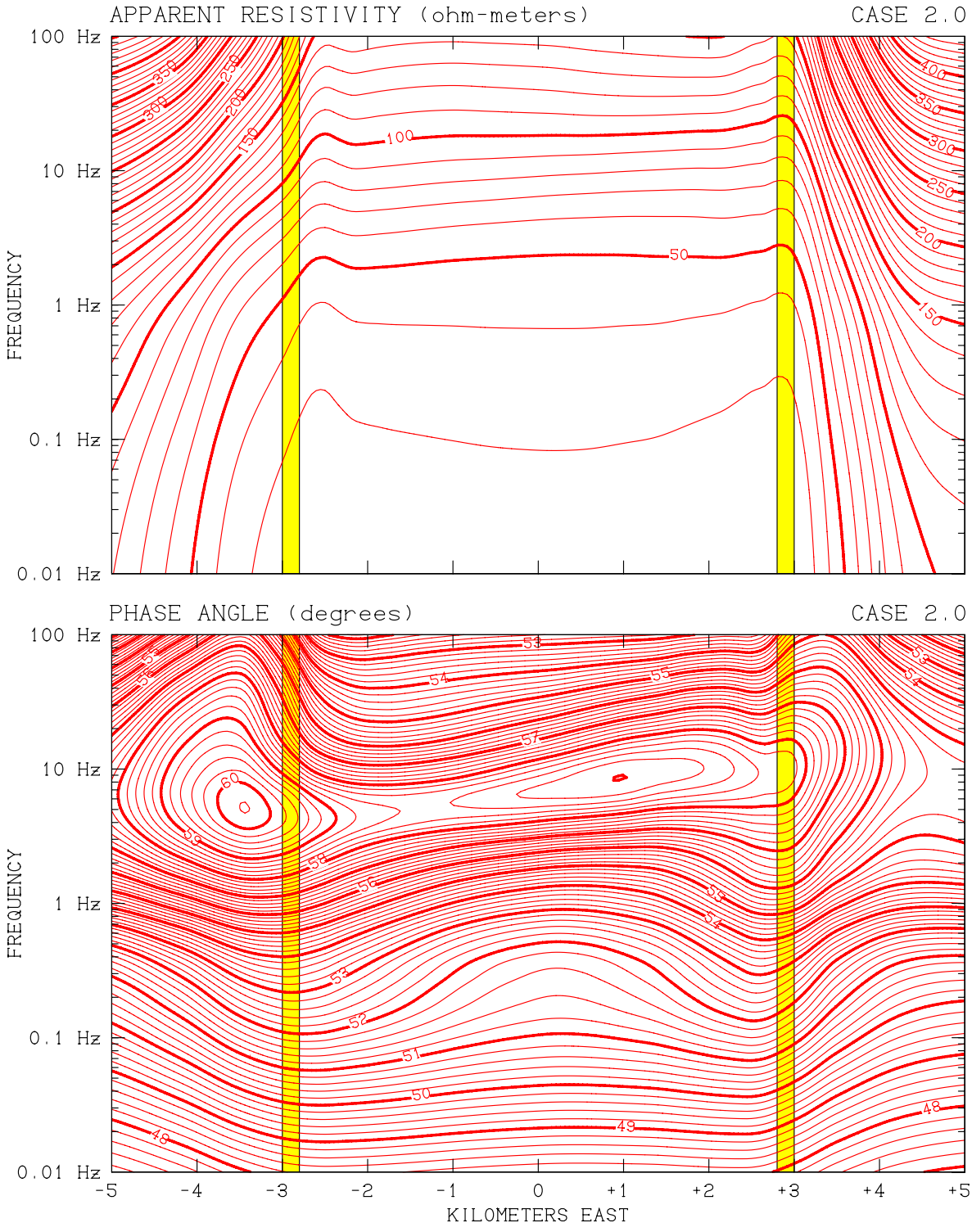

Figure 7.9. Computed results of east-west MT survey traverse of study area at $y = 0$ for Case 2.0. *Upper:* apparent resistivity. *Lower:* phase angle.

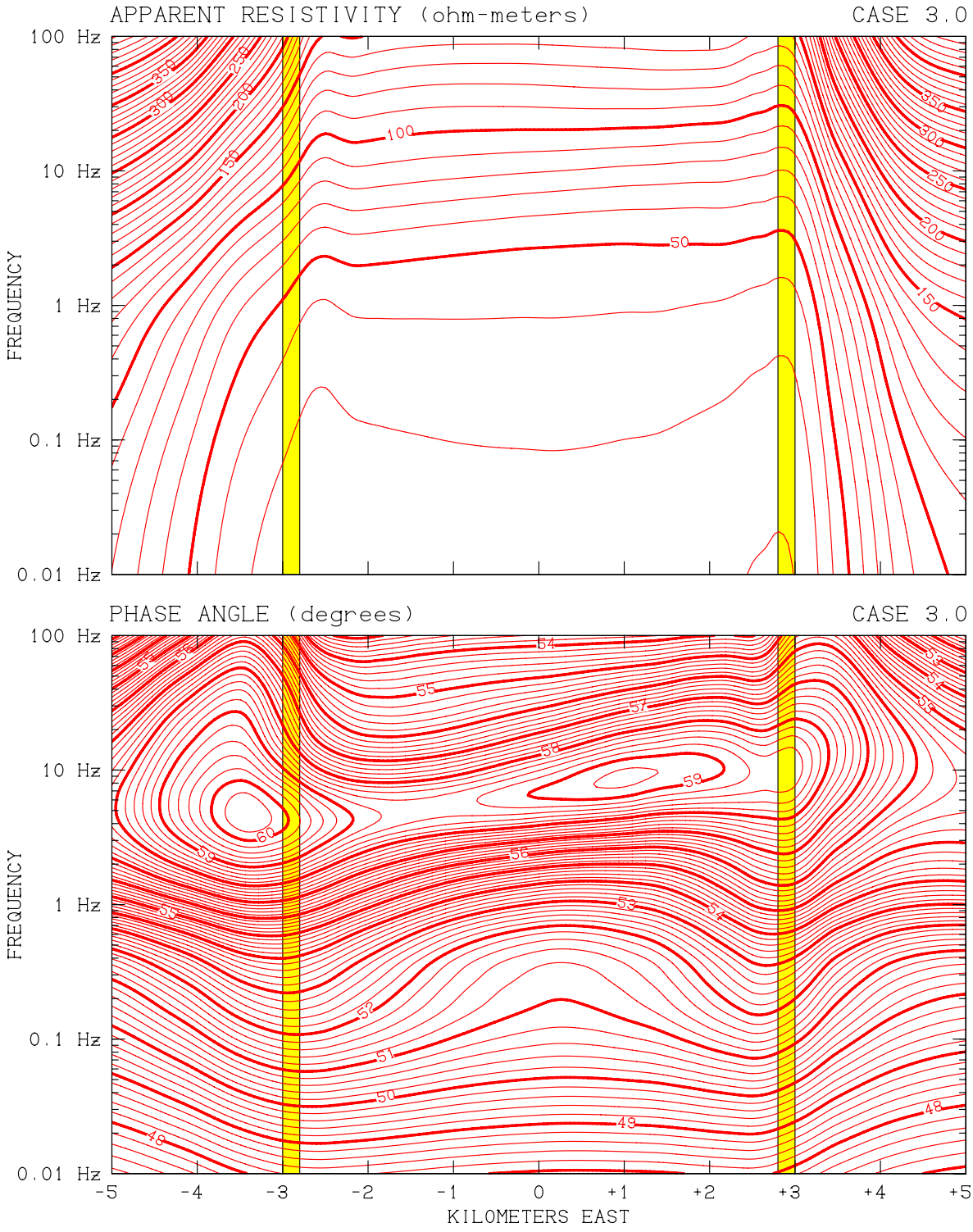

Figure 7.10. Computed results of east-west MT survey traverse of study area at $y = 0$ for Case 3.0. *Upper:* apparent resistivity. *Lower:* phase angle.

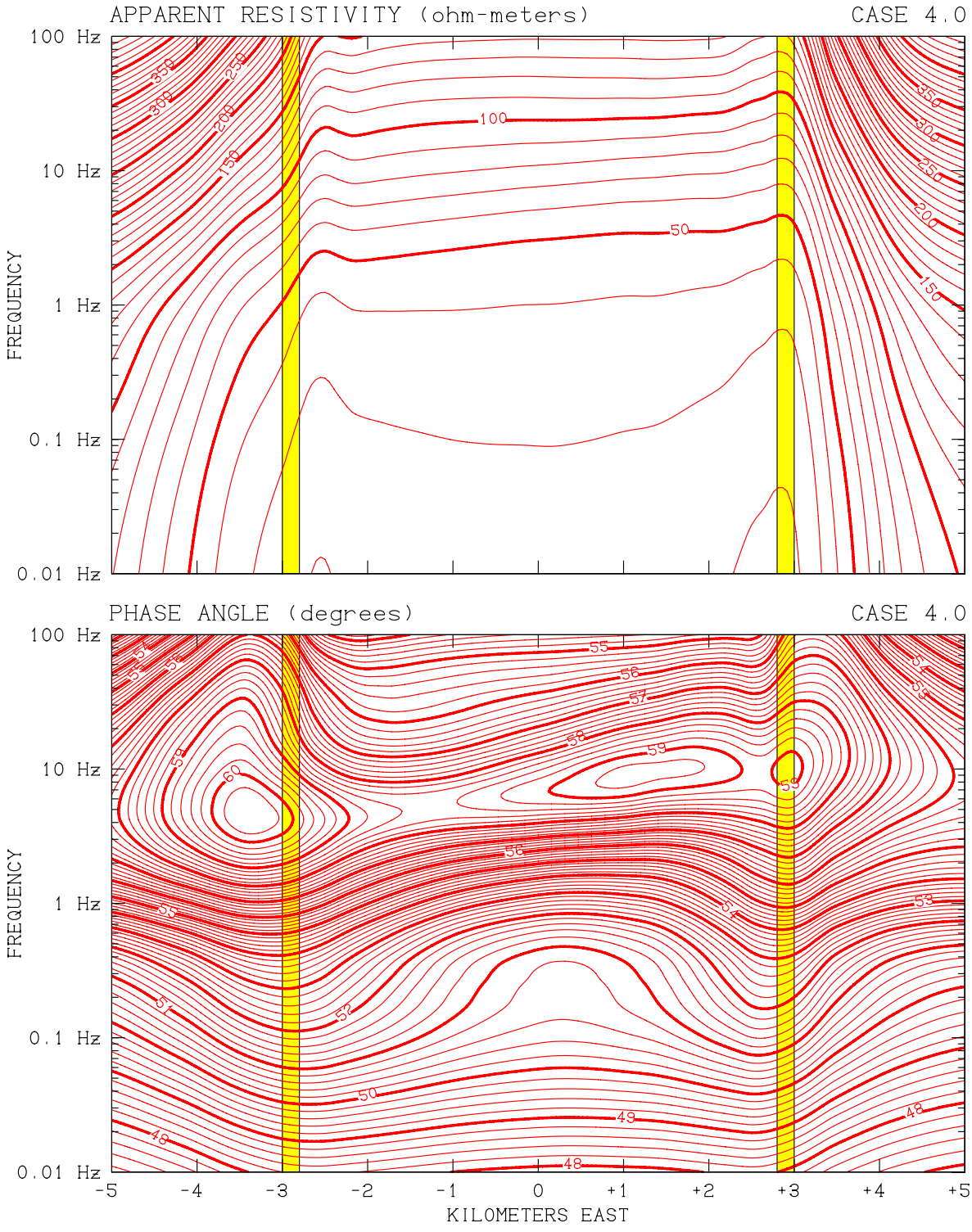

Figure 7.11. Computed results of east-west MT survey traverse of study area at $y = 0$ for Case 4.0. *Upper:* apparent resistivity. *Lower:* phase angle.

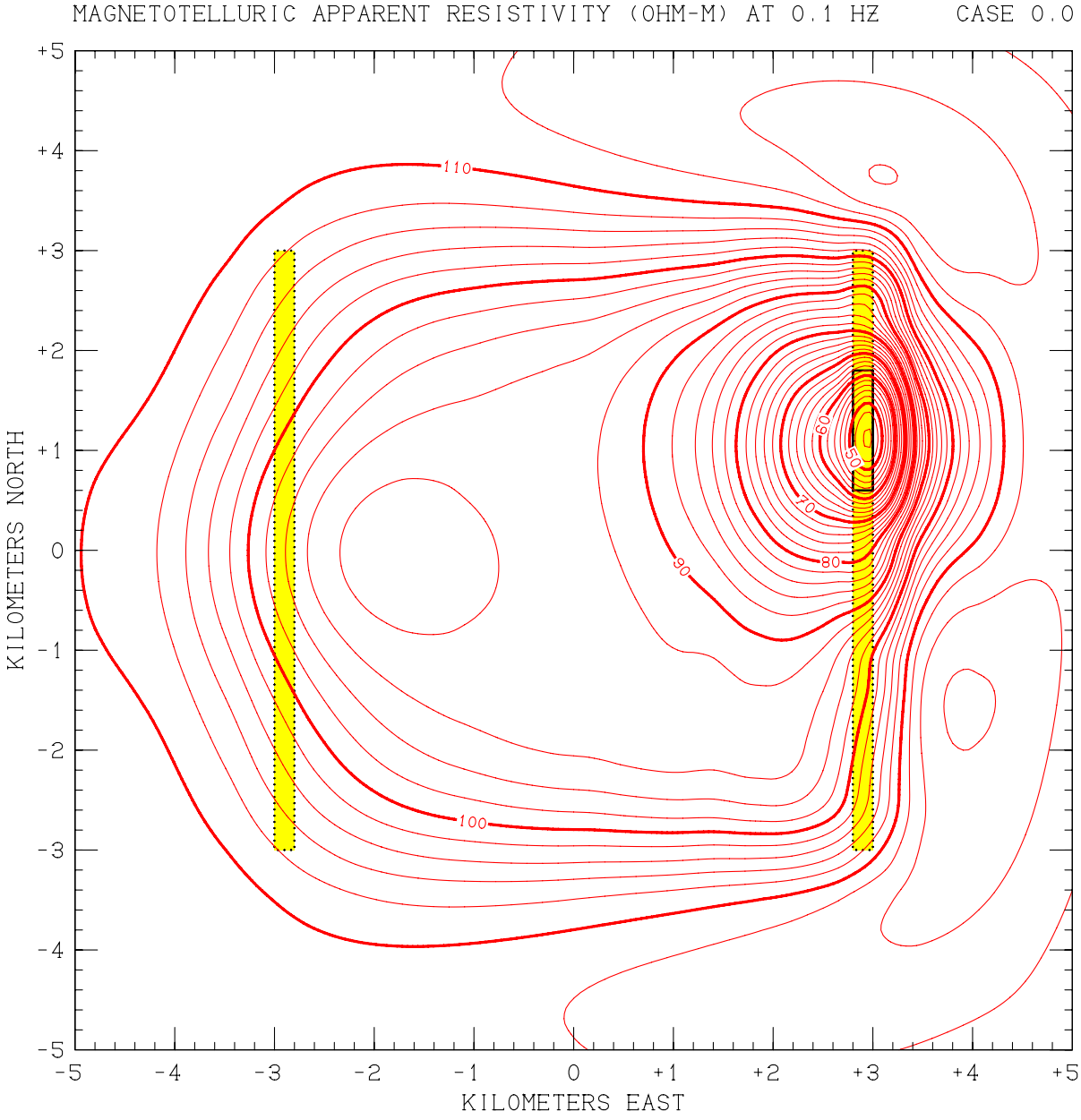

Figure 7.12. Computed results of MT survey of entire 100 km^2 study area at a frequency of 0.1 Hz for Case 0.0. Contour lines represent apparent MT resistivity, with a contour spacing of 2 ohm-m.

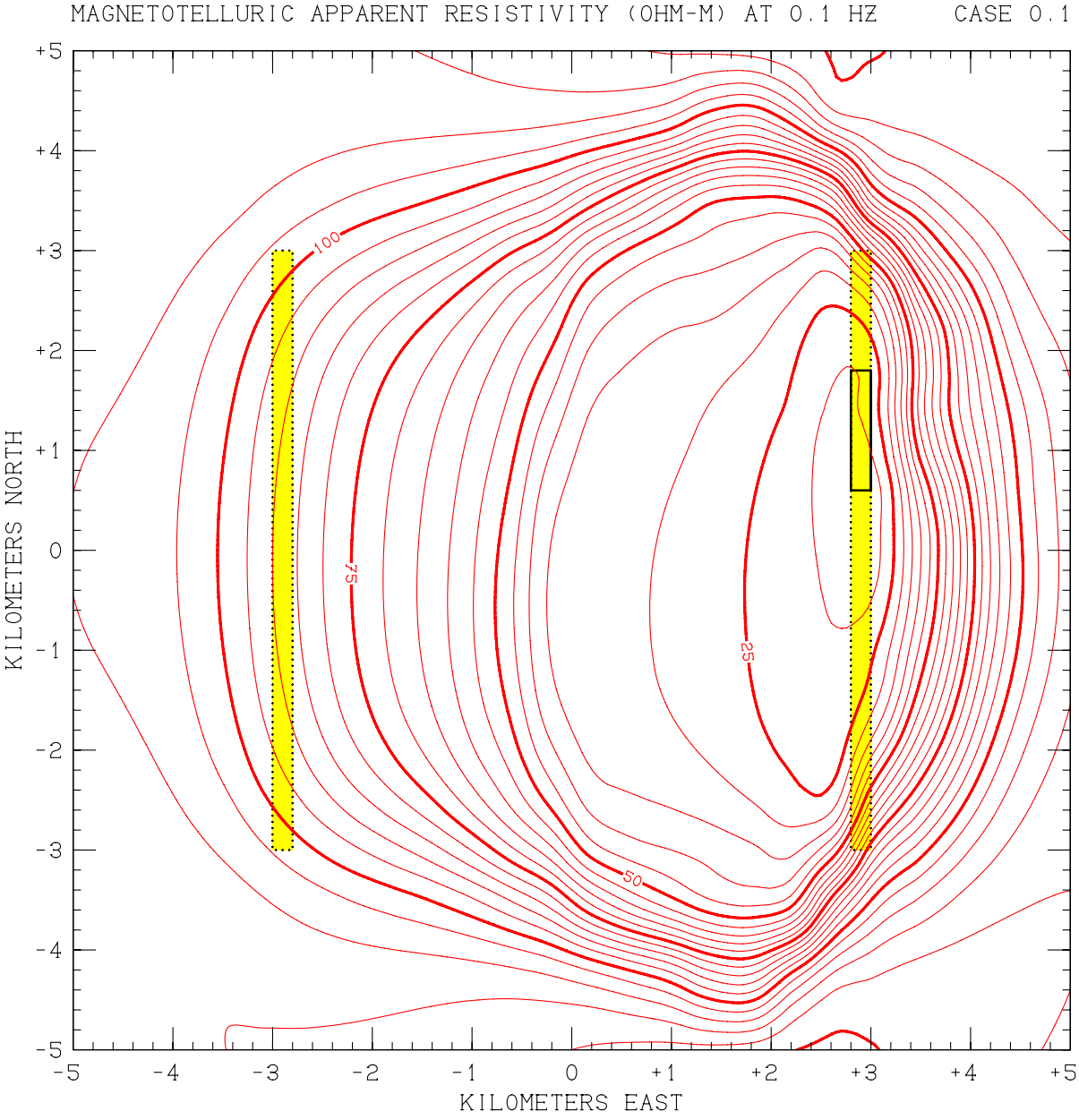

Figure 7.13. Computed results of MT survey of entire 100 km^2 study area at a frequency of 0.1 Hz for Case 0.1. Contour lines represent apparent MT resistivity, with a contour spacing of 5 ohm-m.

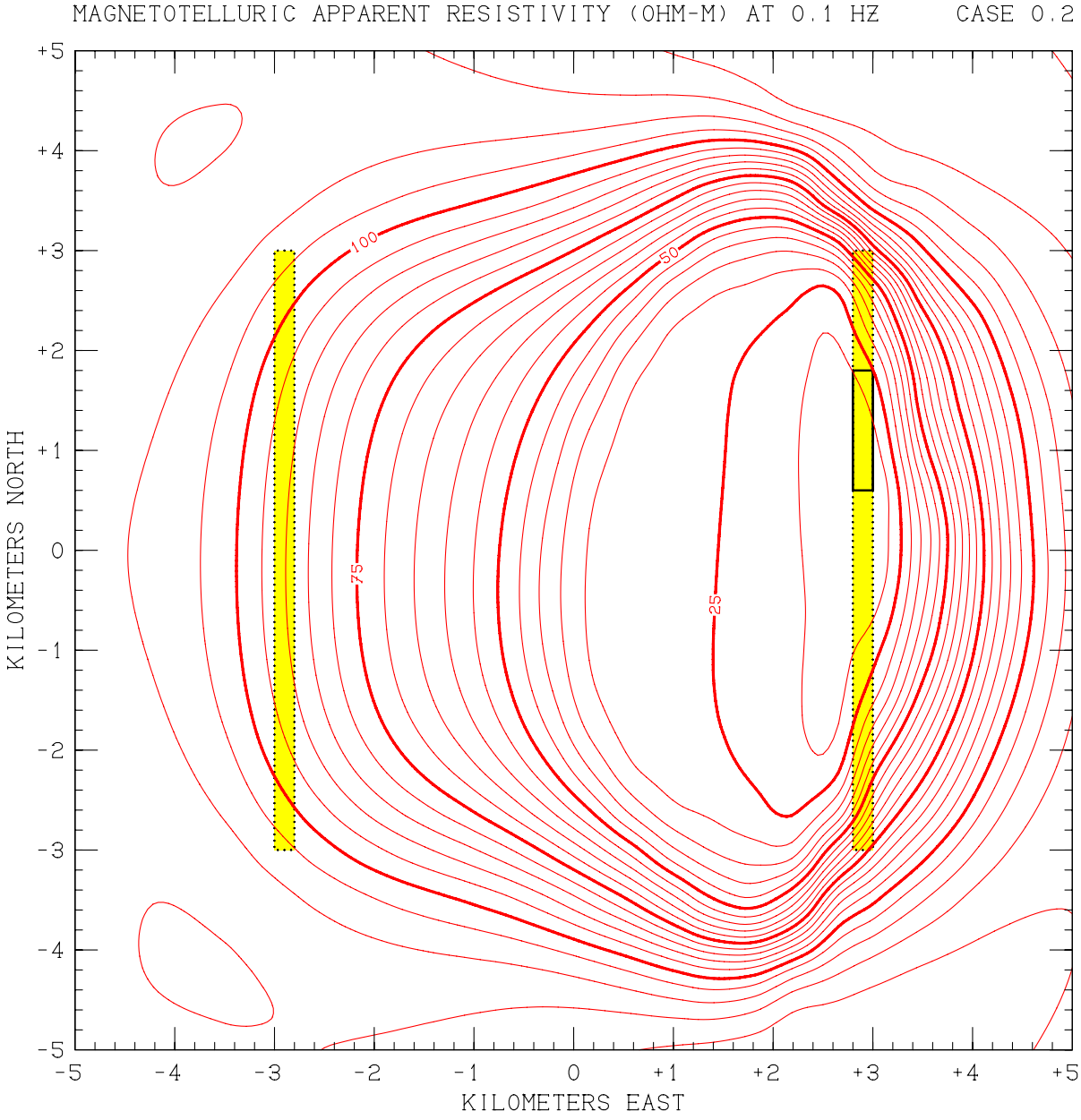

Figure 7.14. Computed results of MT survey of entire 100 km^2 study area at a frequency of 0.1 Hz for Case 0.2. Contour lines represent apparent MT resistivity, with a contour spacing of 5 ohm-m.

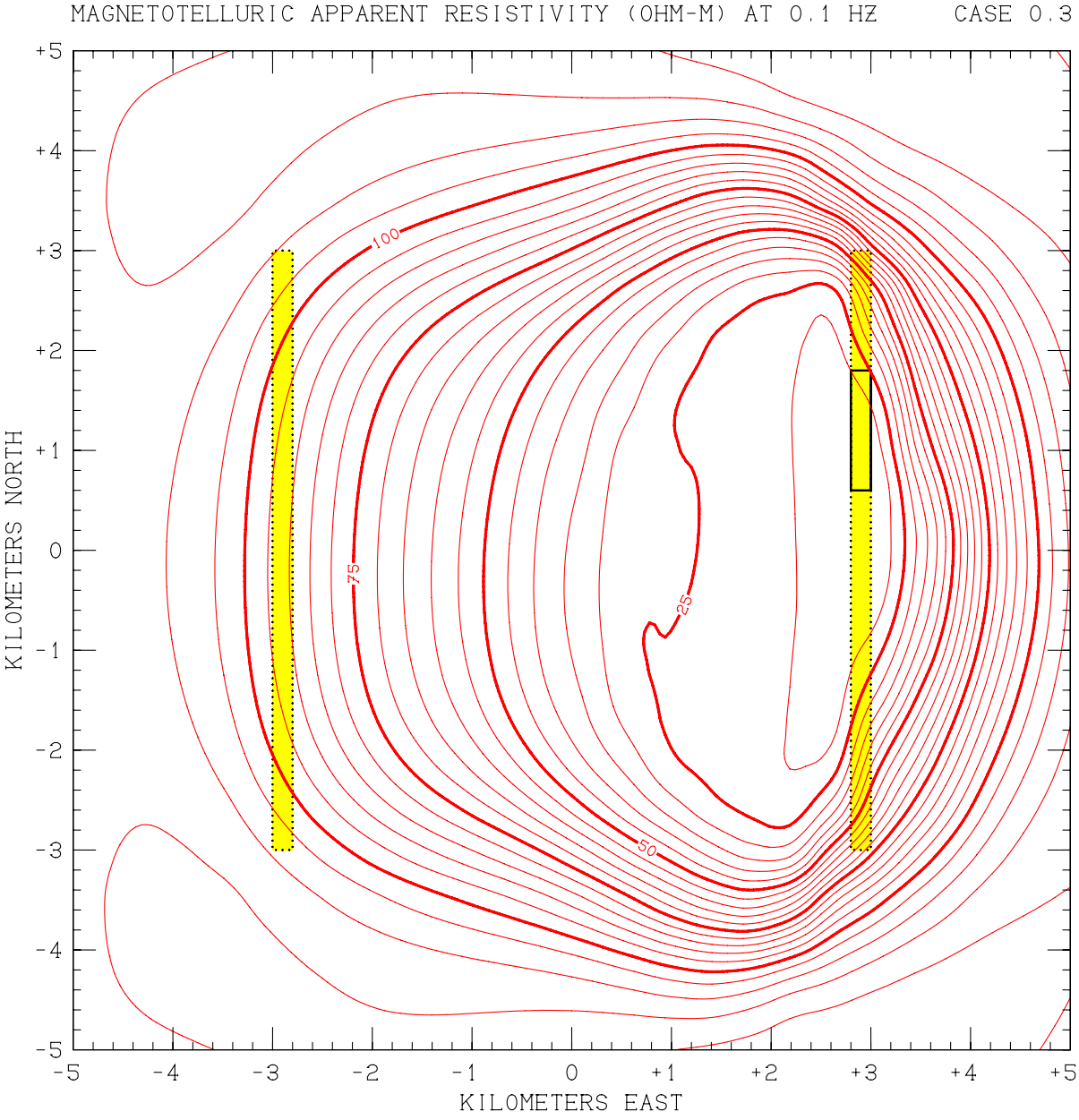

Figure 7.15. Computed results of MT survey of entire 100 km^2 study area at a frequency of 0.1 Hz for Case 0.3. Contour lines represent apparent MT resistivity, with a contour spacing of 5 ohm-m.

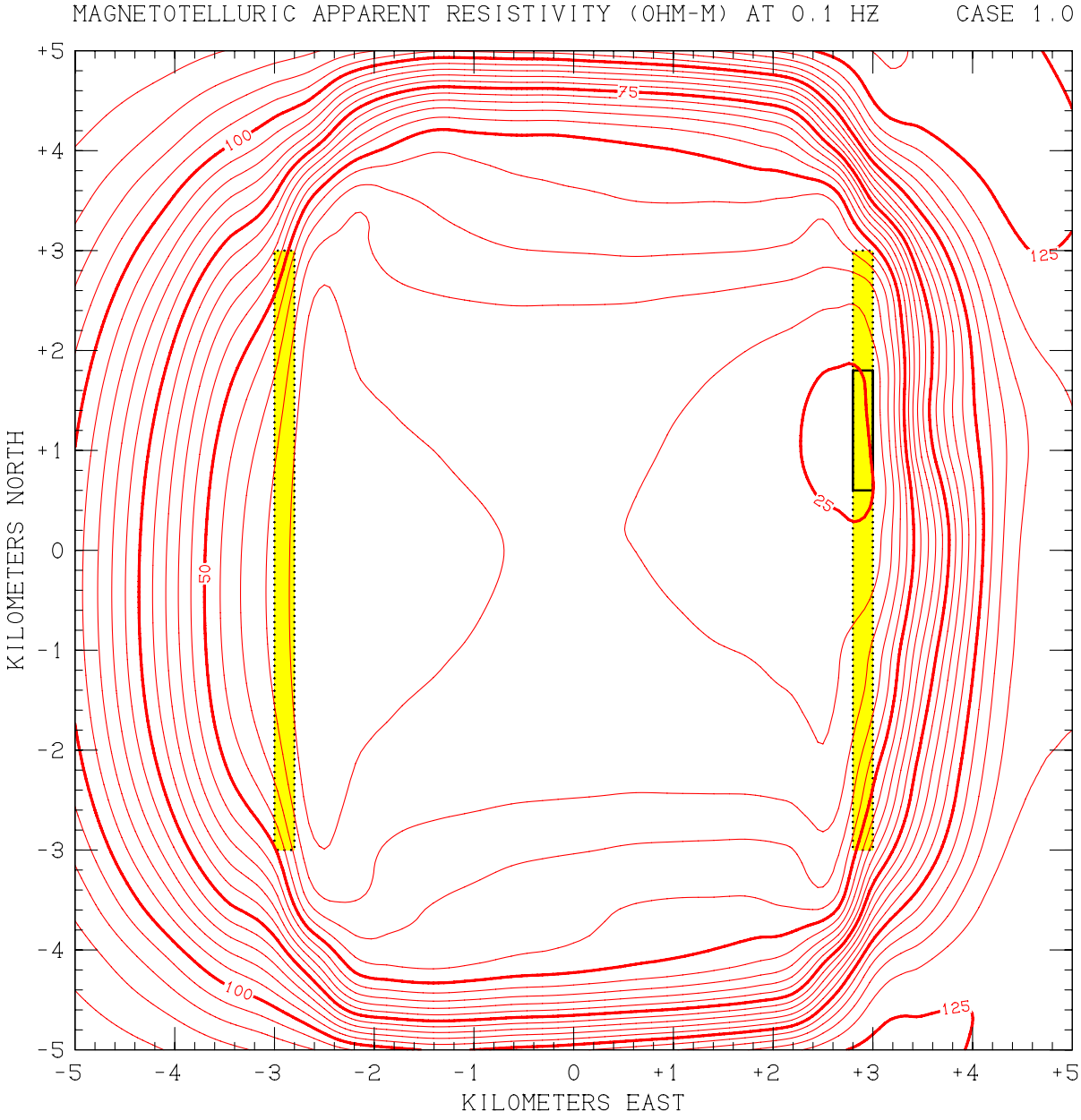

Figure 7.16. Computed results of MT survey of entire 100 km^2 study area at a frequency of 0.1 Hz for Case 1.0. Contour lines represent apparent MT resistivity, with a contour spacing of 5 ohm-m.

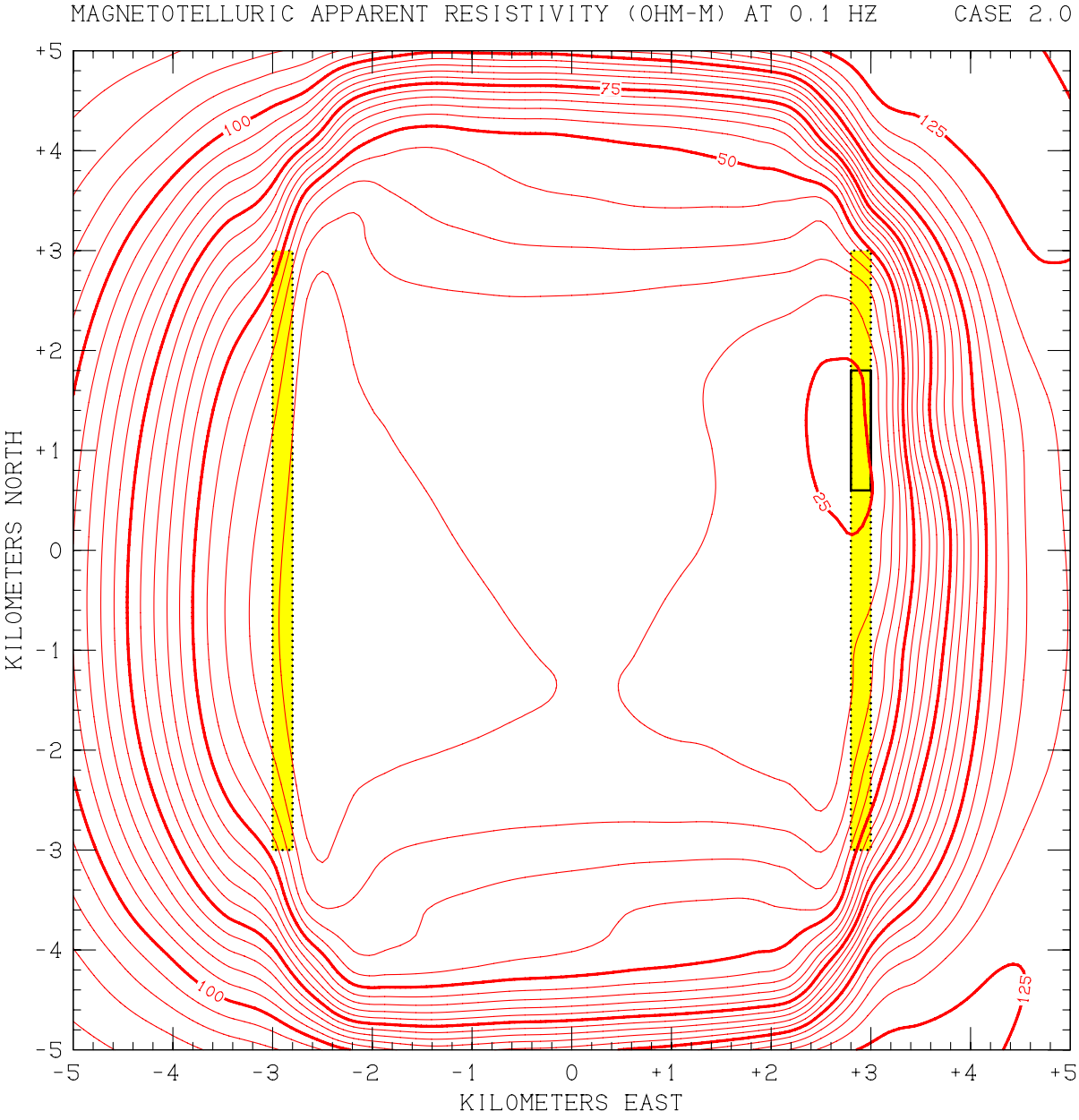

Figure 7.17. Computed results of MT survey of entire 100 km^2 study area at a frequency of 0.1 Hz for Case 2.0. Contour lines represent apparent MT resistivity, with a contour spacing of 5 ohm-m.

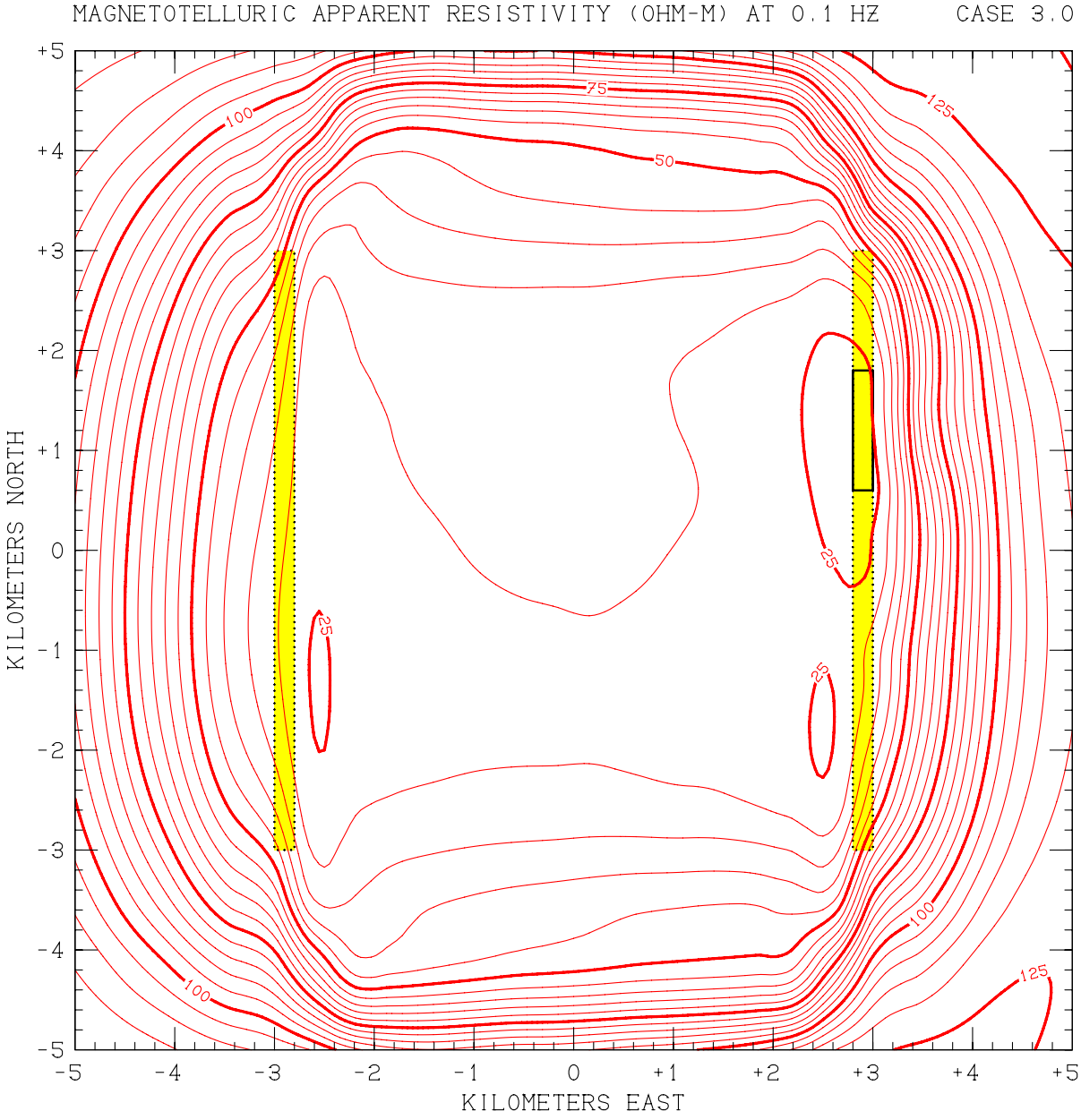

Figure 7.18. Computed results of MT survey of entire 100 km^2 study area at a frequency of 0.1 Hz for Case 3.0. Contour lines represent apparent MT resistivity, with a contour spacing of 5 ohm-m.

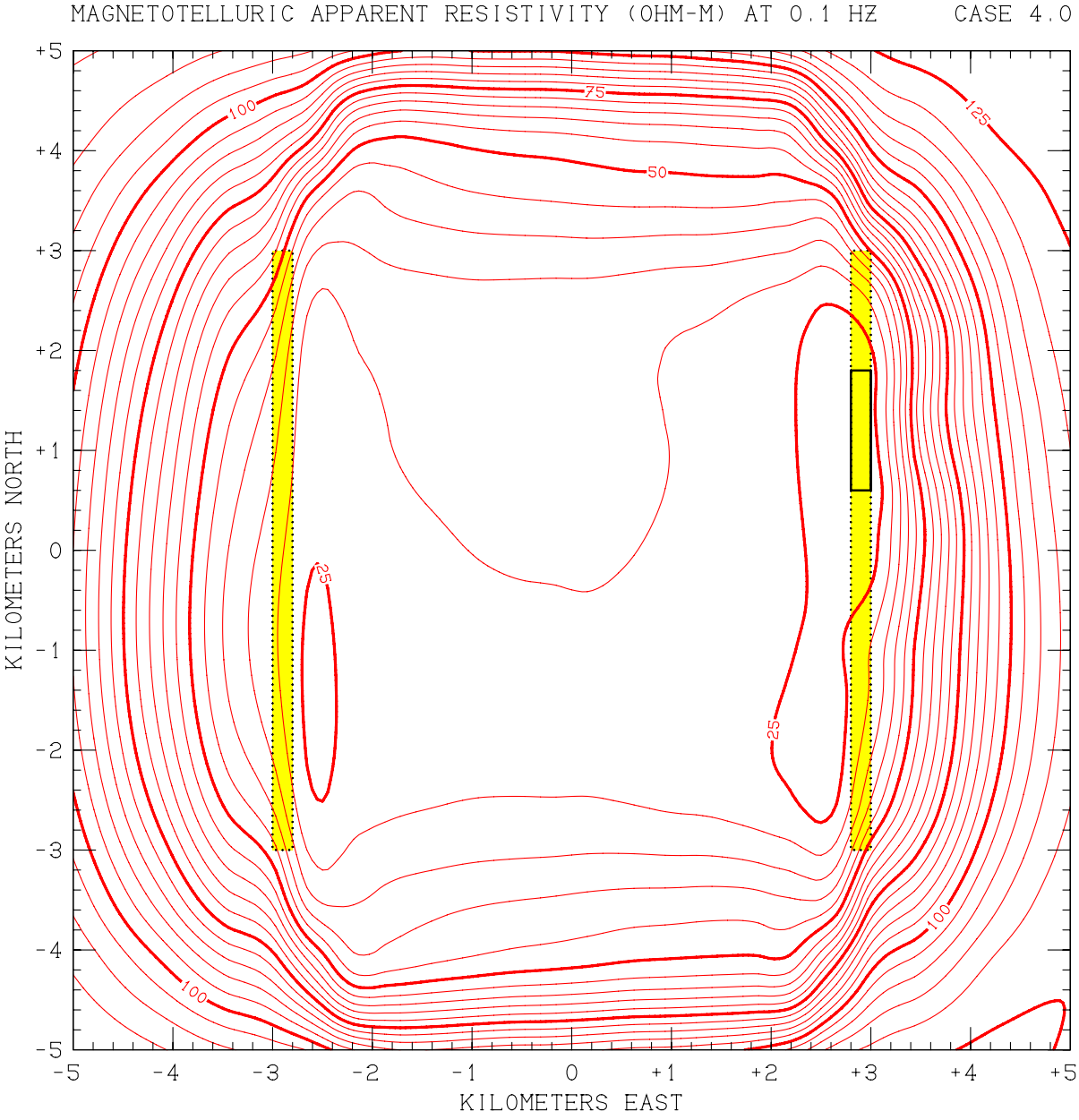

Figure 7.19. Computed results of MT survey of entire 100 km^2 study area at a frequency of 0.1 Hz for Case 4.0. Contour lines represent apparent MT resistivity, with a contour spacing of 5 ohm-m.

8 RESULTS FROM SELF-POTENTIAL SURVEYS

Natural distributions of electrical potential are always present at the earth surface; in geothermal areas, the main cause of heterogeneities in the surface voltage (the *self-potential* or *spontaneous potential*; "SP") is the so-called "electrokinetic effect" or "streaming potential" (*Ishido and Mizutani,* 1981; also see Chapters 5 and 6 of *Telford et. al,* 1990). If liquid water flows underground through a porous medium, electrons will tend to be dragged along with the fluid flow in the molecular-scale "electrical double layer" at the interface between fluid and solid, thereby creating a distributed electric current. This electric current, passing through the resistive geological formation, will result in the creation of a spatial distribution of electrical potential (voltage) in accordance with Ohm's Law. The potential disturbance will extend far beyond the local region where fluid is actually flowing. In particular, voltage gradients will be created at the earth surface far above, which can be detected and characterized using a simple potentiometer. As a result, SP surveys are in effect a technique for remote-sensing of subsurface fluid flow – an essential prerequisite for all hydrothermal reservoirs. SP surveys are quite inexpensive compared to many other geophysical survey techniques, and fairly simple instrumentation can provide good reproducibility down to 10-20 millivolts of electrical potential in practical field situations.

The STAR "SP postprocessor" (*Ishido and Pritchett,* 2000; *Pritchett,* 2003; Chapter 17 of *Pritchett,* 2002) solves the pertinent Poisson equation for electrical potential throughout the volume of the "electrical grid" arising from fluid flows taking place within the STAR "flow grid" (Figure 2.1) and displays the resulting earth-surface distributions of electrical potential at the earth surface. This was done for all eight cases considered in this study – results are shown for the 100 km^2 study area in Figures 8.1 – 8.8, using a contour level spacing of 20 mV. These distributions of SP have features that arise from two main causes. First, of course, is the signal due to convective flow deep within the geothermal reservoir itself, generally located within the valley between $x = -3$ km and $x = 3$ km. In addition, regions of low potential and high potential gradient are present in all cases in both the extreme eastern and western parts of the study area ($x < -3$ km and $x > 3$ km). These latter peripheral disturbances arise from shallow groundwater flow. In these sloping regions, shallow waters have a tendency to flow downhill toward the valley floor, producing east-west potential gradients through electrokinetic coupling. In field practice, most of such topographically induced background noise can usually be eliminated during data analysis using statistical techniques and a good topographic map, but in the present cases the deep-origin signal of primary interest is sufficiently clear that such filtering was not really needed.

It should be noted that SP signals of substantial amplitude, arising from deep hydrothermal convection, are present on the valley floor for all eight cases. Even the "no deep recharge" Case 0.0 exhibits a positive self-potential anomaly of about 100 millivolts amplitude centered near the "Thermal Area", and the remaining cases produce even stronger

Continued on page 8-10

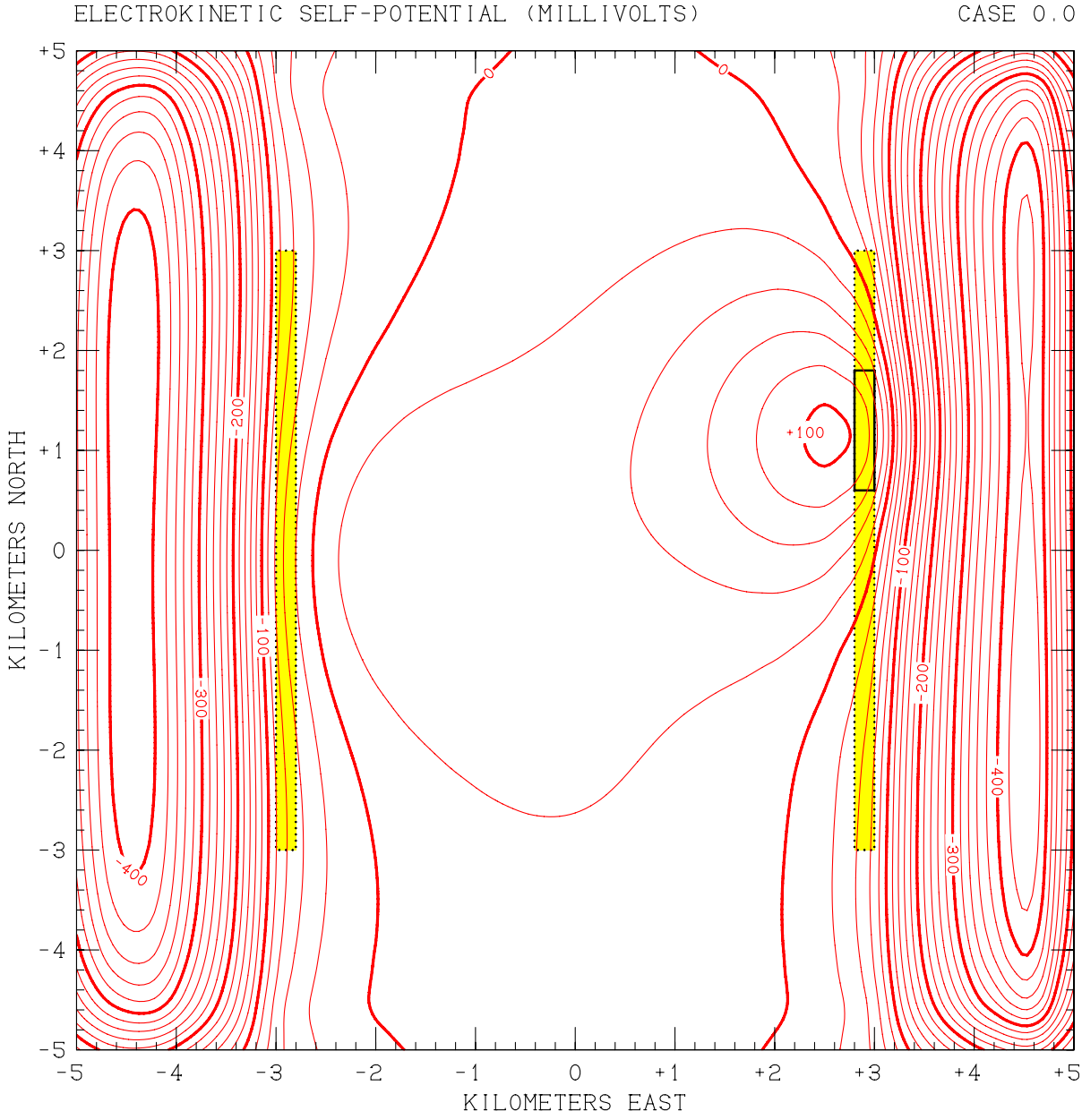

Figure 8.1. Computed results of self-potential (SP) survey of entire 100 km^2 study area for Case 0.0. Contour spacing is 20 millivolts. North-south oriented disturbances in extreme eastern and western parts of study area are of shallow topographic origin and are unrelated to the geothermal reservoir.

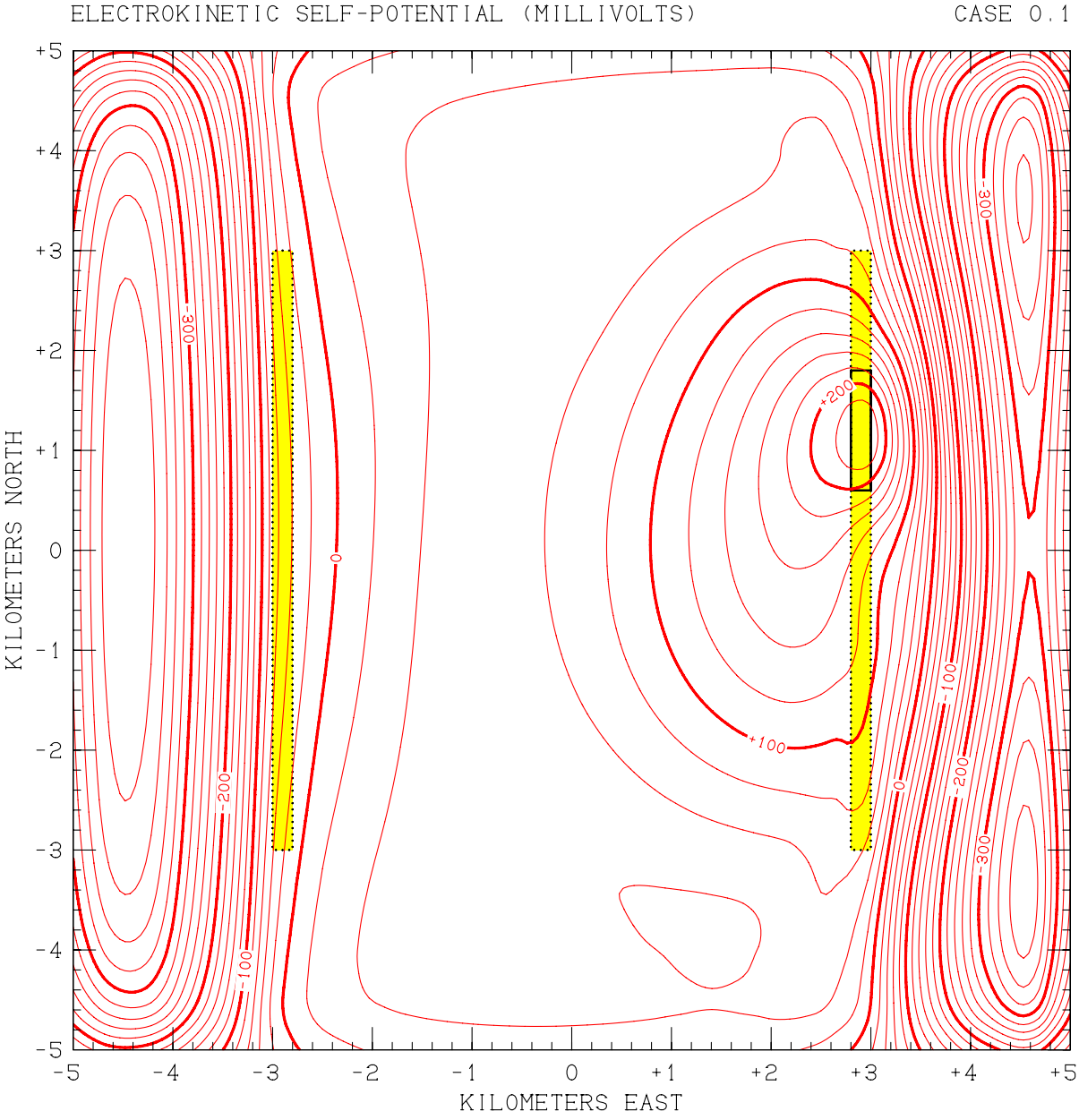

Figure 8.2. Computed results of self-potential (SP) survey of entire 100 km^2 study area for Case 0.1. Contour spacing is 20 millivolts. North-south oriented disturbances in extreme eastern and western parts of study area are of shallow topographic origin and are unrelated to the geothermal reservoir.

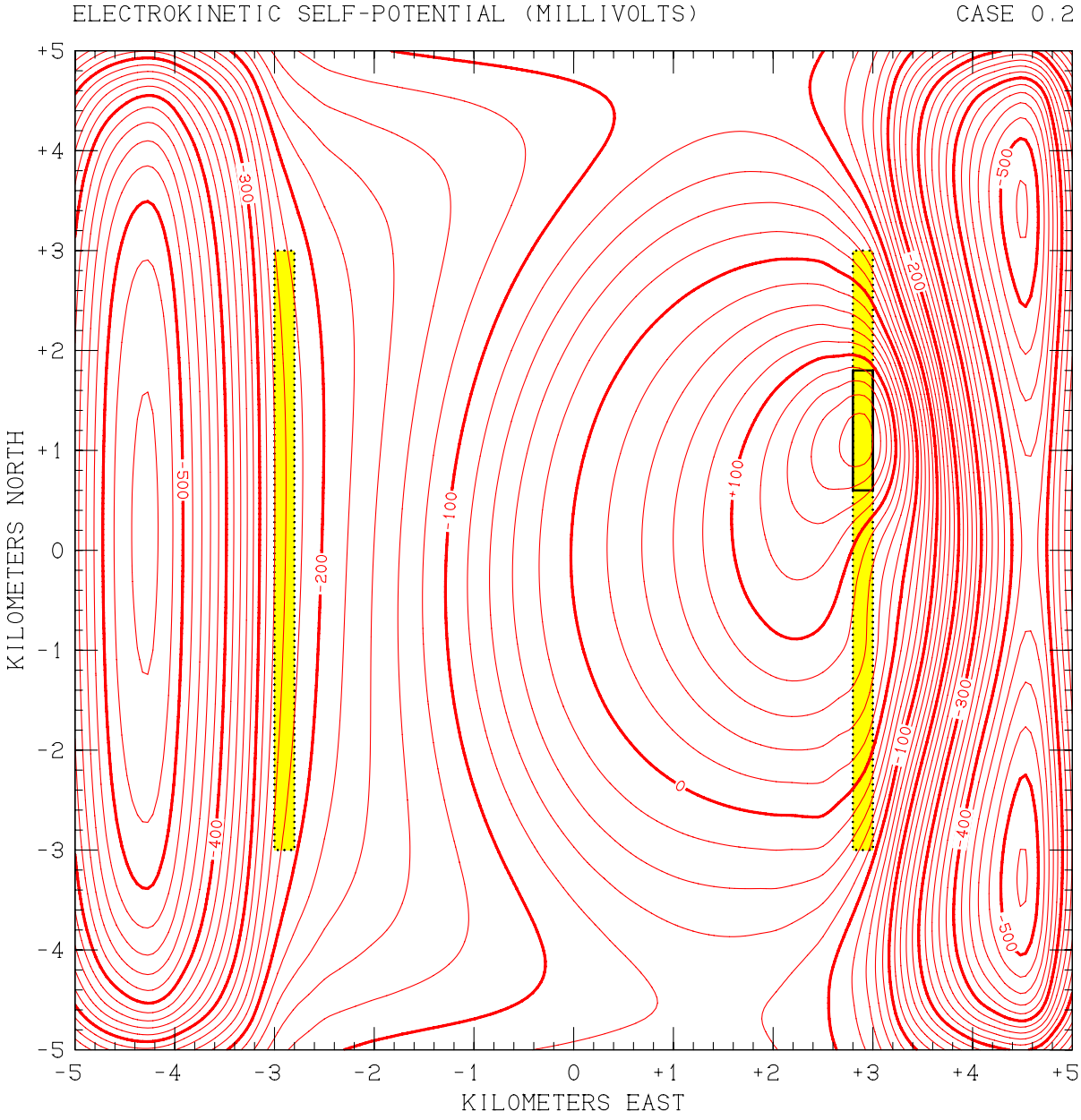

Figure 8.3. Computed results of self-potential (SP) survey of entire 100 km^2 study area for Case 0.2. Contour spacing is 20 millivolts. North-south oriented disturbances in extreme eastern and western parts of study area are of shallow topographic origin and are unrelated to the geothermal reservoir.

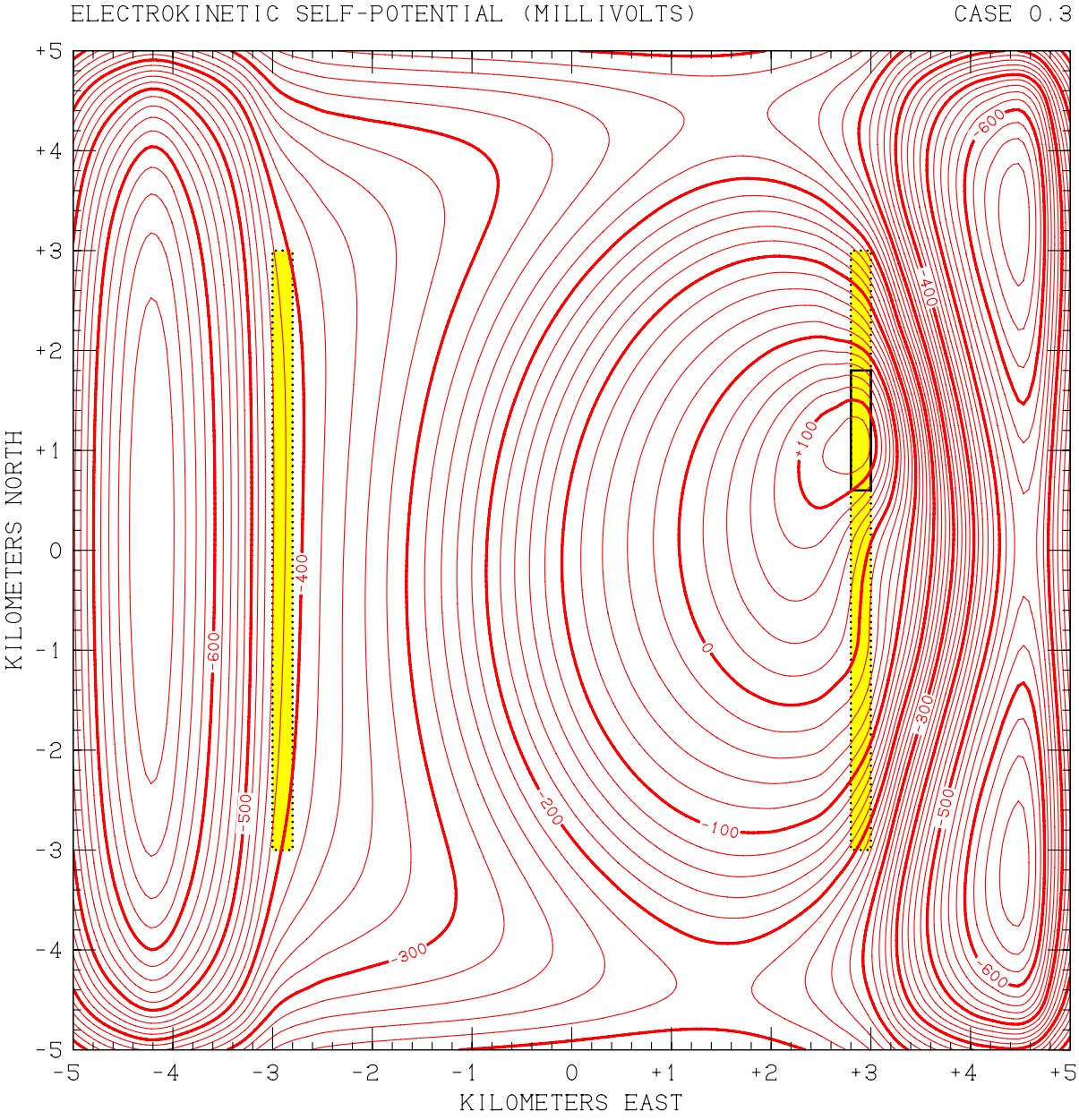

Figure 8.4. Computed results of self-potential (SP) survey of entire 100 km^2 study area for Case 0.3. Contour spacing is 20 millivolts. North-south oriented disturbances in extreme eastern and western parts of study area are of shallow topographic origin and are unrelated to the geothermal reservoir.

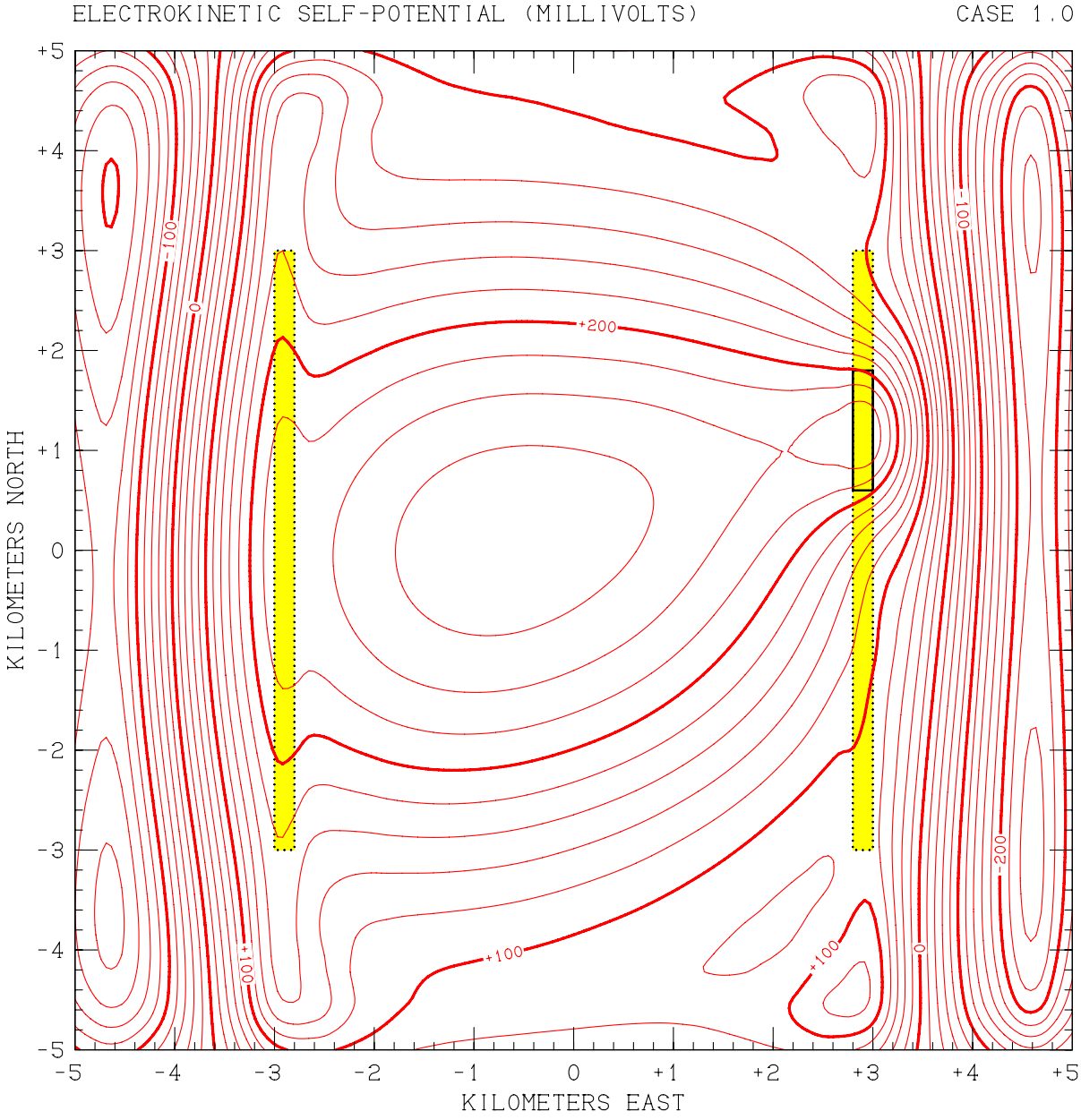

Figure 8.5. Computed results of self-potential (SP) survey of entire 100 km^2 study area for Case 1.0. Contour spacing is 20 millivolts. North-south oriented disturbances in extreme eastern and western parts of study area are of shallow topographic origin and are unrelated to the geothermal reservoir.

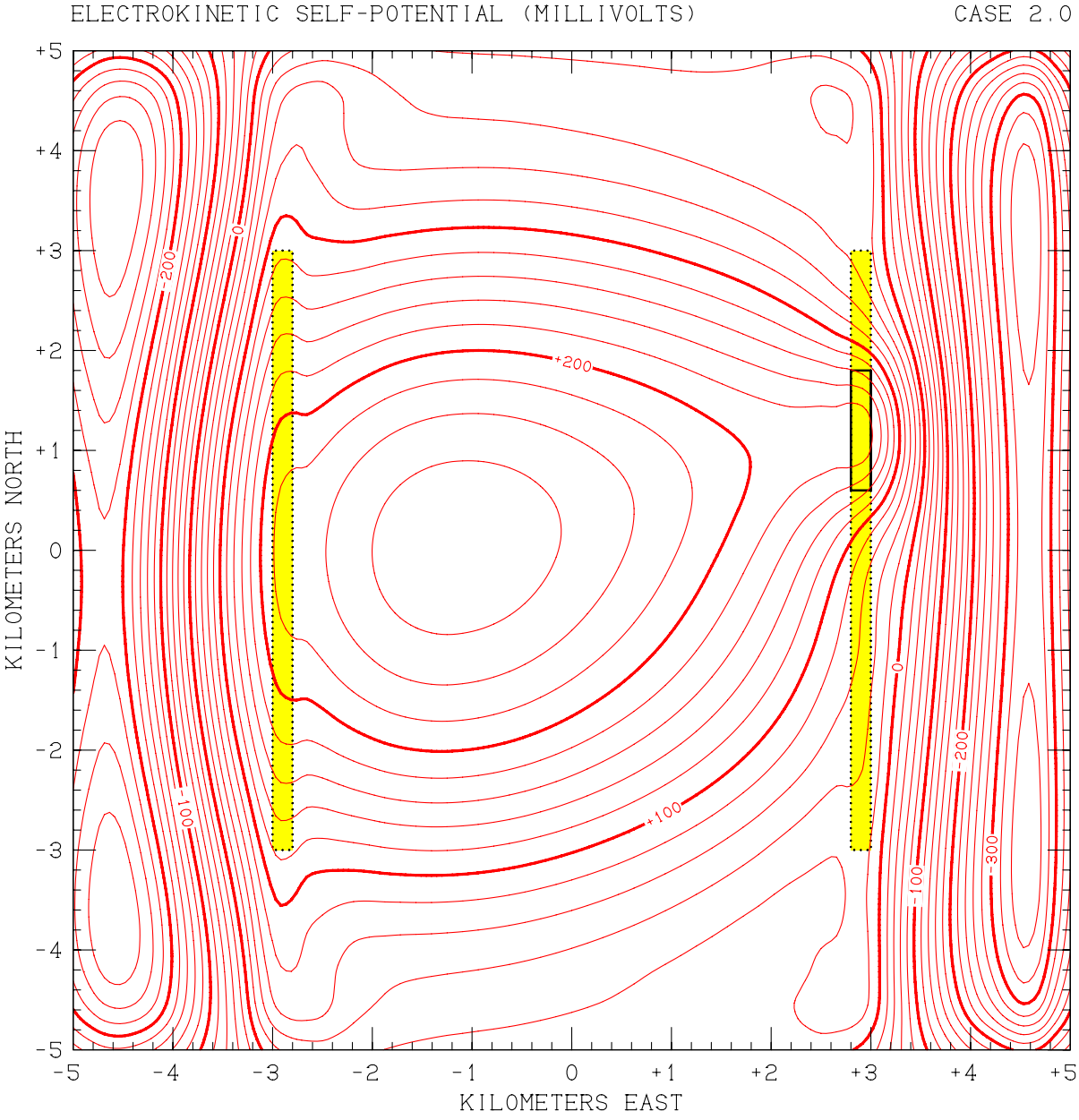

Figure 8.6. Computed results of self-potential (SP) survey of entire 100 km^2 study area for Case 2.0. Contour spacing is 20 millivolts. North-south oriented disturbances in extreme eastern and western parts of study area are of shallow topographic origin and are unrelated to the geothermal reservoir.

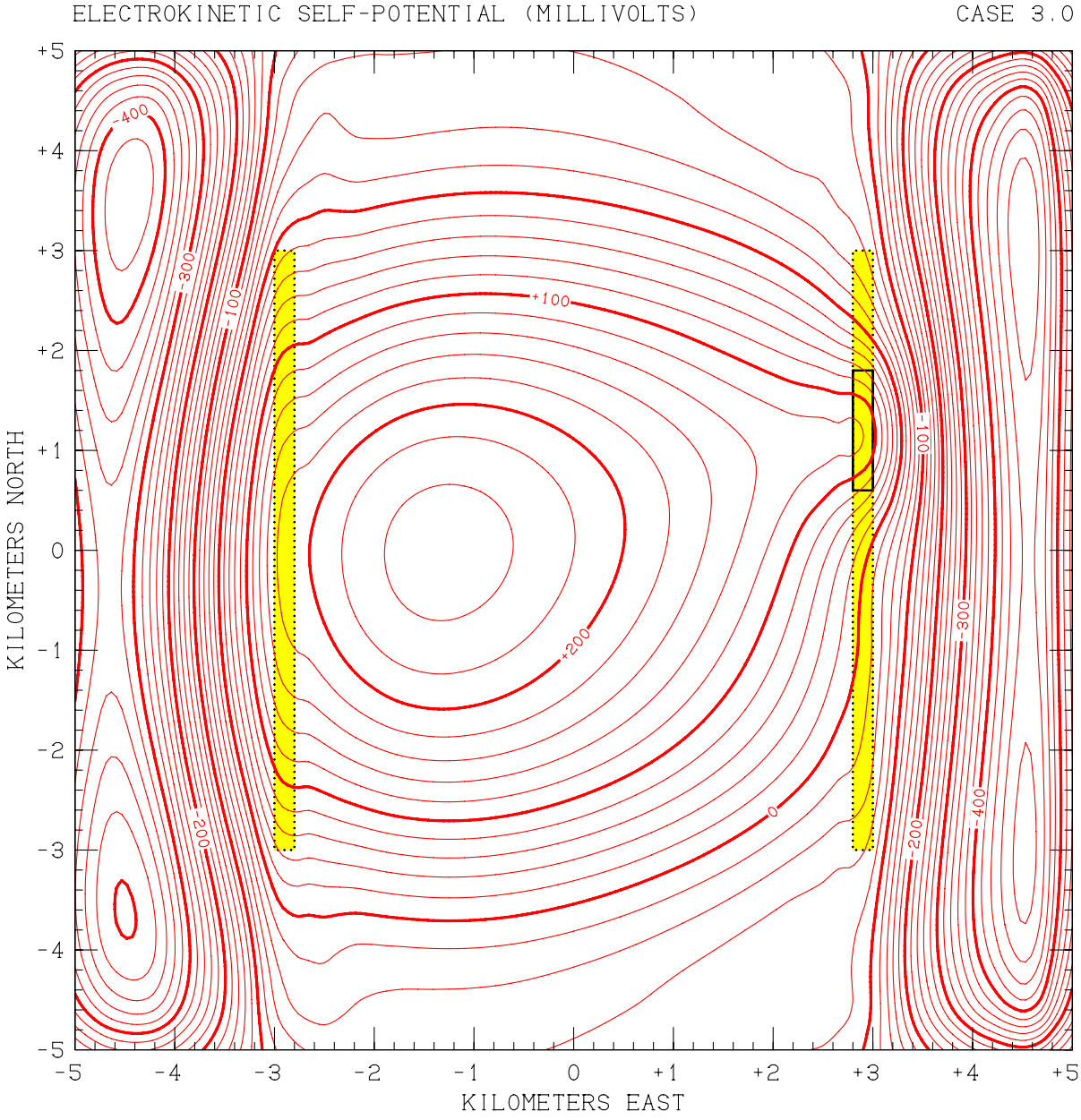

Figure 8.7. Computed results of self-potential (SP) survey of entire 100 km^2 study area for Case 3.0. Contour spacing is 20 millivolts. North-south oriented disturbances in extreme eastern and western parts of study area are of shallow topographic origin and are unrelated to the geothermal reservoir.

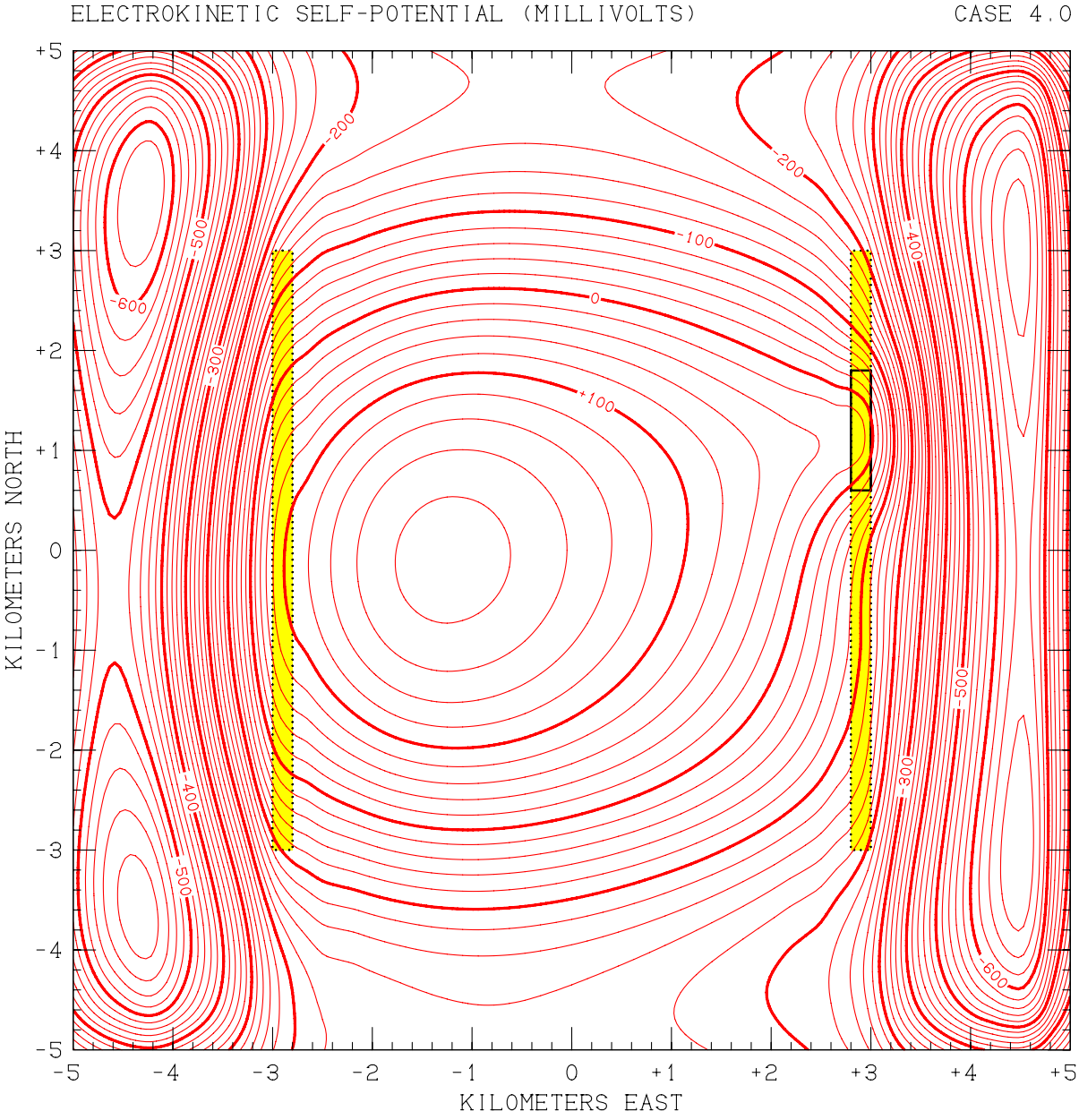

Figure 8.8. Computed results of self-potential (SP) survey of entire 100 km^2 study area for Case 4.0. Contour spacing is 20 millivolts. North-south oriented disturbances in extreme eastern and western parts of study area are of shallow topographic origin and are unrelated to the geothermal reservoir.

signals, ranging from 200 to 500 millivolts. SP signals this strong should be unmistakable in the field. Even more important, these results make it clear that SP surveying has the ability to unambiguously distinguish the "eastern reservoir" situations (Cases 0.1 – 0.3; Figures 8.2 – 8.4) from the "hidden western reservoirs" (Cases 1.0 – 4.0; Figures 8.5 – 8.8). All of the former cases exhibit strong positive SP anomalies centered on the Thermal Area and the Eastern Fault Zone. All of the "hidden reservoir" cases exhibit a completely different pattern, with a major SP maximum located in the western part of the valley, and with only a trailing "tail" extending toward the Thermal Area to the east where the spent fluids are finally discharged.

9 SUMMARY OF EFFECTIVENESS OF SURVEY TECHNIQUES

As noted in Section 2, the "Upper Aquifer" formation is the probable main production horizon for all of these hypothetical geothermal reservoir systems. Thus, all eight cases contain a central 36 km^2 area between the two rangefront faults (-3 km $\leq x \leq +3$ km, -3 km $\leq y \leq +3$ km) below which lies a 1000-meter-thick layer of permeable rock which dips downward to the west. The depth of the top of this "permeable zone" varies linearly with east-west position, from 1700 meters below the surface ($z = -1.7$ km) to the west at $x = -3$ km to 700 meters deep ($z = -0.7$ km) to the east at $x = +3$ km.

For any particular case, at any particular point within this 36 km^2 area, the computed STAR results may be integrated to obtain a "vertically-averaged" temperature value within the 1000-meter-thick permeable zone. If this is done for all (x, y) points in the plane, the total area A* (in km^2) underlain by permeable rock for which the vertically-averaged temperature exceeds a particular value T* may be found. This helps to provide a measure of the true economic value of the hypothetical reservoir under consideration, since both high temperature and high permeability are required for the efficient generation of geothermal electricity. If T* is small enough, of course, A* will be equal to the entire 36 km^2 area of the permeable region. On the other hand, if T* is sufficiently high, A* will decline to zero. Results of this type are listed in Table 9.1 for each case, for T* = 120°C, 150°C, 180°C, 210°C and 240°C.

As noted earlier, the "hidden reservoir" cases (Cases 1.0 – 4.0) have substantially greater potential for electrical power production than the others. Using the values from Table 9.1, the electrical generating capacities represented by the various cases considered may be estimated approximately subject to certain simplifying assumptions:

- All fluid production and injection occurs in the 1000-meter-thick "permeable layer", and no heat is extracted from other strata.
- The thermal "sweep efficiency" achieved by the production/injection wellfield is 35%.
- Electricity is generated by a simple binary plant that uses isobutene as the working fluid, employs recuperation, and constrains heat exchanger outlet temperature to avoid silica scaling. In reality, for the higher temperature reservoirs a flash-steam plant is likely to provide improved performance.

Table 9.1. Total surface areas underlain by permeable hot resources above various temperatures for each computed case (total permeable region area is 36 square kilometers).

	Total Surface Area with Average Permeable-Zone Temperature…				
	> 120°C	**> 150°C**	**> 180°C**	**> 210°C**	**> 240°C**
Case 0.0	1.0 km^2	--	--	--	--
Case 0.1	7.7 km^2	2.8 km^2	--	--	--
Case 0.2	11.7 km^2	5.5 km^2	2.2 km^2	--	--
Case 0.3	16.2 km^2	9.0 km^2	3.9 km^2	1.6 km^2	--
Case 1.0	29.4 km^2	17.3 km^2	4.0 km^2	--	--
Case 2.0	33.4 km^2	26.7 km^2	13.5 km^2	3.1 km^2	--
Case 3.0	35.4 km^2	32.3 km^2	23.2 km^2	10.2 km^2	2.1 km^2
Case 4.0	36.0 km^2	35.4 km^2	32.4 km^2	22.7 km^2	9.2 km^2

With these assumptions, the total amount of electrical energy obtainable in each case is:

Case 0.0:	0.4×10^{16} Joules	(5 MWe for 22 years)
Case 0.1:	4.7×10^{16} Joules	(50 MWe for 30 years)
Case 0.2:	9.5×10^{16} Joules	(100 MWe for 30 years)
Case 0.3:	14.8×10^{16} Joules	(150 MWe for 32 years)
Case 1.0:	25.3×10^{16} Joules	(250 MWe for 32 years)
Case 2.0:	42.1×10^{16} Joules	(300 MWe for 44 years)
Case 3.0:	60.0×10^{16} Joules	(300 MWe for 63 years)
Case 4.0:	82.5×10^{16} Joules	(300 MWe for 87 years)

The above values were obtained with the help of a mathematical model for the performance of such a binary geothermal power station that was reported by *Pritchett* (1998), but which was actually developed (but never published) by G. L. Mines of INEEL in Idaho Falls. These performance figures make allowances for all plant parasitic loads, *except* for the power required to operate downhole pumps in the production wells. Providing power to these pumps would be expected to reduce the net project output by 5% – 10%, except for Case 0.0. In that case, powering the downhole pumps would probably consume most or all of the electrical capacity of the plant.

The issue of present interest is to evaluate how well each of the various survey techniques examined in the preceding sections (shallow heat flow surveys, DC resistivity surveys, MT surveys and SP surveys) are likely to perform locating good drilling targets for a deep "discovery well". As noted previously (see Figure 5.10), simply drilling in the middle of the "Thermal Area" where geothermal fluids discharge to the surface will produce satisfactory results for Cases 0.0 – 0.3, but will fail utterly to find the reservoir for Cases

1.0 – 4.0. Figures 9.1 – 9.32 show, for each of the eight cases, how well the *"bull's-eye"* suggested by each of these four survey techniques is correlated with the actual subsurface hot permeable resource, as categorized by the T* "bins" of Table 9.1.

The 300-meter heat flow holes are essentially useless for finding the "hidden" reservoirs. Clearly, the best results are obtained from the SP and MT surveys, with DC resistivity a close third. It is concluded that the best way to find "hidden" basin and range geothermal resources of this general type is to carry out simultaneous SP and low-frequency MT surveys, and then to combine the results of both surveys with other pertinent information using mathematical "inversion" techniques to characterize the subsurface quantitatively. Many such surveys and accompanying analyses can be carried out for the cost of a single unsuccessful deep "discovery well".

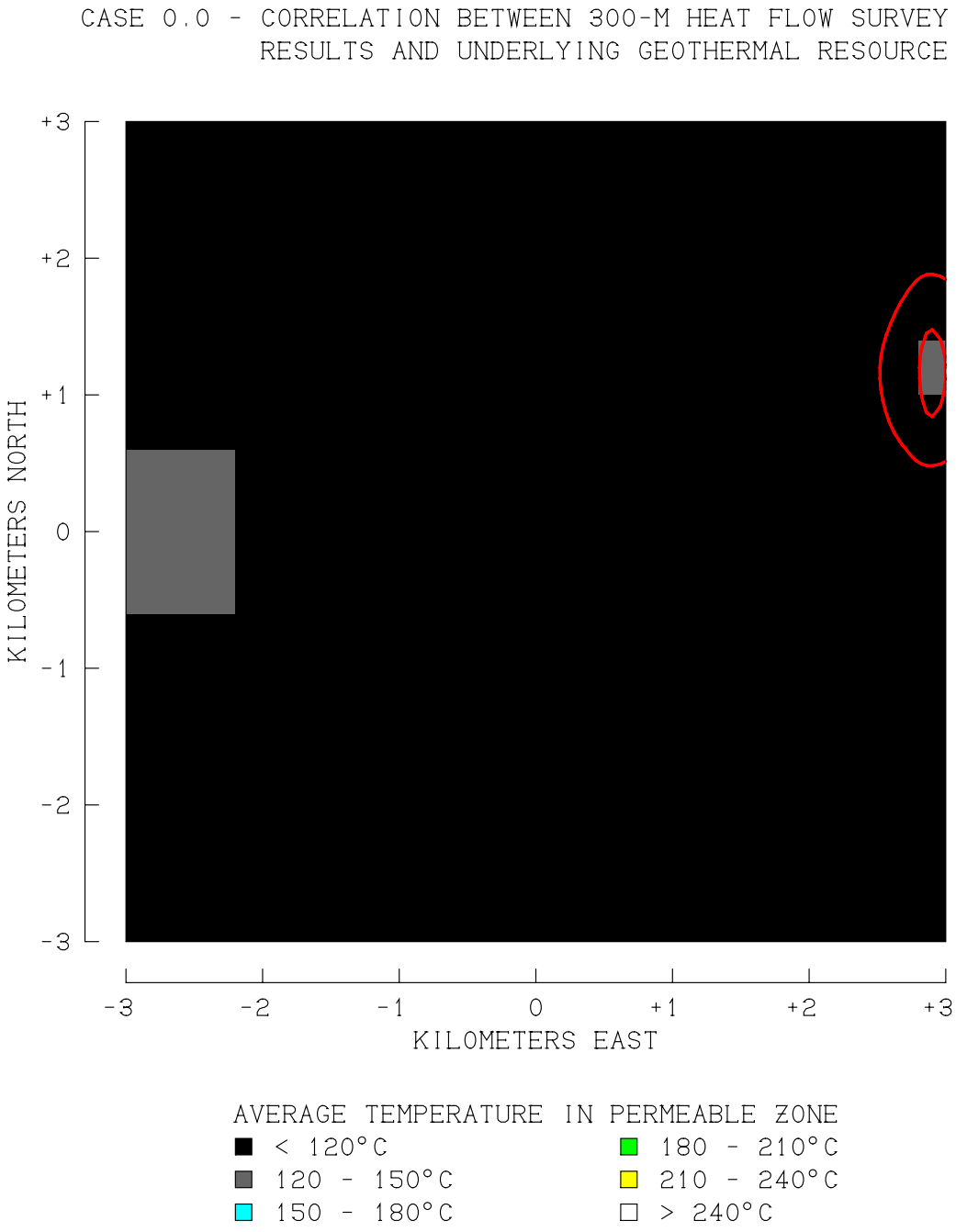

Figure 9.1 Spatial correlation between the results of a 300-meter slimhole heat flow survey of the central 36 km^2 of the study area and the location of the underlying subsurface geothermal resource, for Case 0.0.

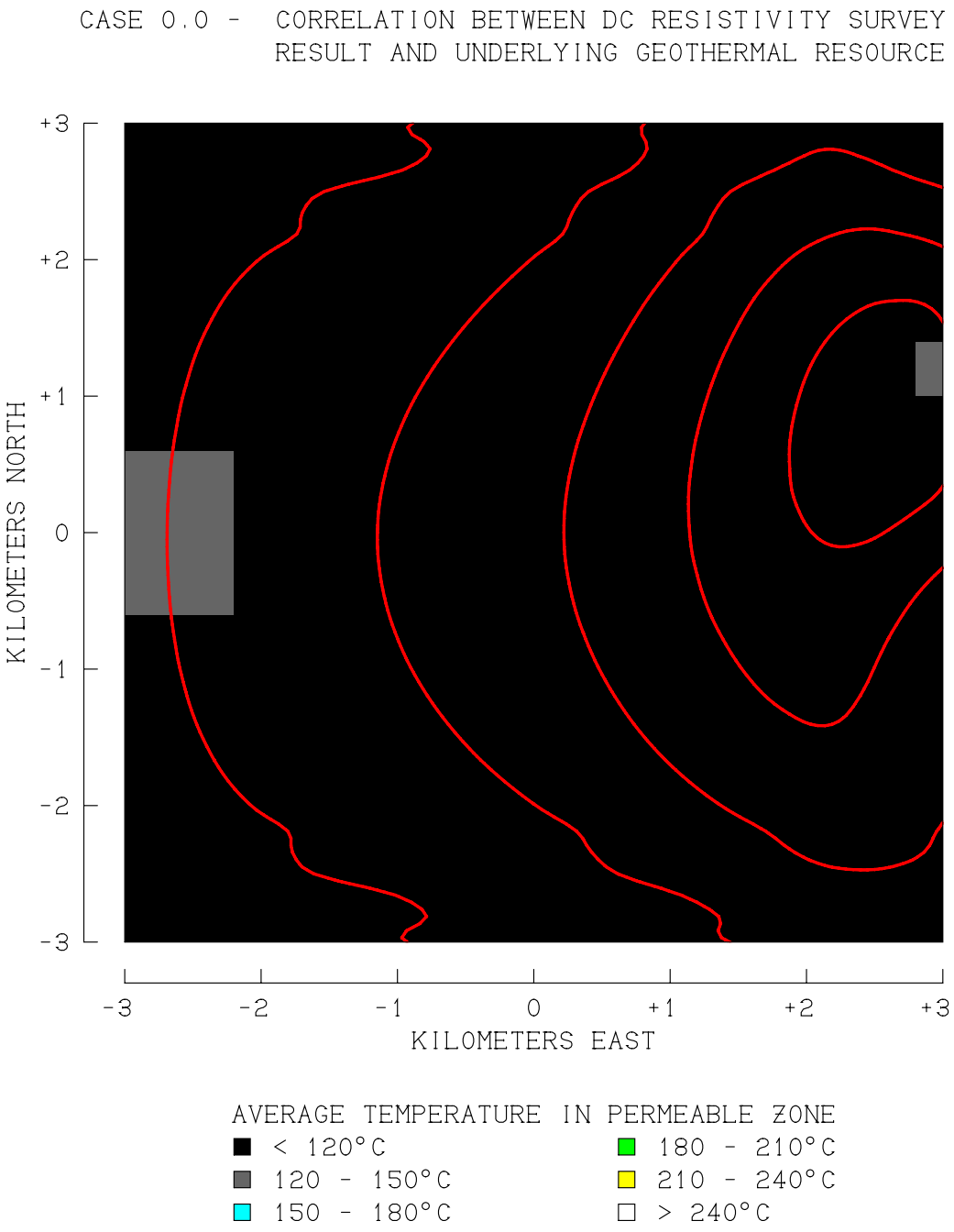

Figure 9.2. Spatial correlation between the results of a Wenner DC resistivity survey (2000 m electrode spacing) of the central 36 km^2 of the study area and the location of the underlying subsurface geothermal resource, for Case 0.0.

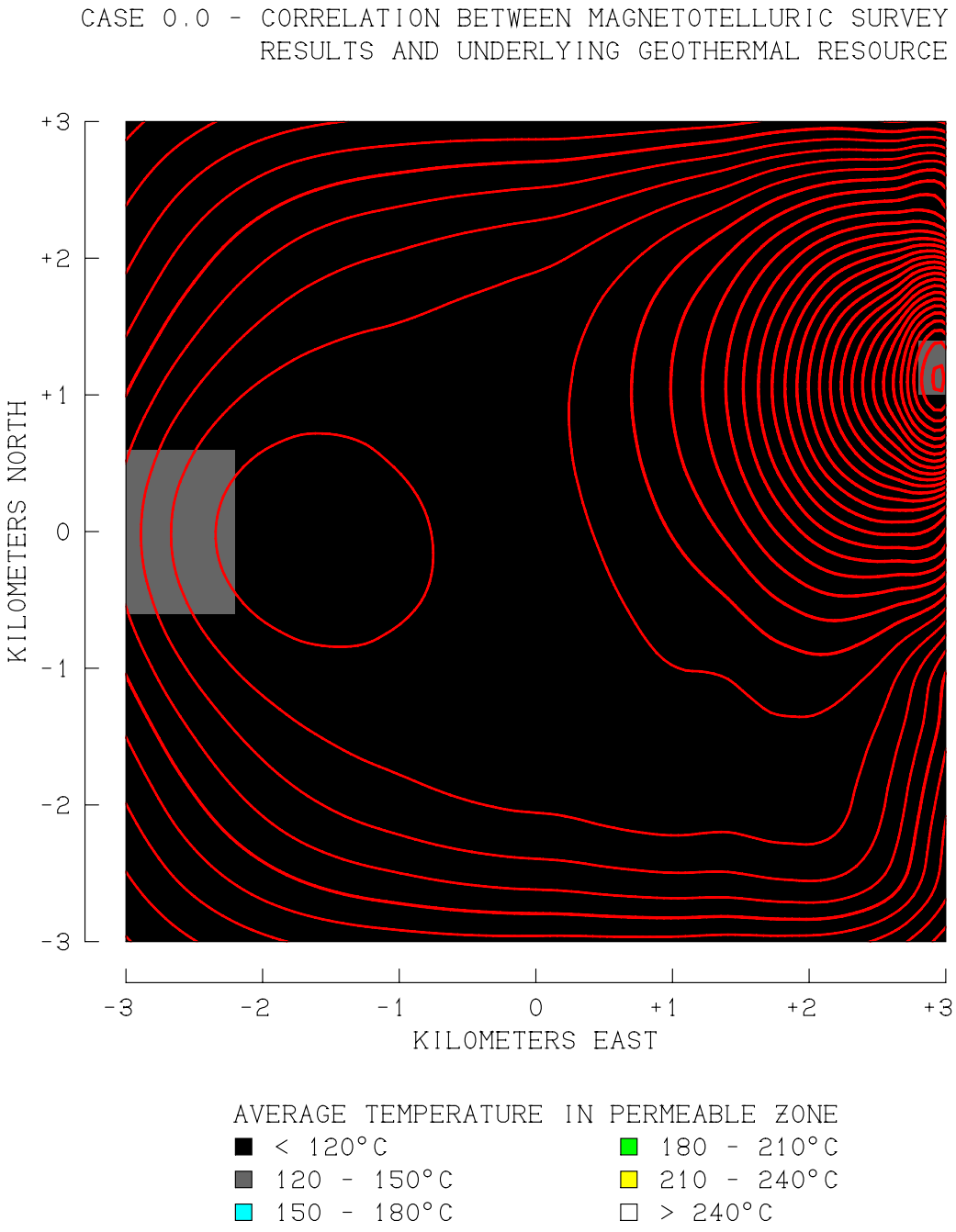

Figure 9.3. Spatial correlation between the results of a magnetotelluric (MT) resistivity survey (0.1 Hz frequency) of the central 36 km^2 of the study area and the location of the underlying subsurface geothermal resource, for Case 0.0.

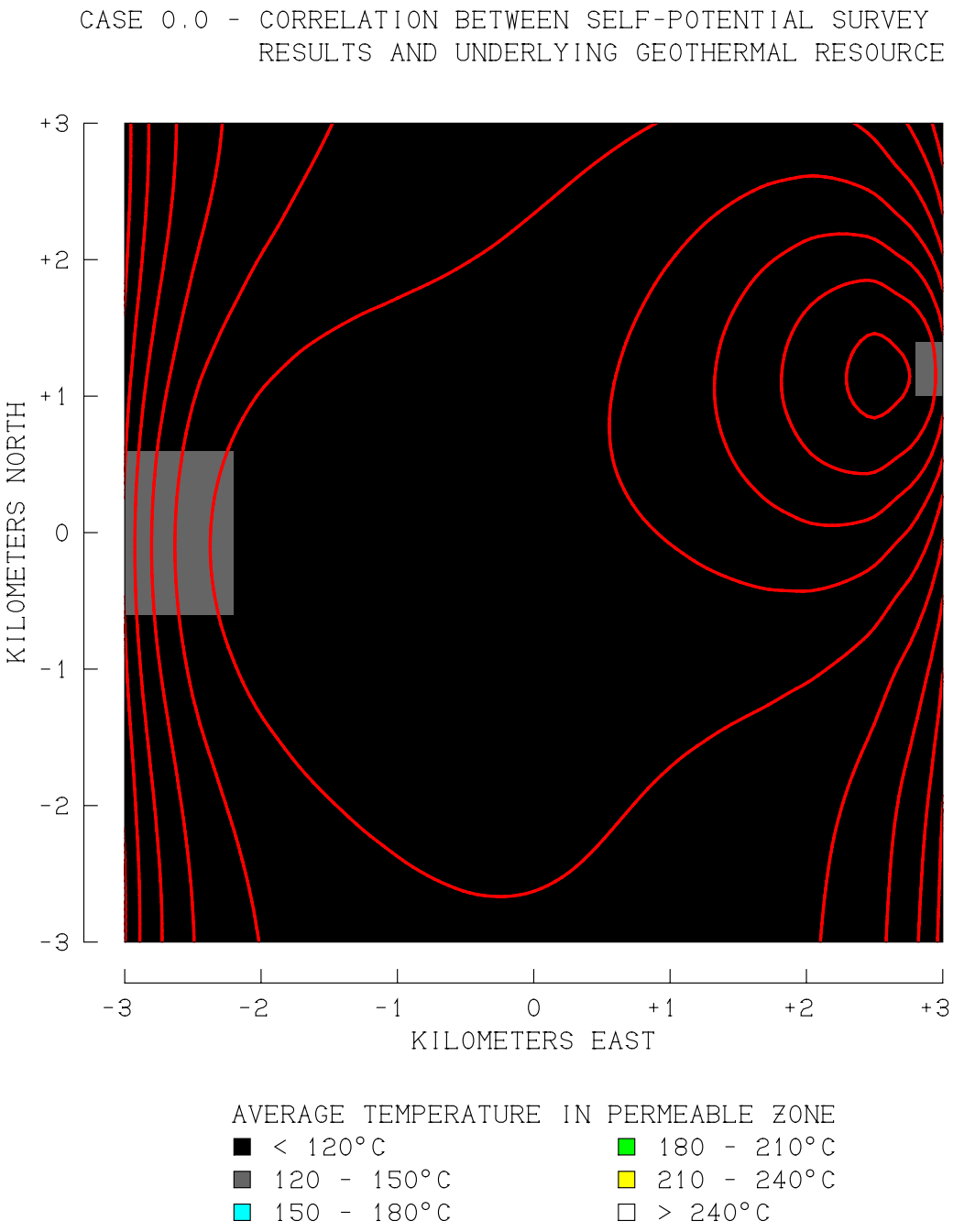

Figure 9.4. Spatial correlation between the results of a self-potential (SP) survey of the central 36 km^2 of the study area and the location of the underlying subsurface geothermal resource, for Case 0.0.

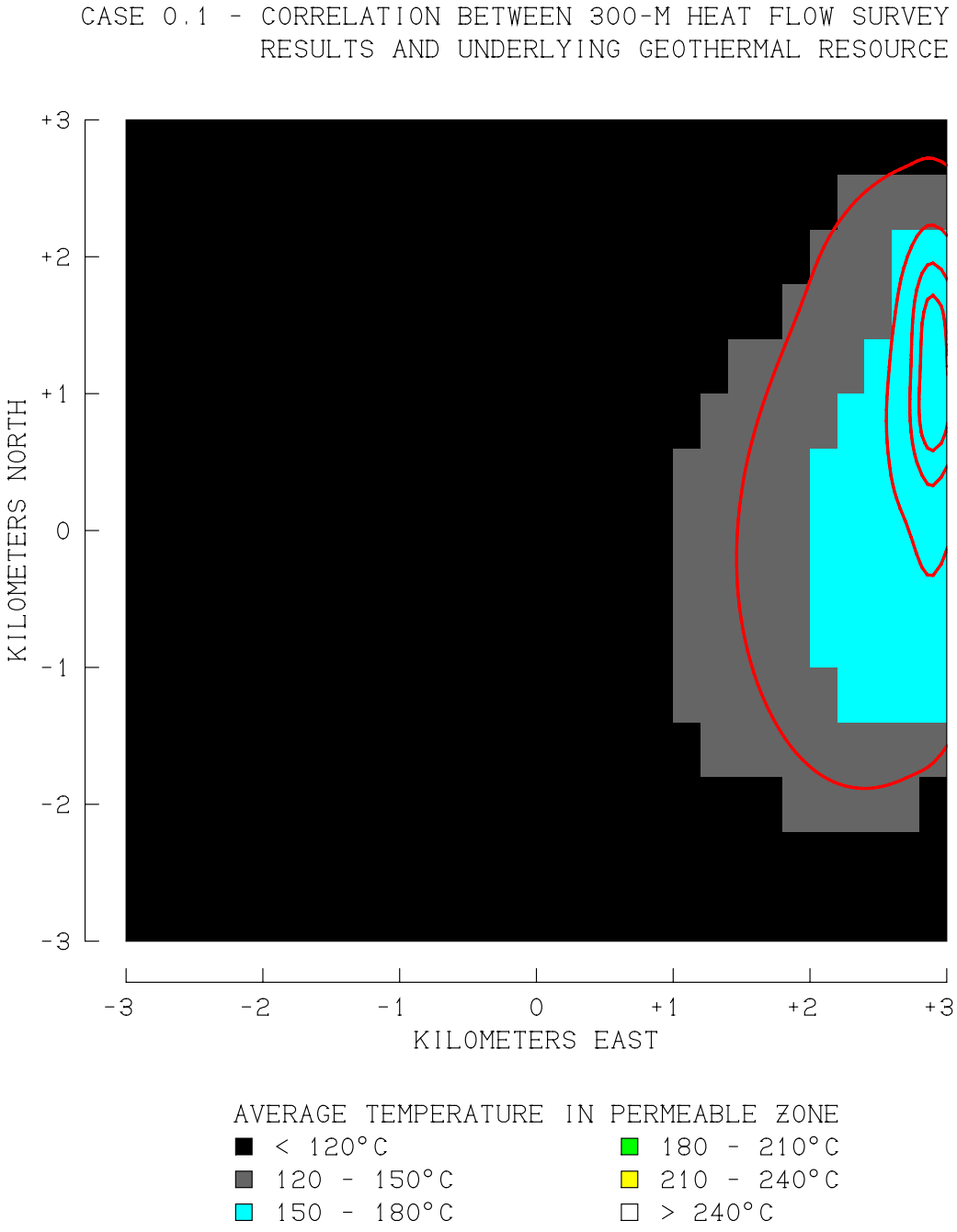

Figure 9.5. Spatial correlation between the results of a 300-meter slimhole heat flow survey of the central 36 km^2 of the study area and the location of the underlying subsurface geothermal resource, for Case 0.1.

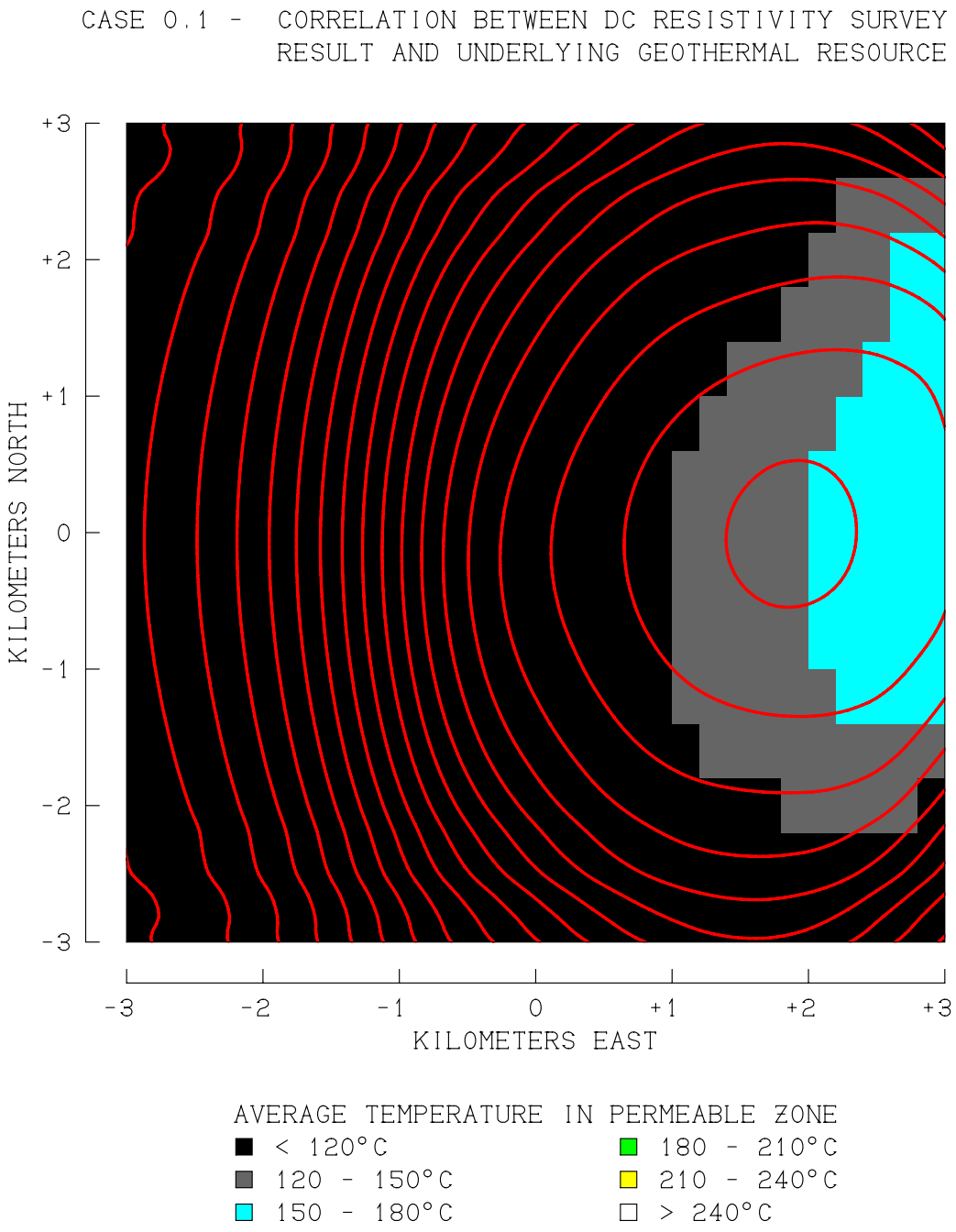

Figure 9.6. Spatial correlation between the results of a Wenner DC resistivity survey (2000 m electrode spacing) of the central 36 km^2 of the study area and the location of the underlying subsurface geothermal resource, for Case 0.1.

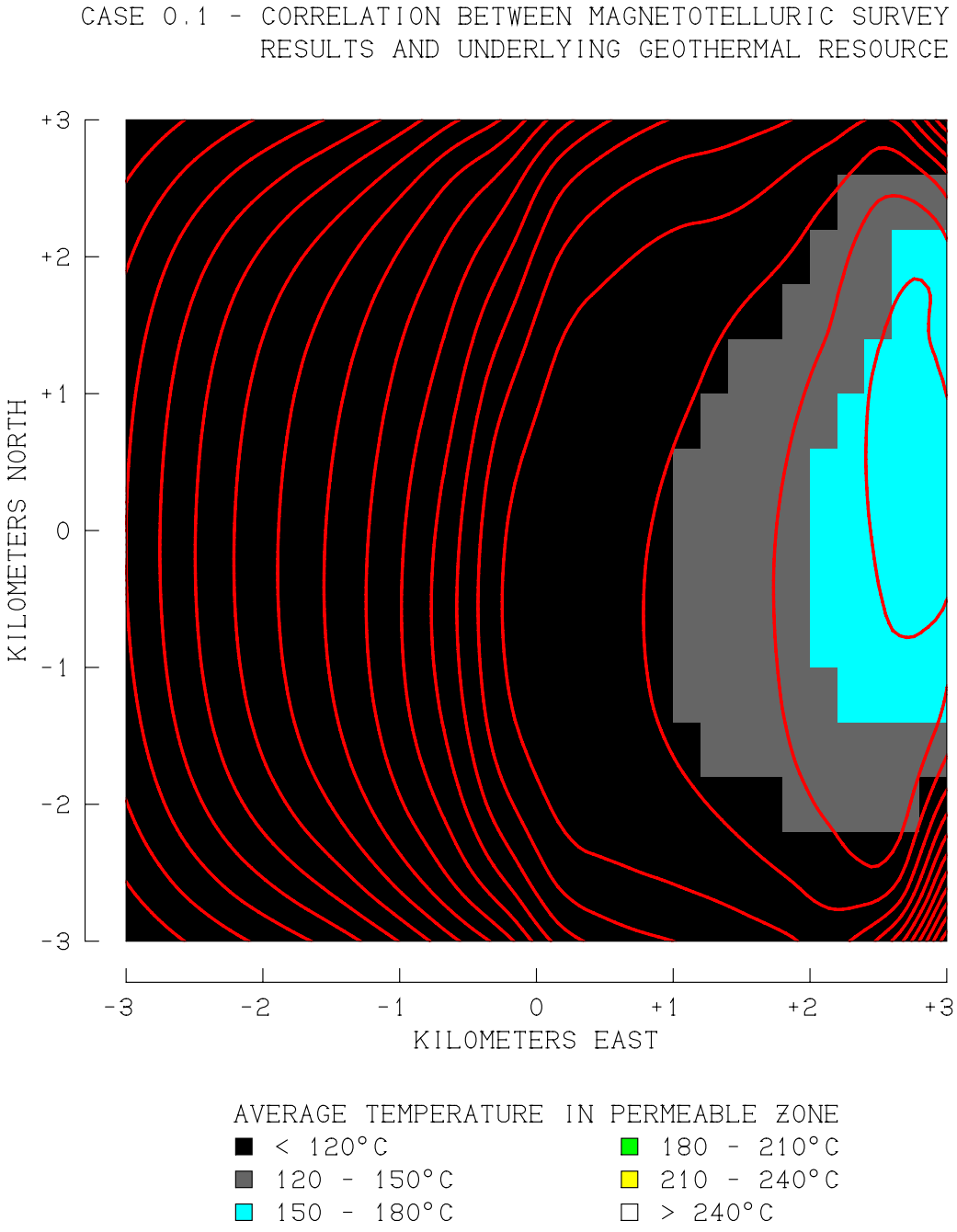

Figure 9.7. Spatial correlation between the results of a magnetotelluric (MT) resistivity survey (0.1 Hz frequency) of the central 36 km^2 of the study area and the location of the underlying subsurface geothermal resource, for Case 0.1.

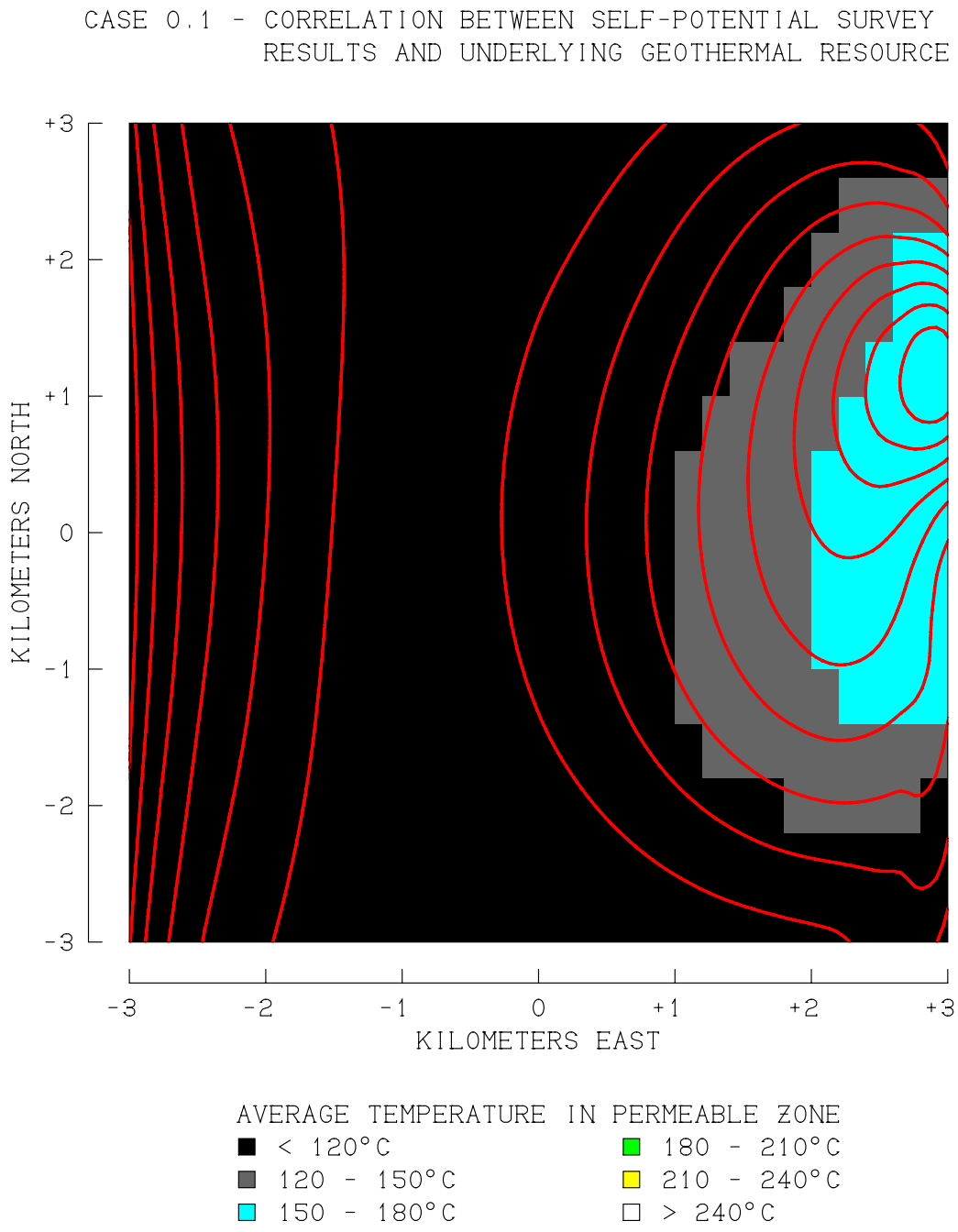

Figure 9.8. Spatial correlation between the results of a self-potential (SP) survey of the central 36 km^2 of the study area and the location of the underlying subsurface geothermal resource, for Case 0.1.

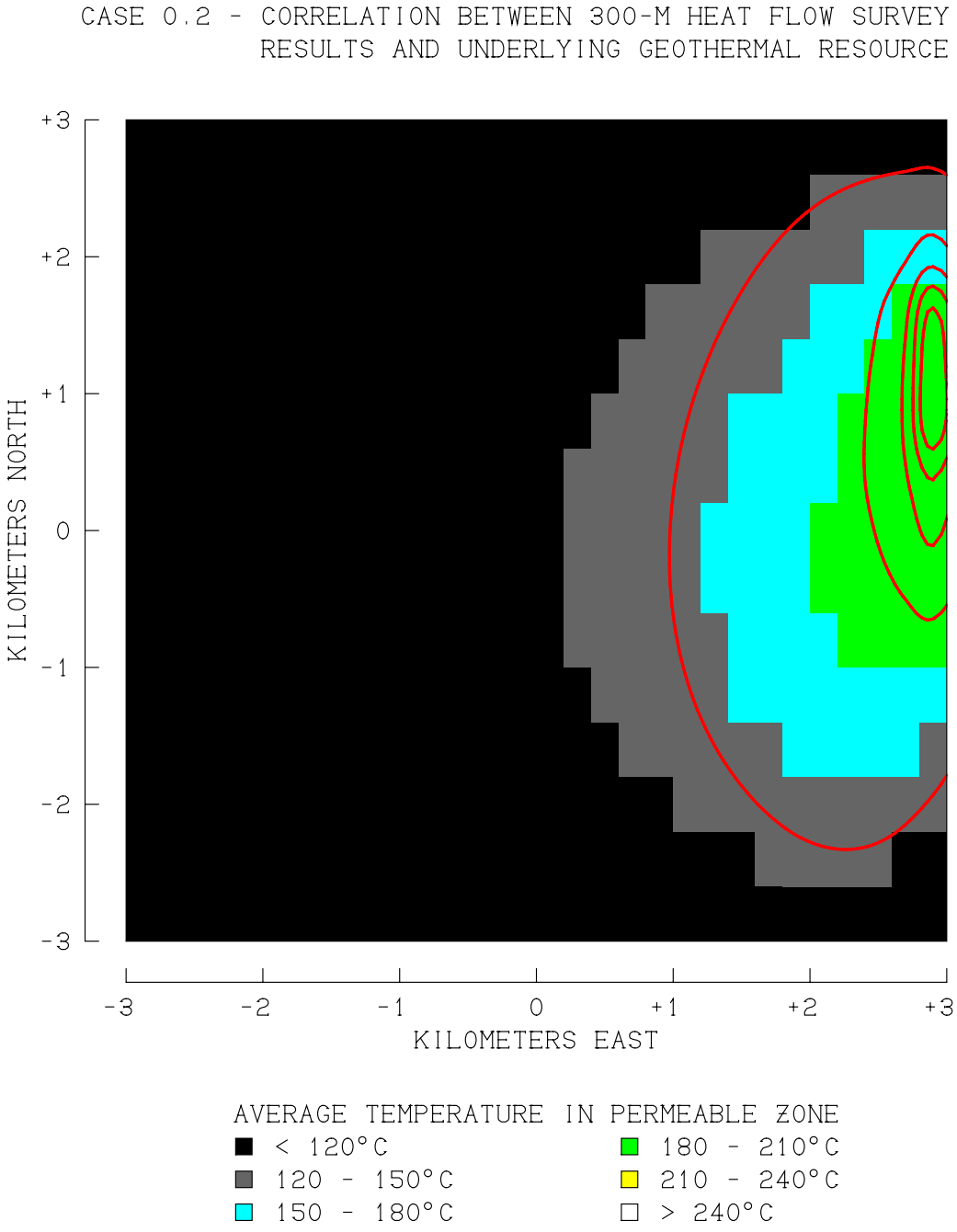

Figure 9.9. Spatial correlation between the results of a 300-meter slimhole heat flow survey of the central 36 km^2 of the study area and the location of the underlying subsurface geothermal resource, for Case 0.2.

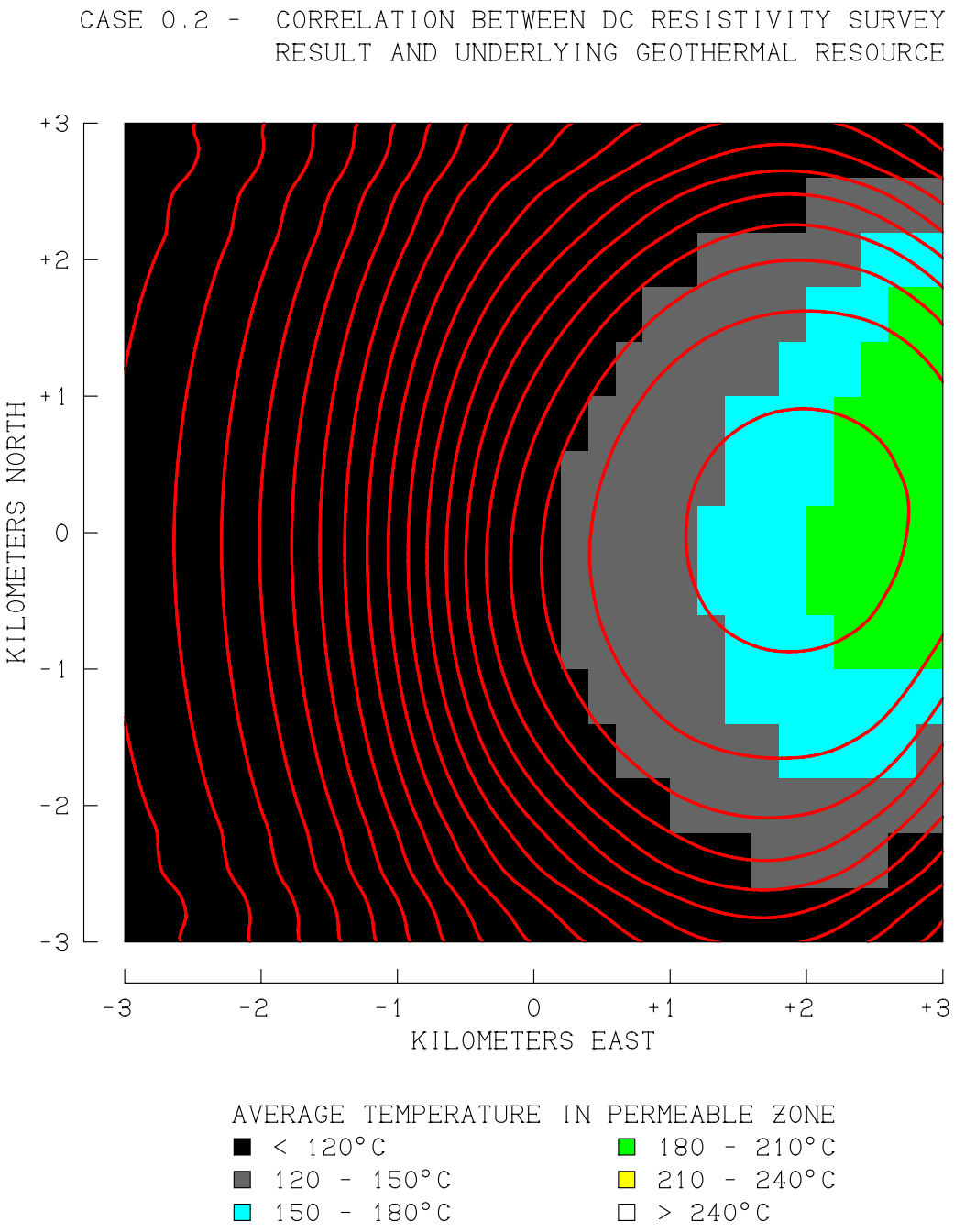

Figure 9.10. Spatial correlation between the results of a Wenner DC resistivity survey (2000 m electrode spacing) of the central 36 km^2 of the study area and the location of the underlying subsurface geothermal resource, for Case 0.2.

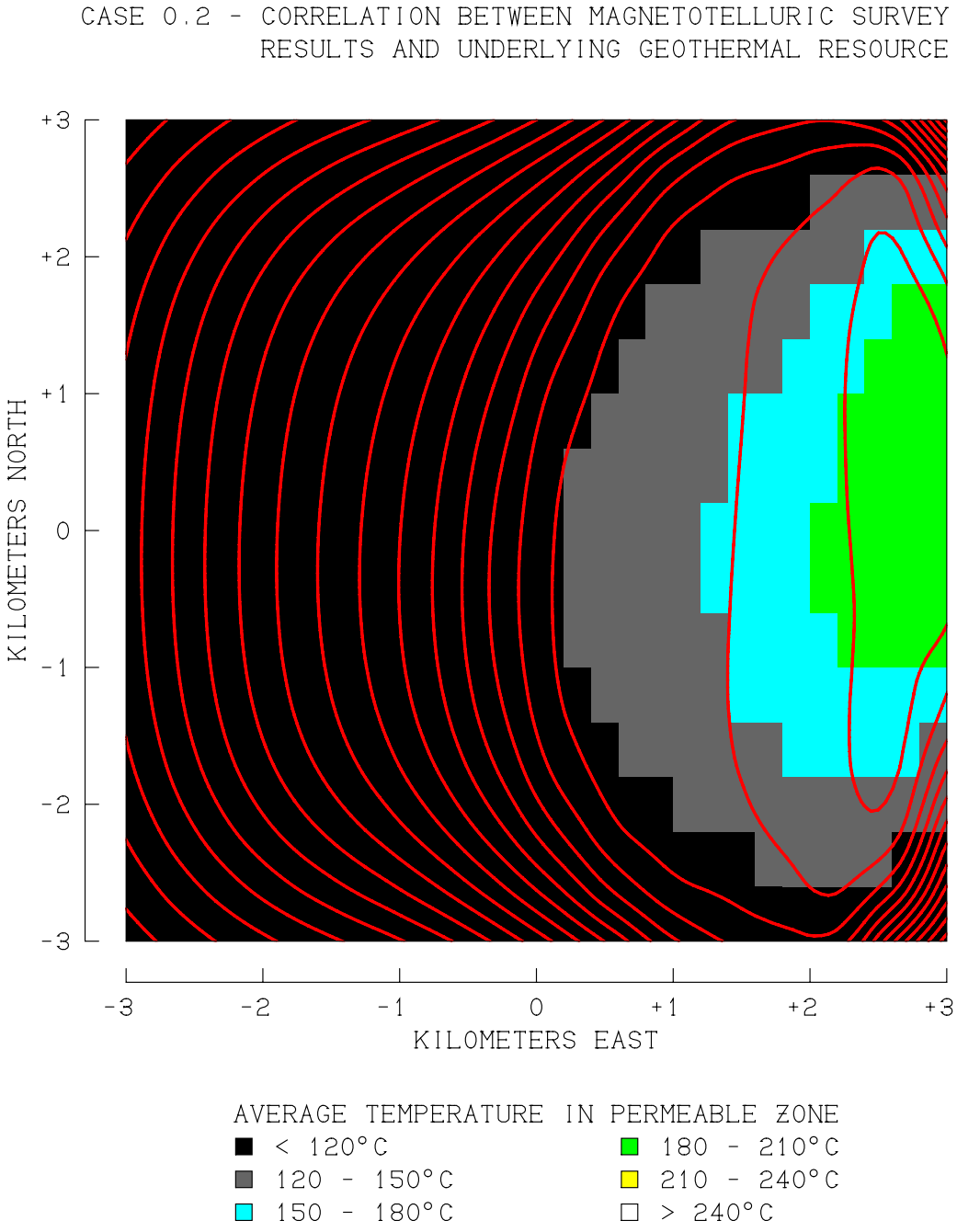

Figure 9.11. Spatial correlation between the results of a magnetotelluric (MT) resistivity survey (0.1 Hz frequency) of the central 36 km^2 of the study area and the location of the underlying subsurface geothermal resource, for Case 0.2.

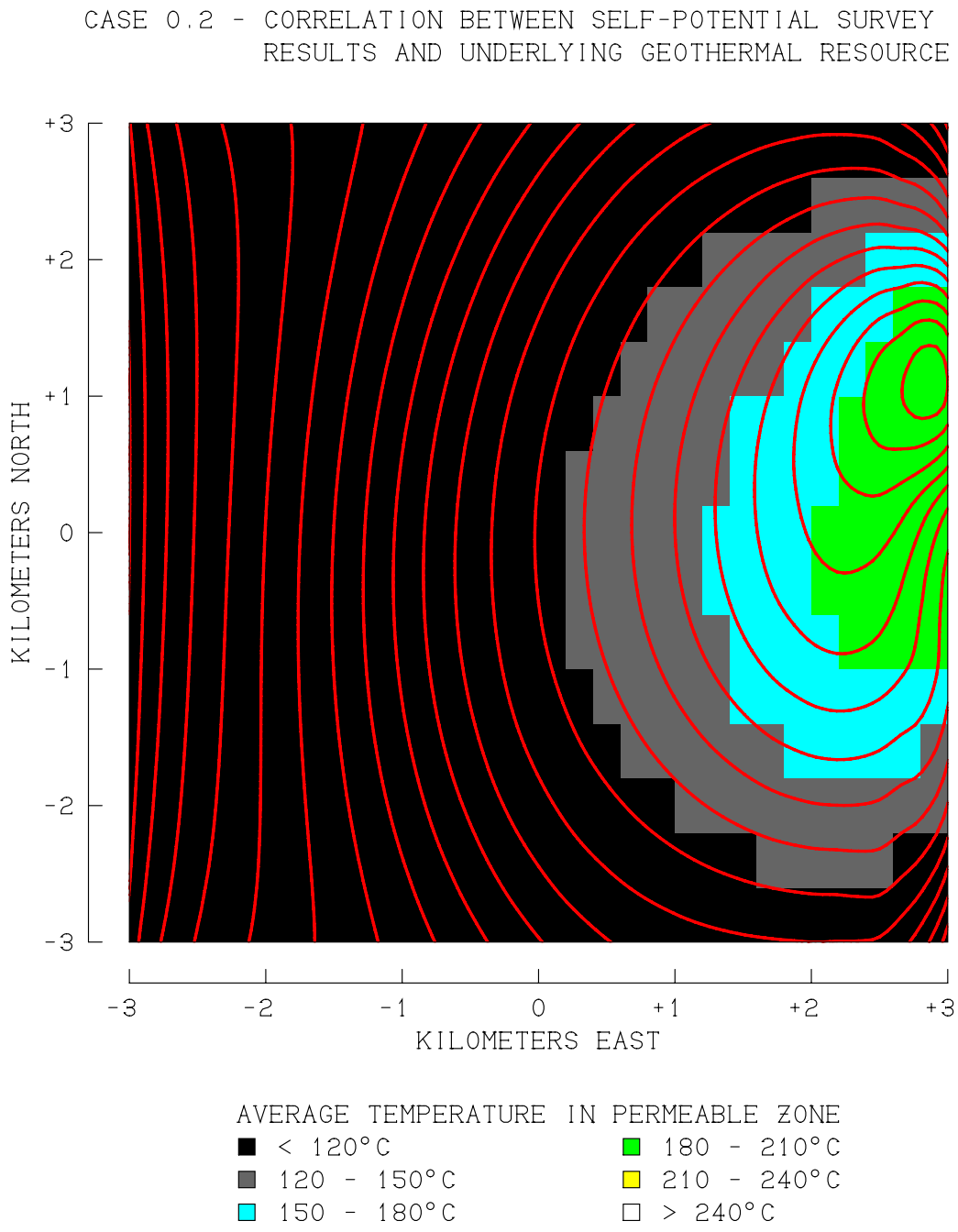

Figure 9.12. Spatial correlation between the results of a self-potential (SP) survey of the central 36 km^2 of the study area and the location of the underlying subsurface geothermal resource, for Case 0.2.

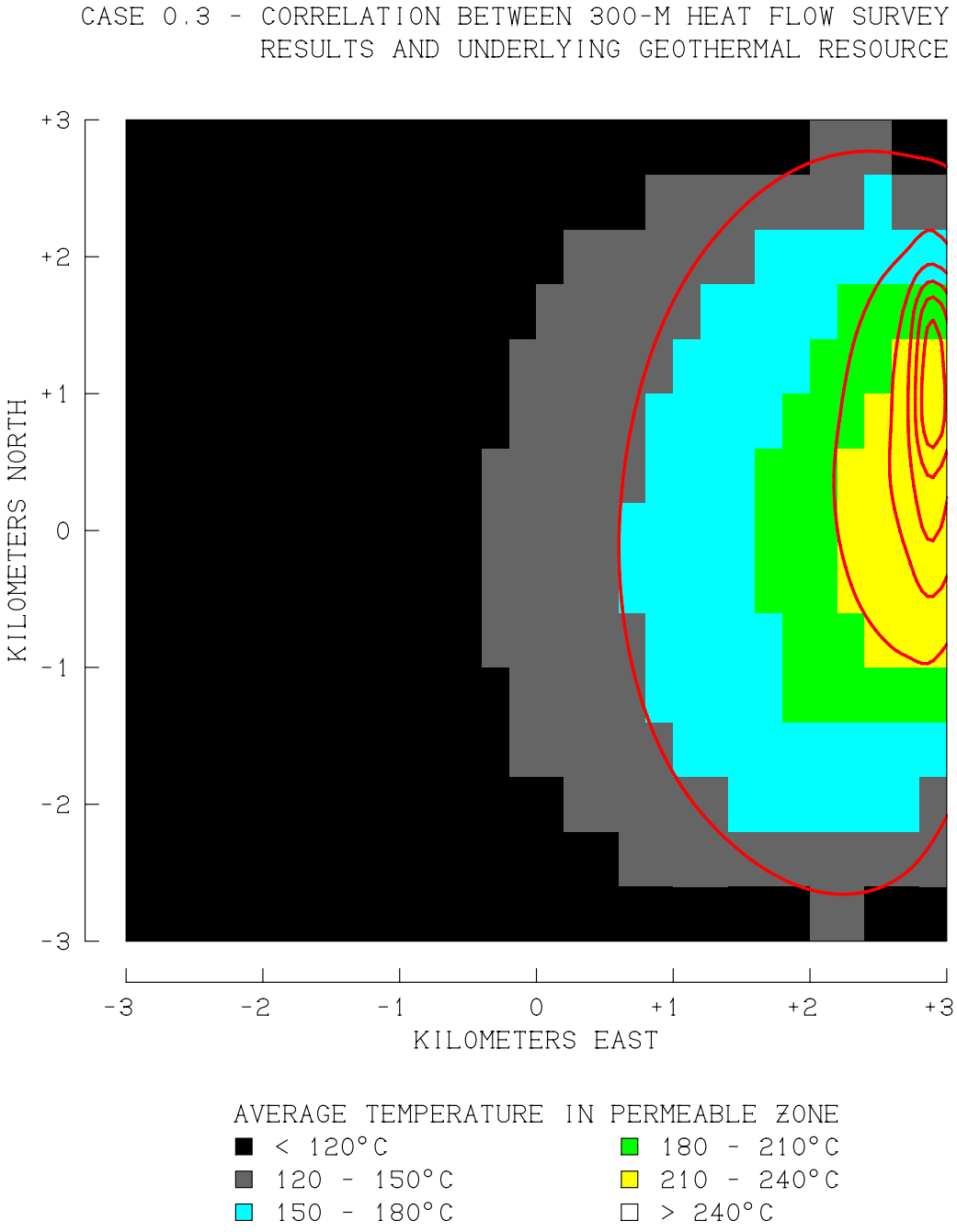

Figure 9.13. Spatial correlation between the results of a 300-meter slimhole heat flow survey of the central 36 km^2 of the study area and the location of the underlying subsurface geothermal resource, for Case 0.3.

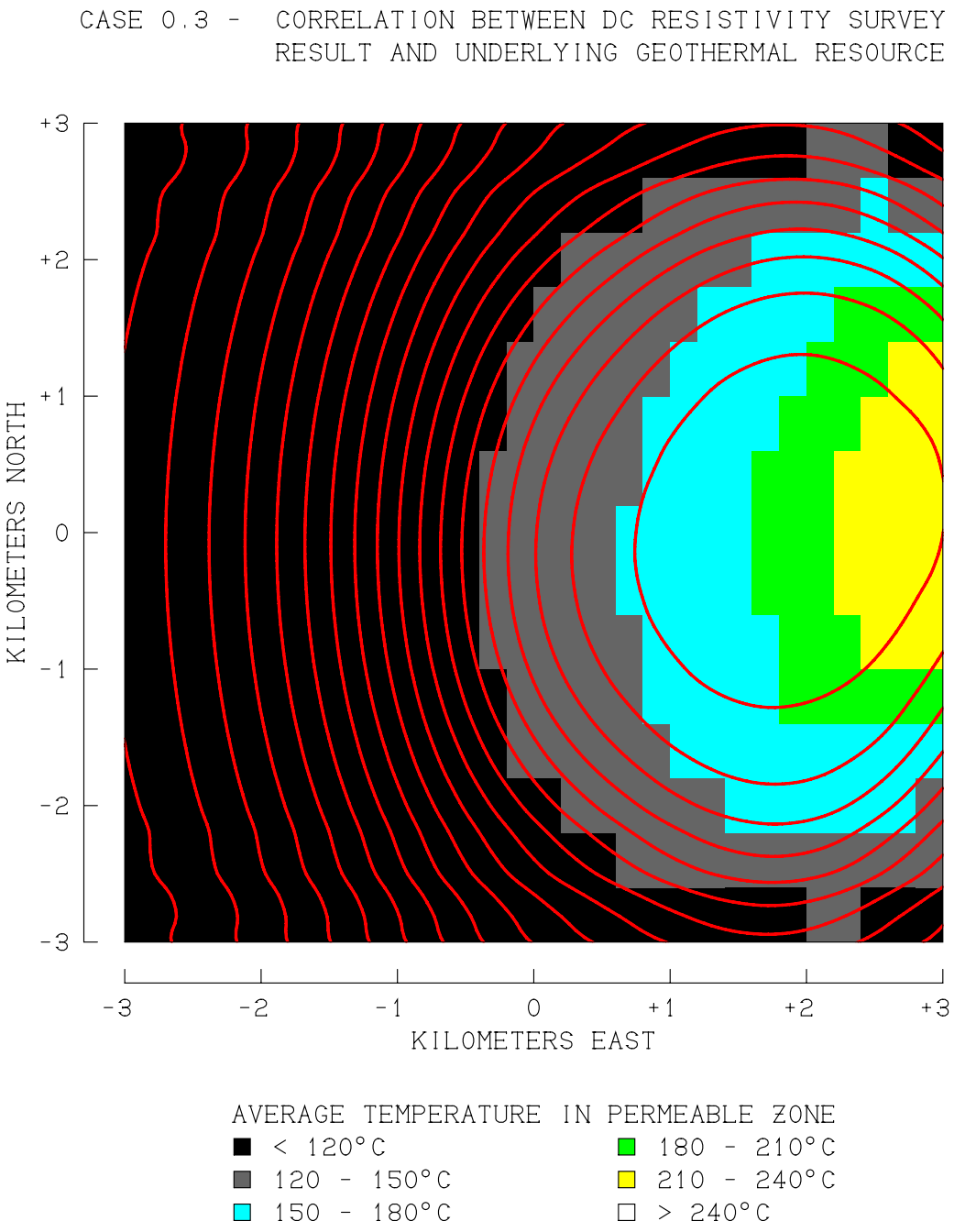

Figure 9.14. Spatial correlation between the results of a Wenner DC resistivity survey (2000 m electrode spacing) of the central 36 km^2 of the study area and the location of the underlying subsurface geothermal resource, for Case 0.3.

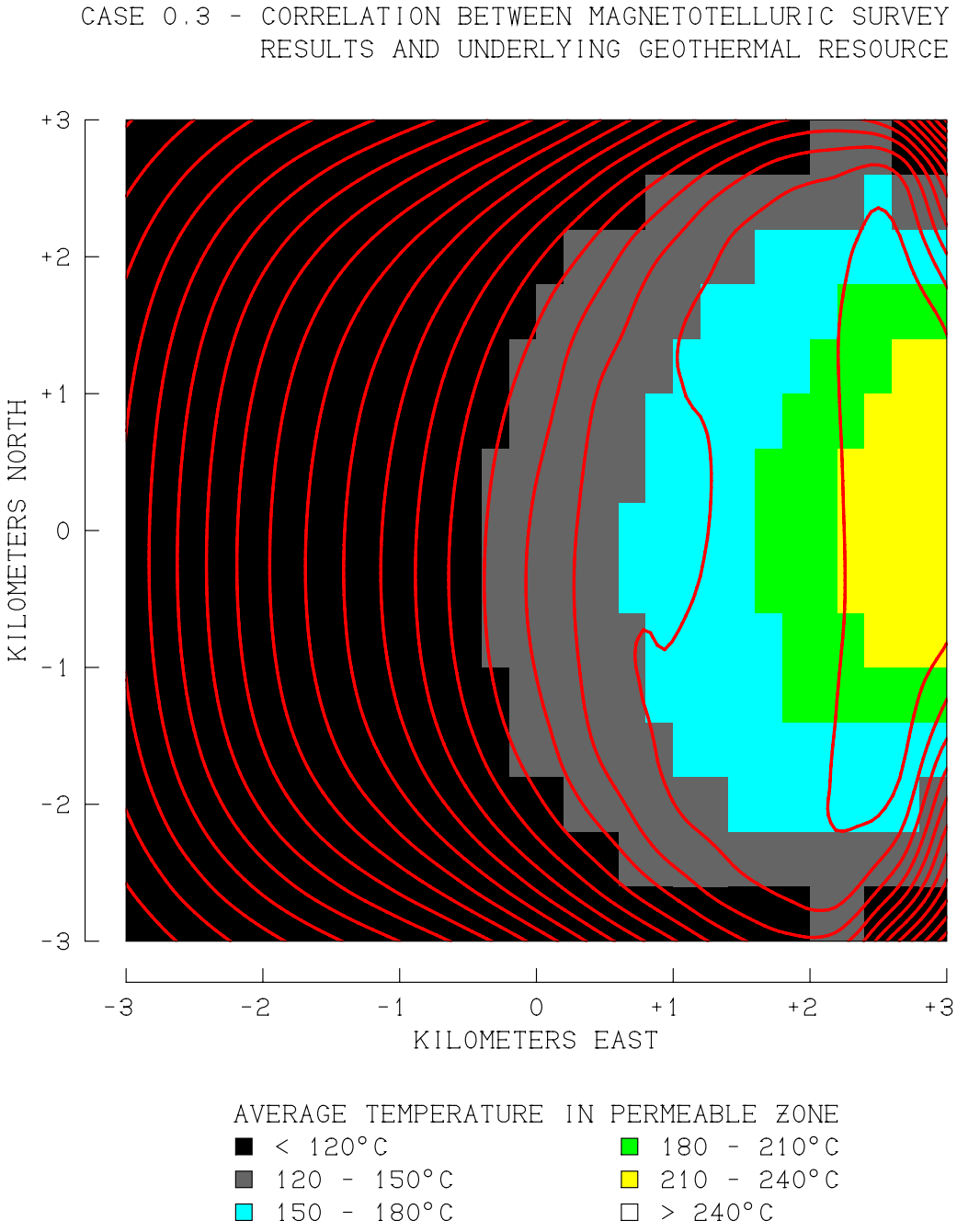

Figure 9.15. Spatial correlation between the results of a magnetotelluric (MT) resistivity survey (0.1 Hz frequency) of the central 36 km^2 of the study area and the location of the underlying subsurface geothermal resource, for Case 0.3.

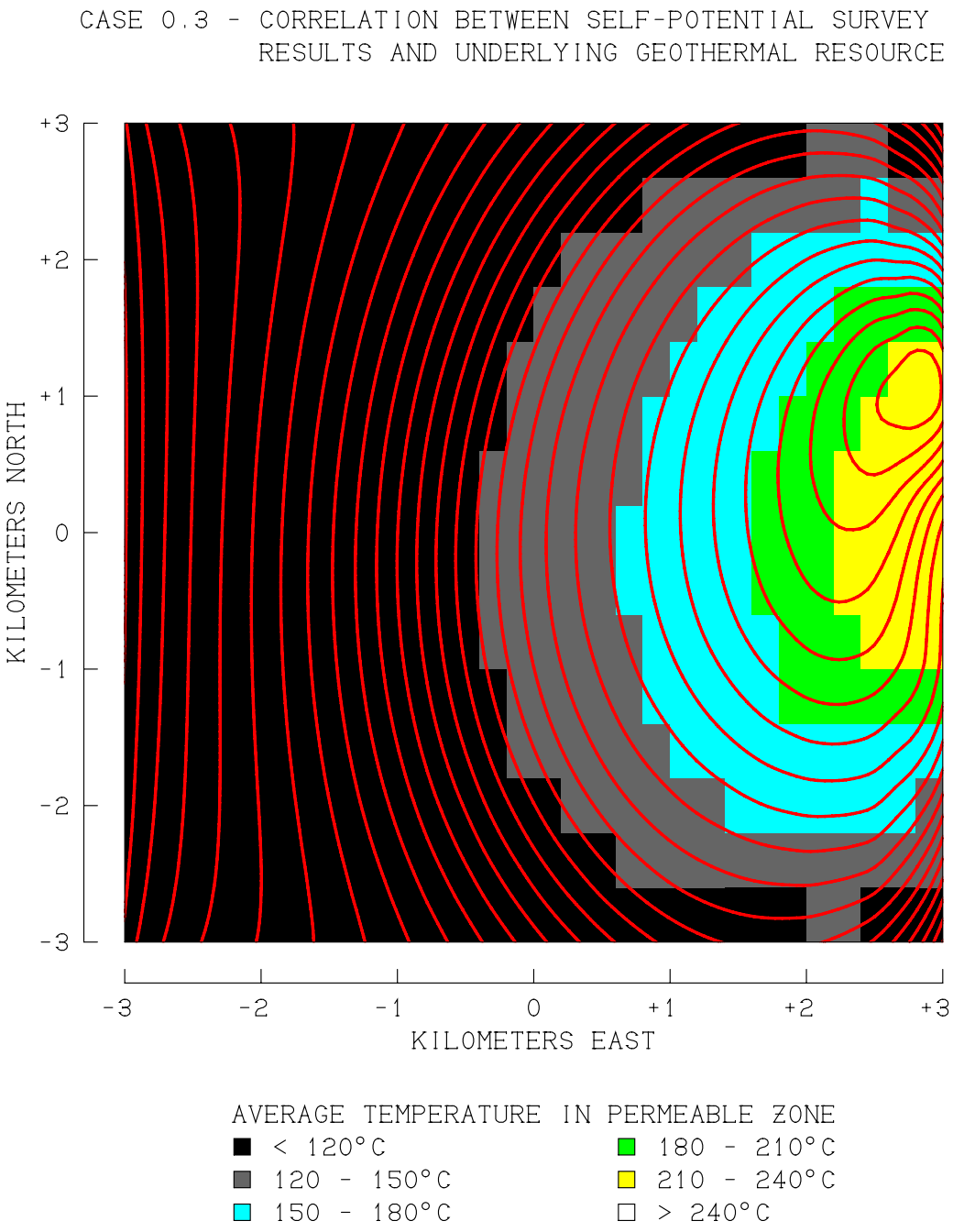

Figure 9.16. Spatial correlation between the results of a self-potential (SP) survey of the central 36 km^2 of the study area and the location of the underlying subsurface geothermal resource, for Case 0.3.

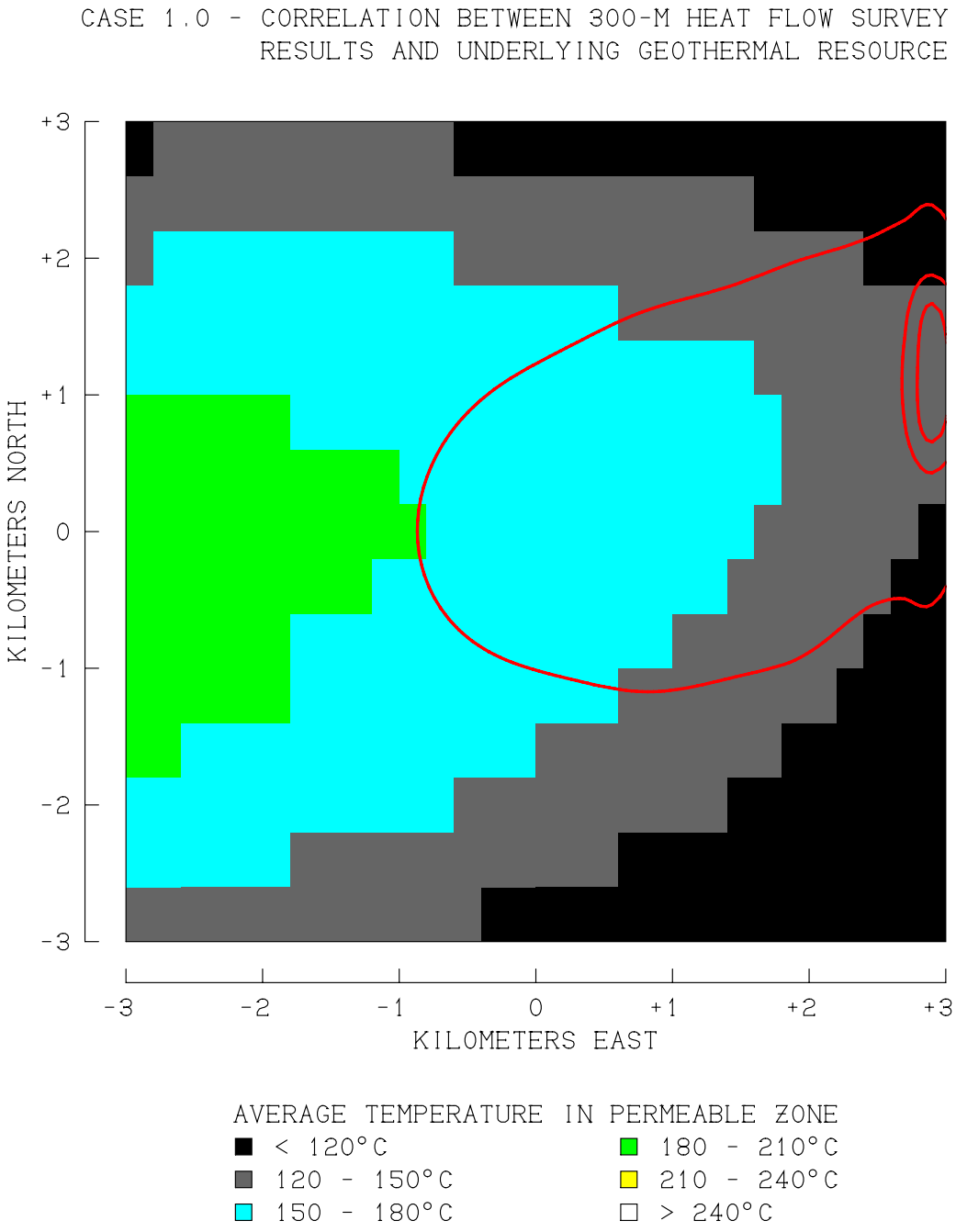

Figure 9.17. Spatial correlation between the results of a 300-meter slimhole heat flow survey of the central 36 km^2 of the study area and the location of the underlying subsurface geothermal resource, for Case 1.0.

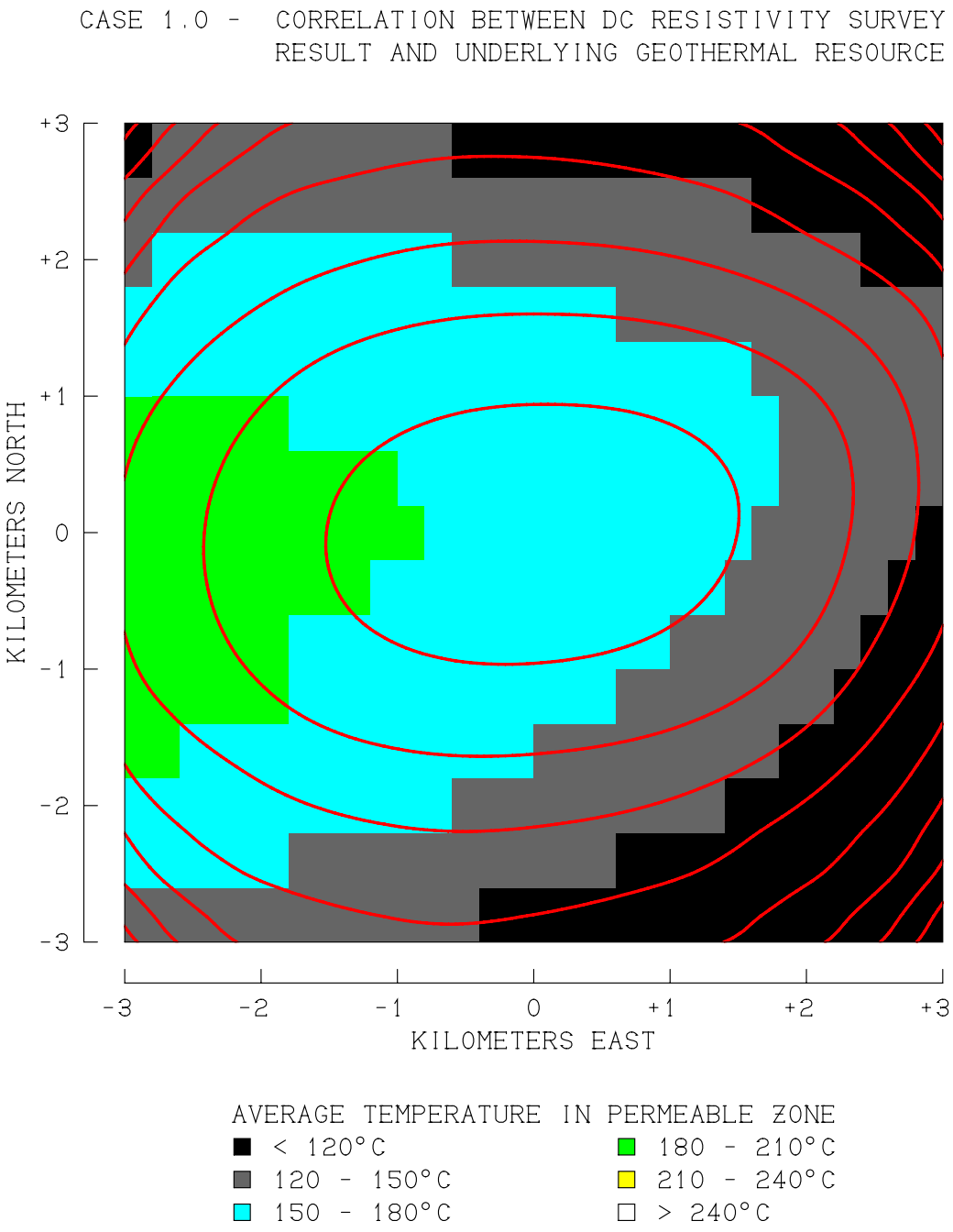

Figure 9.18. Spatial correlation between the results of a Wenner DC resistivity survey (2000 m electrode spacing) of the central 36 km^2 of the study area and the location of the underlying subsurface geothermal resource, for Case 1.0.

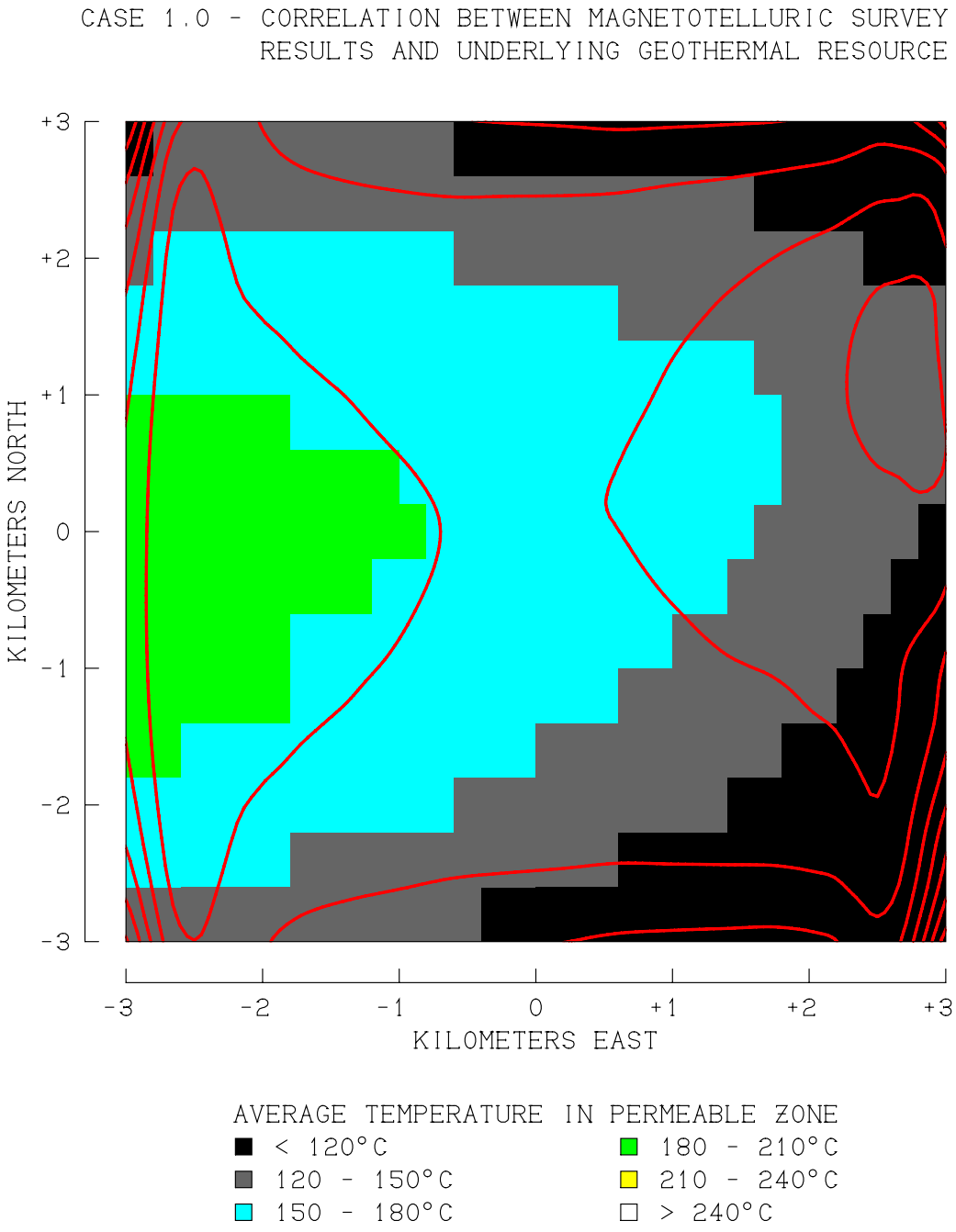

Figure 9.19. Spatial correlation between the results of a magnetotelluric (MT) resistivity survey (0.1 Hz frequency) of the central 36 km^2 of the study area and the location of the underlying subsurface geothermal resource, for Case 1.0.

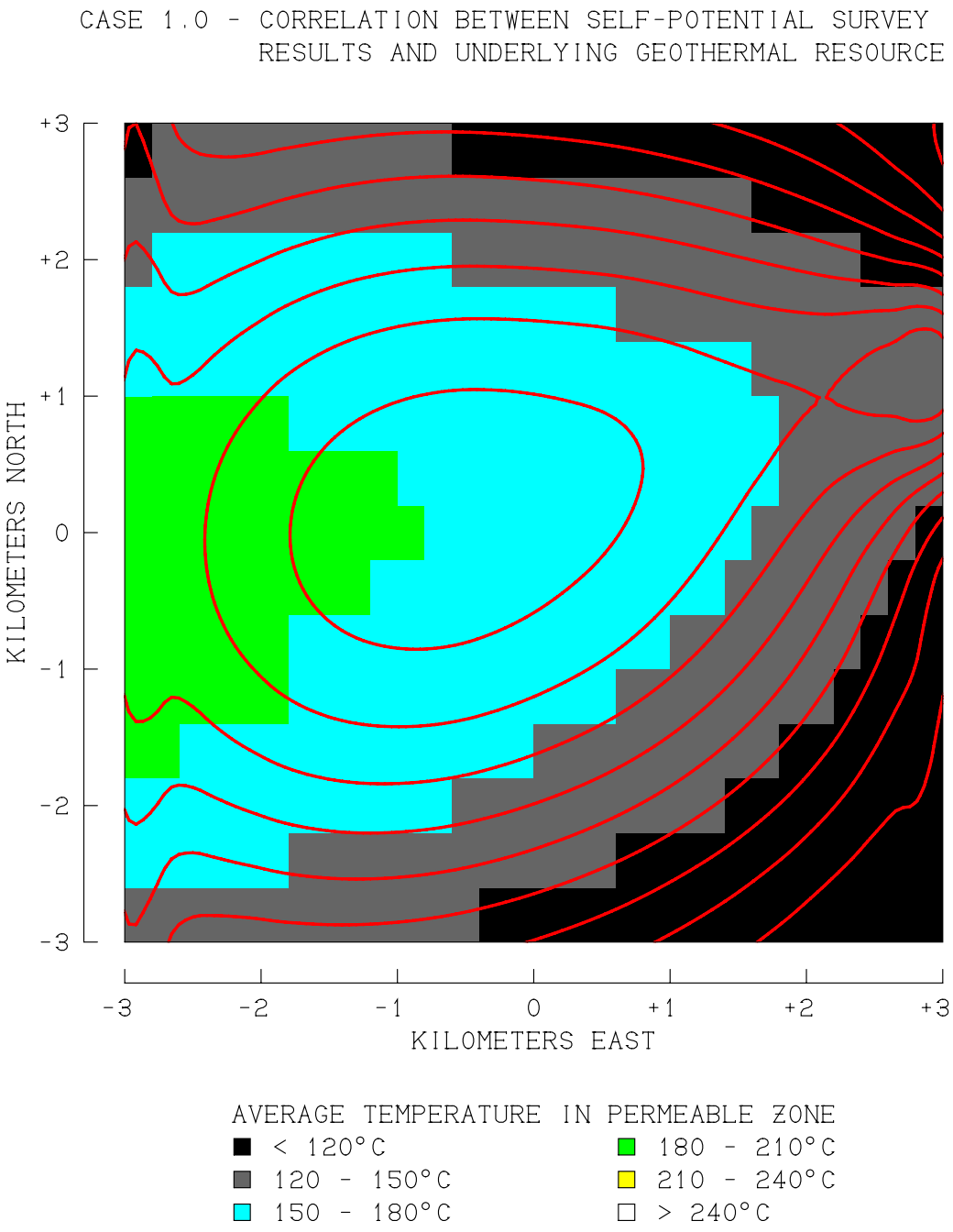

Figure 9.20. Spatial correlation between the results of a self-potential (SP) survey of the central 36 km^2 of the study area and the location of the underlying subsurface geothermal resource, for Case 1.0.

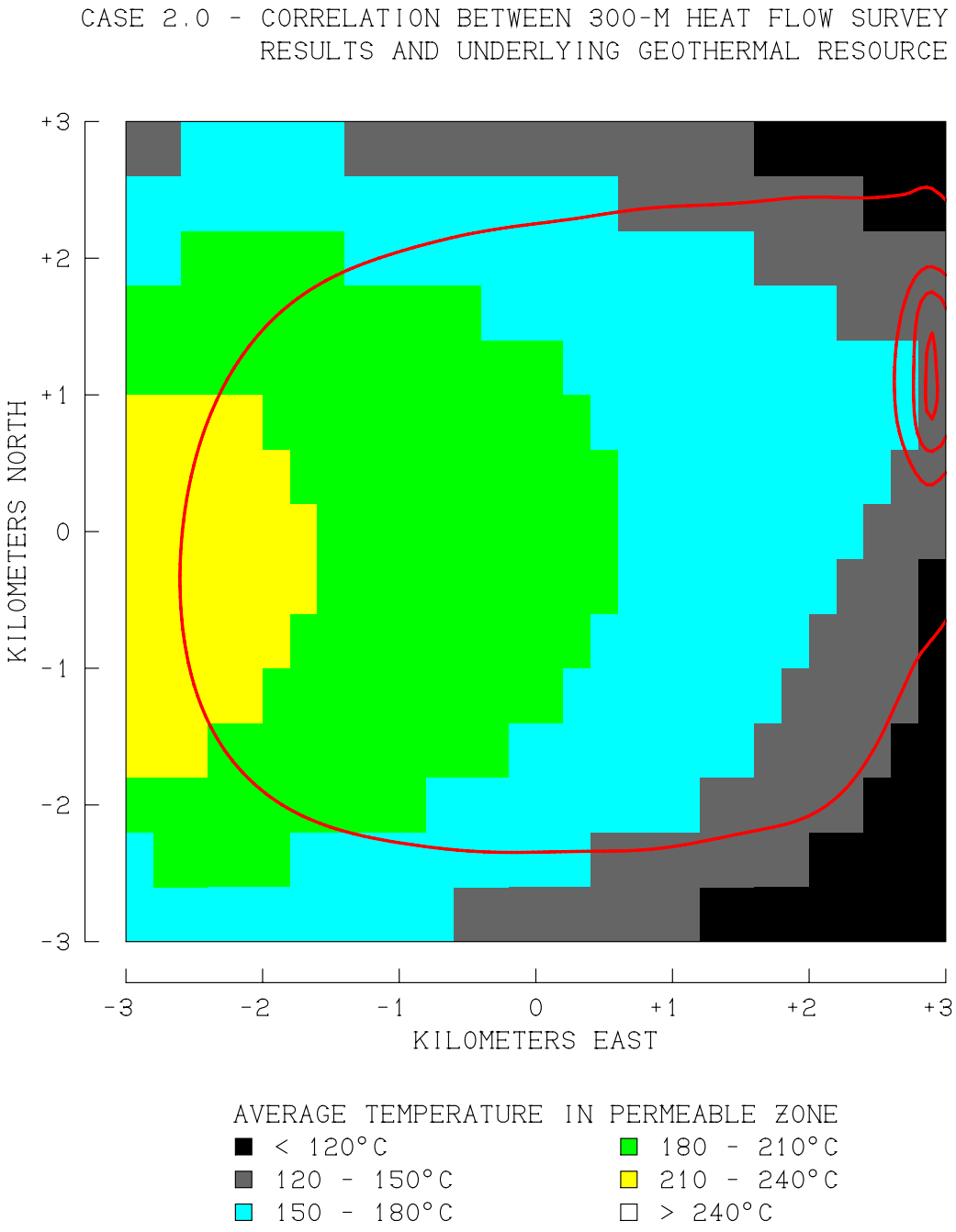

Figure 9.21. Spatial correlation between the results of a 300-meter slimhole heat flow survey of the central 36 km^2 of the study area and the location of the underlying subsurface geothermal resource, for Case 2.0.

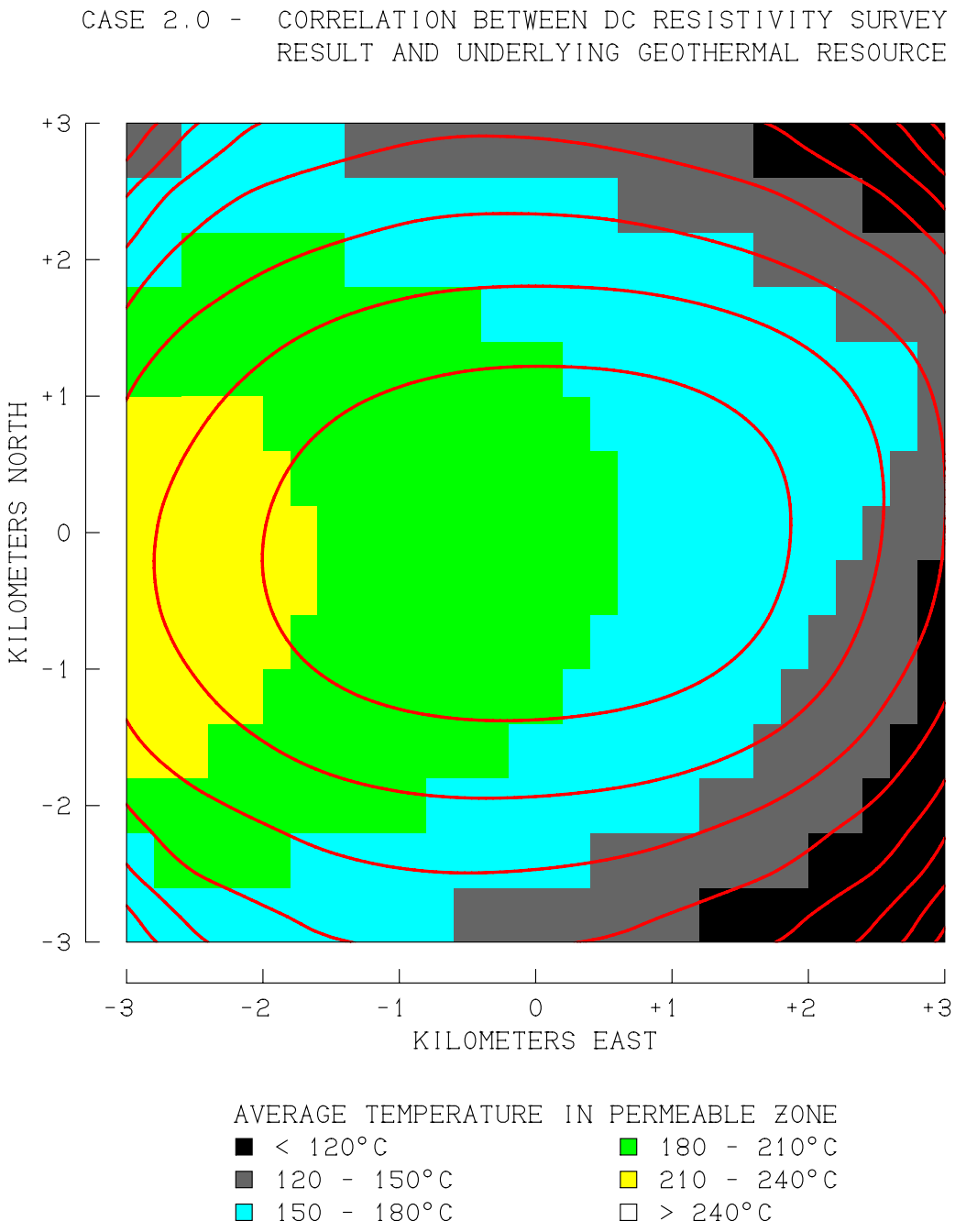

Figure 9.22. Spatial correlation between the results of a Wenner DC resistivity survey (2000 m electrode spacing) of the central 36 km^2 of the study area and the location of the underlying subsurface geothermal resource, for Case 2.0.

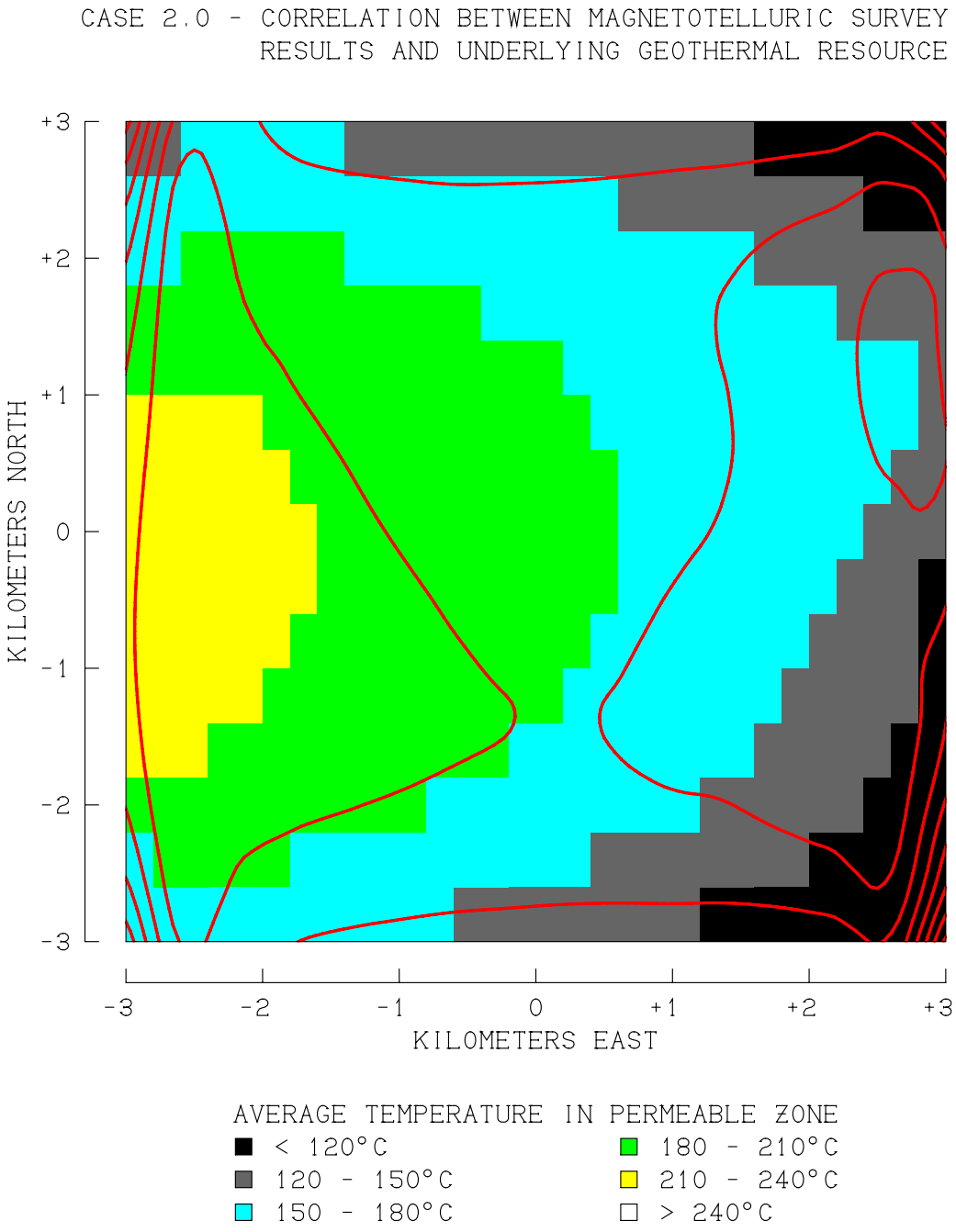

Figure 9.23. Spatial correlation between the results of a magnetotelluric (MT) resistivity survey (0.1 Hz frequency) of the central 36 km^2 of the study area and the location of the underlying subsurface geothermal resource, for Case 2.0.

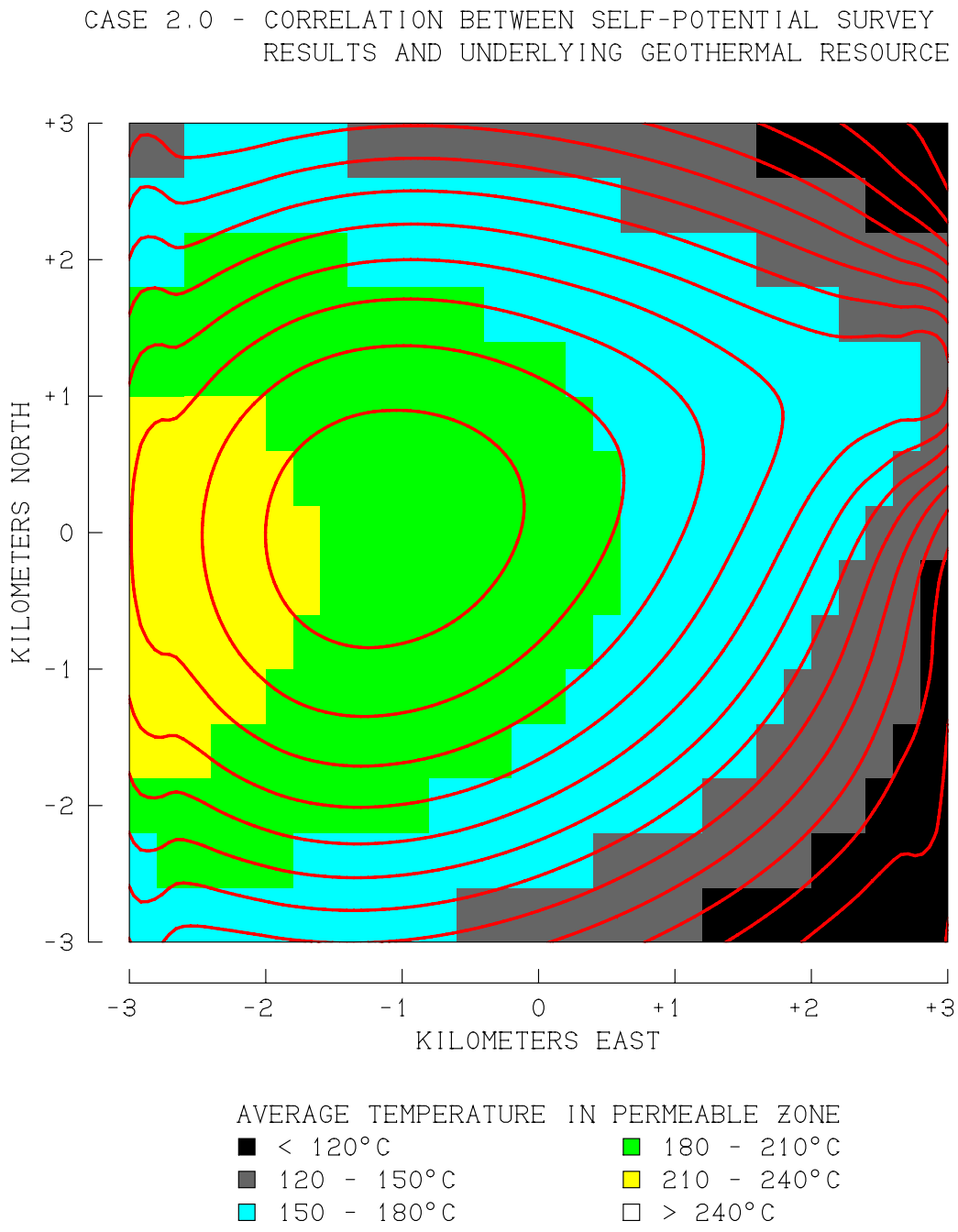

Figure 9.24. Spatial correlation between the results of a self-potential (SP) survey of the central 36 km^2 of the study area and the location of the underlying subsurface geothermal resource, for Case 2.0.

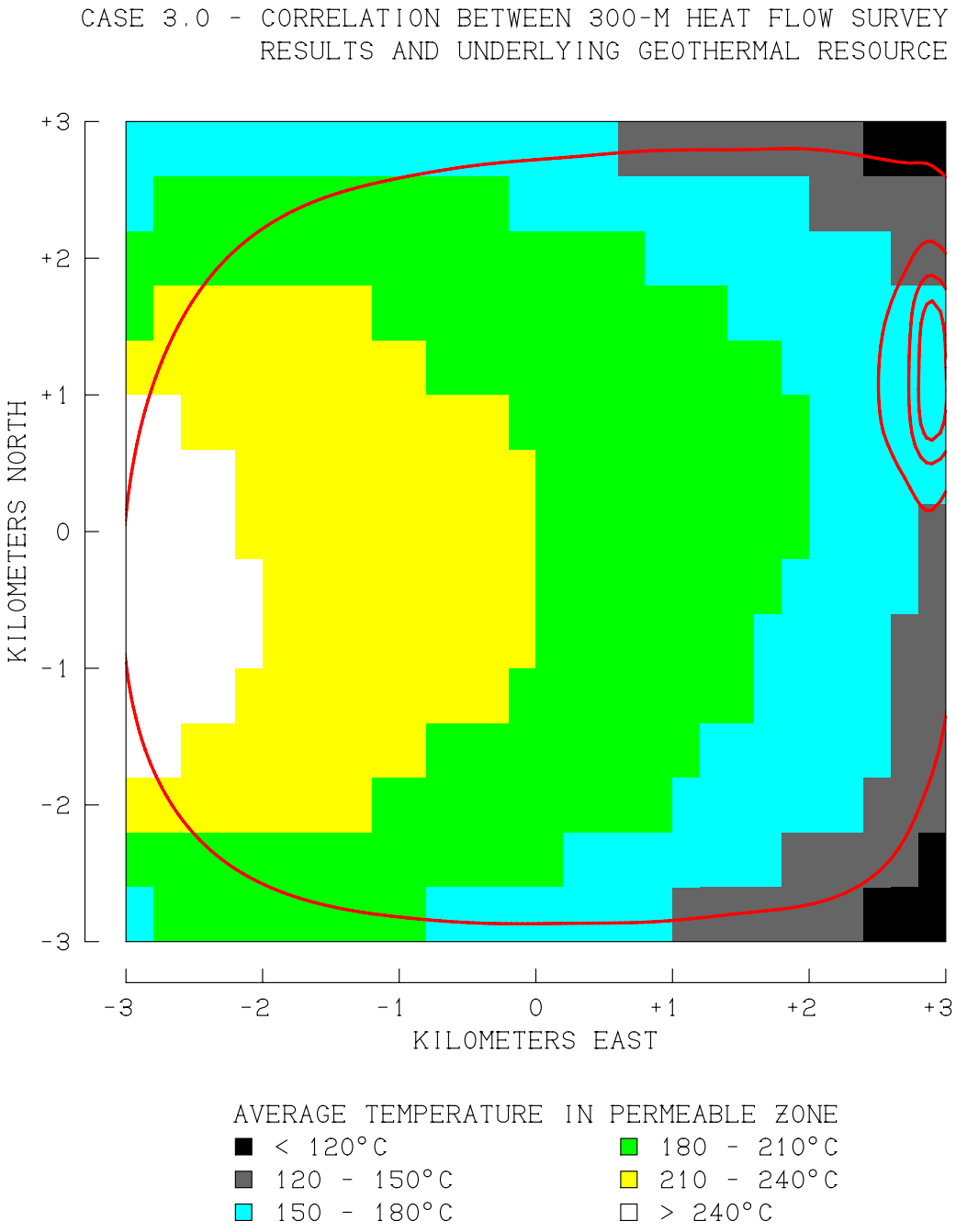

Figure 9.25. Spatial correlation between the results of a 300-meter slimhole heat flow survey of the central 36 km^2 of the study area and the location of the underlying subsurface geothermal resource, for Case 3.0.

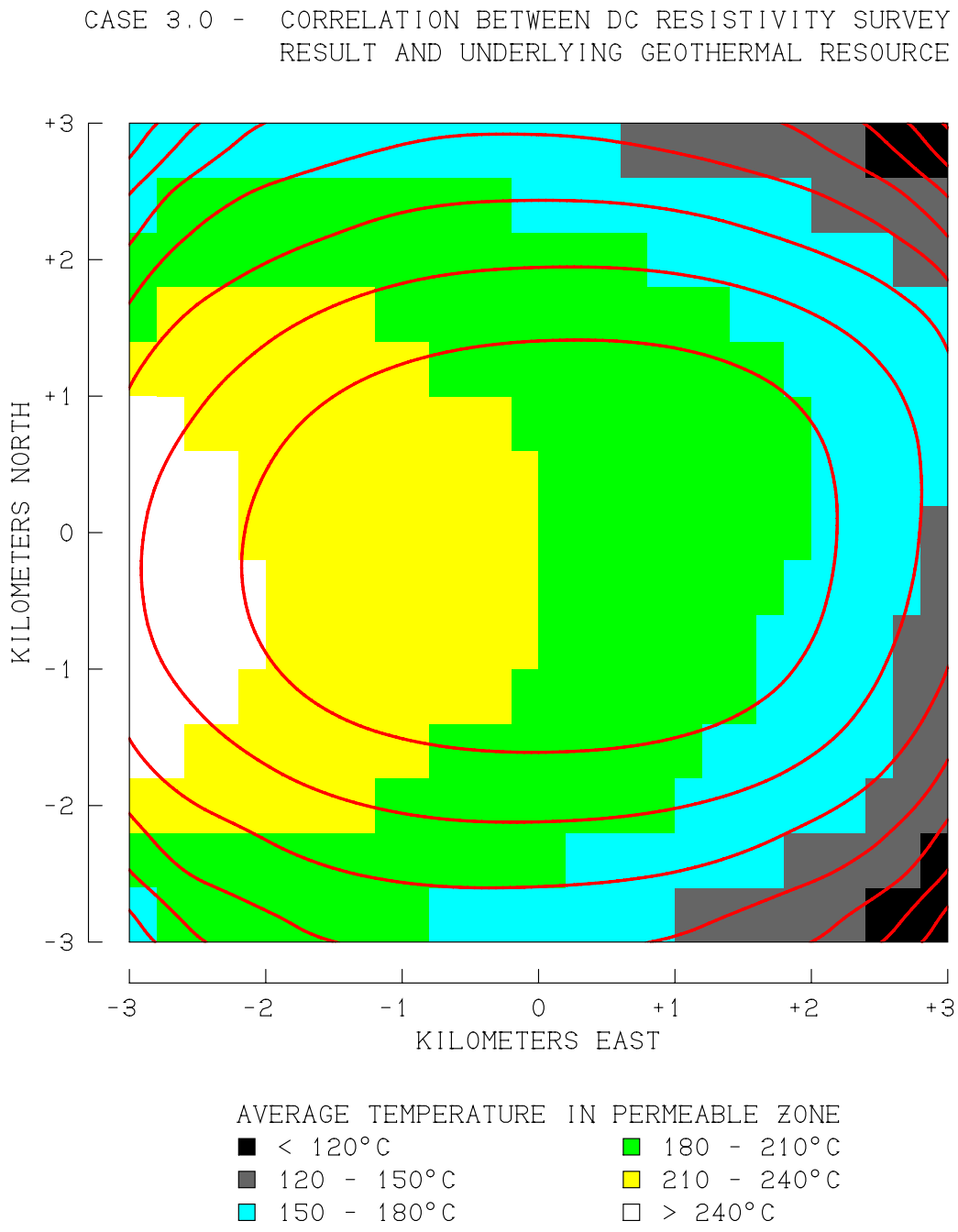

Figure 9.26. Spatial correlation between the results of a Wenner DC resistivity survey (2000 m electrode spacing) of the central 36 km^2 of the study area and the location of the underlying subsurface geothermal resource, for Case 3.0.

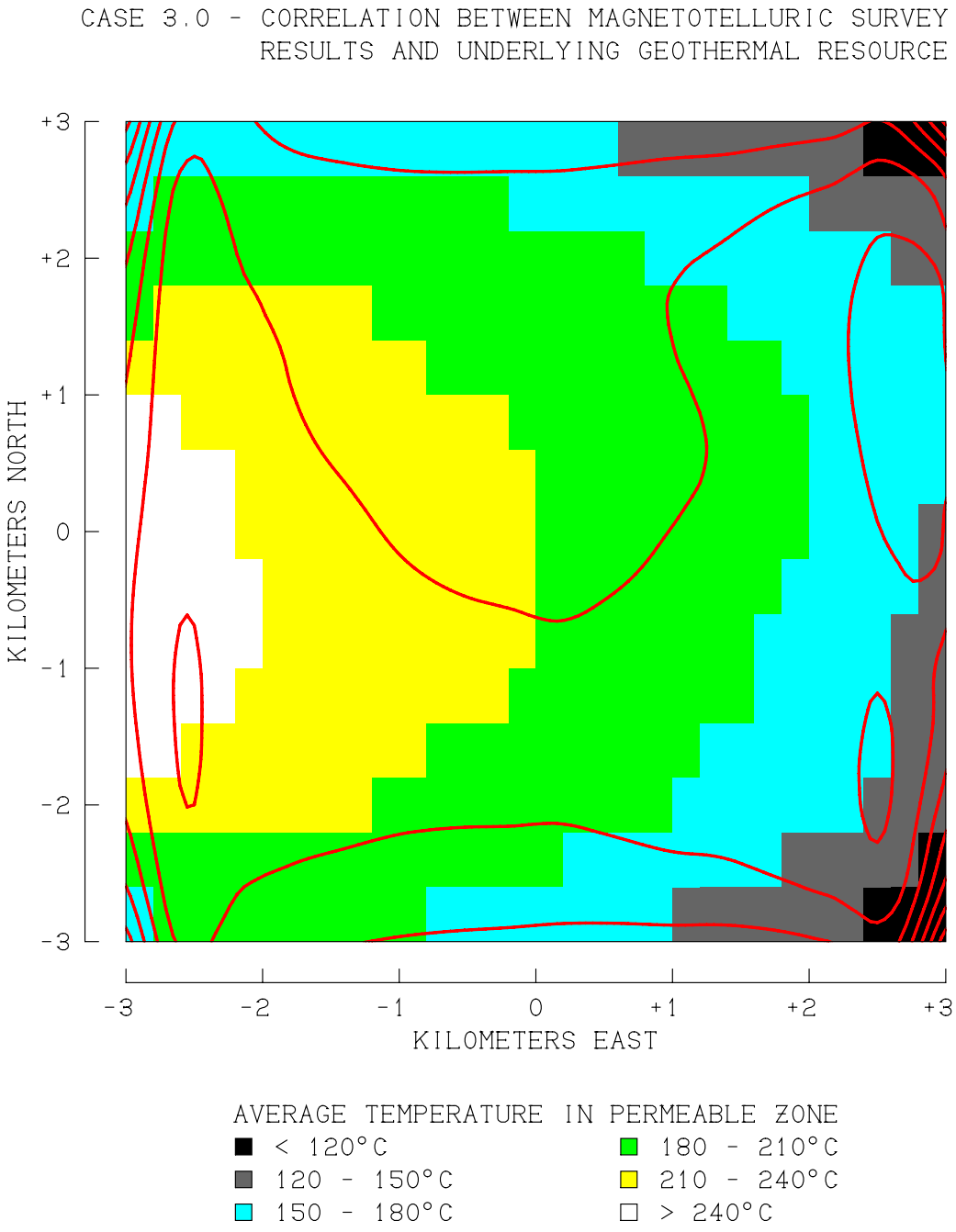

Figure 9.27. Spatial correlation between the results of a magnetotelluric (MT) resistivity survey (0.1 Hz frequency) of the central 36 km^2 of the study area and the location of the underlying subsurface geothermal resource, for Case 3.0.

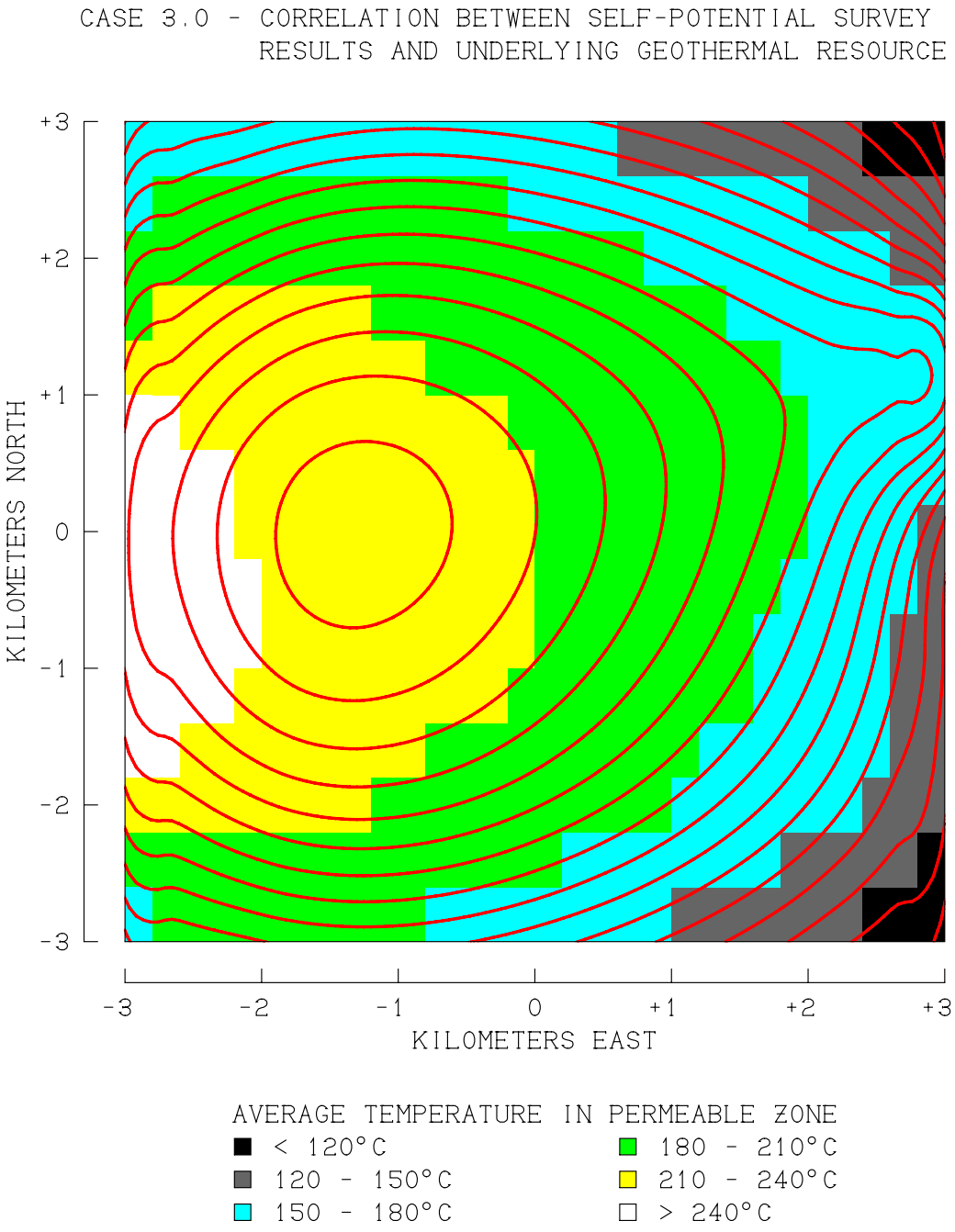

Figure 9.28. Spatial correlation between the results of a self-potential (SP) survey of the central 36 km^2 of the study area and the location of the underlying subsurface geothermal resource, for Case 3.0.

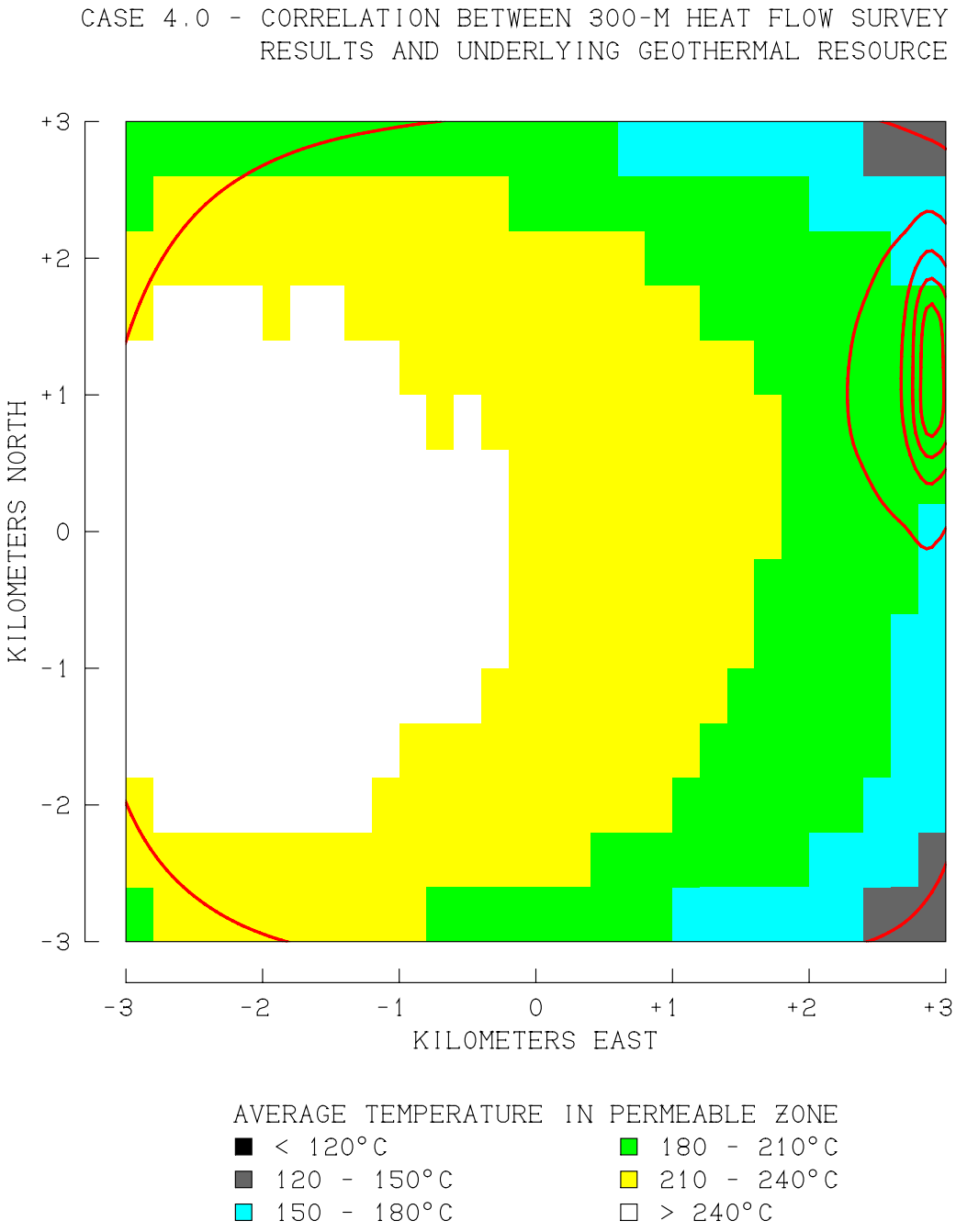

Figure 9.29. Spatial correlation between the results of a 300-meter slimhole heat flow survey of the central 36 km^2 of the study area and the location of the underlying subsurface geothermal resource, for Case 3.0.

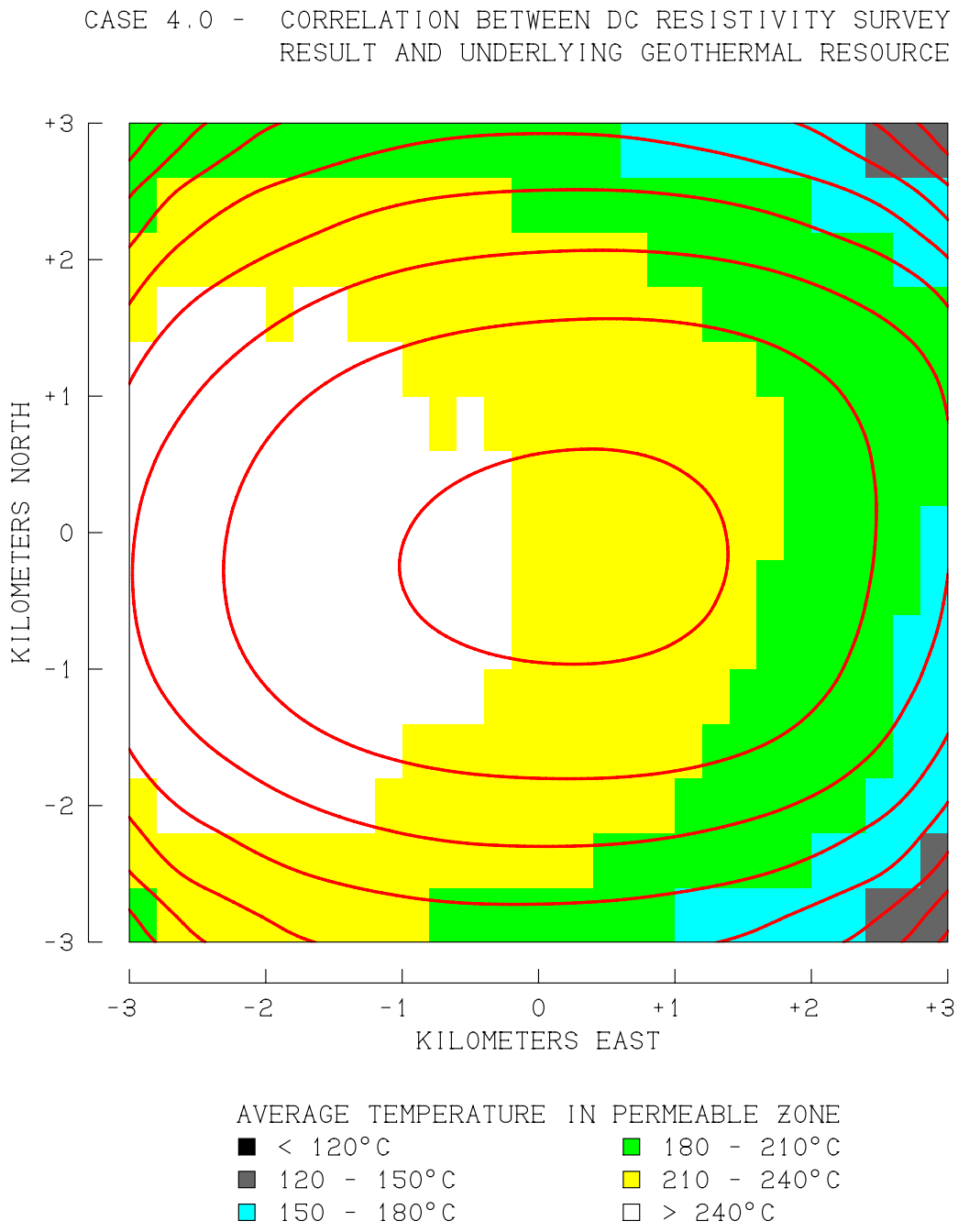

Figure 9.30. Spatial correlation between the results of a Wenner DC resistivity survey (2000 m electrode spacing) of the central 36 km^2 of the study area and the location of the underlying subsurface geothermal resource, for Case 4.0.

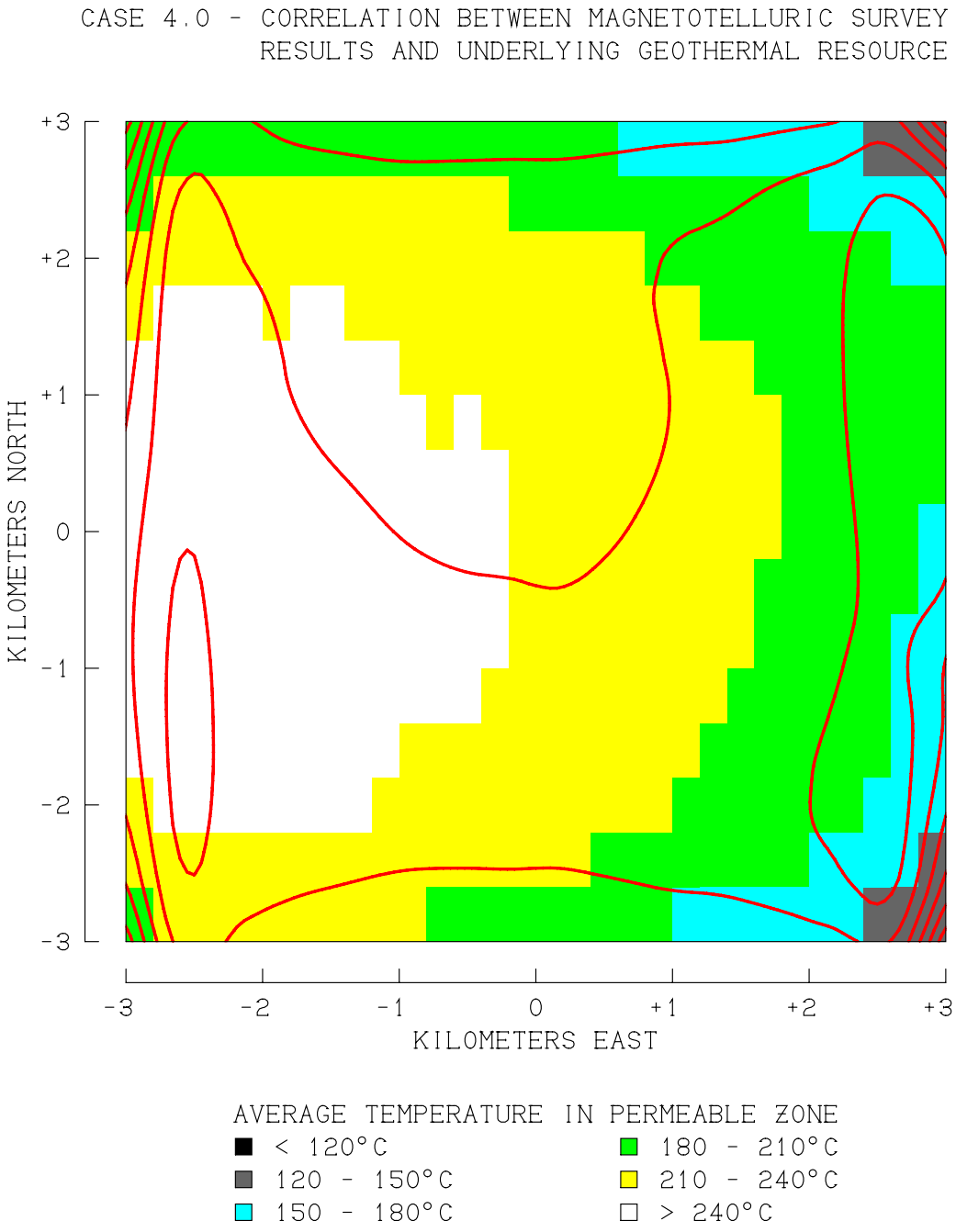

Figure 9.31. Spatial correlation between the results of a magnetotelluric (MT) resistivity survey (0.1 Hz frequency) of the central 36 km^2 of the study area and the location of the underlying subsurface geothermal resource, for Case 4.0.

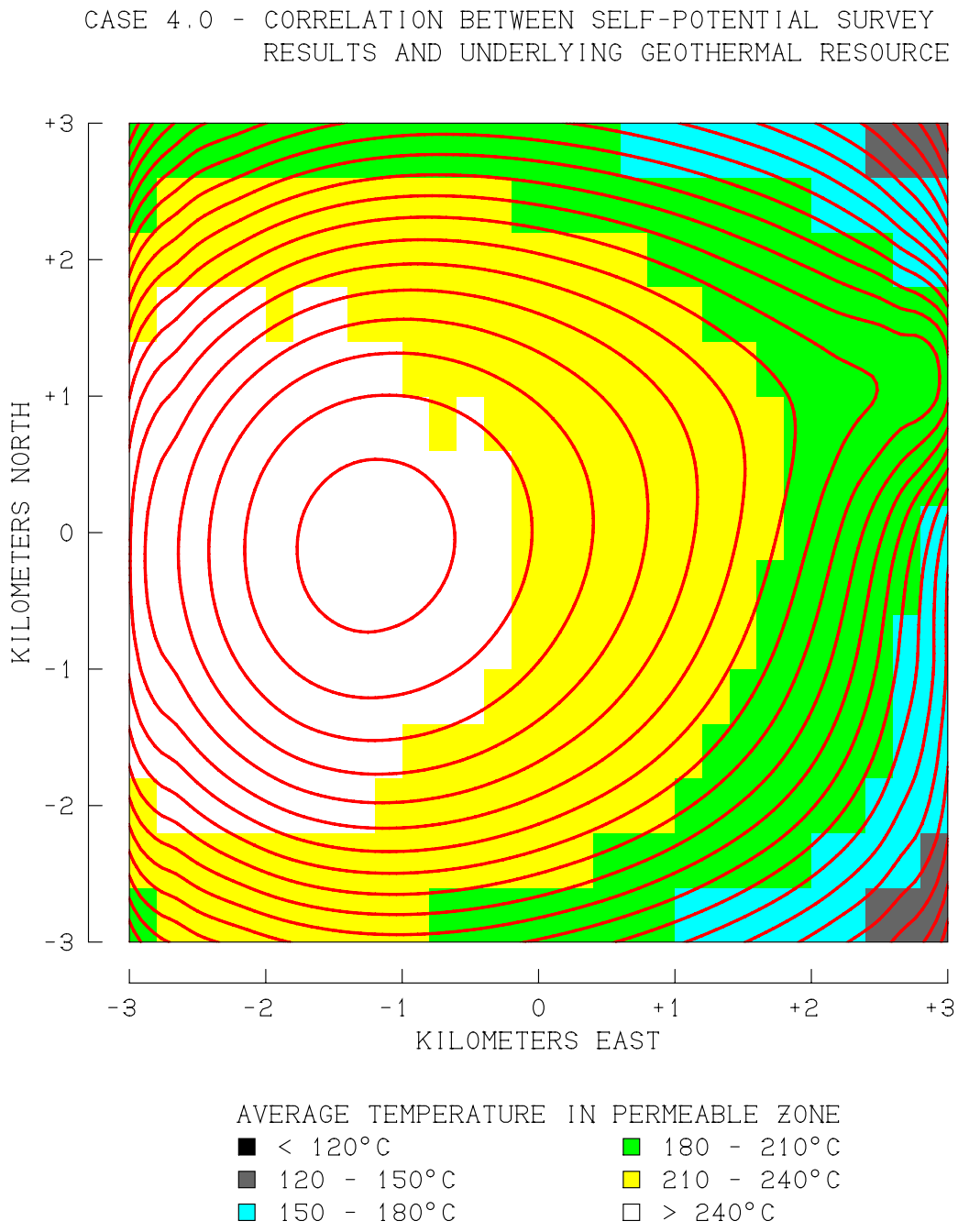

Figure 9.32. Spatial correlation between the results of a self-potential (SP) survey of the central 36 km^2 of the study area and the location of the underlying subsurface geothermal resource, for Case 4.0.

10 ACKNOWLEDGEMENTS

This study was supported by the U. S. Department of Energy. This report is submitted in partial fulfillment of the Statement of Work for Contract No. 00018084, Bechtel BWXT Idaho, LLC (BBWI) and, in combination with a previously-submitted report entitled ***Verification and Validation Calculations Using the STAR Geophysical Postprocessor Suite*** (*Pritchett,* 2003), constitutes the Final Report for the contract.

11 REFERENCES

Ishido, T. and H. Mizutani (1981), "Experimental and theoretical basis of electrokinetic phenomena in rock-water systems and its application to geophysics", *J. Geophysical Research, v. 86,* pp. 1763-1775.

Ishido, T. and J. W. Pritchett (2000), "Using numerical simulation of electrokinetic potentials in geothermal reservoir management", *Proc. World Geothermal Congress 2000*, Kyushu-Tohoku, Japan, pp. 2629-2634.

Pritchett, J. W. (1995), "STAR: a geothermal reservoir simulation system", *Proc. World Geothermal Congress 1995,* Florence, Italy, pp.2959-2963.

Pritchett, J. W. (1998), *Electrical Generating Capacities of Geothermal Slim Holes,* Maxwell Technologies Report No. MTSD-DFR-98-16223.

Pritchett, J. W., J. L. Stevens, P. E. Wannamaker, S. Nakanishi and S. Yamazawa (2000), "Theoretical feasibility studies of reservoir monitoring using geophysical survey techniques', *Proc. World Geothermal Congress 2000,* Kyushu-Tohoku, Japan, pp. 2803-2808.

Pritchett, J. W. (2002), *STAR User's Manual, Version 9.0,* Science Applications International Corp. Report SAIC-02/1055.

Pritchett, J. W. (2003), *Verification and Validation Calculations Using the STAR Geophysical Postprocessor Suite,* Science Applications International Corp. Report SAIC-03/1040.

Sasaki, Y (1999), "3-D inversion of electrical and electromagnetic data on PC's", *Three-Dimensional Electromagnetics, Proc. 2nd Intl. Sym. in Mem. Gerald W. Hohmann,* Univ. of Utah, pp. 128-131.

Sasaki, Y. (2001), "Full 3-D inversion of electromagnetic data on PC", *J. Appl. Geophys. v. 46*, pp. 45-54.

Sass, John H., S. S. Priest, A. J. Blanton, O. C. Sackett, S. L. Welch and M. A. Walters (1999), *Geothermal Industry Temperature Profiles from the Great Basin,* U. S. Geological Survey Open File Report 99-425.

Telford, W. M., L. P. Geldart and R. E. Sheriff (1990), *Applied Geophysics: Second Edition,* Cambridge Univ. Press.

Wannamaker, P. E. (2001), MTCALC: Finite Difference Computer Algorithms for 3D EM Simulation of Resistivity Changes Induced by Production from Geothermal Reservoirs, Science Applications International Corp. Report SAIC-02/1053.

APPENDIX: INFLUENCE OF A SHALLOW CONDUCTIVE LAYER

The preceding analysis indicates that combining earth-surface SP (self-potential) and low-frequency MT (magnetotelluric) survey techniques could be useful for finding "hidden" geothermal resources in the Basin and Range. Locations where anomalies in both surveys coincide are promising drilling targets even if the anomalous region contains no obvious visible surface manifestations of geothermal activity. But experience has shown that, under certain circumstances, some electrical survey techniques have been unable to adequately characterize the subsurface in geothermal areas.

Layers of unusually high-conductivity soil or rock near the earth surface have been observed at some geothermal fields, and can arise from a variety of causes including the presence of a layer of clay sediments and/or minerals left behind by an evaporated body of water, the effects of hydrothermal alteration caused by leakage from the underlying geothermal reservoir itself, or even cultural effects (the presence of conductive metallic artifacts such as steam gathering pipelines associated with geothermal development projects). If the electrical resistivity of the surface layer is unusually low relative to that of the deeper strata, and if the shallow high-conductivity region is of substantial horizontal extent and has good electrical continuity, it can result in a "short-circuit". With a DC resistivity survey, for example, most of the electric current from the electrodes may then flow through the conductive surface layer and no current may penetrate to depth. If this happens, the underlying electrical structure cannot be imaged by the survey, which "sees" only the highly conductive layer at the earth surface.

It would therefore be prudent to determine the extent to which the promising results of the preceding calculations are sensitive to the possible presence of a thin laterally-extensive layer of unusually conductive material at the earth surface, which might mask the deeper electrical anomalies that arise from the presence of the geothermal reservoir. To examine this question, Cases 0.2 and 4.0 were chosen. These two cases are characterized by approximately equivalent heat-flow-survey results in the neighborhood of the "Thermal Area", and also exhibit similar natural water and steam discharges at the surface. Case 0.2 is an "eastern recharge" case with an estimated thirty-year electrical capacity of about 100 MWe and with natural surface manifestations directly overlying the reservoir. Case 4.0 is a "hidden" western recharge case with more than eight times the resource potential for generation of electricity, but for which the deep permeable thermal anomaly itself is several kilometers distant from the surface fluid outlet.

In this Appendix, calculated results are presented for simulated MT (magnetotelluric) and SP (self-potential) surveys for both of these cases, using three different "resistivity models" (models *"A", "B"* and *"C"*). As discussed previously in Section 2, the electrical resistivity of the earth is represented in these calculations using Archie's Law, which relates

the earth's electrical resistivity (Ω) to that of the interstitial fluid (Ω_F, a function of pressure, temperature and dissolved solids content), formation porosity φ (in the present cases, a constant equal to 0.10) and an empirical dimensionless coefficient C_A, ordinarily of order unity, which tends to increase with increasing formation permeability:

$$\Omega = \frac{\Omega_F}{\left(C_A \varphi^2\right)}$$

The resistivity model that was previously employed for the calculations reported in Sections 6–9 is herein designated *"Model A",* and specifies C_A = 2 for the "high permeability formations" (the Upper Aquifer, the Western Fault Zone and the Eastern Fault Zone) and C_A = 1 for the remaining lower-permeability formations.

For *"Model B"* and *"Model C",* the same resistivity prescription is used for elevations below z = –200 meters. But at shallower horizons (in a region 200 meters thick on the valley floor and increasing to 700 meters thick to the east and west of the study area), the values of C_A are larger (resulting in lower shallow formation resistivities), by a factor of ten for *"Model B"* and by a factor of fifty for *"Model C",* as indicated in Table A-1. Note that this results in C_A = 100 for the high-permeability formations in the case of *"Model C",* which means that the resistivity of the shallow permeable rock formations in the Thermal Area using that model is the same as that of a tank full of saline liquid geothermal brine. Lower values of electrical resistivity (higher values of C_A) would therefore be difficult to justify.

Table A.1. Values of Archie's Law coefficient (C_A) for various resistivity models.

	Model "*A*"	Model "*B*"	Model "*C*"
Above z = –200 meters:			
High-permeability formations	2	20	100
Low-permeability formations	1	10	50
Below z = –200 meters:			
High-permeability formations	2	2	2
Low-permeability formations	1	1	1

Shallow-layer resistivity for *"Model C"* ranges from 1.9 ohm-meters up to 9.8 ohm-meters. For *"Model B",* the range is from 9.6 to 49 ohm-meters. The lowest surface resistivities are found in the Thermal Area. The reduced values of electrical resistivity for elevations above z = –200 meters for models *"B"* and *"C"* are imposed throughout the entire 100 km^2 study area and also in the "exterior volume" of the larger 400 km^2 "electrical grid" beyond the STAR flow-grid. These "exterior" distributions of electrical resistivity with elevation for the three models are shown in Figure A.1.

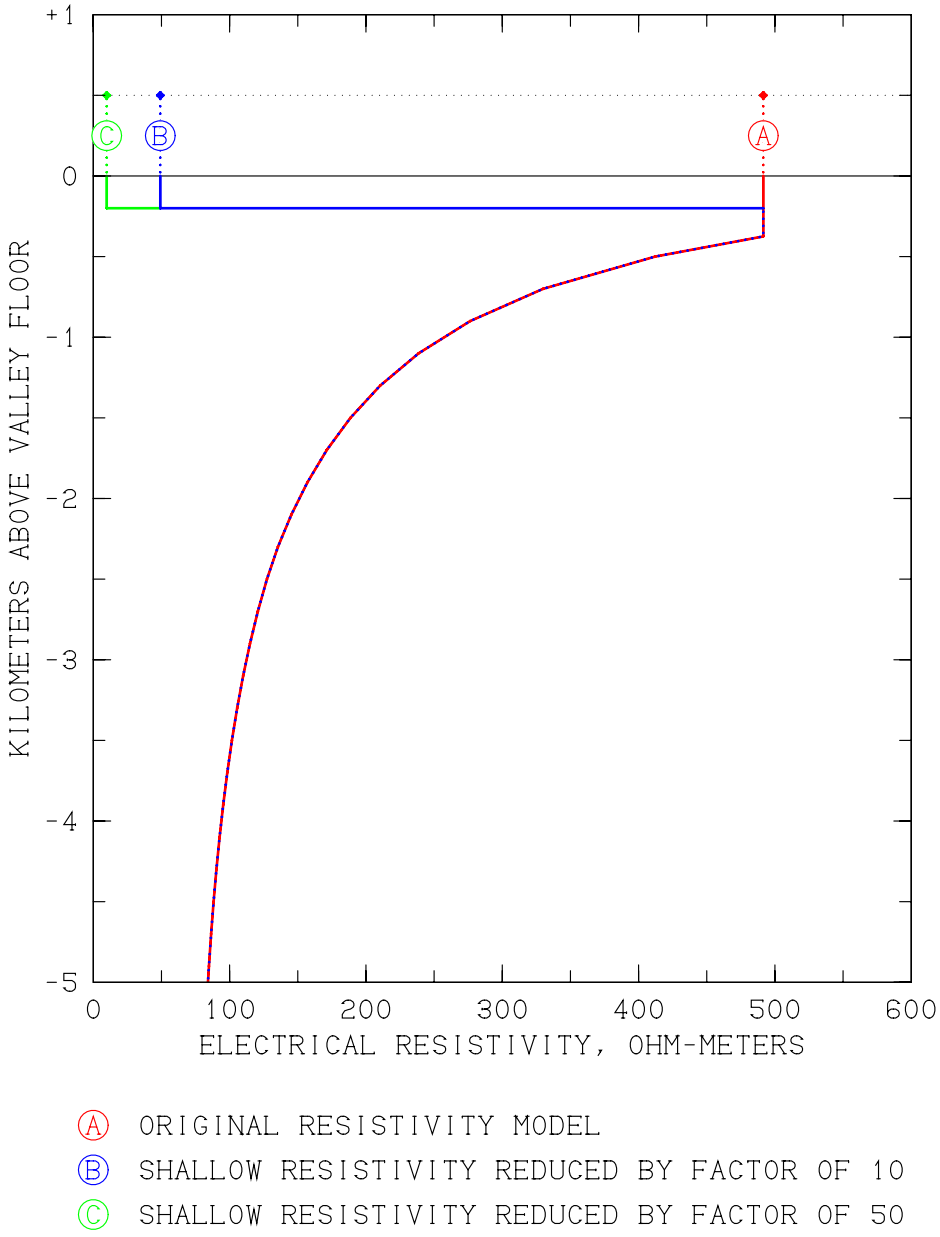

Figure A.1. Vertical distribution of electrical resistivity imposed outside "STAR" flow grid volume for electrical models *"A", "B"* and *"C".*

First, consider a series of MT stations that are situated along an east-west survey line at $y = 0$ (Figure 7.3). Figure A.2 indicates the survey results using resistivity model *"A"* for Case 0.2, for apparent resistivity (upper) and phase angle (lower). These are the same as presented previously in Figure 7.6. Analogous results for this same "eastern reservoir" but with enhanced electrical conductivity near the earth surface are presented in Figures A.3 and A.4 for resistivity models *"B"* and *"C",* respectively. Comparing these three traverses shows that results are very different from one to the next at high frequencies (shallow penetration depths), with apparent resistivities at ~100 Hz that are comparable to the electrical resistivity of the 200-meter-thick shallow layer itself. But so long as the frequency is low enough (< 0.5 Hz or so in these cases), the same basic apparent-resistivity pattern can be recognized in all of them, with a major low-resistivity anomaly located adjacent to the "Eastern Fault Zone" centered on the underground geothermal reservoir.

Similarly, Figures A.5 – A.7 display MT traverses for the "hidden" reservoir (Case 4.0). Again, results at high frequencies are sensitive to the presence of the shallow conductive layer, but at sufficiently low frequencies the characteristic broad resistivity anomaly filling the entire valley floor between the fault zones is unmistakable, and readily distinguished from the pattern exhibited by Case 0.2. Clearly, while high-frequency signals are masked by the presence of the conductive surface layer, low-frequency signals are able to penetrate to the deep underlying geothermal reservoir in both Case 0.2 and Case 4.0.

Figures A.8 – A.10 show the 2-D distribution of MT apparent resistivity at 0.1 Hz for Case 0.2 (eastern reservoir) using Models *"A", "B"* and *"C"* respectively. Figures A.11 – A.13 display corresponding results for Case 4.0 (the larger western "hidden" system). The presence of the shallow conductive layer has the net effect of reducing the average apparent-resistivity value somewhat throughout the area, but the low-resistivity anomalies representing the subsurface geothermal reservoirs still exhibit substantial contrast against background (generally 4:1 or better), retain their characteristic shapes and spatial locations, and should be easy to locate and distinguish in practice, even in the extreme case represented by *"Model C".*

Finally, the "SP postprocessor" was used to re-calculate the earth-surface distribution of self-potential for Cases 0.2 and 4.0 using the various "resistivity models". Results are presented in Figures A.14 – A.16 for Case 0.2 (for models *"A", "B"* and *"C"* respectively); analogous results for Case 4.0 are shown in Figures A.17 – A.19. Increasing the electrical conductivity of the surface layer has the net effect of decreasing the amplitude of the deep-origin SP anomalies for both cases. Relative to *"Model A",* the signal amplitudes for Models *"B"* and *"C"* are only about 70% and 35% respectively. But even with *"Model C",* the amplitude of the anomaly still exceeds 100 millivolts – well above the reliable detection threshold of the survey technique.

It is noteworthy that, while the deep-origin SP signal declines with increasing surface conductivity, the shallow-origin topographic "noise" to the east and west of the valley decreases by an even larger factor, actually improving the signal-to-noise ratio if a shallow

Continued on page A–23

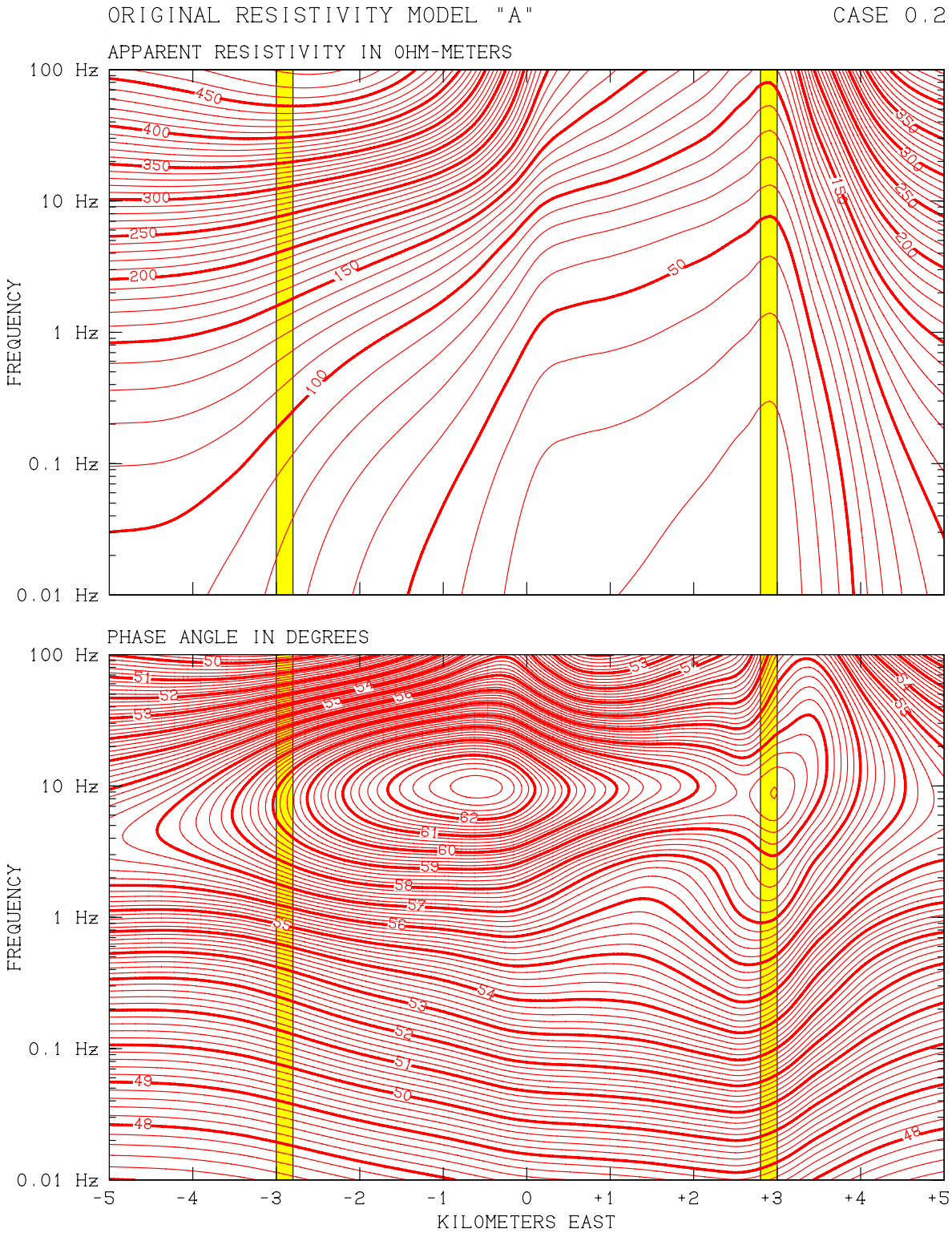

Figure A.2. Results of east-west MT sounding profile at $y = 0$ for "eastern" geothermal reservoir (Case 0.2) using "original" electrical resistivity model *"A"*. *Upper:* apparent resistivity. *Lower:* phase angle.

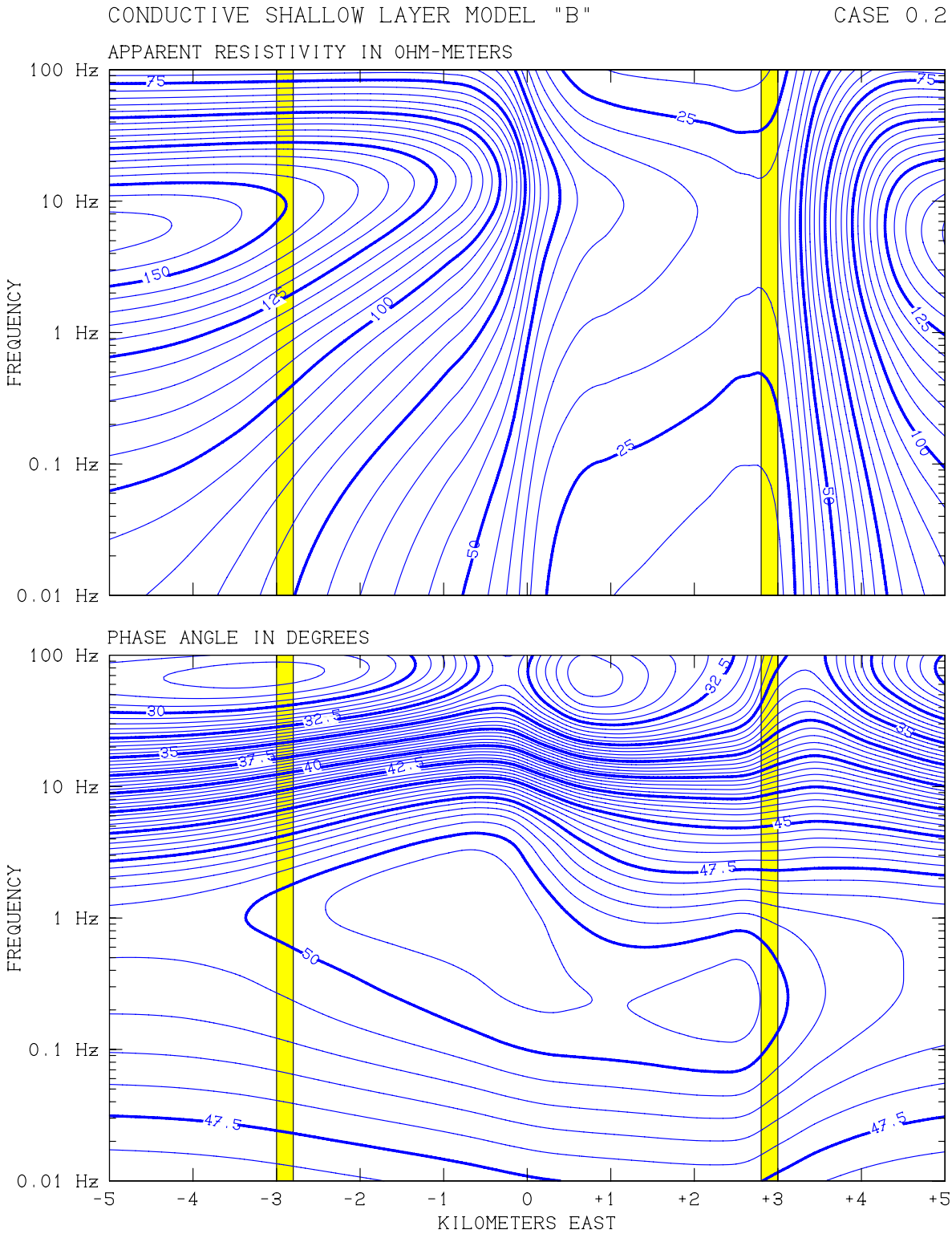

Figure A.3. Results of east-west MT sounding profile at $y = 0$ for "eastern" geothermal reservoir (Case 0.2) using "shallow conductive" electrical resistivity model *"B"*. *Upper:* apparent resistivity. *Lower:* phase angle.

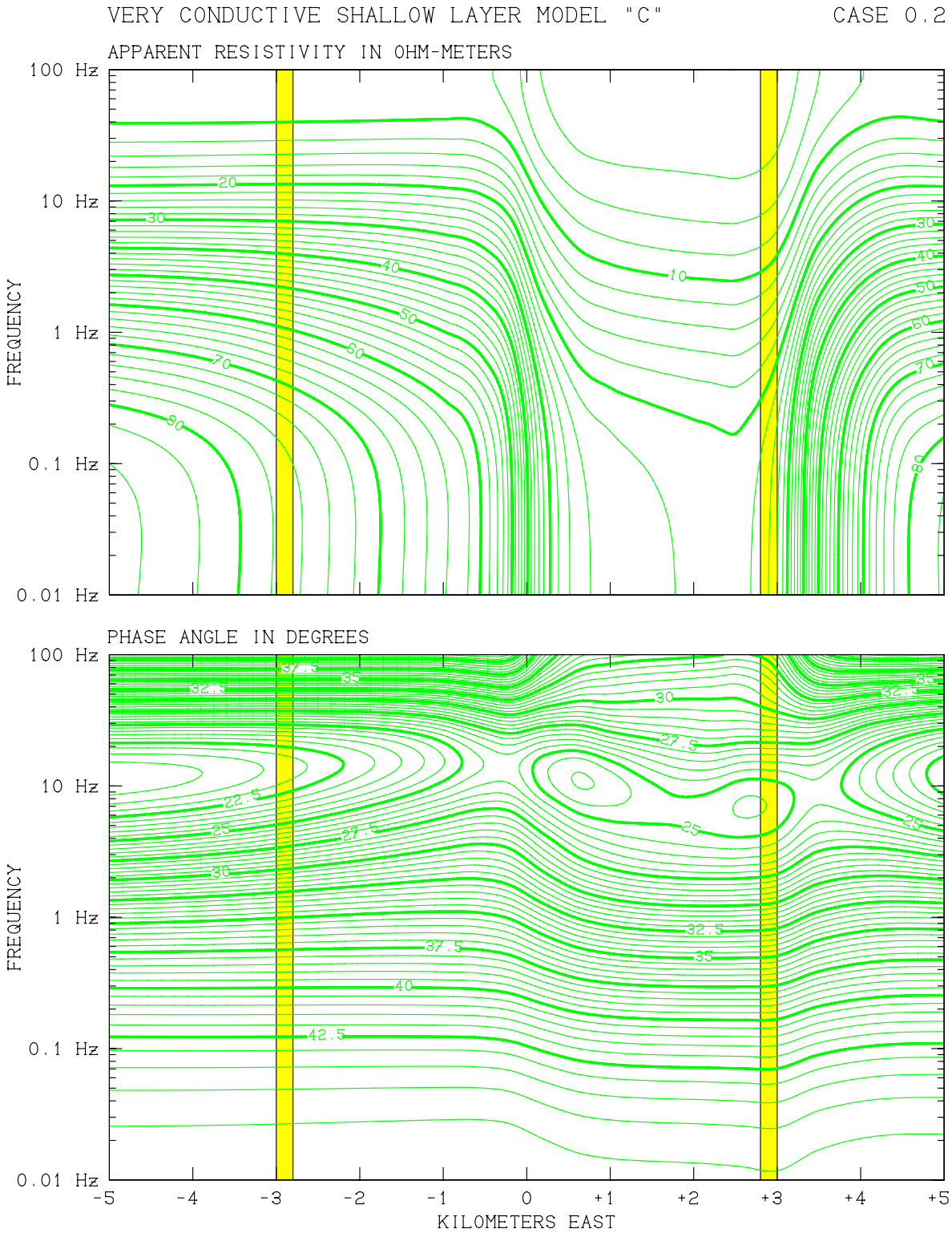

Figure A.4. Results of east-west MT sounding profile at $y = 0$ for "eastern" geothermal reservoir (Case 0.2) using "shallow very conductive" electrical resistivity model "*C*". *Upper:* apparent resistivity. *Lower:* phase angle.

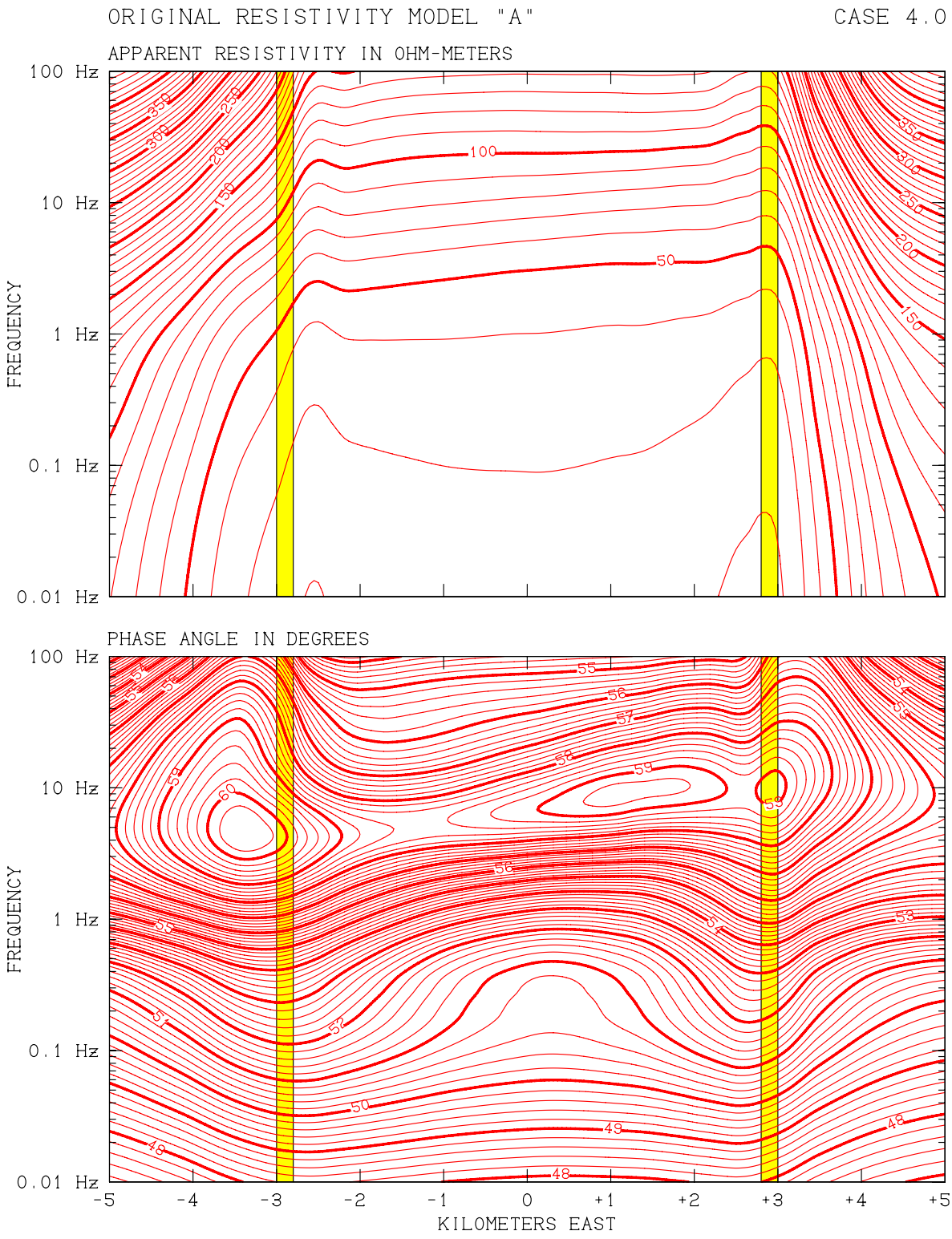

Figure A.5. Results of east-west MT sounding profile at $y = 0$ for "hidden western" geothermal reservoir (Case 4.0) using "original" electrical resistivity model *"A"*. *Upper:* apparent resistivity. *Lower:* phase angle.

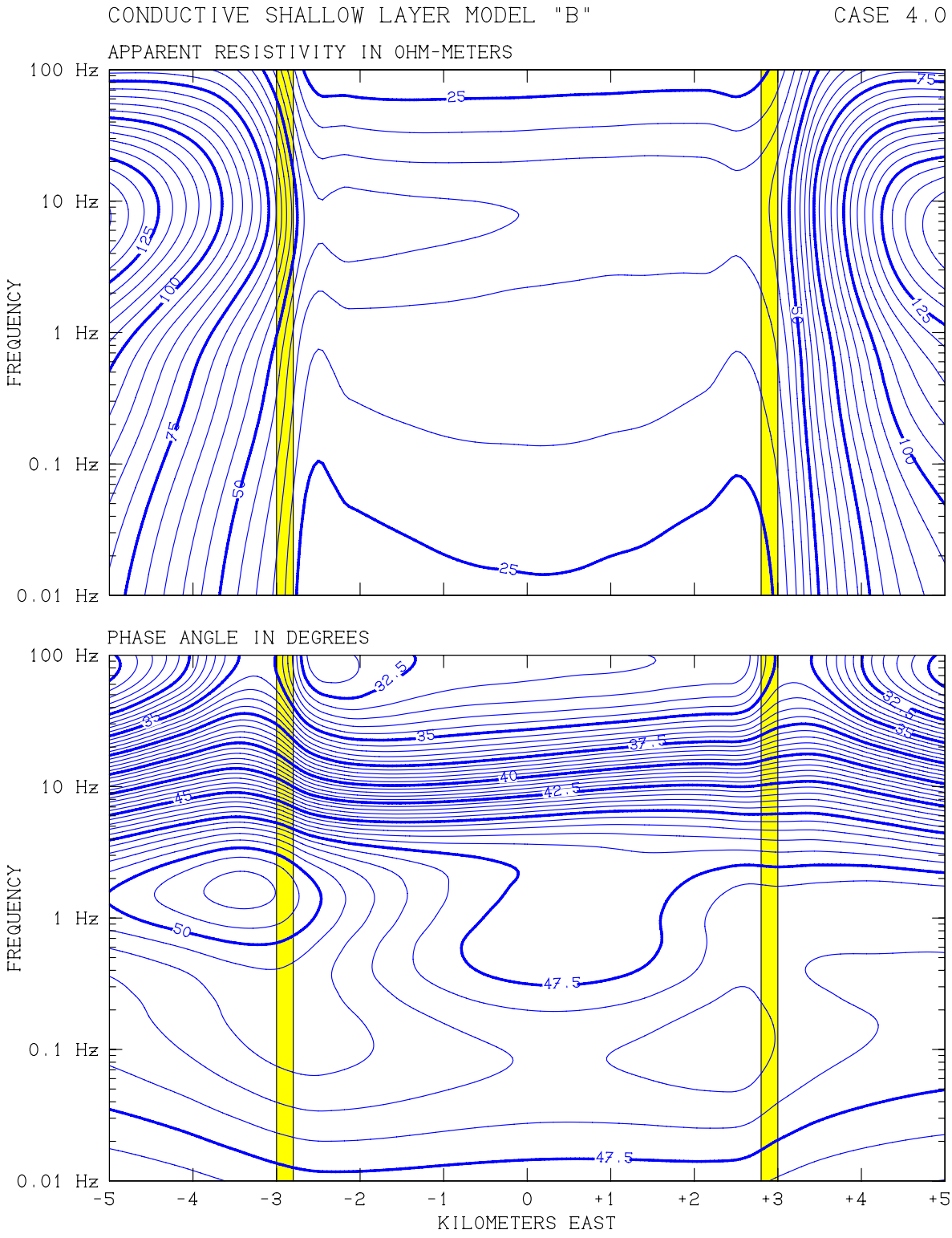

Figure A.6. Results of east-west MT sounding profile at y = 0 for "hidden western" geothermal reservoir (Case 4.0) using "shallow conductive" electrical resistivity model *"B"*. *Upper:* apparent resistivity. *Lower:* phase angle.

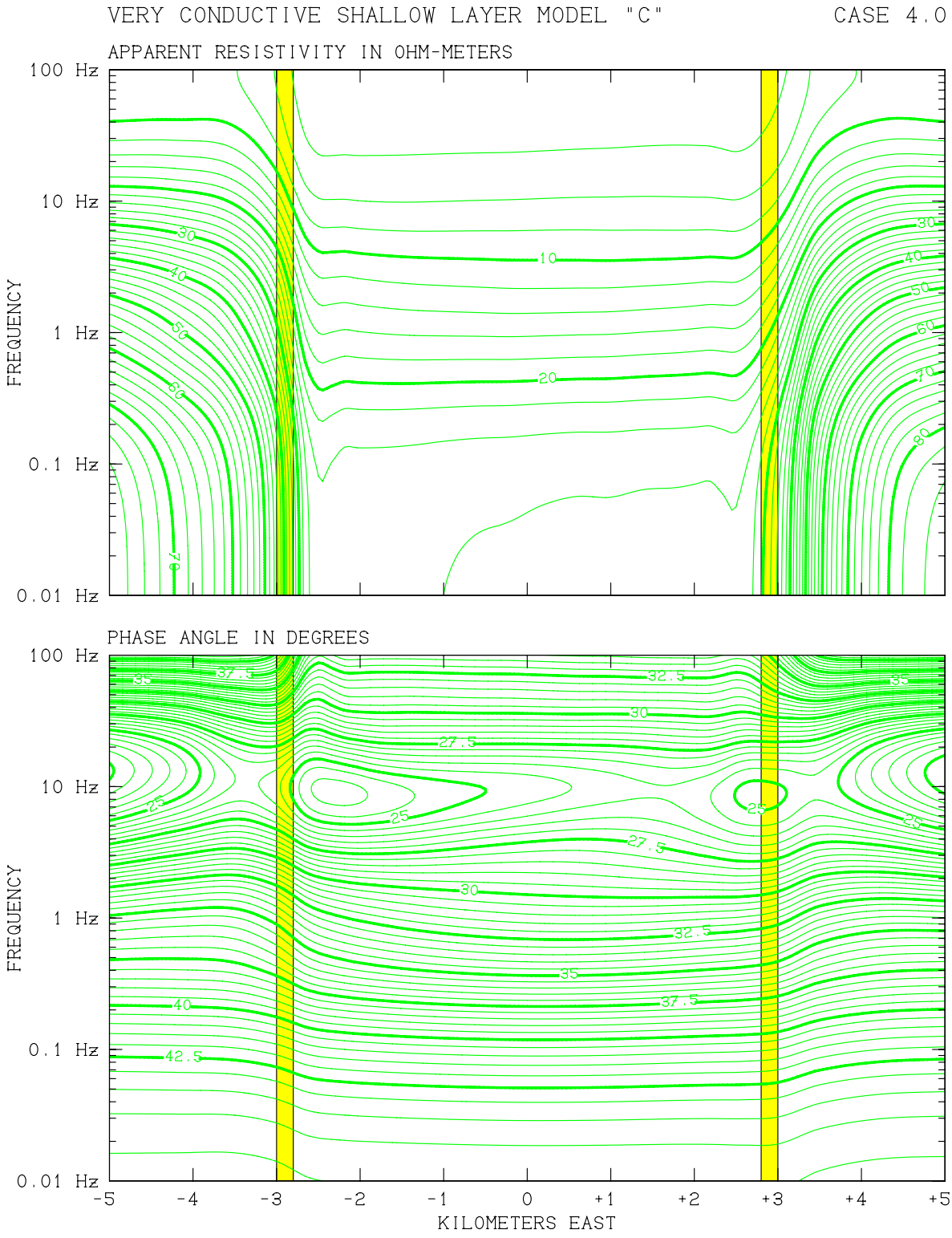

Figure A.7. Results of east-west MT sounding profile at $y = 0$ for "hidden western" geothermal reservoir (Case 4.0) using "shallow very conductive" electrical resistivity model *"C"*. *Upper:* apparent resistivity. *Lower:* phase angle.

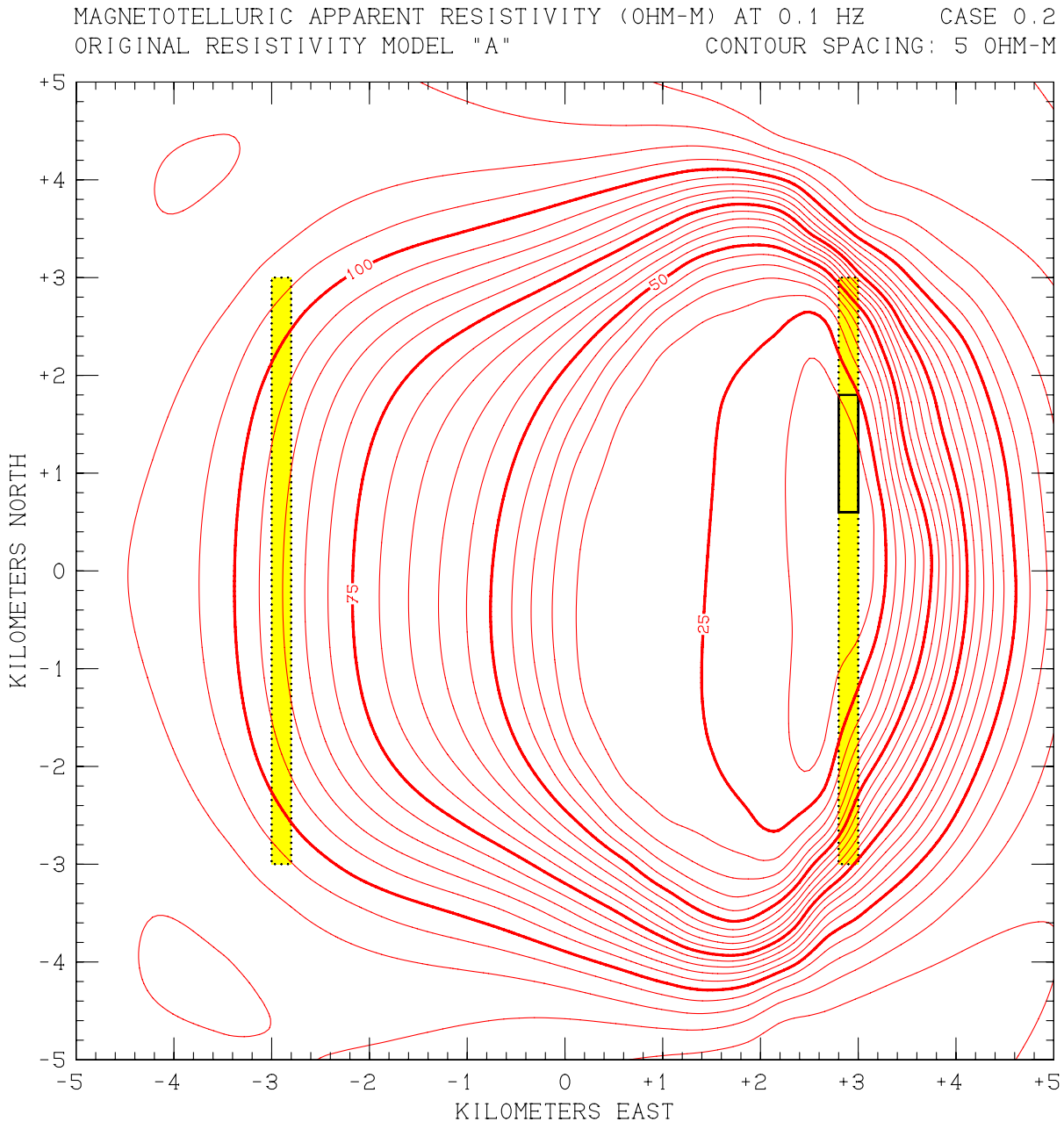

Figure A.8. Distribution of MT apparent resistivity at 0.1 Hz for "eastern" reservoir (Case 0.2) using "original" electrical resistivity model *("A")*. Contour spacing is 5 ohm-meters.

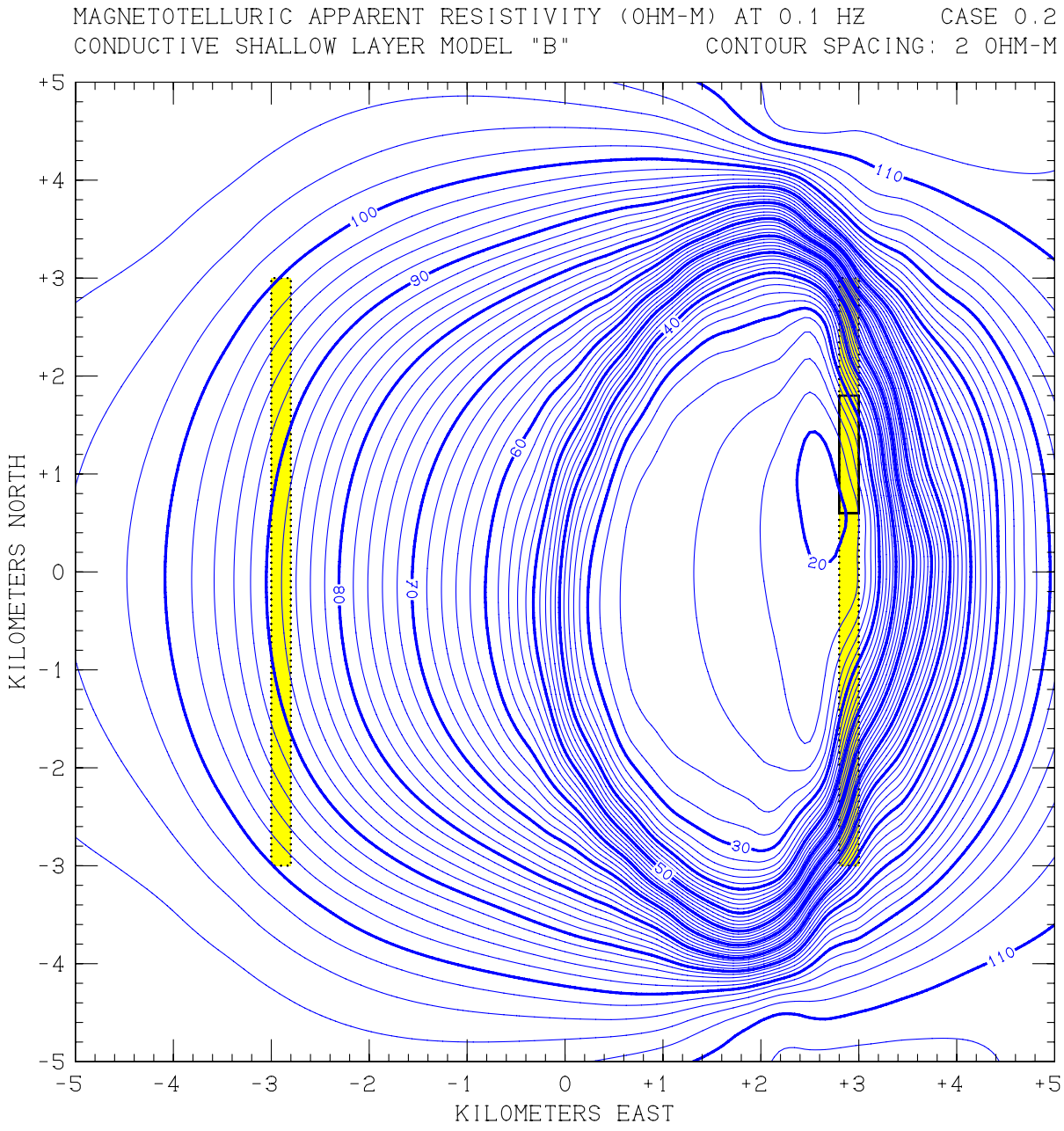

Figure A.9. Distribution of MT apparent resistivity at 0.1 Hz for "eastern" reservoir (Case 0.2) using "shallow conductive" electrical resistivity model *("B")*. Contour spacing is 2 ohm-meters.

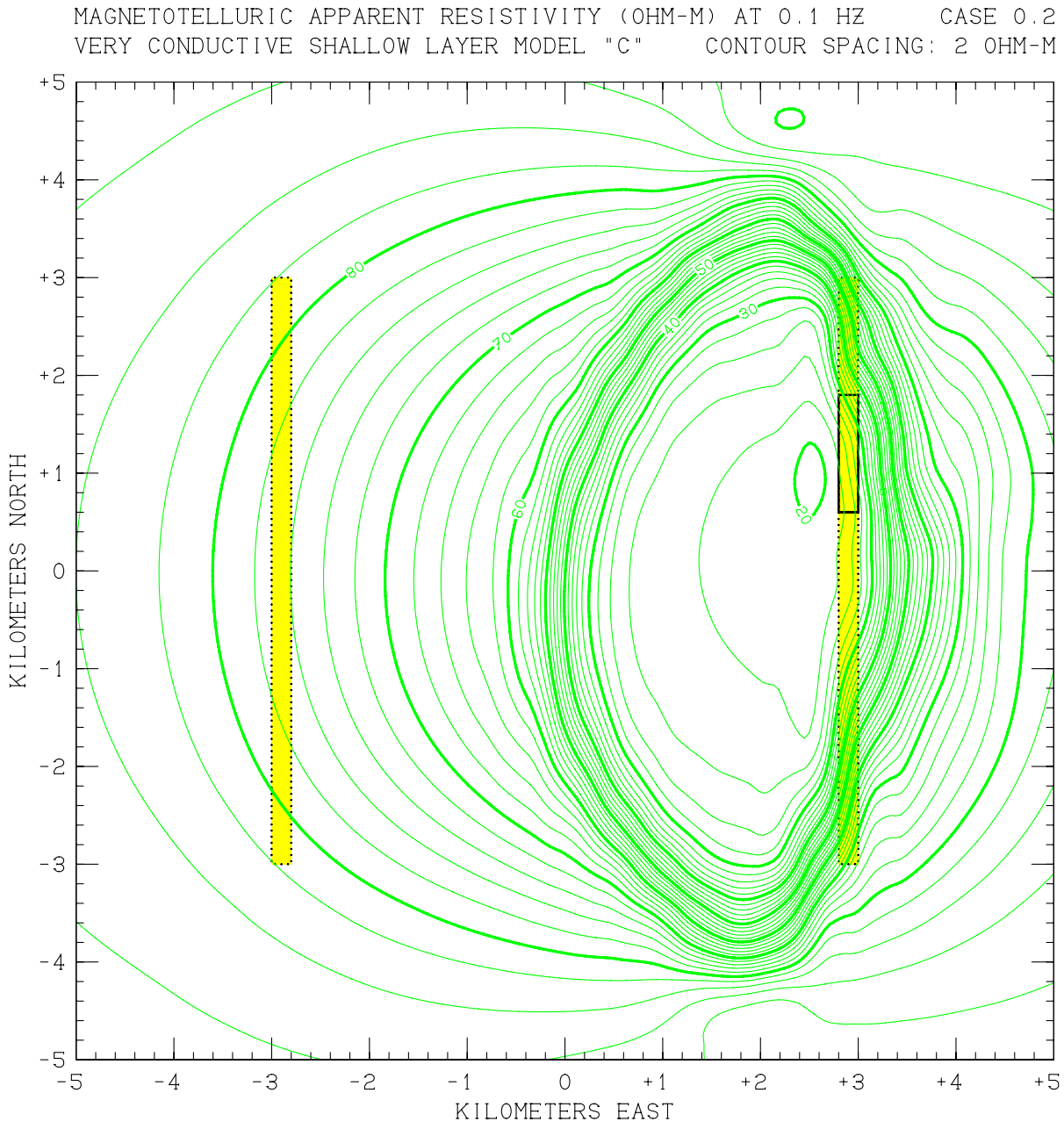

Figure A.10. Distribution of MT apparent resistivity at 0.1 Hz for "eastern" reservoir (Case 0.2) using "shallow very conductive" electrical resistivity model *("C")*. Contour spacing is 2 ohm-meters.

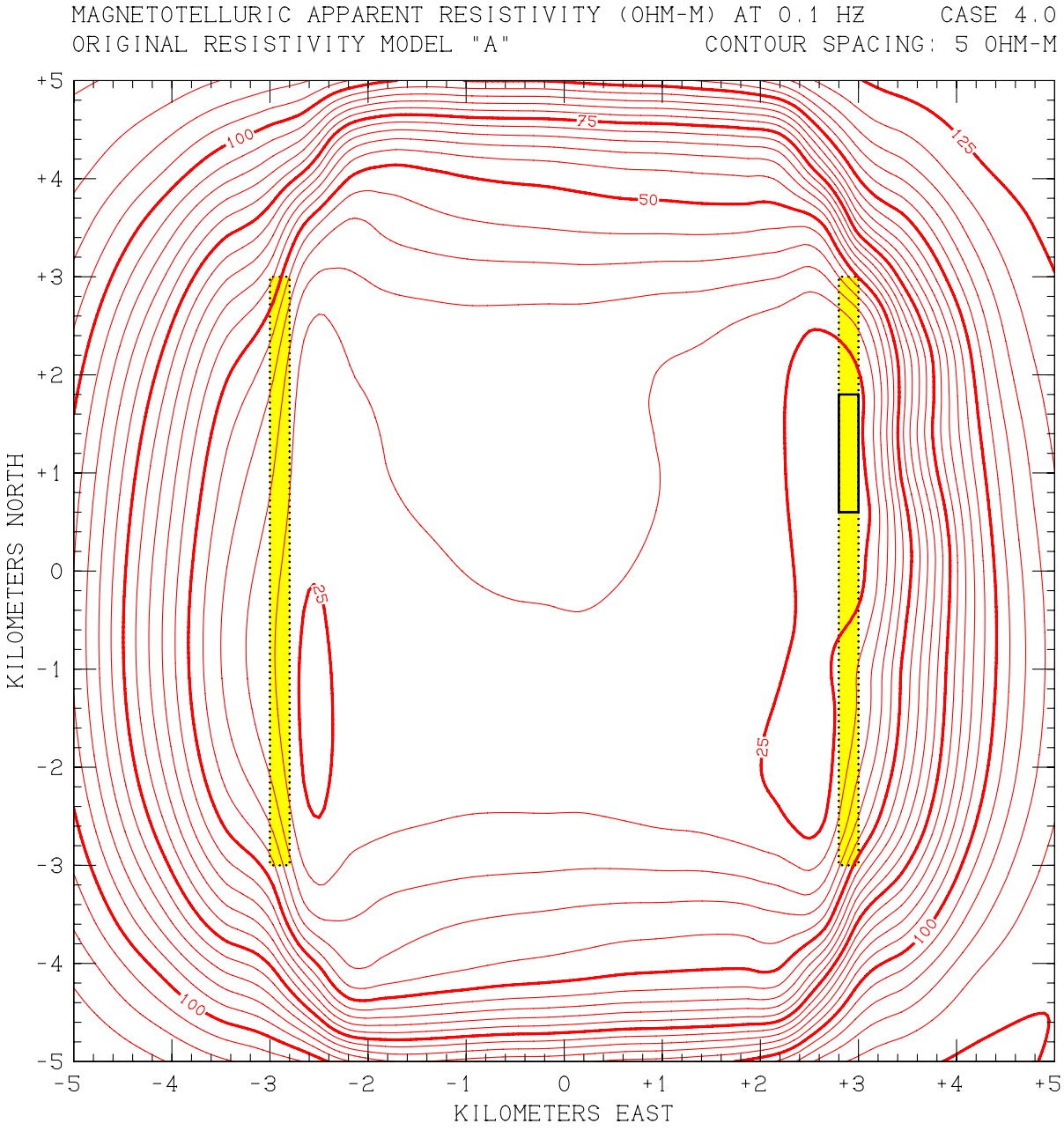

Figure A.11. Distribution of MT apparent resistivity at 0.1 Hz for "hidden western" reservoir (Case 4.0) using "original" electrical resistivity model *("A")*. Contour spacing is 5 ohm-meters.

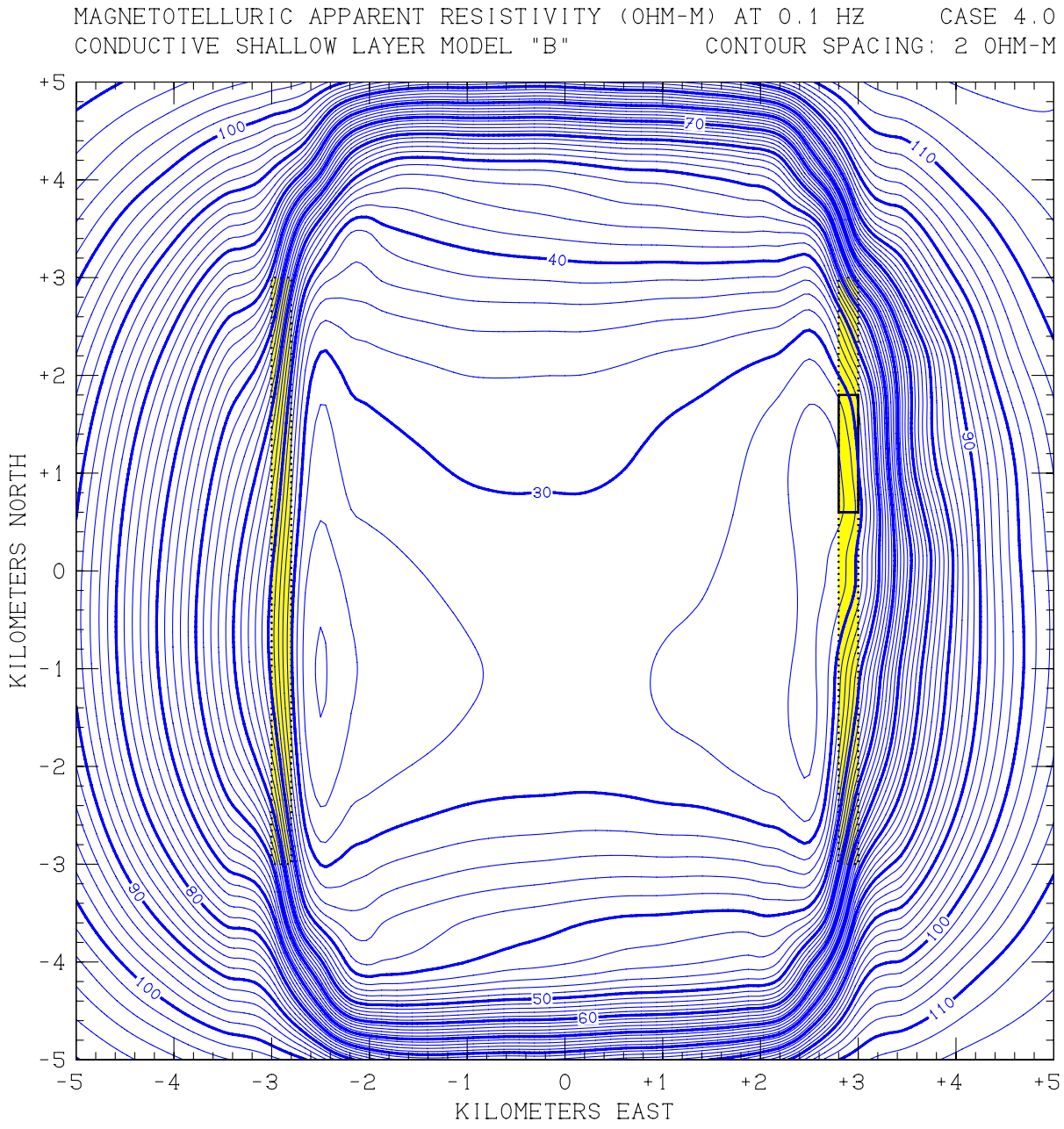

Figure A.12. Distribution of MT apparent resistivity at 0.1 Hz for "hidden western" reservoir (Case 4.0) using "shallow conductive" electrical resistivity model *("B")*. Contour spacing is 2 ohm-meters.

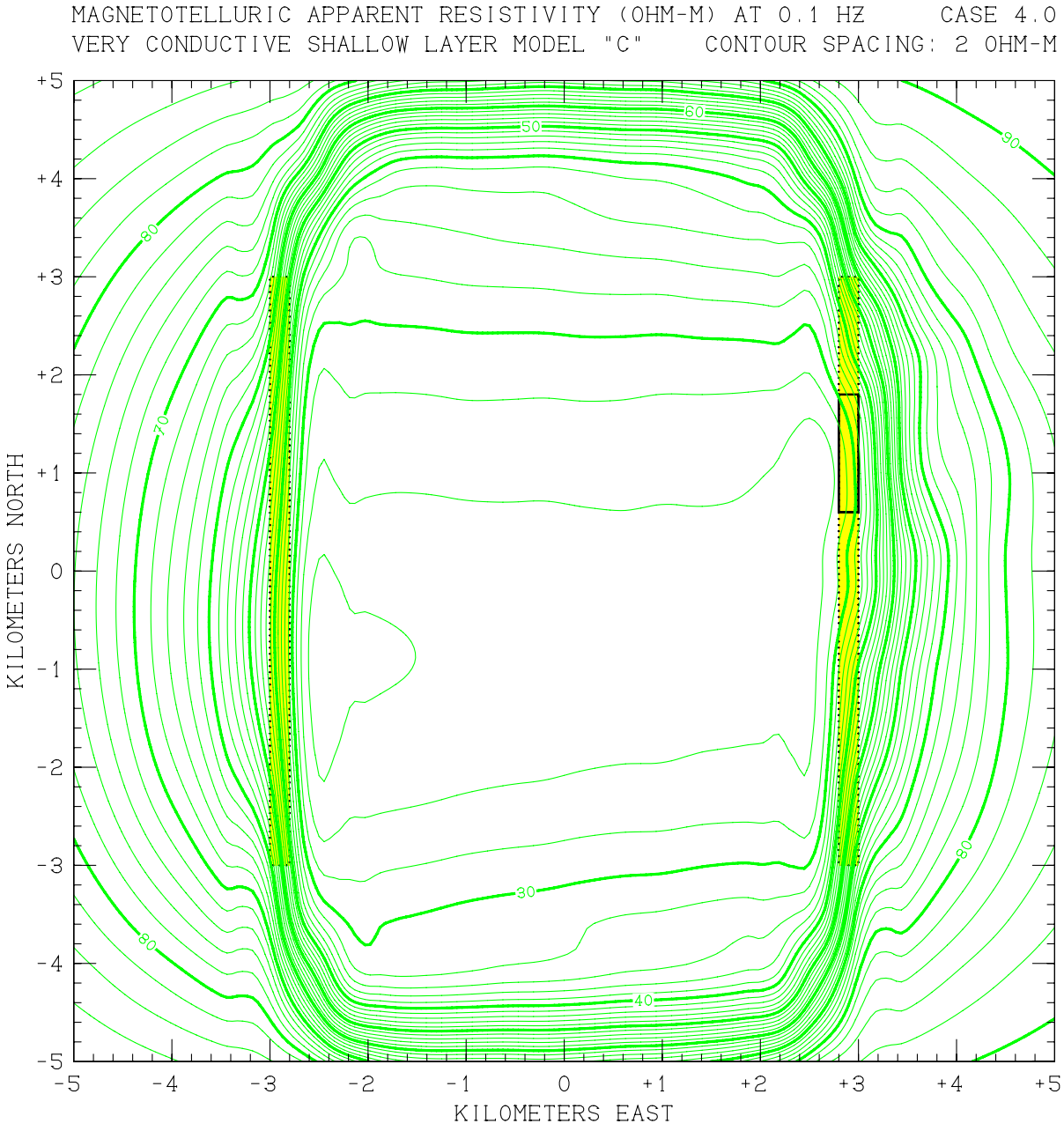

Figure A.13. Distribution of MT apparent resistivity at 0.1 Hz for "hidden western" reservoir (Case 4.0) using "shallow very conductive" electrical resistivity model *("C")*. Contour spacing is 2 ohm-meters.

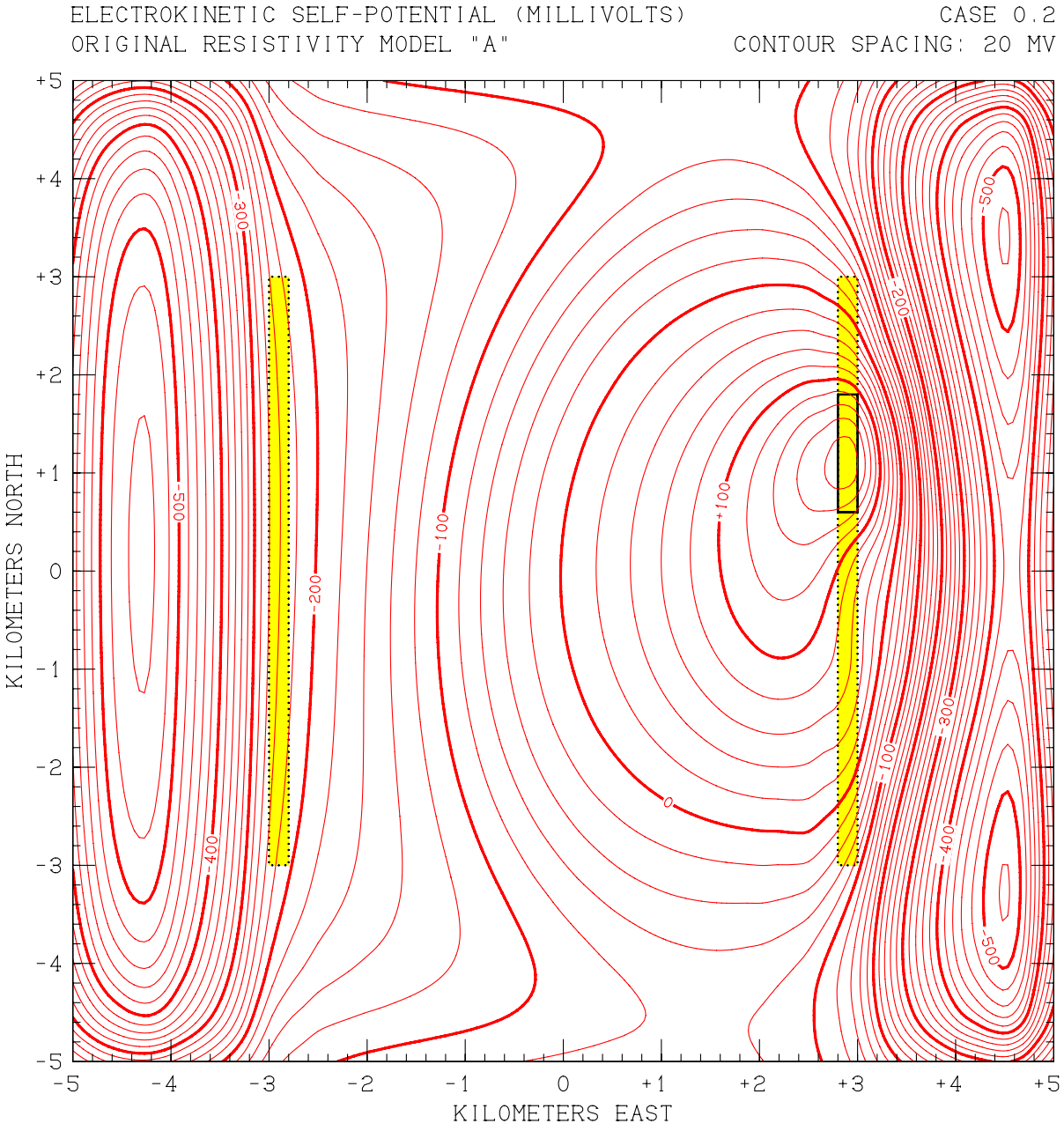

Figure A.14. SP distribution for "eastern" reservoir (Case 0.2) using "original" electrical resistivity model *("A")*. Contour spacing is 20 millivolts.

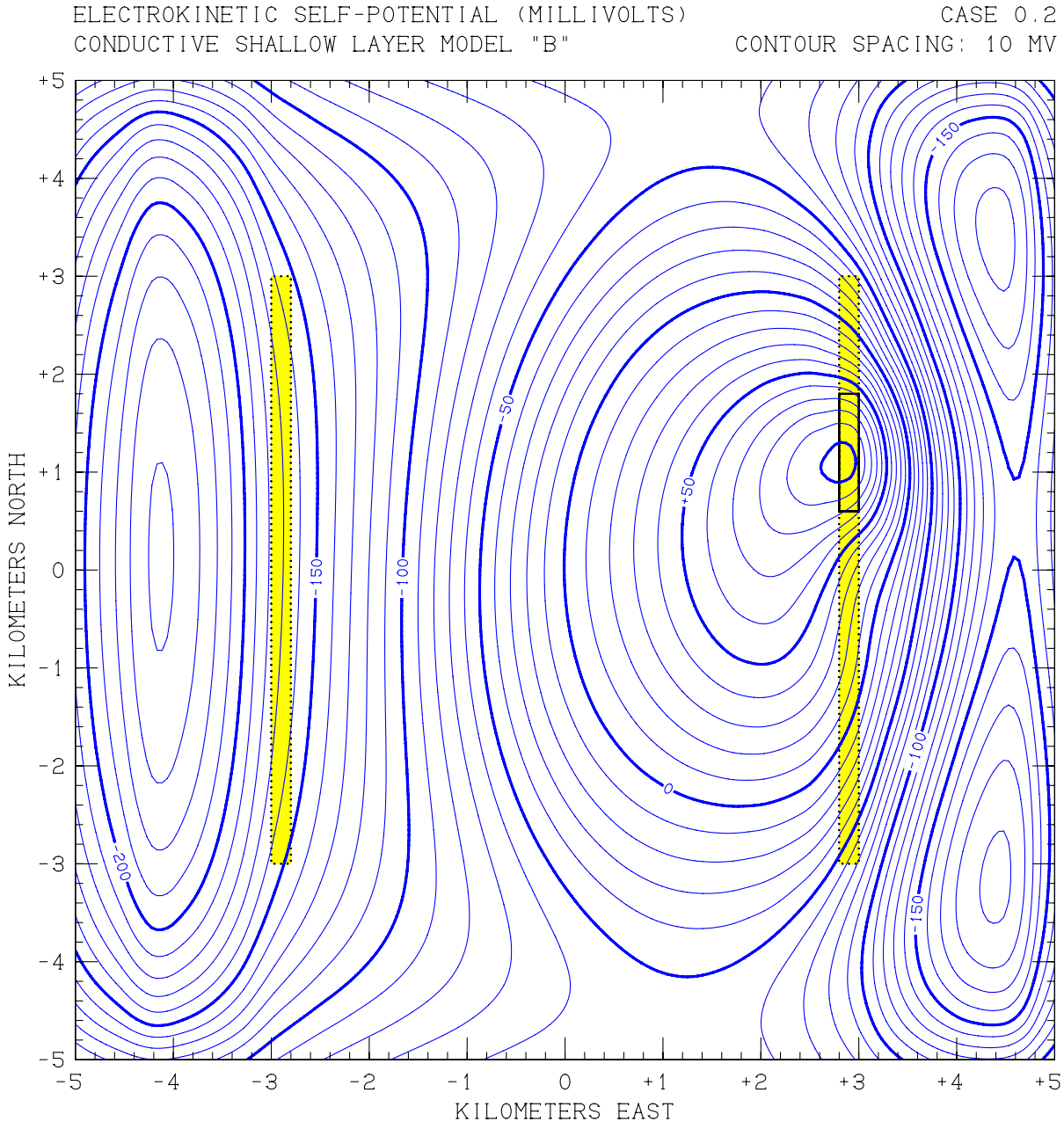

Figure A.15. SP distribution for "eastern" reservoir (Case 0.2) using "shallow conductive" electrical resistivity model *("B")*. Contour spacing is 10 millivolts.

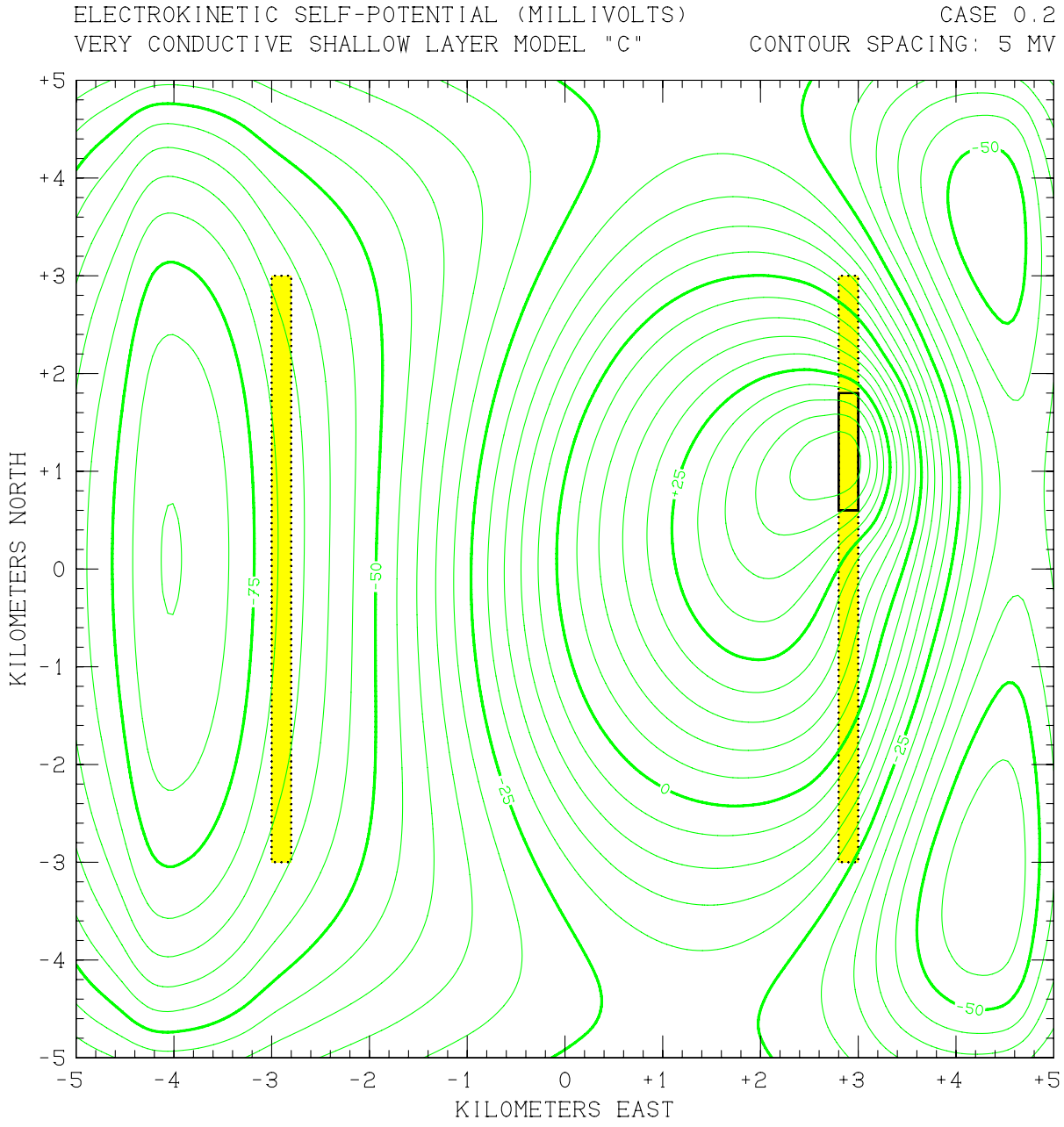

Figure A.16. SP distribution for "eastern" reservoir (Case 0.2) using "shallow very conductive" electrical resistivity model *("C")*. Contour spacing is 5 millivolts.

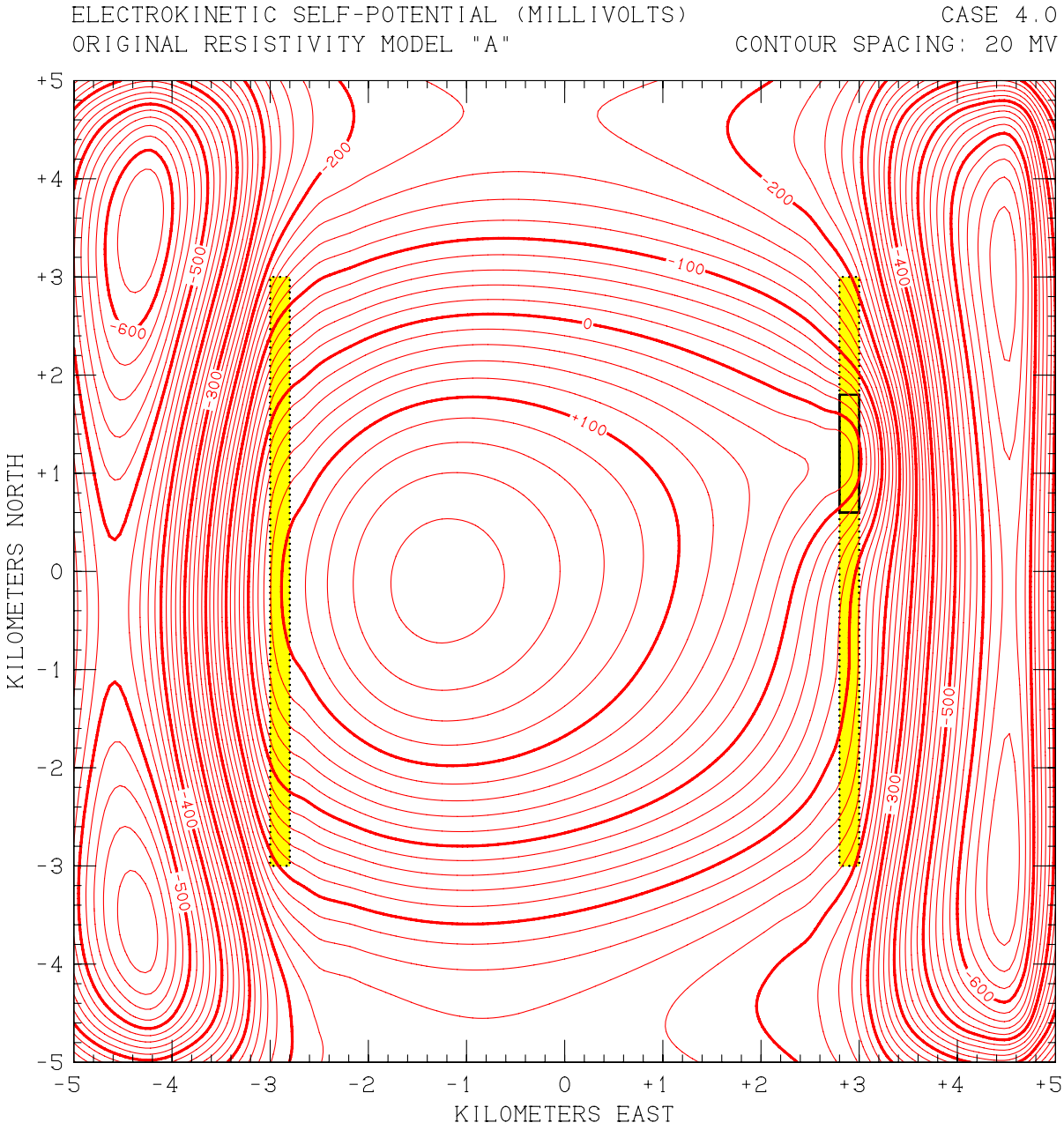

Figure A.17. SP distribution for "hidden western" reservoir (Case 4.0) using "original" electrical resistivity model *("A")*. Contour spacing is 20 millivolts.

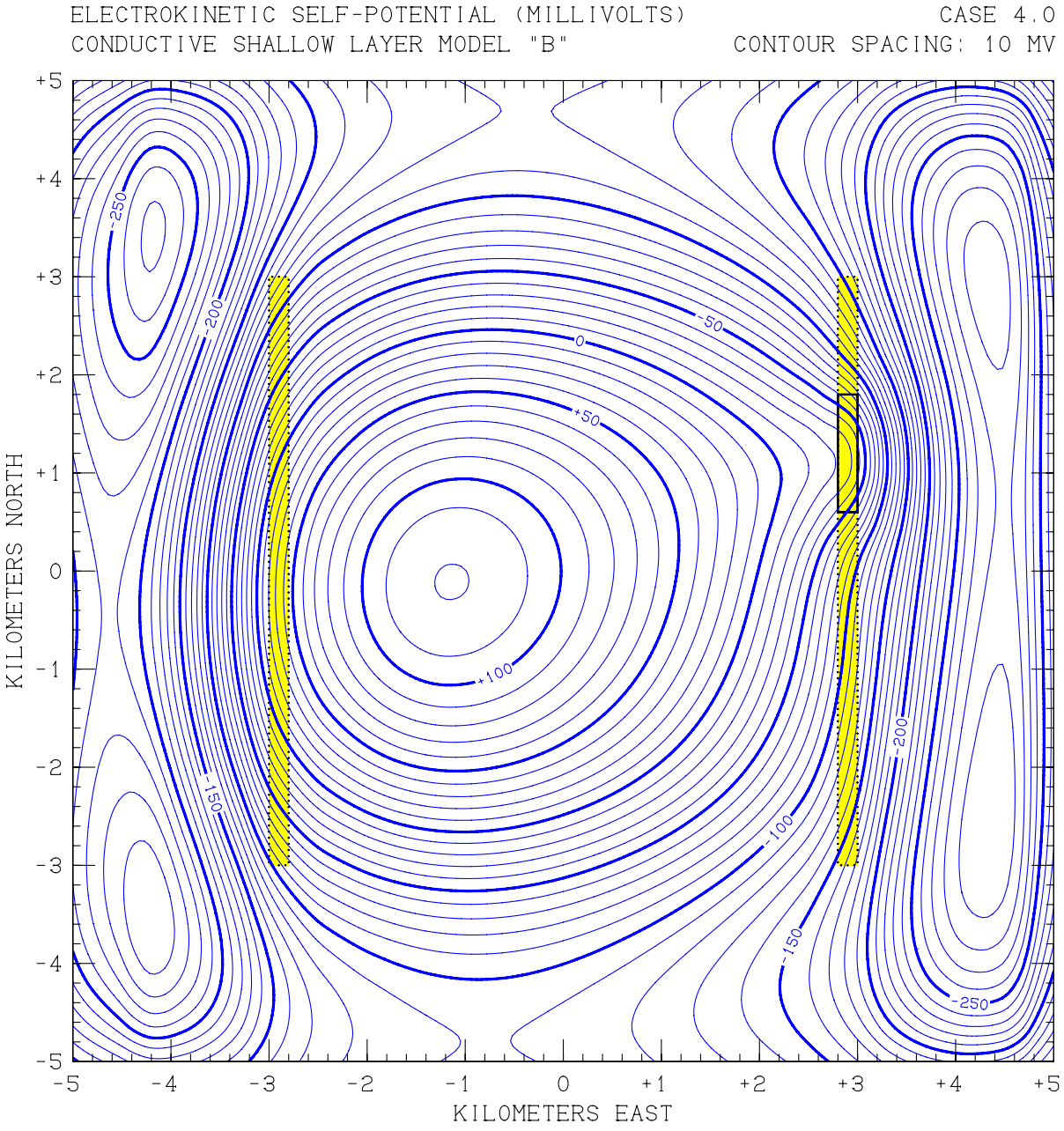

Figure A.18. SP distribution for "hidden western" reservoir (Case 4.0) using "shallow conductive" electrical resistivity model *("B").* Contour spacing is 10 millivolts.

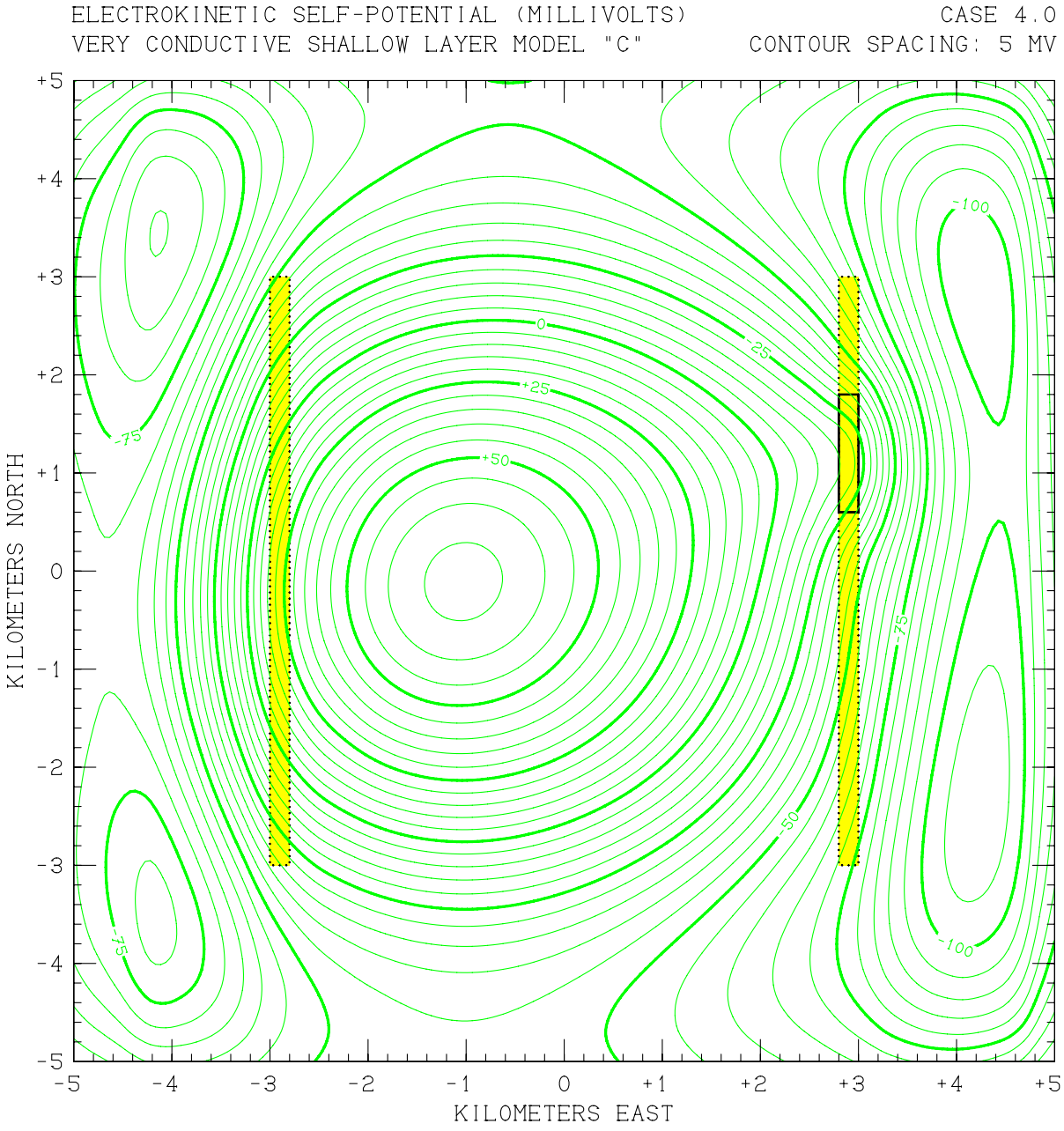

Figure A.19. SP distribution for "hidden western" reservoir (Case 4.0) using "shallow very conductive" electrical resistivity model *("C").* Contour spacing is 5 millivolts.

conductor is present. This topographic noise arises mainly from down-slope groundwater flow in the shallow part of the system where the electrical conductivity has been enhanced, reducing the resulting voltage disturbance according to Ohm's Law.

Despite the general decline in signal amplitude, the characteristic shapes and locations of the deep-origin SP anomalies for both Cases 0.2 and 4.0 are preserved and appear to be essentially independent of shallow conduction effects. As a consequence, it should be easy to distinguish Case 0.2 from Case 4.0 based on the self-potential distribution even if the shallow conductivity anomaly is as extreme as *"Model C"*. As noted above, the apparent resistivity signatures from the magnetotelluric (MT) survey are also distinct, and these distinctions persist whether or not a shallow conductive layer is present near the earth surface. It is concluded that the proposed prospecting approach is reasonably robust and should be effective even with significant variations in earth electrical structure.